Pulsed Power Driven Industrial Plasma Processing

PROEFSCHRIFT

door

Frank Jozef Cornelis Marie Beckers

Dit proefschrift is goedgekeurd door de promotoren en de samenstelling van de promotiecommissie is als volgt:

voorzitter:	prof.dr.ir. A.C.P.M. Backx
1^e promotor:	prof.ir. W.L. Kling †
2^e promotor:	prof.dr.ir. J.H. Blom
copromotor:	dr.ir. E.J.M. van Heesch
leden:	prof.dr. B.M. Novac (Loughborough University)
	Prof.Dr.Ing.habil. P. Zacharias (Universität Kassel)
	prof.dr. V. Hessel
	dr.ing. A.J.M. Pemen
adviseur:	ir. R.W.J. Smulders (Antea Group)

prof.dr.ir. J.H. Blom neemt tijdens de promotiezitting de taken van wijlen prof.ir. W.L. Kling over

Het onderzoek of ontwerp dat in dit proefschrift wordt beschreven is uitgevoerd in overeenstemming met de TU/e Gedragscode Wetenschapsbeoefening.

Contents

Summary

The work focuses on up-scaling of pulsed power induced corona plasmas for industrial processing. This kind of plasma processing ranges from removal or conversion of pollutants to synthesis of fuels. It is an electric processing technology that offers the advantage of time and space compressed high power enabling relatively small plasma reactors and high chemical efficiency at ambient temperature and pressure. Up-scaling of pulsed corona technology relates to pulsed power source and reactor, lifetime, reliability and efficiency. Processing relates to an instationary and inhomogeneous plasma-chemical system driven by nanosecond pulsed power. Industry appears through applications in pollution control problems in special cases: traffic emissions, toluene, and various other compounds.

The general frame of the work can be explained as conversion of electrical energy into pulsed corona discharges that initiate chemical processes. Not only high electrical efficiency but also high chemical efficiency is essential for successful introduction of corona technology in the industry. The field of study can be divided into three main topics: 1. Pulsed power generation: conversion of mains supply to nanosecond high voltage pulses. 2. Plasma generation: conversion of electrical pulses into streamer-corona plasma in a reactor volume. 3. Plasma processing: conversion of chemical components by streamer-corona discharges. Practical plasma processing is a challenge because industrial waste flows often contain various compounds under different circumstances (e.g. temperature, humidity, oxygen level, bulk gas) making it difficult to predict by-products and required plasma energy density. To investigate this, a semi-industrial scale pilot wire-cylinder type corona reactor and pulsed power modulator was constructed for on-site demonstrations and application research in the industry. Several applications are studied in detail using chemical diagnostics. The applied reactor has a multiple cylinder-wire type structure. If nanosecond pulses are applied to such a large structure, design rules are required to optimize energy distribution in the reactor. The energy sharing between multiple cylinders is investigated by applying nanosecond ICCD imaging. The role of cylinder length is investigated. Development of a robust long lasting switch is essential for the introduction of large scale pulsed corona systems and therefore widely discussed in this thesis. The repetition rate is

boosted by a novel circuit topology of a fast 30 kV, 5 kHz repetition rate capacitor charger. The work has led to the following results:

Development and proof of stand-alone apparatus for pulsed plasma driven processing. The spark gap power modulator is capable of generating 80 ns FWHM, 20 ns rise time, (up to) 10 J pulses with a maximum repetition rate of 1 kHz. This 10 kW power supply consists of a resonant capacitor charger, spark gap switch and a transmission line transformer. The corona unit is autonomous, can serve in continuous operation and is incorporated in a 20 feet freight container.

Demonstration and analysis of processing cases: pollution control for NO_x, toluene, limonene, ammonia and hydrogen sulfide. Pulsed corona technology was successfully demonstrated during several lab and field pilot tests. Removal of low levels of NO_x in traffic tunnels proves to be difficult. The pulsed corona discharges intrinsically produce ppm level NO_x at high energy densities, limiting the removal of low inlet levels. NO_x removal levels of 60-80 % were obtained for reactor inlet concentrations of 2-10 ppm. Removal of high level NO_x was successfully demonstrated at an incineration plant and during lab experiments. Up to 80 % conversion of 60-70 ppm NO_x was obtained. The conversion efficiencies for converting 14-59 ppm NO_x during lab experiments are 9.7-12.3 g/kWh. The degradation of VOCs requires high energy densities (up to 92 J/L). The degradation product spectra can be complex and can contain toxic compounds if the applied energy density is too low. Acceptable residual products at high energy densities are acetic and formic acid. A conversion rate near 100 % was achieved for H_2S. The conversion efficiencies were 7.4-10.8 g/kWh for 9-31 ppm inlet concentration. The conversion efficiency for 13.5 ppm NH_3 is 3.7 g/kWh. Reasonable results of particulate matter removal were achieved during a field test. The collection efficiency of the largest particle range is the highest, 94 % on average. The collection efficiency lowers as the particle size decreases: 89 % and 58 % for respectively the 2.5-10 μm and 1-2.5 μm range. The total collection efficiency (0.25-10 μm) is 60 %.

Modeling and design of an intelligent power modulator reliably feeding a stochastically behaving spark gap. Adaptive control, high pulse repetition rate, wide voltage regulation, and high output power are features of this device. A spark gap switch can fire spontaneously during charging (pre-firing) of the capacitor due to stochastic breakdown behavior. The resulting near short circuit of the output can easily be handled repetitively by the novel circuit. A 15 kW prototype has been built and proof of concept has been demonstrated. The charger is capable of charging a 8.4 nF capacitor to 30 kV in 35 μs with 91 % efficiency. The maximum repetition rate of this 3.8 J/cycle charger is 5 kHz.

Design, modeling and characterization of a long lifetime spark-gap system. The spark gap is probably the most critical component in the pulsed power system because of the recovery and erosion behavior. A novel N_2 closed loop spark gap purging system was developed which enhances the recovery (and thus increases the repetition rate)

of the switch efficiently. The required purging power was reduced to 14 % of the transferred power by the switch. This is a major energy saving improvement compared to spark gap switches which are purged with compressed air. The overall best recovery result was obtained by applying a N_2/H_2 (95/5) mixture in the closed loop system. The spark gap was able to operate up to 1 kHz in the triggered mode and the voltage recovery voltage was 62 % at 5 kHz repetition rate during continuous pre-fire operation. Multiple spark gap electrode materials were tested and copper proved to be the best material in this application. Erosion of the cathode length was reduced to zero and erosion of the anode was reduced to 165 μm/day. A model based on the heat diffusion equation has been developed to gain insight in the erosion behavior.

Design, modeling and characterization of a pulsed plasma reactor system. Nanosecond ICCD imaging has been applied to the demonstrator reactor to study streamer inception and propagation of the streamer plasma simultaneously in sixteen cylinders. Significant deviations in the development of the discharges were not observed when comparing the cylinders mutually. A 4.5 m long corona reactor has been constructed and equipped with voltage and current sensors (8 in total) to study plasma generation inside corona reactor cylinders as a function of reactor length. Strong reflections at the end of the reactor are observed during measurements for pulse rise times which are shorter than the transient time of the reactor. Local development of the streamers (number of streamers and/or speed) is affected by the reflection behavior resulting in an uneven energy distribution along the reactor. A lumped element SPICE model is developed to simulate the reflection behavior of the reactor. The source voltage has a strong effect on the impedance matching between source and reactor. Higher voltages result in more intense plasma generation and lower reactor impedances. Even if mismatches occur due to low reactor impedances, the energy transfer efficiency always increases when the voltage is increased. The high source voltage allows reflections in the system to be consumed by the plasma.

Introduction

The application of non–thermal plasmas for pollution control was first studied by Schwarz in 1876 to destruct hydrogen sulfide using ozone [1]. Werner Von Siemens invented the Dielectric Barrier Discharge (DBD) reactor for ozone generation earlier that year. Corona discharges for conversion of pollutants have been widely investigated since then. Some DBD and DC corona based systems are commercially available nowadays for degradation of relatively easy compounds. Much later work showed that nanosecond pulsed corona discharges are the most efficient [2–4] and most powerful. A few pulsed corona demonstration pilot plants were constructed since the 90s [5]. Most of them were deployed for conversion of NO_x and SO_x in flue gas. Energetic electrons in pulsed discharges create highly reactive radical species which are capable of degrading target pollutants such as NO_x. Although pulsed corona discharges are the most efficient and versatile for the conversion of pollutants, commercial devices are not available. However, strict legislation demands new technologies brought to market for specific emission problems where conventional technologies have poor performance or are economically not viable. Pulsed corona is especially suitable for low ppm (parts per million) pollutant concentration levels, typically between 1–1000 ppm, and can handle a variety of components simultaneously. Another unique feature is the capability to adapt the plasma power (and the required conversion level) on–demand.

A challenging task is the up-scaling of pulsed corona technology to handle large flows and to design pulsed power devices which are capable of energizing large reactors at high electrical efficiencies. In this thesis we focus on efficient high repetition rate pulsed corona plasma generation and plasma processing for large scale air purification applications.

1.1 Electrical discharges & plasma processing

Electrical discharges can be generated by an electric field produced between two electrodes [6]. To initiate a discharge, one or more free electrons are required. Free electrons as a result of e.g. cosmic radiation or radioactivity are always present in our atmosphere, typically 10^4–10^6 electrons/m^3. The electric field is highest near a sharp electrode (e.g. wire or point) with a strong non-uniform electric field. Initiation of the discharge will likely be in this inception zone. A free electron will be accelerated in

(a) Anode directed streamer.

(b) Cathode directed streamer.
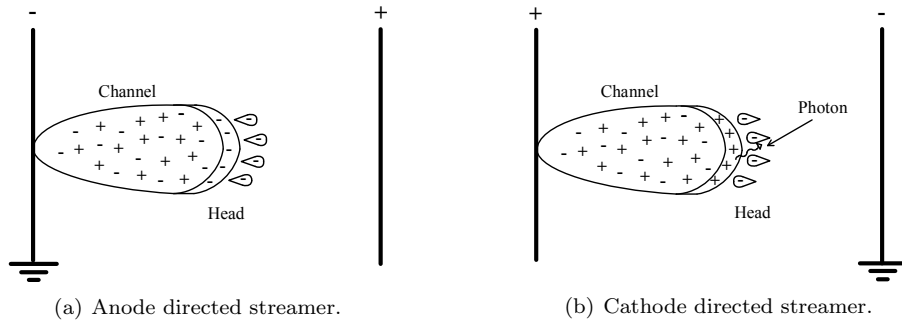
Figure 1.1

the electric field and is capable of liberating an electron from a molecule upon collision if sufficient energy is gained by the electron. The molecule is now ionized and an additional electron has become available which is also accelerated in the electric field. The electrons multiply rapidly causing an electron avalanche. The avalanche develops a self–induced electric field because electrons and less mobile positive ions move in the opposite direction. The avalanche transits into a streamer when the self–induced electrical field is of the same order of magnitude as the applied electric field. A large field enhancement is present in front of the head of the streamer, resulting in many new electrons which are created in front of the head. A channel like appearance of the streamer results from the head which propagates in the direction of the electric field. This type of streamer formation is called anode directed (ADS) because the negative electrons travel in the same direction as the streamer head towards the anode, see Figure 1.1.

Cathode directed streamer (CDS) formation is more complicated because electrons travel in the opposite direction of the electrical field. The discharge will be initiated near the non-uniform electric field of the sharp anode. Accelerated electrons create high energy photons upon collision with molecules, the electrons are sunk into the anode as they reach the electrode. The photons are capable of initiating ionization and secondary electron generation in front of the streamer head in the opposite direction. CDS or positive streamers can therefore propagate in the opposite direction of the electrons.

In this thesis we will only consider cathode directed streamers because they have a lower inception voltage and lower resistance [2]. Energy transfer to the reactor is therefore more easy to accomplish. This is essential for large scale systems with high electrical efficiency.

Some of the high energy electrons in the streamer discharge are also capable of dissociating molecules upon collision. The fragments of these molecules are highly reactive reactive species, called radicals. Dissociated oxygen and water vapor molecules result in atomic oxygen and hydroxyl radicals. The species have a short lifetime, typically in the microsecond range [7]. Ozone (O_3) is a strong oxidizer which is also created and can exist for a long time at low temperatures. During air purification plasma processes,
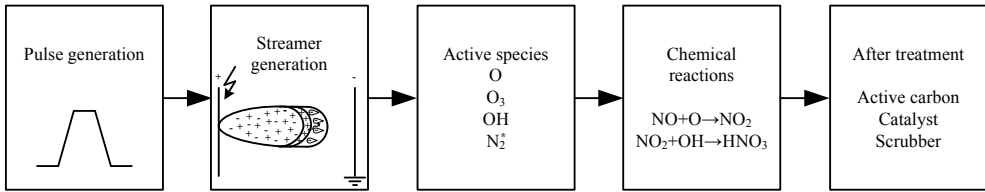
Figure 1.2: Streamers are generated by applying nanosecond high voltage pulses to a reactor. Fast electrons in the streamer heads create active species upon collision with the bulk gas. These species react with the pollutants. Conventional technologies are used to remove conversion products if necessary.

these species react with other target molecules (pollutants), converting hazardous pollutants into less harmful compounds or compounds which can be easily removed with conventional technologies such as wet scrubbers, catalysts or active carbon [8]. The plasma processing steps for air purification are summarized in figure 1.2.

The streamers travel with a speed of 1–$2 \cdot 10^6$ m/s in atmospheric conditions if a fast rise–time high voltage pulse is applied to the electrodes. Basically, the higher the voltage and rate of rise applied to the electrodes, the higher the electron acceleration (and energies), and the more efficient radicals are produced. A fast nanosecond rise time is required to build up the electric field between the electrodes as fast as possible after the discharge is initiated in the inception zone. Research shows that the number of streamers and streamer thickness increases with faster rise times and higher voltages [2, 9]. For processing efficiency, a large streamer volume is desirable. The streamer head propagates to the opposite electrode until it crosses the gap. An ionized channel is now formed which will heat up if the voltage over the electrodes remains present. If sufficient energy is applied, the channel can heat up to thousands of degrees Kelvin, transiting from a streamer discharge into a spark discharge. Streamers are a form of non-thermal plasma while sparks are thermal plasma. The resistance of a streamer channel is relatively high, typically in the multi kΩ range for 5–10 cm long discharges. Spark discharges on the other hand, have a very low resistance, in the Ohms range. To prevent transition into a spark and resulting energy dissipation, we allow only the primary streamer to cross the gap. A small amount of additional energy fed to the ionized channel is allowed because radicals can still be produced (less efficiently) in the channel for a limited time frame. This time frame is referred to as the secondary streamer regime. Ideally we want to apply a square high voltage pulse to the electrodes. The width of the pulse should be equal to the propagation time of the primary streamer. Figure 1.3a shows the top view of a typical corona reactor for air purification, a wire–cylinder reactor. The process gas flows axially through the grounded cylinders which are visible in the image. A 20–ns rise time pulse is applied to the wires in the center of reactor cylinders. Figures 1.3b–d show the inception of streamers and propagation of the streamers at multiple moments in time. The streamers cross the 7.5 cm gap in approximately 80 ns. The images are captured using an intensified CCD camera,

| (a) | (b) 10-20 ns | (c) 40-50 ns | (d) 80-90 ns |
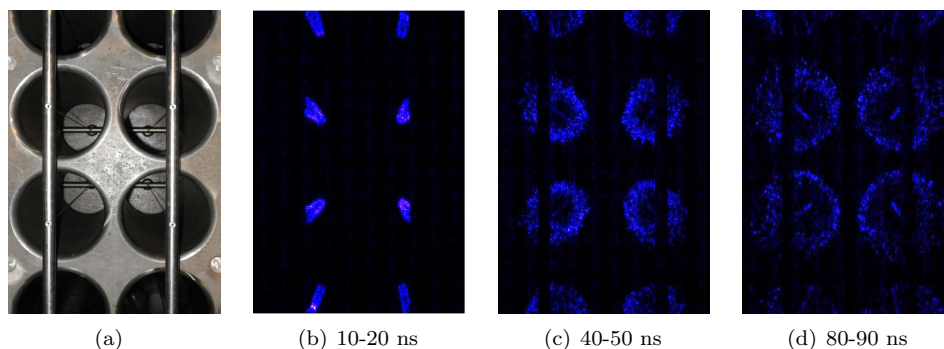
Figure 1.3: Streamer propagation in 8 parallel wire–cylinder reactor cylinders. The diameter of the cylinders is 15 cm. The wires are suspended on the vertical bars which are visible in (a). The streamers propagate with a typical speed of 1–$2 \cdot 10^6$ m/s. Images b–d illustrate the development of the streamers from the wire in the center to wall of the cylinders. These images are captured using an ultra fast ICCD camera with exposure times of less than 10 ns.

especially the heads of the streamer are bright and appear as dots in the images. Typically 1–2 streamers per mm leave the wire in a random direction, creating an inhomogeneous and instationary plasma.

Exposure of a full pulse clearly shows the streamers which develop like channels between the wire and cylinder wall, see Figure 1.4a. Figure 1.4b shows a 30–s exposure image of a repetitive streamer plasma (500 pulses per second) in the same reactor. The plasma looks homogeneous to the naked eye because excited nitrogen molecules emit photons during their de–excitation on a much longer time scale than the nanosecond streamers and because the image shows an overlap of 15000 repeated random streamer developments.

1.2 Pulsed power technology for plasma generation

Pulsed power technology is the vital tool to generate the high voltage pulses which are required for streamer plasma generation. A challenging task is the up-scaling of pulsed corona technology to handle large flows, typically 10.000-100.000 $\mathrm{Nm^3}$/h (Normal cubic meter per hour). The needed plasma power for removal of compounds can be between 10–300 kW depending on the flow, pollutant, concentration level, needed conversion level, etc. All this power needs to be compressed into repetitive pulses which are less than 100 ns wide. A multiple stage pulsed power system has been developed to achieve this goal. Figure 1.5 shows an overview of the components in our pulsed corona setups. First, a capacitor charger is applied to charge a high voltage energy storage capacitor. The energy is released into a pulse forming network via a high power closing switch. Finally, a high voltage pulse is generated and fed to the reactor. There are multiple

(a) ICCD camera (100 ns exposure)

(b) DSLR camera (30 s exposure)
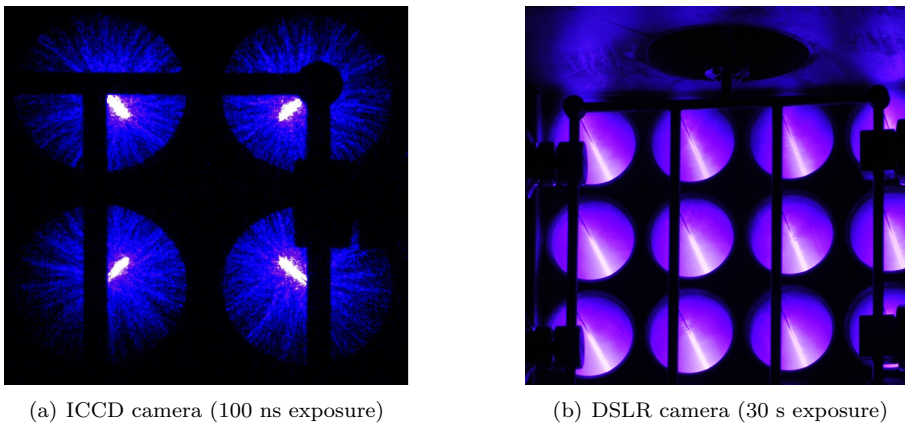
Figure 1.4: Top view of a 16 cylinder corona reactor.

strategies possible to feed the needed power to the reactor. One option could be to use a large electrode distance. Streamers propagate for a longer time period, pulses can be wider, a higher voltage is needed, resulting in a large amount of energy per pulse which can be applied to the reactor. A second strategy would be to apply a limited amount of energy per pulse but at a higher repetition rate. The last option is preferred because on average the plasma in the reactor becomes more homogenous. Radicals are short-lived and quench if they are not able to initiate chemical reactions. From a plasma processing efficiency point of view it is better to create the radical flux more distributed in time [10]. So an efficient switch is needed which is capable of switching tens of kilovolts, multiple kilo amperes with nanosecond rise time and repetition rates in the kHz range. Solid state switches are unfortunately not capable or not suitable for handling these switching characteristics. High switching losses, high risk of damage, a large number of parallel and/or series elements are required and the resulting high cost are major drawbacks. Magnetic pulse compression (MPC) [11, 12], drift step recovery diodes [13] or SOS diodes can be considered but the efficiencies are often limited. Spark gaps are very efficient compared to other switching methods but are often considered unreliable because of their erosion, recovery and stochastic breakdown behavior. A thermal plasma between two electrodes evaporates a small amount of electrode material at every switch moment. The gas between the electrodes which acts as a dielectric insulator needs to recover after switching before it can hold off the full switching voltage again. The repetition rate of the switch is therefore limited. Designing an efficient, high repetition rate, robust spark gap will be the key for creating industrial size pulsed corona systems.

Capacitor charging	Energy storage	Switching	Pulse forming voltage doubling	Plasma generation
30-90 kV	10-100 J	3.7 kA ns rise time	60-180 kV 100-300 ns	Ø 15-45 cm
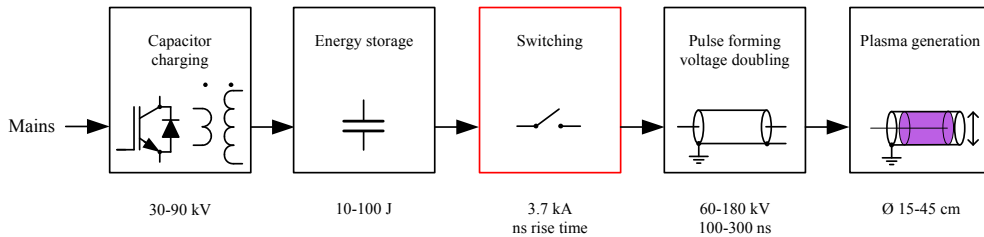
Figure 1.5: Component overview of a pulsed corona system. A high voltage capacitor is charged by a fast capacitor charger. The energy is discharged in nanoseconds into a pulse forming line via a high power closing switch. The generated pulse is fed to the corona reactor.

1.3 Project goals

Eindhoven University of Technology and HMVT-Antea Group started a collaboration to explore the applicability of the technology with as ultimate goal development and introduction of successful products. The first step was to construct a prototype for on-site demonstrations to show the potential of pulsed corona technology to customers in the air purification business. During this process, a view into up-scaling of the technology resulted into several research topics which acquired attention. Multiple technical challenges need te be resolved for successful introduction of pulsed corona technology into the market. The power level and the repetition rate of the plasma system needs to be increased. Reactors need to be designed for large flow handling and large plasma volumes.

The first project goal resulted from the desire to explore the applicability in the industry.

- Development of a robust and fully autonomous pulsed corona demonstration unit which can be applied for on-site air purification pilots.

- Exploring multiple air purification applications with the demonstration unit.

TU/e and HMVT-Antea Group developed a 10 kW pilot unit which was successfully demonstrated during a series of field and lab experiments. Experimental data of multiple air purification applications were acquired. The repetition rate and output power of the pulsed power supply proved to be limited. Mainly caused by the spark gap switch which was therefore a focus area. Also the life-time of spark gap switches is limited, therefore lifetime estimation and improvement is of great importance. Energizing a large corona reactor with nanosecond pulses proved also to be challenge. Industrial size reactors need to be capable of handling thousands of cubic meters of air per hour. Due to the physical size of the reactor, pulse rise-times approach the transient time of the reactor structures, resulting in reflections and interaction with plasma generation. The latter focus areas resulted in the following project goals:

- Development and characterization of an efficient pulsed power system which can operate in the kHz range.

- Life-time and recovery characterization of the spark gap switch. Modeling of the erosion behavior of the spark gap electrodes.

This goal was achieved by creating a novel fast capacitor charger (5 kHz repetition rate) which is optimized for spark gap switches. A closed loop purging system was developed to enhance the recovery time of the spark gap. Switching performance was characterized and a model was developed which gives insight in the erosion behavior.

- Study the energy coupling between the pulsed power source and large corona reactors.

An additional pulsed corona setup was composed with a long corona reactor to investigate the energy distribution and reflection behavior inside long reactor cilinders. Energy sharing between multiple reactor cilinders was investigated in the demonstration unit. Also the impedance matching between source and reactor and the effect on energy transfer efficiency was investigated.

1.4   Chapter overview

- **Chapter 2**   In this chapter we describe the demonstration unit for air purification. Design considerations for the pulse source are discussed. Reactor and required ancillary devices are described.

- **Chapter 3**   A novel 5 kHz repetition rate capacitor charger which is optimized for spark gap based pulsed power systems is described in this chapter. Circuit modeling, design and implementation are discussed.

- **Chapter 4**   In this chapter we extensively discuss the switching performance of the pressurized spark gap. Electrode erosion is modeled and measured. Recovery and switching performance is characterized.

- **Chapter 5**   Design considerations for the reactor are discussed and energy distribution in large corona reactors is characterized with multiple setups. Also the electrical transfer efficiency from source to the plasma is investigated.

- **Chapter 6**   Plasma processing data of multiple applications which is gathered during field and lab experiments with the demonstration unit is presented in this chapter.

- **Chapter 7**   In the final chapter we present the conclusions and our recommendations for future work.

2

Pulsed power technology for industrial demonstration

Abstract

An autonomous semi-industrial scale pilot wire-cylinder type corona system has been constructed for on-site air purification demonstrations in the industry. The reactor is powered by a 10 kW spark gap based pulsed power supply, capable of generating 60 kV 80 ns wide pulses with 1 kHz repetition rate. The pulses are optionally superimposed on a 0-30 kV DC-bias to enable electrostatic precipitation. Autonomous operation of the system is enabled by a PLC system and dedicated control system.

2.1 Introduction

Pulsed corona technology for air pollution control has been widely investigated by lab experiments in a controlled environment. A challenging task is the up-scaling of pulsed corona technology to handle large flows and finding suitable applications. Although pulsed plasma technology has increased complexity in comparison to dielectric barrier discharge (DBD) [15,16] or DC plasmas [17,18], it offers more advantages making it more suitable for scale-up. It enables high plasma energy in a relative small reactor volume, enables plasma generation in harsh conditions (e.g. temperature, dust/contamination, varying gas composition) and has increased radical production efficiency due to short pulses [2–4].

Waste flows often contain various components under different circumstances (e.g. temperature, humidity, oxygen level, bulk gas) making it difficult to predict by-products and required plasma energy density to convert or remove the target components to an acceptable level. Thereby the air purification business consists mainly of conventional technologies and is sceptical towards novel concepts. On-site demonstrations in the

Part of the content in this chapter has been published previously in [14]:

- F.J.C.M. Beckers, W.F.L.M. Hoeben, T. Huiskamp, A.J.M. Pemen, and E.J.M. van Heesch. Pulsed corona demonstrator for semi-industrial scale air purification. *IEEE Transactions on Plasma Science*, 41(10):2920–2925, 2013
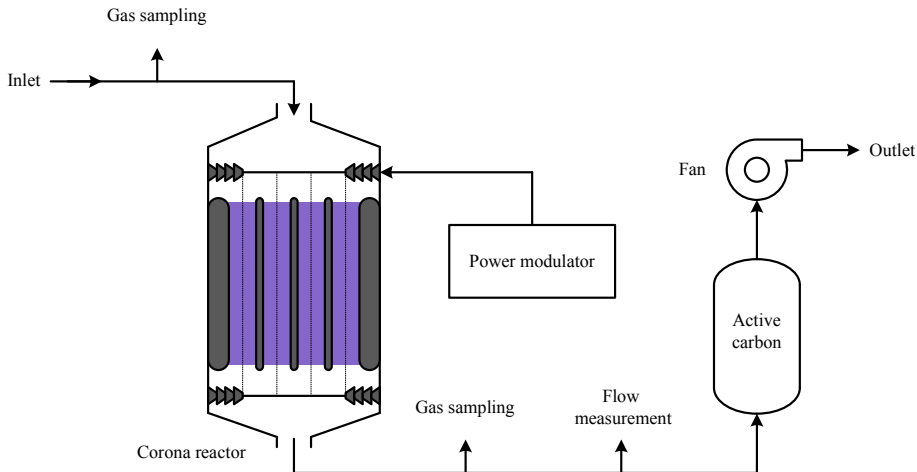
Figure 2.1: Schematic overview pulsed corona demonstrator.

industry of pulsed corona technology are required to verify applications, estimate investment and operational costs (e.g. energy consumption) and to stimulate interest by costumers for the technology. To achieve these goals, an autonomous semi-industrial scale pilot wire–cylinder type corona reactor has been constructed for on-site demonstrations and application research in the industry. Only limited examples of on-site corona research are available in literature [19–28]. The majority of these pilot tests focussed on removal of NO_x and SO_x in flue gas.

Our first demonstration setup consisted of an electrode–plate type reactor and nanosecond spark gap based pulsed power supply which was used for initial lab experiments. The reactor was initially designed for DC/AC corona generation [29] and converted for pulsed operation. This reactor setup was later discarded because of poor electrical transfer efficiency from the pulse source to the reactor. A robust wire–cylinder type corona reactor and more powerful 10 kW pulsed power supply is subsequently applied for further research. The corona reactor was build for tar cracking in syngas and first described in the PhD thesis of Yan [30]. Winands [2] performed the first successful air purification test with this reactor at a compost processing facility. At that point the reactor, power supply and ancillary equipment were separate parts which needed to be assembled on-site.

The system is now substantially redesigned and almost completely rebuild for continuous operation. The reactor was fitted on a new frame so it could be incorporated in a 20 feet freight container for easy transportation (see image 2.2). The reactor was fitted with new high voltage feedthrough insulators, the spark gap was partially redesigned, the DC-bias system was completely redesigned and a different resonant charging unit was composed. The only part of the system which remained untouched was the transmission line transformer. Multiple newly designed systems enable au-

Figure 2.2: Pulsed corona pilot container at a domestic waste handling facility.

tonomous operation and remote control of the pilot demonstrator. Various characteristics such as plasma power, pulse source performance, reactor process flow and temperatures are continuously monitored. Multiple supporting ancillary devices were installed in the container to enable plug and play on-site demonstrations. A fan pulls the processed air at a pilot facility through the corona system (see Figure 2.1). An active carbon filter is added to remove ozone [31] and residual components [32] from the effluent gas flow which enables safe emission at ground level outside the container. Advanced chemical diagnostics can be applied to sample the in- and effluent process gas of the corona reactor to study conversion efficiency of components and formation of by-products.

This chapter will give an overview of the demonstrator components and the most important design considerations for the pulse source. A part of this work has been previously described in [2,30] and will therefore not be extensively repeated. Multiple ancillary devices will be described in Section 2.3.2. The plate–electrode reactor setup which was initially applied for some of the plasma processing experiments is briefly described in the last Section.

2.2   Power supply

The spark gap based power modulator can be divided into multiple parts which compresses mains power into 80 kV, 1.5 kA, 80 ns FWHM pulses with 1 kHz maximum repetition rate, see figure 2.3. A resonant capacitor charger charges the energy storage capacitor C_h to 30 kV. The spark gap switch is subsequently triggered by an RLC circuit and the energy is discharged into the reactor via a transmission line transformer
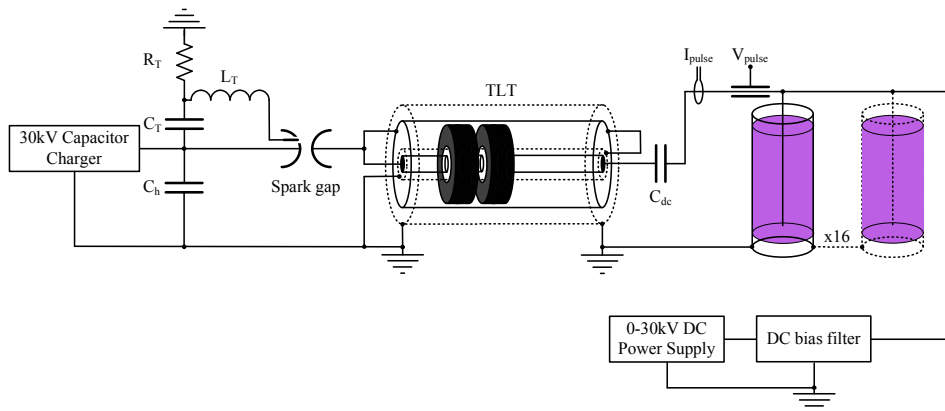
Figure 2.3: Schematic overview of the power modulator.
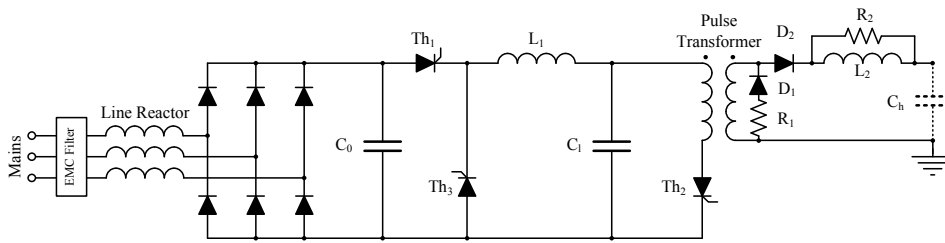
Figure 2.4: Resonant capacitor charger schematic.

(TLT) which doubles the voltage to 60 kV. The generated pulse is superimposed on the DC-bias voltage (typically 20 kV) via coupling capacitor C_{dc}. The DC-bias filter network holds off the 60 kV pulses to protect the DC supply and recharges C_{dc} after pulse generation to restore the bias voltage on the reactor.

2.2.1 Resonant capacitor charger

C_h (15 nF) is charged in 40 μs to 30 kV with 1 kHz repetition rate by the resonant capacitor charger which is described in [33]. A simplified schematic is shown in Figure 2.4, snubber circuits over the thyristors, inrush relays and thyristor gate drive circuits are omitted. The component values are shown in Table 2.1.

The charger operates by successively triggering three thyristors during each charging cycle. Each schematic in Figure 2.5 corresponds to a thrysitor which is triggered and a time slot (t_x-t_{x+1}) of the voltage and current waveforms in Figure 2.6. C_0 is continuously charged by mains to 500–540 V via a three phase rectifier, a line reactor is added to improve the power quality of the device [34].

Table 2.1: Capacitor charger component values.

Component	value
C_0	3300 μF
C_l	18 μF
C_h	15 nF
L_1	25 μH
L_2	600 μH
R_1	5 kΩ
R_2	4 kΩ
N	40
L_s	15.7 μH
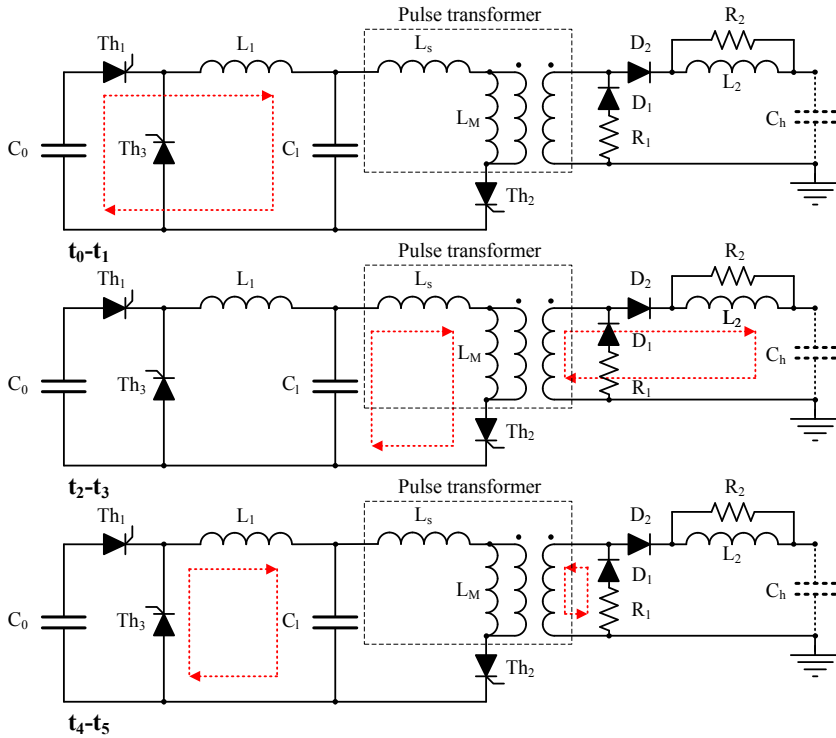
Figure 2.5: Equivalent circuit of the resonant capacitor charger. Each schematic corresponds to the current path (red arrows) in the circuit after triggering a thyristor.
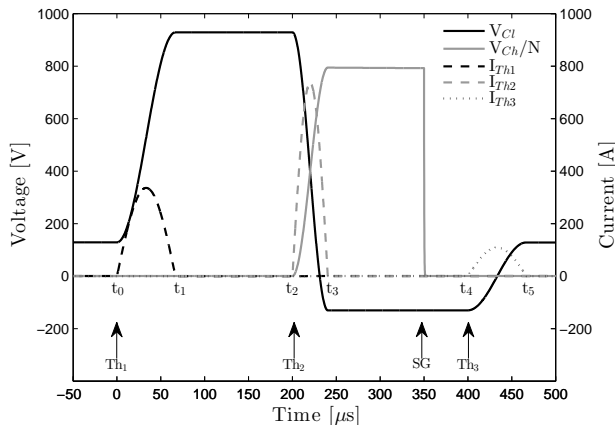
Figure 2.6: Resonant capacitor charge cycle (Full charge operation).
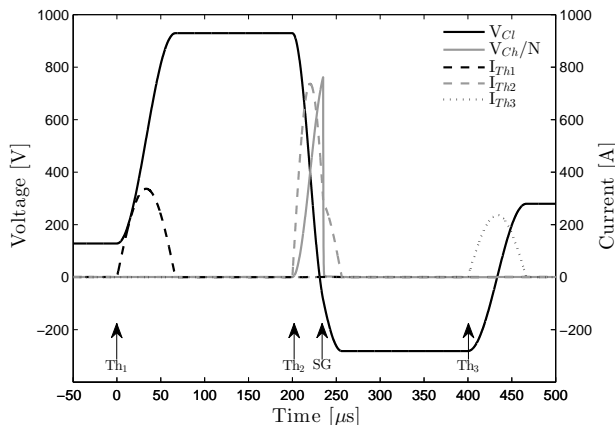
Figure 2.7: Resonant capacitor charge cycle (Pre-fire operation).

$(t_0 - t_1)$ C_l (18 μF) will be resonantly charged after the first thyristor (Th_1) is triggered. The charging level is determined by the initial voltage on C_l $(V_{Cl}(t_0))$ and the voltage on the supply buffer, see Equation 2.1. The equation can be simplified to Equation 2.2 because $C_0 >> C_l$ (3300 μF $>>$ 18 μF).

$$V_{Cl}(t_1) = V_{Cl}(t_0) + \frac{2C_0}{C_0 + C_l}\left(V_{C0}(t_0) - V_{Cl}(t_0)\right) \tag{2.1}$$

$$V_{Cl}(t_1) \approx 2V_{C0}(t_0) - V_{Cl}(t_0), \quad C_0 >> C_l \tag{2.2}$$

The charging time T_{Th1} can be calculated by Equation 2.3 and has a value of 66.5 μs. The peak current through Th_1 can be calculated by Equation 2.4.

$$T_{Th1} = \pi\sqrt{L_1 C_{tot}} \;, \quad C_{tot} = \frac{C_0 C_l}{C_0 + C_l} \tag{2.3}$$

$$\hat{I}_{Th1} = \frac{V_{C0}(t_0) - V_{Cl}(t_0)}{\sqrt{L_1/C_{tot}}} \tag{2.4}$$

($t_2 - t_3$) The energy stored in C_l will subsequently be resonantly transferred to C_h after triggering Th_2. L_2 (600 μH) and R_2 (5 kΩ) form a low pass filter which enables lossless transfer of the charging energy to C_h but dampens transients which occur when the capacitor rapidly discharges during pulse generation. The stray inductance (L_s) of the pulse transformer is part of the resonant circuit. The winding ratio of the transformer (N) and L_s is respectively 40 and 15.7 μH. A complete energy transfer will be achieved under the condition that $C_l = N^2 C_h$ (see Equation 2.5 and 2.6).

$$V_{Ch}(t_3) = \frac{2N C_l}{C_l + N^2 C_h} V_{Cl}(t_1) \tag{2.5}$$

$$V_{Cl}(t_3) = \left(1 - \frac{2N^2 C_h}{C_l + N^2 C_h}\right) V_{Cl}(t_1) \tag{2.6}$$

These capacitor values are not matched in practise to create a negative residual voltage on C_l ($C_l < N^2 C_h$), see Figure 2.6 at t_3. Thyristors need a negative voltage after the zero crossing of the current for proper turn-off [35]. The fast thyristors which are applied in the circuit need at least 100 V negative voltage during their specified turn-off time (t_q). The negative voltage over Th_1 is typically 300–500 V after the zero-crossing of the current through the device, additional attention is not required for this thyristor. The charging time T_{Th2} can be calculated by Equation 2.7 and has a value of 42 μs. The peak current through Th_2 can be calculated by Equation 2.8.

$$T_{Th2} = \pi\sqrt{\left(L_s + \frac{L_2}{N^2}\right) C_{tot}} \;, \quad C_{tot} = \frac{C_l N^2 C_h}{C_l + N^2 C_h} \tag{2.7}$$

$$\hat{I}_{Th2} = \frac{V_{Cl}(t_1)}{\sqrt{\frac{L_s + (L_2/N^2)}{C_{tot}}}} \tag{2.8}$$

($t_4 - t_5$) C_h is now fully charged and the spark gap can be triggered. When firing of the spark gap occurs during charging, the closed gap and TLT acts as a low load impedance. The resulting underdamped $R_{gap} - L_{stray} - L_2 - C_l$ circuit causes

the remaining voltage on C_l to reverse, see Figure 2.7. Although the energy is not lost, the voltage on C_l becomes more negative as the spark gap fires earlier during the charging of C_h. Recharging C_l during the following cycle would lead to excessive overcharging of the capacitor, see Equation 2.2. This will result in a higher charging voltage on C_h and increased prefire probability, reversing the voltage on C_l even more. This unstable operation can destroy the charger by over voltage of the thyristors. The problem is solved by reversing the voltage on C_l after each charging cycle by the additional thyristor Th_3. The voltage is resonantly reversed via $Th_3 - C_l - L_1$ resulting in $V_{Cl}(t_5) = -V_{Cl}(t_3)$. The voltage on C_l at the start of the cycle ($V_{Cl}(t_0)$) stabilizes when it is equal to the voltage at the end of the cycle ($V_{Cl}(T_{Th3})$). Substitution of this condition in Equation 2.2 results in Equation 2.9.

$$V_{Cl}(t_1) = 2V_{C0} - V_{Cl}(t_5), \quad V_{Cl}(t_0) = V_{Cl}(t_5) = -V_{Cl}(t_3) \tag{2.9}$$

Solving this equation results in expressions for the maximum charging voltage on V_{Cl} and V_{Ch} during stable operation, see equations 2.10 and 2.11. The values for $V_{Cl}(t_1)$ and $V_{Ch}(t_3)$ are respectively 910 V and 31.2 kV for an average supply voltage (V_{C0}) of 520 V. The reverse voltage on C_l ($V_{Cl}(t_3)$) will -130 V. The peak currents through Th_1 and Th_2 are respectively 331 A and 765 A.

$$V_{Cl}(t_1) = \frac{C_l + N^2 C_h}{N^2 C_h} V_{C0} \tag{2.10}$$

$$V_{Ch}(t_3) = \frac{2C_l}{NC_h} V_{C0} \tag{2.11}$$

($t_3 - t \rightarrow$) The voltage which is imposed over the primary winding of the transformer during charging increases the magnetization current (I_{L_M}) of the transformer. The total ΔI_{L_M} at the end of the charging period T_{Th2} can be calculated by equation 2.12. $L_M = kL_{prim}$, where k is the coupling coefficient and L_{prim} the primary inductance of the transformer. The magnetization current is able to freewheel via $D_1 - R_1$ after Th_2 switches off. First the voltage over the secondary winding has to reverse which implies that the charged stray capacitance of the secondary winding needs to oscillate with the secondary inductance of the transformer. Energy in the stray capacitance will be transferred to the magnetization inductance which slightly increases the magnetization current. This effect will be neglected for this analysis but will be discussed in detail for the novel circuit topology with increased repetition rate capability in Chapter 3. These losses will affect the efficiency of the charger for higher repetition rates more significantly. The energy in L_M will be dissipated in R_1 and the magnetization current will decay according to Equation 2.13. The transformer only operates in the upper halve of the B–H curve so the current needs to decay sufficiently before

the next charging cycle to avoid an accumulating magnetization current which could eventually drive the core into saturation. A large value for R_1 is needed which allows a large negative voltage over the secondary winding. Care has to be taken that diode (D_1) is able to hold-off the voltage since C_h will be charged to 30 kV and the voltage over the secondary winding will be negative during the demagnetization process. The losses in R_1 due the magnetization process can be approximated by: $P_{R_1} = \frac{1}{2}L_M \hat{I}_{L_M}^2 f$, assuming I_{L_M} decays to zero between cycles.

$$\Delta I_{L_M} = \frac{1}{L_M} \int_0^{T_{Th2}} V_{prim} dt = \frac{V_{Cl}(t_2)T_{Th2}C_l}{L_M(C_l + C_h)} \tag{2.12}$$

$$I_{L_M}(t) = I_{L_M}(t_3)\left(1 - e^{-\frac{R_1}{N^2 L_M}t}\right) \tag{2.13}$$

The final output voltage of the charger is initially (after startup) and after a pre-fire event not stable because the voltage on C_l at the beginning and the end of the cycle is not equal. Stabilization of the voltage takes typically 3–5 cycles. The voltage has to re-stabilize after each pre-fire event. Additional stability analysis can be found in [33]. Although the output voltage of the charger stabilizes, it is still unregulated. Component heating and mains load (higher repetition rate) can cause the output voltage to deviate up to 6 %. A novel circuit topology will be introduced in Chapter 3 which solves the instability issues, enables control of the output voltage, increases the repetition rate and features an active circuit which resets the transformer core.

2.2.2 Spark gap construction

The spark gap is probably the most critical component in the pulsed power system because of the recovery and erosion behavior. Performance characterization and design trade-offs will therefore be extensively discussed in Chapter 4. The triggered spark gap in the setup has a coaxial capacitor bank (C_h) which is located at the rear of the spark gap housing. A schematic overview is shown in Figure 2.9.

The trigger electrode is a concentric disc which is suspended in the hollow anode. The gas flow is directed through the hollow anode and subsequently through the gap between the trigger disc and anode. The gas diffuses in the trigger-gap which ensures a homogenous gas flow through the main gap (anode-cathode). The casing of the spark gap has eight outlet tubes to minimize distortion of the gas flow. The tubes are combined again in a loop (spoke wheel-like structure). The inner diameter of the anode and cathode is 26 mm. Electrodes with different outer diameters (d_o) were used during experiments to investigate recovery behavior. The gap distance between anode and cathode is fixed at 3.2 mm. The operating pressure of the switch is between 3 and 3.5 bar in practise.

The sensors of a DI (Differentiating Integrating) measurement system are incorporated in the spark gap housing to study the switching behavior. A capacitive voltage
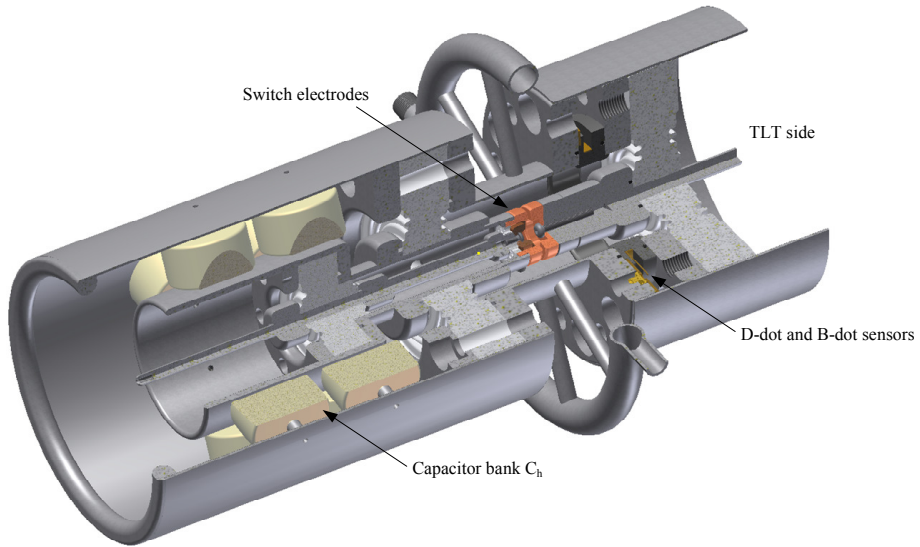
Figure 2.8: 3D CAD image of the spark gap and capacitor bank.
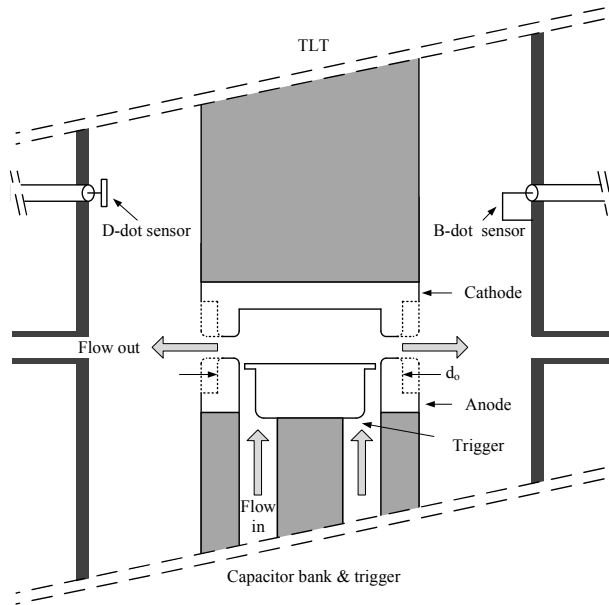
Figure 2.9: Schematic overview of the spark gap electrode arrangement.
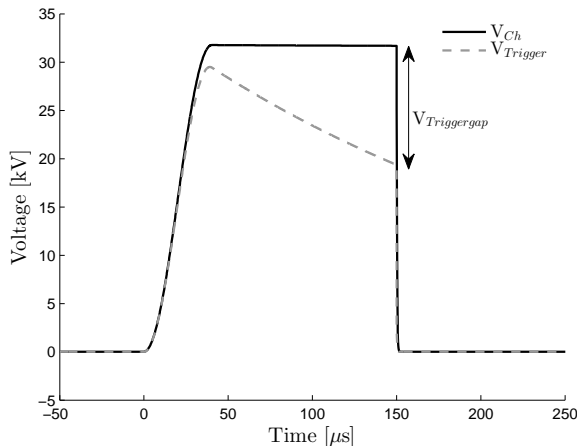
Figure 2.10: Trigger voltage as a function of time.

sensor (D-dot sensor) as well as a single winding B-dot sensor are installed between two flanges in the interface between TLT and spark gap housing to measure the voltage on and current through the cathode of the spark gap, see Figure 2.9. The DI-system will be discussed in Section 2.2.6.

2.2.3 Spark gap triggering

2.2.3.1 RLC circuit for robust triggering

The RLC trigger is a robust and simple circuit to trigger the spark gap, see Figure 2.3 $(R_T - L_T - C_T)$. The values of R_T, L_T and C_T are respectively 2.2 MΩ, 5 μH and 200 pF. C_T is much smaller compared to C_h (15 nF) and C_T and C_h are uncharged at the beginning of a cycle. C_T charges gradually via $C_h - C_T - R_T$ during and after the charging of C_h, resulting in a decreasing voltage on the trigger electrode of the spark gap (see Figure 2.10). The voltage on the trigger electrode can be expressed by Equation 2.14 [30].

$$V_{Trigger}(t) = \frac{V_{Ch}(t_3)}{2} \frac{\omega_{Th2}^2 (R_T C_T)^2}{1 + \omega_{Th2}^2 (R_T C_T)^2} \left([e^{-\frac{t}{R_T C_T}} - cos(\omega_{Th2}t)] + sin(\omega_{Th2}t) \right) \quad (2.14)$$

$$\omega_{Th2} = \sqrt{\frac{L_s + (L_2/N^2)}{C_{tot}}} \ , \quad C_{tot} = \frac{C_l N^2 C_h}{C_l + N^2 C_h} \quad (2.15)$$

The voltage difference between the main electrode (anode) and the trigger electrode will eventually become large enough to create a discharge in the trigger gap. The additional inductor L_T causes an underdamped oscillation with C_T to maintain the trigger spark for several microseconds. The discharge creates UV light, ionization and

19

decreased density of the switching medium which results in breakdown of the main gap. The circuit is failsafe because C_T recharges if the discharge in the trigger gap quenches without initiating the main discharge. Multiple trigger attempts can occur as long as C_h remains charged and the main gap is not fired. The RLC trigger circuit is used for continuous operation of the demonstrator because of the very robust behavior.

2.2.3.2 Solid state circuit for accurate triggering

Although the RLC trigger circuit is very robust, it can not be applied when accurate trigger timing is required. Streamer propagation in the reactor is studied in Chapter 5 which requires synchronization between the spark gap and the ICCD camera. Spark gap impedance measurements in Chapter 4 also require stable triggering. A simple solid state pulse circuit was developed to trigger the spark gap with reasonable accuracy. The trigger unit is controlled by the capacitor charger and is initiated after a presettable time when the capacitor charger has charged C_h. The circuit is able to apply 30 kV pulses to the trigger electrode of the spark gap with a rise time of less than 1 μs. The basic circuit topology of the pulse generator is shown in figure 2.11. The component values can be found in Table 2.2.

The pulse transformer is constructed with a double ETD59 Epcos N97 E-core. The primary coil consists of two foil windings. The secondary winding lays on top of the primary winding on a self made teflon bobbin and consists of 184 windings. A grounded screen is placed between the primary and secondary winding to couple transient currents originating from the trigger electrode to ground.

The circuit operates in three steps. Steps t_x–t_{x+1} in figure 2.11 refer to time slots t_x–t_{x+1} in figure 2.12. Capacitor C_1 is the power supply buffer which is typically charged to 25 V. The value of C_2 is 660 nF and will be charged to approximately 300 V during operation.

($t_0 - t_1$) MOSFET M_1 is closed and C_2 is discharged via the high voltage pulse transformer, generating the 30 kV pulse. The stray inductance of the transformer and parasitic capacitances of the high voltage winding and trigger electrode limit the rise time of the pulse. The trigger electrode fires at 30 kV ($t = t_1$) in the figure and C_{load} discharges rapidly. The trigger will fire at approximately 20 kV in practise. Two MOSFETs are used in parallel to achieve the required switching speed with a peak current capability of up to 200 A. Thyristors are too slow for this application, IGBTs could potentially be applied but are not optimal for sub-microsecond pulse generation

($t_1 - t_2$) M_1 stays closed for 130 μs and the current through L_1 (200 μH) will linearly increase via $C_1 - L_1 - D_1 - L_{prim} - M_1$ to approximately 15 A. The primary inductance of the pulse transformer (L_{prim}) is much lower than the value of L_1 so the energy is mainly stored in L_1.
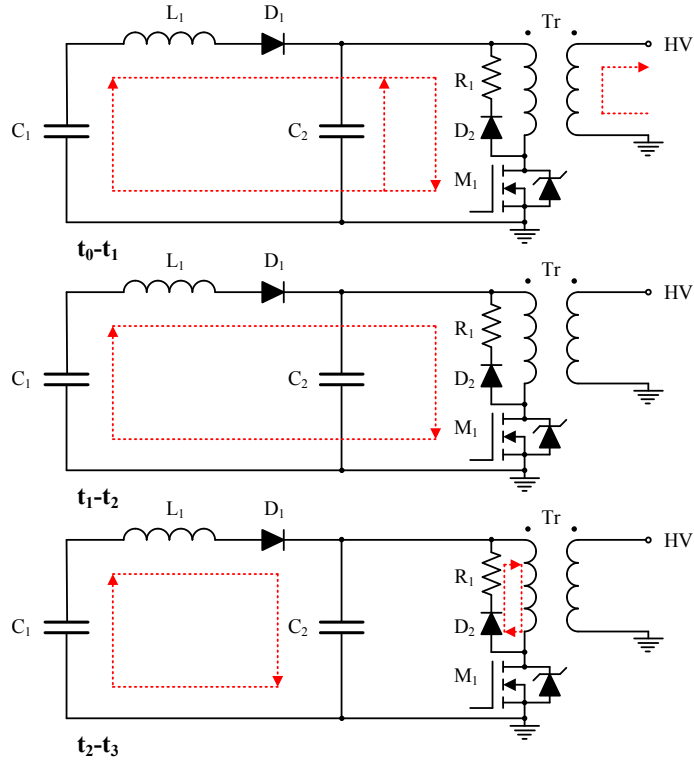
Figure 2.11: Equivalent circuits of the solid state trigger unit. Each circuit represents a different mode of a single pulse cycle. The current paths are indicated by the red arrows.

Table 2.2: Solid state trigger component values.

Component	value
C_1	4400 μF
C_2	660 nF
L_1	200 μH
R_1	4.7 Ω
N	92
L_s	220 nH
L_{prim}	15.6 μH
L_{sec}	227 mH
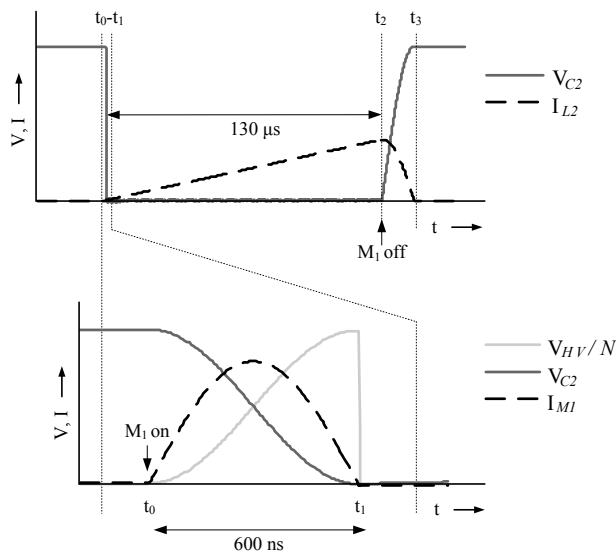
Figure 2.12: Typical voltage and current waveforms for the solid state trigger unit.

$(t_2 - t_3)$ M_1 opens and the current through L_1 freewheels into C_2, charging the capacitor to 300 V again. Simultaneously freewheels the magnetization current of the pulse transformer via the $R_1 - D_2$-snubber.

The single switch circuit enables control of the output voltage by setting the on-time of the M_1. The voltage on C_2 as a function of the on-time of M_1 (t_0–t_2) can be calculated by equations 2.16 and 2.17. The peak output voltage of the transformer depends on the capacitive load and can be calculated using Equation 2.18. The charging time of the load capacitance (T_{HV}) can be calculated using Equation 2.19, where L_s is the stray inductance and N the winding ratio of the pulse transformer. T_{HV} is approximately 600 ns in practise which results in a load capacitance (C_{load}) value of 19.5 pF.

$$I_{L1}(t_2) = \frac{1}{L_1 + L_{prim}} \int_{t_0}^{t_2} V_{C1}dt = \frac{V_{C1}(t_2 - t_0)}{L_1 + L_{prim}} \tag{2.16}$$

$$V_{C_2}(t_3) = V_{C1} + I_{L_1}(t_2)\sqrt{\frac{L_1}{C_2}} \tag{2.17}$$

$$V_{HV}(t_1) = \frac{2NC_2}{C_2 + N^2C_{load}}V_{C_2}(t_0), \quad V_{C_2}(t_0) = V_{C_2}(t_3) \tag{2.18}$$

$$T_{HV} = \pi\sqrt{L_sC_{tot}} \ , \quad C_{tot} = \frac{N^2C_2C_{load}}{N^2C_{load} + C_2} \tag{2.19}$$

2.2.4 Transmission line transformer

The transmission line transformer (TLT) [36] is used for several reasons:

- The two stage TLT doubles the voltage on C_h which is needed to generate plasma in the reactor. Designing a 60 kV capacitor charger would also be possible but the high voltage engineering would be more challenging.

- The pulse waveform can be shaped because the TLT has a fixed input impedance and sets the discharge time of C_h (and thus the pulse width).

- The output impedance of the TLT can be matched to the impedance of the reactor. Although the plasma is a dynamic load, the plasma impedance can settle near the output impedance of the TLT. A section in Chapter 5 will also be devoted to impedance matching of long corona wire–cylinder reactors.

- The TLT is able to dissipate residual energy in C_h as a result of non-ideal impedance matching with the reactor. The spark gap is only able to turn-off if there is no current to maintain the the discharge in the switch. C_h has to be completely discharged each pulse.

- The TLT provides a charging current path to ground for the coupling capacitor C_{dc}. This will be explained in the following section.

The high power TLT of the corona demonstrator consists of two 10 Ω transmission lines which are constructed inside each other, see Figure 2.3. The inner line structure consists of two concentric stainless steel tubes submerged in transformer oil (Shell Diala). The outer line structure is connected in parallel at the spark gap side and connected in series at the reactor side to create the two stage TLT. The center conductor of the outer line is actually a set of bars which are placed in a circular pattern to create the correct impedance. A magnetic core is stacked around the inner line. The radii ratios of the inner and outer line are equal to create the same impedance, see Equation 2.20. d_i is the inner diameter of one line and d_o is outer diameter of the same line.

$$Z_0 \approx \frac{60}{\sqrt{\epsilon_r}} \ln \frac{d_o}{d_i} \qquad (2.20)$$

A schematic overview of a two stage TLT is shown in Figure 2.13, the line and magnetic core characteristic can be found in Table2.3. Two transmission lines with characteristic impedance Z_0 (10 Ω) are connected in parallel at the input side and connected in series at the load side. The 1 m transmission lines have a transient time (T_{line}) of 4.95 ns. T_{line} can be calculated by formula 2.21 where c, ϵ_r and μ_r are respectively the transient time in vacuum, relative permittivity and relative permeability. The ϵ_r of the transformer oil is 2.2.

$$T_{line} = \frac{c}{\sqrt{\epsilon_r \mu_r}} \qquad (2.21)$$

23
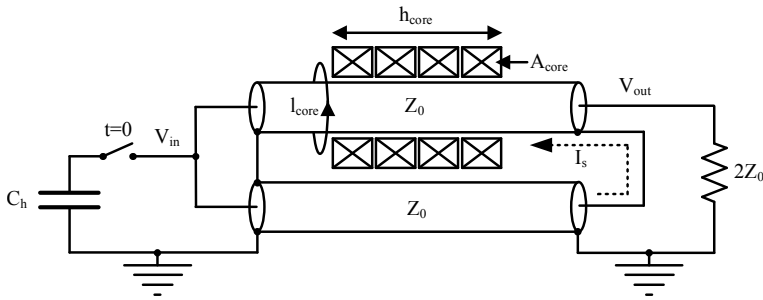
Figure 2.13: Transmission line transformer with magnetic cores.
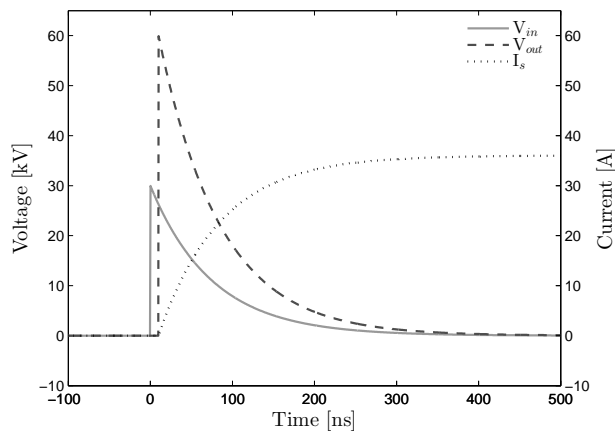
Figure 2.14: TLT input voltage, output voltage and secondary mode current as a function of time for a matched load.

The input impedance of the TLT is $Z_0/2$ and the output impedance is $2Z_0$. Current is able to flow via the inner conductor of the lower line and the outer conductor of the upper line after T_{line} when the pulse reaches the output side of the TLT. This secondary mode current (I_s) reduces the gain and efficiency of the TLT. The current is reduced by stacking magnetic cores (National Magnetics Group CMD5005) around the upper line to increase the secondary mode impedance (Z_s). The cores act as a common mode choke which only affects the secondary mode current.

Three items are imported for the magnetic core sizing. 1. Z_s should be much larger than Z_0 for maximum gain of the TLT. 2. The cores are not allowed to saturate during the pulse. 3. The transient time in the cores should be high enough to avoid multiple secondary mode reflections.

The secondary mode impedance can be calculated using Equation 2.22, where A_{core} is the sum of the cross sections of all magnetic cors, l_{core} is the mean magnetic path of cores, μ_0 the vacuum permeability ($4 \pi \cdot 10^{-7}$) and μ_r the relative permeability of

Table 2.3: TLT line and magnetic core characteristic.

Component	value
Z_0	10 Ω
T_{line}	4.95 ns
A_{core}	370 cm^2
l_{core}	400 mm
h_{core}	1 m
μ_r	537
B_{sat}	3.2 T

the core material.

$$Z_s = j\omega \frac{A_{core}\mu_0\mu_r}{l_{core}} \tag{2.22}$$

The value of C_h and input impedance determine ideally the output pulse shape, see Equation 2.23. The rise time of the pulse is in practise limited by the L/Z_{in} time constant, where L is the parasitic circuit inductance (e.g. spark gap and connections). Coaxial connections are essential for fast rise times.

$$V_{in}(t) = V_{Ch}(0)e^{\frac{-2t}{Z_0C_h}} \tag{2.23}$$

$$V_{out}(t) = 2V_{Ch}(0)e^{\frac{-2t}{Z_0C_h}} \tag{2.24}$$

The secondary mode current can be approximated by Equation 2.25. The Equation is valid under the condition that $(Z_s >> Z_0)$ because Z_s causes a mismatch which affects the output voltage of the lower line. Substitution of Equation 2.23 results in Equation 2.25. The result of the calculated input voltage, output voltage and secondary mode current as a function of time is shown in Figure 2.14.

$$I_s(t) = \frac{l_{core}}{A_{core}\mu_0\mu_r}\int V_{in}dt = \frac{l_{core}Z_0C_h}{2A_{core}\mu_0\mu_r}V_{Ch}(0)\left(1 - e^{\frac{-2t}{Z_0C_h}}\right) \tag{2.25}$$

The second design consideration is saturation of the magnetic core. The flux in the core can be calculated by Equation 2.26. The saturation flux density B_{sat} of the core material should be higher than the actual flux density at the end of the pulse. The minimum core cross section can be calculated by Equation 2.27. This condition is met because A_{core} is 37 cm^2 and only 7 cm^2 is required.

$$\Phi = \int V_{in}dt = \int_0^\infty V_{Ch}(0)e^{\frac{-2t}{Z_0C_h}}\,dt = \frac{1}{2}Z_0C_hV_{Ch}(0) \tag{2.26}$$

$$A_{core} > \frac{\Phi}{B_{sat}} = \frac{Z_0C_hV_{Ch}(0)}{2B_{sat}} \tag{2.27}$$

25

The third design consideration is the height h_{core} of the total magnetic core. The transient time in the magnetic core is much lower than the transient time in the lines due to the high permeability of the core material. A secondary mode wave starts to propagate back through the core as the pulse reaches the load side of the TLT. The secondary mode wave reflects again at the left side of the core because of the abrupt impedance transition. Distortion of the output voltage of the TLT can be minimized by choosing the secondary mode transient time longer than the pulse width ΔT. The back and forth time of the magnetic core should than be equal or larger than ΔT. Some energy is reflected back in the TLT due to initial mismatch between source and reactor. This reflection is able reflect again at the input side of the TLT and can eventually be absorbed by the plasma. ΔT should be chosen large enough to allow these reflections. The core height h_{core} and minimum TLT length can now be calculated by Equation 2.28 [33]. The core has a length of 1 m resulting in a maximum pulse width (ΔT) of 154 ns.

$$h_{core} > \frac{1}{2} \frac{c\Delta T}{\sqrt{\epsilon_r \mu_r}} \tag{2.28}$$

The corona plasma will eventually quench as the reactor voltage drops below a threshold level, the output of the TLT will subsequently only be loaded with the reactor capacitance and secondary mode path. The residual energy in C_h will be dissipated in the cores during the resulting low frequent oscillation between Z_s and C_h. The spark gap will remain closed as long as there's current to maintain the spark in the gap. The core can saturate and de-saturate, positively and negatively during the oscillation. Different core materials can be used to enhance the damping of the oscillation [30]. The spark gap should be quenched as soon as possible to maximize the recovery time between pulses.

2.2.5 DC bias network

The DC-bias network charges the coupling capacitor C_{dc} and blocks the high voltage pulse to protect the DC power supply. The value of the bias level is typically 20 kV during continuous operation and can be set to 25 kV maximum. A schematic of the circuit is shown in Figure 2.15. The component values can be found in Table 2.4. Associated waveforms of the voltages and currents are shown in Figure 2.16. The secondary mode impedance Z_s of the TLT is an inductance to ground which is used as a charging path for C_{dc}. The TLT is therefore represented by inductance Z_s for the DC-bias circuit analysis.

The coupling capacitor should have a minimum value depending on the DC-bias voltage level and the amount of charge which is injected by the TLT during pulse generation. The charge in C_{dc} at the beginning of the pulse should be larger than the total charge which is transferred via the TLT to prevent negative undershoot (or negative charging) of the voltage on C_{dc}. $Q_{TLT_{out}} = C_h V_{Ch}(t_0)/2$ since the output
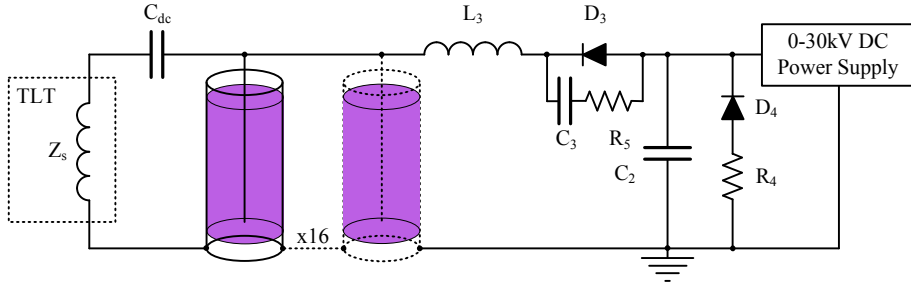
Figure 2.15: DC bias filter circuit. The circuit enables fast charging of coupling capacitor C_{dc}.

Table 2.4: DC-bias component values.

Component	value
C_{dc}	14 nF
C_2	26 nF
C_3	380 pF
L_3	4.5 mH
Z_s	185 μH
R_4	7 kΩ
R_5	5 kΩ

current is halved by the TLT. The minimum value of C_{dc} can be calculated by Equation 2.29 [33].

$$C_{dc} > \frac{C_h V_{Ch}(t_0)}{2V_{Cdc}(t_0)} \qquad (2.29)$$

The energy contribution per pulse of C_{dc} to the plasma can be determined by considering the injected charge: $Q_{Cdc}(t_1) = Q_{Cdc}(t_0) - Q_{TLT_{out}}$. The residual voltage (see Equation 2.30) and energy in C_{dc} after the pulse can thus be calculated. The difference with the initial energy in C_{dc} results in Equation 2.31. C_{dc} is discharged to approximately 4 kV and 2.7 J from C_{dc} is transferred to the reactor.

$$V_{Cdc}(t_1) = V_{Cdc}(t_0) - \frac{C_h}{2C_{dc}} V_{Ch}(t_0) \qquad (2.30)$$

$$E_{Cdc} = V_{Cdc}(t_0)\frac{C_h V_{Ch}(t_0)}{2} - \frac{C_h{}^2 V_{Ch}(t_0)^2}{8C_{dc}} \qquad (2.31)$$

C_{dc} is discharged in a few hundred nanoseconds during pulse generation until the plasma in the reactor quenches. Inductor L_2 has a high impedance for the transient high voltage pulse and holds off the voltage partially. Snubber resistor R_5 holds the

27
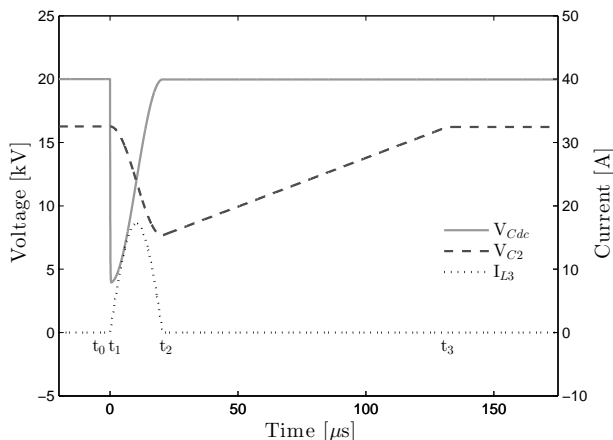
Figure 2.16: Simulated DC bias waveforms.

remaining voltage due to the low transient impedance of the snubber capacitor C_3. The ratio and blocking voltage of diode D_3 should be considered to prevent damage to the diode ($j\omega L_3 > R_3 + 1/j\omega C_3$). C_{dc} is now discharged almost instantaneously and will be resonantly recharged in tens of microseconds via $C_2 - D_3 - L_3 - C_{dc} - Z_s$ because the voltage over C_{dc} has become (abruptly) lower than the voltage on the supply buffer C_2. The DC bias level is restored very fast to enable almost continuously precipitation of particulate matter in the reactor. The $R_5 - C_3 - L_3 - C_{dc} - Z_s - C_2$ circuit should be critically damped to avoid oscillations after recharging. The value of C_3 is relatively small: $C_3 << (C_{dc}//C_2)$ thus $(C_{dc}//C_2//C_3) \approx C_3$. The value of snubber resistor R_5 can be approximated by Equation 2.32.

$$R_5 = \sqrt{\frac{4(L_3 + Z_s)}{C_3}} \tag{2.32}$$

The residual voltage C_{dc} ($V_{Cdc}(t_1)$) and voltage level on C_2 ($V_{C2}(t_1)$) determine the new voltage $V_{Cdc}(t_2)$ if assumed that C_{dc} is discharged instantaneously during pulse generation (Equation 2.33). The peak current through the diode and inductor can be calculated by Equation 2.35, the charging time by Equation 2.34.

$$V_{Cdc}(t_2) = V_{Cdc}(t_1) - \frac{2C_2}{C_{dc} + C_2}\left(V_{C2}(t_1) - V_{Cdc}(t_1)\right) \tag{2.33}$$

$$T_{L3} = \pi\sqrt{(L_3 + Z_s)C_{tot}} \ , \quad C_{tot} = \frac{C_2 C_{dc}}{C_2 + C_{dc}} \tag{2.34}$$

$$\hat{I}_{L3} = \frac{V_{C2}(t_0) - V_{Cdc}(t_1)}{\sqrt{(L_3 + Z_s)/C_{tot}}} \tag{2.35}$$

C_2 is recharged with a linear ramp by a current mode controlled commercial available DC power supply. The set value of the voltage on C_2, the injected charge by the TLT and capacitor values will define the DC-bias voltage level ($V_{Cdc}(t_0)$). The system is stable when $V_{Cdc}(t_0) = V_{Cdc}(t_2)$, substitution of Equation 2.30 in Equation 2.33 and subsequently solving results in an equation for the stable DC-bias voltage as a function of the supply voltage ($V_{C2}(t_0)$).

$$V_{Cdc}(t_0) = V_{C2}(t_0) + \frac{C_h C_2 - C_h C_{dc}}{4 C_2 C_{dc}} V_{Ch}(t_0) \, , \quad V_{Cdc}(t_0) = V_{Cdc}(t_2), \ V_{C2}(t_0) = V_{C2}(t_3)$$
(2.36)

The set value of the supply voltage ($V_{C2}(t_0)$) can now be calculated by Equation 2.37. The calculated values for $V_{C2}(t_0)$, $\hat{I}_{L3}$ and T_{L3} are respectively 16.3 kV, 17.1 A and 20.5 μs.

$$V_{C2}(t_0) = V_{Cdc}(t_0) - \frac{C_h C_2 - C_h C_{dc}}{4 C_2 C_{dc}} V_{Ch}(t_0) \, , \quad V_{Cdc}(t_0) = V_{Cdc}(t_2), \ V_{C2}(t_0) = V_{C2}(t_3)$$
(2.37)

The next step is deriving the required output current of the DC power supply. The minimum voltage on the buffer capacitor $V_{C2}(t_2)$ can be calculated by Equation 2.38. C_2 has to be recharged from this voltage.

$$V_{C2}(t_2) = \left(1 - \frac{2 C_{dc}}{C_2 + C_{dc}} \right) V_{C_2}(t_0)$$
(2.38)

The voltage on C_2 after charging for a time period T_{ps} can be expressed by equation 2.39, where I_{ps} is the DC charging current. The pulse repetition rate determines the charging current needed to recharge C_2 before the next pulse cycle, see Equation 2.40.

$$V_{C2}(t_3) = V_{C2}(t_2) \frac{1}{C_2} \int_{t_2}^{t_2 + T_{ps}} I_{ps} dt$$
(2.39)

$$I_{ps} = \frac{C_2}{T_{ps}} \left(V_{C2}(t_3) - V_{C2}(t_2) \right) \, , \quad T_{ps} < \frac{1}{f}$$
(2.40)

The minimum required supply current I_{ps} can be derived by substitution of Equation 2.38. The power supply current should be at least 297 mA for 1 kHz repetition rate. A margin for T_{ps} needs to be taken in account because of the jitter in the spark gap fire moment. The time between two successive pulses is never equal due to the RLC trigger method. A 12.5 kJ/s 30 kV adjustable DC power supply was applied which is capable of recharging C_2 in approximately 300 μs.

$$I_{ps} > \frac{C_2}{T_{ps}} \frac{2 C_{dc}}{C_2 + C_{dc}} V_{C2}(t_0) \, , \quad T_{ps} < \frac{1}{f}$$
(2.41)

The size of the buffer capacitor C_2 needs to be large to minimize the voltage ripple and T_{ps} needs to be as large as possible to limit the supply current. This has the advantage that the power supply is able to continuously deliver maximum power to the buffer capacitor which minimizes peak power handling capability, physical size and cost of the DC supply. The drawback of a large C_2 is the stored energy which is released when a breakdown occurs in the reactor. The spark in the reactor will be maintained by the current which is fed via $C_2 - D_2 - L_3$. The oscillating current is dampened by $D_4 - R_4$ as the current becomes negative. R_4 has a low value to limit excessive voltage reversal on the output of the DC supply.

The voltage on C_{dc} will drop gradually after charging if the DC-bias voltage is beyond the DC corona inception voltage. The DC-bias voltage can eventually settle near the supply voltage V_{C2} depending on the DC corona current, inception voltage and pulse repetition rate. This dynamic behavior is beyond the scope of the circuit analysis.

2.2.6   Measurement system

The reactor voltage and current waveforms need to be measured to determine the energy input of the plasma, observe pulse characteristics (e.g. rise time, peak voltage, peak current, pulse width, etc.) and to assess the performance of the pulse source e.g. spark gap switching characteristics.

Interference free measurement of transient high voltage and high current waveforms in presence of strong electromagnetic fields requires special attention. DI (Differentiating-Integrating) measurement systems [37] [33] are applied because of their high bandwidth, high voltage and high current measurement capability, relative easy design procedure and the possibility of full integration in pulsed power devices. Pulsed power devices are often constructed coaxially for impedance matching, reduction of inductance and EMI shielding. The DI-system sensors can be incorporated in the design of the pulsed power components with limited disturbance of the coaxial structure.

Sensors are incorporated in the spark gap housing and TLT output. Capacitive voltage sensors (D-dot sensors) as well as a single winding B-dot sensors are installed in the interfaces between spark gap and TLT and TLT and reactor. These sensors measure the derivatives of the voltage on and current through the center conductor. The D-dot sensor consists of a ring which is concentrically placed around the conductor, see Figure 2.17. An insulating medium is present between the ring and the center conductor. The capacitance between the ring and center conductor causes a displacement current which results in a voltage signal on the coaxial measurement cable: $V_D = Z_{cable} C_D \frac{dV}{dt}$, where Z_{cable} is the characteristic impedance of the measurement cable (50 Ω), C_D is the capacitance between the ring and the cathode. The parasitic capacitance of the ring to ground (C_p) limits the bandwidth of the sensor. The cut-off frequency is determined by C_p and the cable impedance $f_{cut-off} = 1/(2\pi Z_{cable} C_p)$. The capacitance C_D can be estimated analytically. C_p is more difficult to estimate, especially when the sensor ring is located between two flanges like in our designs (example Figure 2.9). FEM (Finite Element Method) analysis is applied to approximate C_D and C_p. The value
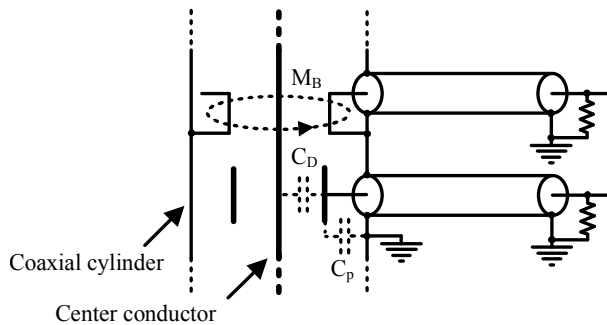
Figure 2.17: Schematic DI measurement system in a coaxial structure. The upper coaxial measurement cable is connected to a toroidal single winding B-dot sensor (current). The lower cable is connected to a D-dot sensor (voltage).

of C_D needs to be between 0.1 and 1 pF to obtain sufficient signal strength in this specific application. A 2d (rz plane) electrostatic solver is used (Ansoft Maxwell) to iteratively obtain a value within the desired capacitance range. The actual value will be determined during the calibration procedure. The value can be measured accurately once the sensor has been constructed.

Similarly the B-dot sensor generates a voltage impulse that is transferred to oscilloscope by a coaxial cable: $V_B = M_B \frac{dI}{dt}$, where M_B is the mutual inductance between the B-sensor (loop) and the center conductor. The cutt-off frequency is determined by the inductance of the loop and cable impedance $f_{cut-off} = R_2/(2\pi L_{loop})$. The inductance of a square loop can be approximated by: $L_{loop} = (\mu_0 h_B l_B)/(w_B)$ where h_B, l_B and w_B are respectively the height, length and width of the loop. More elaborate equations can be found in literature, e.g. [38]. Constructing the loop from a strip rather than a wire increases the bandwidth of the sensor. A toroidal loop which coaxially encloses the center conductor has the lowest inductance. The capacitance of the gap in the loop and the inductance of the loop has an oscillation frequency which can become an issue for very high frequencies. M_B can be estimated by Equation 2.42, where r_{o_B} and r_{i_B} are the inner and outer radius (to the center of the reactor) of the loop. The exact value is also determined during the calibration procedure.

$$M_B = \frac{\mu_0 h_B}{2\pi} ln\left(\frac{r_{o_B}}{r_{i_B}}\right) \tag{2.42}$$

The system is especially suitable for pulsed power systems because of the extreme dV/dt and dI/dt characteristics. Only small C_D and M_B values are required to obtain sufficient signal amplitude. This profits construction of compact high bandwidth sensors with limited parasitic effects. The DI-system has also the advantage that high frequency components result in high amplitude signals on the measurement cables and thereby have an excellent signal to noise ratio. The disadvantage of the system is the limited ability to measure low-frequency and DC signals.
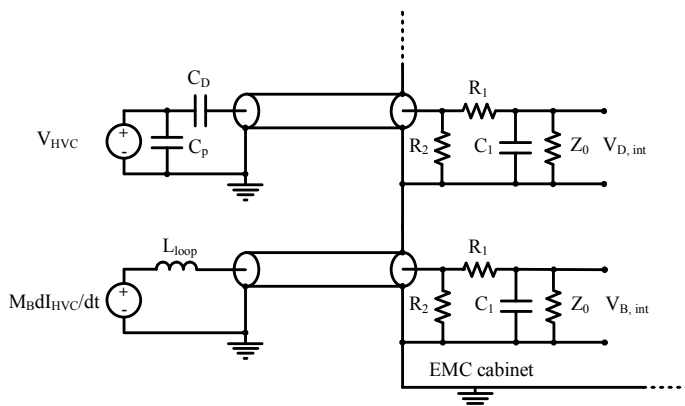
Figure 2.18: Equivalent circuit of the DI measurement system. The integrators are placed at the wall of an EMC cabinet. The oscilloscope is placed in the same EMC cabinet and measures signals $V_{D,int}$ and $V_{B,int}$

The differentiated sensor signals are restored to the original waveforms by passive integrators which are mounted on the wall of an EMC cabinet for excellent measurement properties, see Figure 2.18. The integrators attenuate not only the high frequency signal components but also suppress high frequency noise. R_1 and C_1 form the actual integrator, R_2 terminates the measurement cable and Z_0 is the impedance of the cable to the oscilloscope. The transfer function of the DI system is given by equations 2.43 and 2.44. Assumed is that the integrator does not load the terminated output of the cable ($R_1 >> R_2$). This is required to avoid mismatch and resulting reflections. There is some tuning possibility by choosing the value of R_2 slightly higher because the equivalent impedance of $R_1 - C_1 - Z_0$ (where R_1 is dominant) is in parallel with R_2.

The transfer functions can be applied numerically after measurement by the oscilloscope to fully restore the waveform. The $\left(1 + \frac{1}{R_2 C_p} \frac{d}{dt}\right)$ term in equation 2.43 can be omitted if the D-dot sensor is used in a frequency range far below the cut-off frequency.

$$V(t) = \frac{1}{R_2 C_D}\left(R_1 C_1 V_{D,int}(t) + \left(1 + \frac{R_1}{Z_0}\right)\int V_{D,int}(t)dt\right)\left(1 + \frac{1}{R_2 C_p}\frac{d}{dt}\right) \tag{2.43}$$

$$I(t) = \frac{1}{M_B}\left(R_1 C_1 V_{B,int}(t) + \left(1 + \frac{R_1}{Z_0}\right)\int V_{B,int}(t)dt\right) \tag{2.44}$$

The calibration values (C_D and M_B) were determined with separate calibration setups. Commercially available probes (North Star PVM-2 high voltage probe and Pearson 6600 current monitor) are fitted to a load resistor which is attached to the TLT or spark gap. The D-dot sensor can be calibrated with a high value load resistor

to limit the current which results in negligible magnetic interference on the external voltage probe. A loop is always created when a high voltage probe is connected over the load which could result in a significant induction voltage contribution to the probe signal. Careful placement of the probe and a reduced dI/dt limits the loop contribution and increases the accuracy of the high voltage probe measurement.

The B-dot sensor can be calibrated by using a low resistance value (e.g. impedance of the TLT) to create a current amplitude in the range where the sensor will be ultimately used.

The bandwidth of the system is in practise limited by the passive integrators which were used. A compact integrator design in a screened housing is needed for optimal performance. Components with low parasitic characteristics (e.g. feedthrough capacitors, carbon composite resistors) need to be applied. Up to several hundred Mhz bandwidth is achievable but not necessary in this application. The rise time of the reactor pulses are approximately 20 ns which corresponds to 17.5 MHz ($BW = 0.35/t_r$). The bandwidth of the integrators were measured by a vector network analyzer and can be applied to at least 70 MHz.

The system is not capable to measure low-frequency and DC signals. The DC-bias voltage is measured by a separate low bandwidth voltage divider which is is integrated in the DC-bias filter cabinet. A North Star PVM-2 high voltage probe is used to monitor the voltage on C_h in the low frequency range during measurements in the corona setup. The energy per pulse which is transferred to the reactor can be calculated by equation 2.45.

The energy density is a useful parameter to compare conversion efficiencies of compounds with literature and to estimate power requirements for high flow industrial applications. The energy density (E_d) is the reactor power scaled to the volumetric flow of the process gas which passes through the reactor. E_d can be calculated by Equation 2.46, where $\overline{E_p}$ [J] is the average pulse energy, f [Hz] is the pulse repetition rate of the and F [L/s] the volumetric reactor flow.

$$E_p = \int (V_{pulse}(t) + V_{dc}(0))I_{pulse}(t)dt \tag{2.45}$$

$$E_d = \frac{f\overline{E_p}}{F} \ [J/L] \tag{2.46}$$

2.2.7 High voltage and sensor layout

The layout of the high voltage components and reactor is shown in figure 2.19. The spark gap, TLT and coupling capacitor C_{dc} are constructed coaxially for optimal impedance matching and minimized EMI. The D-dot and B-dot sensors are installed near the high voltage feedthrough of the reactor. The TLT and coupling capacitor part are filled with transformer oil for electrical insulation and heat transportation from the magnetic cores to the outer wall. The bottom of the spark gap is insulated with ambient air and connects to the RLC cabinet. The cabinet holds the trigger components and
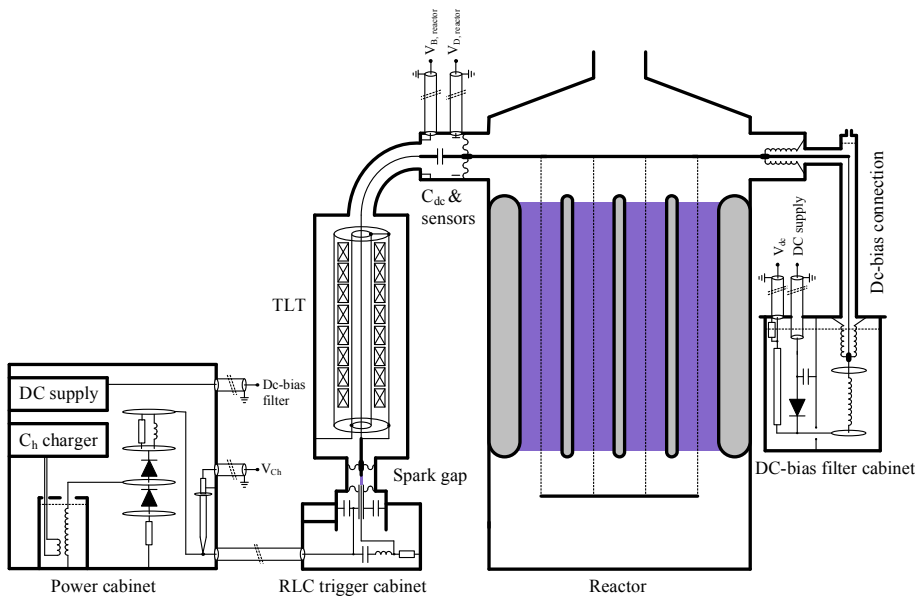
Figure 2.19: High voltage and sensor layout.

is also air insulated. A high voltage coaxial cable connects the RLC trigger cabinet to the power cabinet which contains the capacitor charger and high voltage transformer. The transformer is oil insulated and the other components in the cabinet are air insulated. The rectifier and demagnetization snubber are constructed between field control rings to prevent corona discharges. A North Star PVM-2 probe is fixed in the setup to monitor the voltage on C_h. An oil insulated coaxial structure (DC-bias connection) connects the reactor to the DC-bias filter. This connecting structure needs to be as short as possible to prevent significant distortion of the pulse waveform by multiple reflections. The helical air (oil) inductor in the filter acts as a high impedance for the line, causing some voltage gain. Large field control rings are placed on the inductor to reduce voltage stresses on the windings. The other components and high voltage divider in the DC-bias filter cabinet are fixed to a screen. The cabinet is completely filled with transformer oil.

2.3 Corona reactor

2.3.1 Reactor construction

The wire–cylinder type corona reactor consists of sixteen 150 mm diameter stainless steel 1 m long cylinders [30] [2]. The 3 mm wires are suspended between two frames which are fixed to the reactor interior by ceramic high voltage insulators, see figures
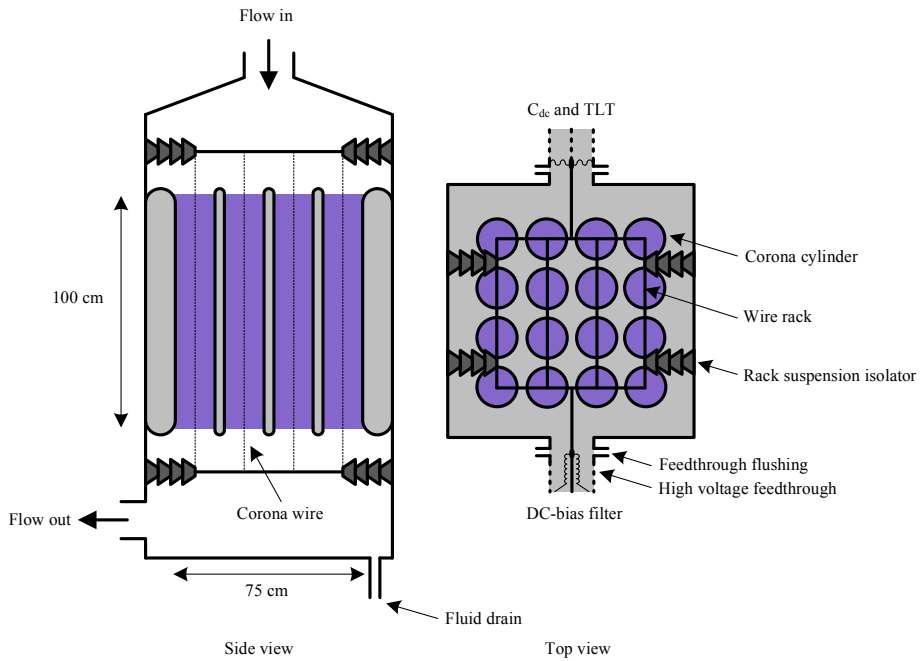
Figure 2.20: Schematic overview corona reactor.
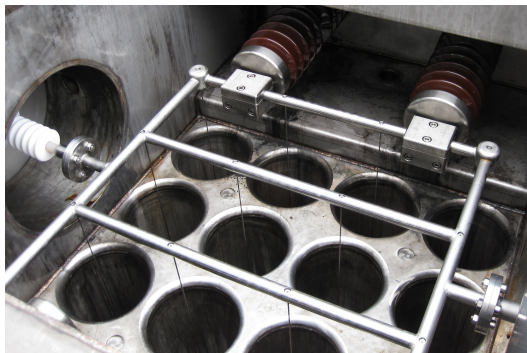
Figure 2.21: Top view corona reactor.

2.20 and 2.21. The reactor has an active plasma volume of 0.28 m^3.

High voltage is fed to the reactor by two feedthroughs. Coupling capacitor C_{dc} is connected in series with the TLT at one side of the reactor. The charging voltage of C_{dc} is applied to the other side. Process gas is often saturated with water vapor (e.g. flue gas). The vapor condenses partially in the supply pipe and reactor. It is drained at the

bottom of the reactor to prevent accumulation of water in the ventilation system. A continuous flow of filtered and heated gas is purged over the surfaces of the feedthrough insulators to prevent contamination and condensation. Moisture and contamination can cause surface discharges and consequently failure of the feedthrough. Ambient air can usually be used to purge the insulator surface but in this case filtered and condensation free process gas is used in the demonstrator to prevent dilution of the treated process gas. The flow handling of the demonstrator is limited by the ventilation system to 700 m^3/h. The insulator purging flow can be up to 20 % of the total flow resulting in significant errors during chemical conversion experiments when ambient air would be used.

2.3.2 Reactor ancillary equipment

A complete piping and instrumentation diagram of the pilot setup is shown in Figure 2.22. Most of the ancillary devices are controlled by a PLC system. An image of the container interior is shown in Figure 2.23.

The spark gap is continuously purged with gas to enhance the recovery behavior of the switch. A closed-loop purging system which can be pressurized with N_2 is used in the setup. The gas is circulated by a rootsblower which is fed by a motordrive to control the flow. The volumetric flow is measured by a vortex flow meter. The absolute pressure in the system is measured at the gas inlet of the spark gap and controlled by an electronic pressure regulator. The gas is guided through a particle filter after passing the spark gap to remove particles which originate from the electrode erosion process e.g. metal particles and metal-oxides resulting from impurities in the gas (reaction between water vapor, oxygen and the electrode material in the discharge) and metal-nitrides (reaction between nitrogen and the electrode material in the discharge). A differential pressure sensor enables early detection of filter clogging. The gas in the system will be heated by the plasma in the spark gap and the compression of the rootsblower during operation. A water cooled heat exchanger cools the gas. The gas temperature is monitored at several points in the system to detect overheating.

Several diagnostics are built in the reactor exhaust pipe. A vortex flow meter, an absolute pressure, humidity and temperature sensor. The process (in the reactor exit) gas is pre-heated a few degrees Celsius by a heater to prevent condensation on the sensors and in the active carbon filter. The process fan is placed behind the carbon filter to create a low pressure in the piping and reactor which prevents leakage of toxic fumes in the container. A motor drive and feedback enables continuous control of the process gas flow.

A level sensor in the bottom of the reactor detects flooding of the reactor by condensation in case of a clogged drain line.

The feedthrough insulators are purged with heated and filtered process gas. The minimum required purge flow is monitored by a flow threshold detector. Minimum required heating of the gas is monitored by a temperature sensor to ensure condensation free gas and dry insulators.

Cooling water for the DC power supply, capacitor charger transformer and closed-loop spark gap system is provided by a heat exchanger and a pump. Water flow and temperatures are monitored to detect overheating or pump failure.

For autonomous operation the charger, DC-supply, spark gap and reactor are monitored by multiple microcontrollers and electrical circuits. Ancillary devices are controlled by a PLC system. A schematic overview of the complete control system is shown in Figure 2.24.

The capacitor charger and DC-bias supply can be fully controlled via the master controller and a graphical user interface (GUI) on the PC. Operation of the spark gap, pulse energy, DC voltage and reactor breakdown events are monitored and evaluated each pulse. Statistics of C_h charging voltage and spark gap trigger moment are captured to evaluate the spark gap performance. Pulse energy is measured by analog hardware. The reactor flow value is forwarded via the PLC and the master controls the energy density in the reactor by adjusting the repetition rate. The DC-bias level is monitored to detect reactor breakdown events. The embedded software is capable of shutting down the system if serious fault events occur.

The analog circuit enables measurement of the energy per pulse. The output of the circuit is an analog voltage which is sampled after each pulse by the controller. A schematic overview is shown in Figure 2.25. The circuit calculates the voltage similar as in Equation 2.45. The sensor signals are integrated by the passive integrators. The waveforms are restored to their actual shapes by an active compensation circuit which consists of op-amp circuits. An adder and active integrator is used to restore the signal as in Equations 2.44 and 2.43 (without the C_p compensation term). The DC-bias voltage at the beginning of the pulse needs to be added to the restored voltage pulse. The voltage is held constant during the pulse by a low pass filter. Voltage and current input stages are built symmetrically to prevent phase shift of the voltage waveform compared to the current waveform. The actual voltage and current waveforms are now multiplied by a four quadrant analog multiplier and integrated by an op-amp integrator. The integrator has a finite open-loop gain to prevent drift of the output and to enable resetting before the next pulse. The output voltage of the integrator needs to be sampled by a high speed sample and hold chip directly after the pulse when all energy is transferred to the reactor. The sample and hold is triggered at a fixed time after the rising edge of the current pulse via an edge detector and adjustable delay. V_{Ep} can now be sampled by the ADC of the master controller.

The DC-bias voltage drops to a certain value after pulse generation during normal operation, see Equation 2.30. C_{dc} is discharged fully during a breakdown in the reactor. A breakdown event is detected by the controller when the DC-bias voltage drops below a threshold value.

The falling edge of the voltage on C_h is detected to monitor the trigger time, pre-fire events, and late/no-fire events. Average trigger time and average number of pre-fire events are evaluated continuously and can be applied to automatically adjust the pressure and flow of the spark gap. The gas pressure in the spark gap controls the breakdown voltage of the trigger gap and main gap. It changes gradually as the gas and electrodes heat up and the electrodes erode. The pressure can be controlled by the
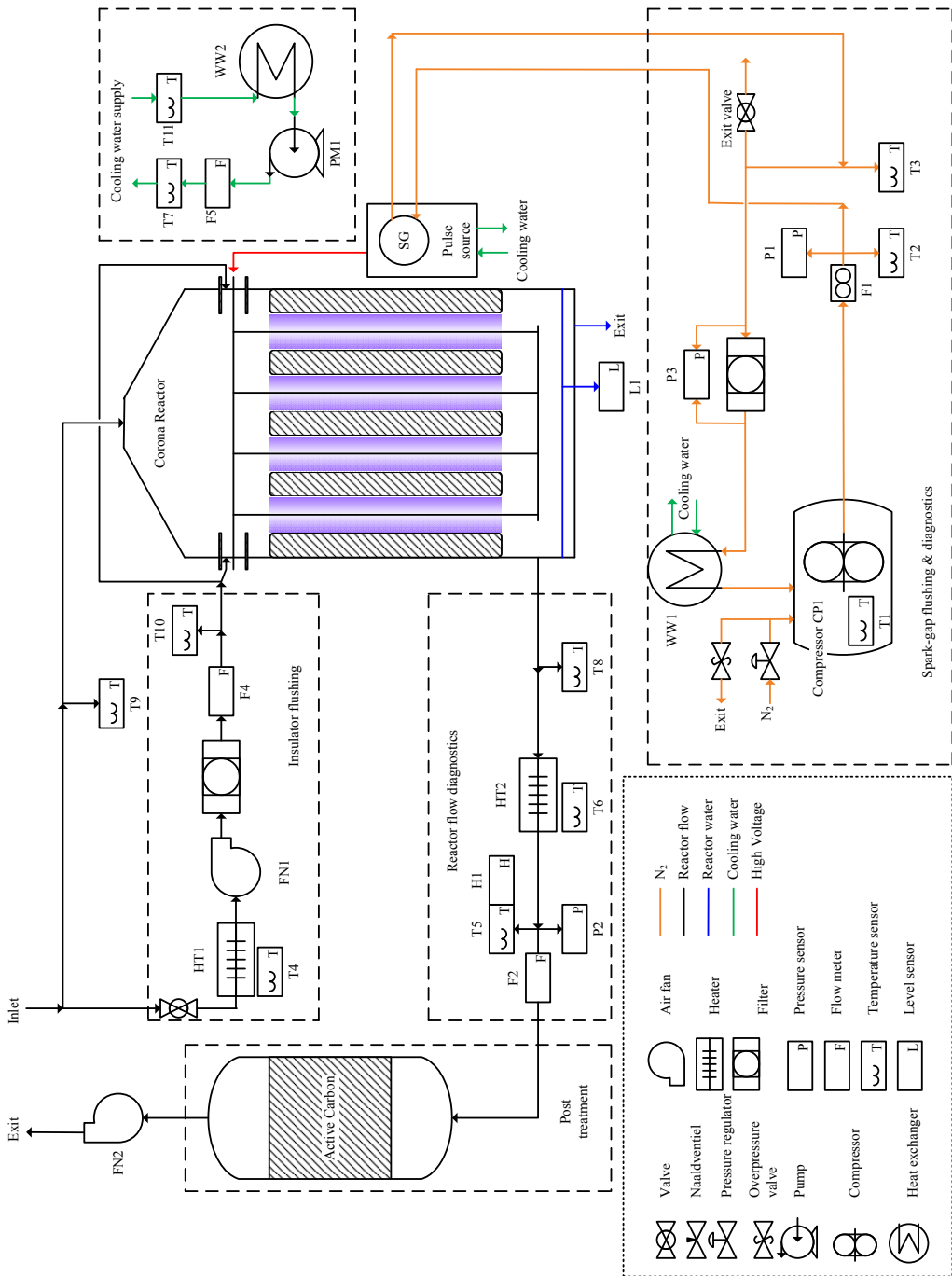
Figure 2.22: Piping and instrumentation diagram.
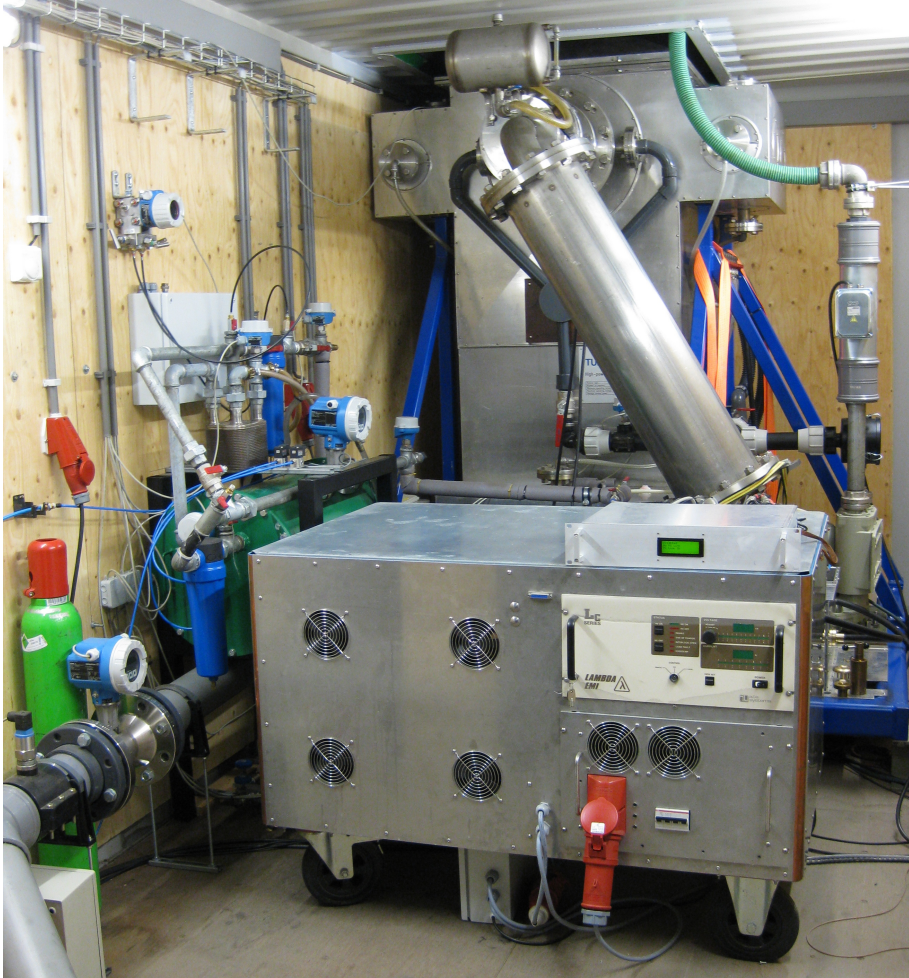
Figure 2.23: Pulsed corona demonstrator interior. The reactor is placed in the back of the container on top of the blue frame. The TLT is the 45 degree angled stainless steel tube in front of the reactor, the spark gap is mounted at the underside and not visible in the image. The cabinet in front of the reactor contains the capacitor charger and DC power supply. The green drum with peripherals to the left of the cabinet is the spark gap purging system. The process gas enters the reactor via the roof of the container, the effluent pipe is the grey pipe which is visible at the left near the floor. Process fan and active carbon filter are placed in the front of the container and not visible in the image.
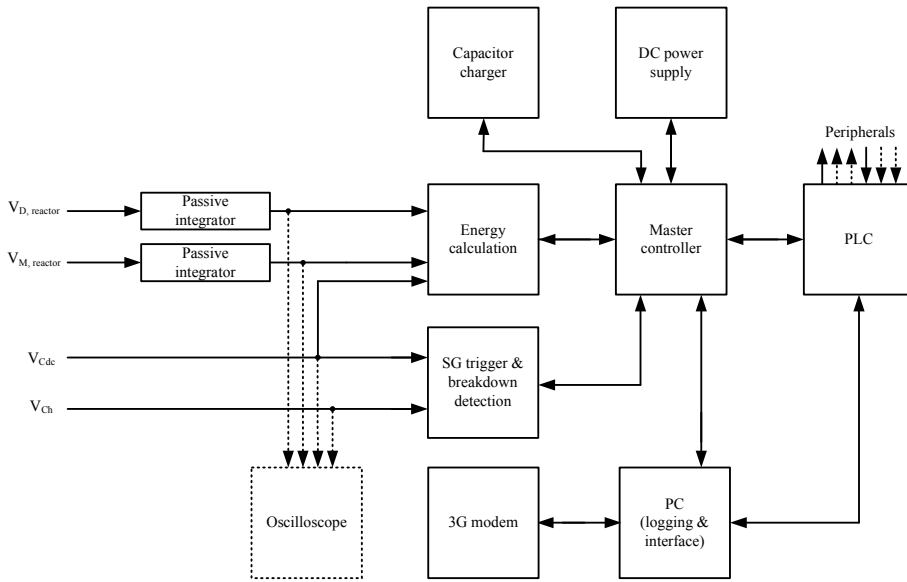
Figure 2.24: Schematic overview of the control and monitoring circuit.
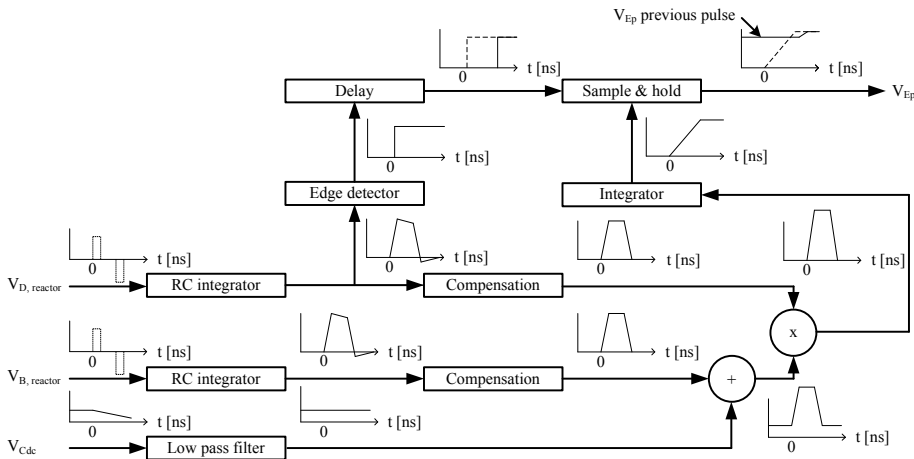
Figure 2.25: Schematic energy measurement circuit. The analog output signal V_{Ep} is proportional to the energy of the last pulse.

system to meet an average trigger time without causing the spark gap to fail to trigger, typically 100-150 μs. Once tuned, the pressure can be maintained for at least 40 hours of operation. A higher flow through the spark gap is needed for increased repetition rates to enhance recovery of the spark gap and prevent pre-firing. The flow is controlled
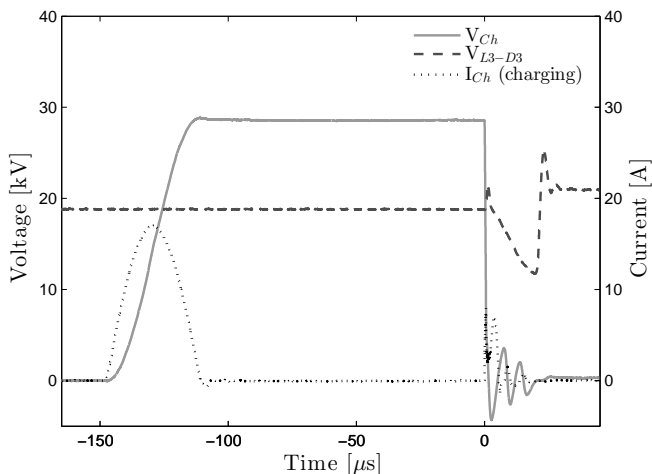
Figure 2.26: Typical DC-bias voltage and C_h charge voltage and current waveforms.

to meet a relative number of pre-fire events compared to the repetition rate, typically 5 %. Total elimination of pre-fire events is not possible and near zero pre-firing would increase the flow significantly. The 5 % threshold is used since it provides acceptable overall performance of the system and has little more flow requirement compared to 10 % pre-firing.

2.4   Electrical characterization

2.4.1   Charging of the energy storage capacitors

The pulse energy storage capacitor C_h is charged in 40 μs to 28.5–32.5 kV (28.5 kV cold system, 32.5 kV warm system) by the resonant capacitor charger, see figure 2.26. The peak charging current is 19 A. The trigger voltage increases in 110 μs until the spark gap fires at $t = 0$. The DC-bias voltage is measured at the intersection of L_3 and D_3 (figure 2.3). The voltage is initially equal to V_{Cdc} as the current through L_3 is zero and diode D_3 is blocking. C_{dc} discharges rapidly at $t = 0$. D_3 and L_3 conduct subsequently the recharging current from the DC buffer C_2 to C_{dc}. The measured voltage is now equal to the voltage on C_2 minus the forward voltage of the diode. The current becomes zero again at $t \approx 20\mu$s, the diode subsequently blocks. The voltage is now equal to the voltage on C_{dc} again. The DC voltage is not equal before discharging and after recharging because of the low repetition rate during the measurement. C_{dc} is slightly discharged between cycles by the high voltage divider and some DC corona discharge activity in the reactor.
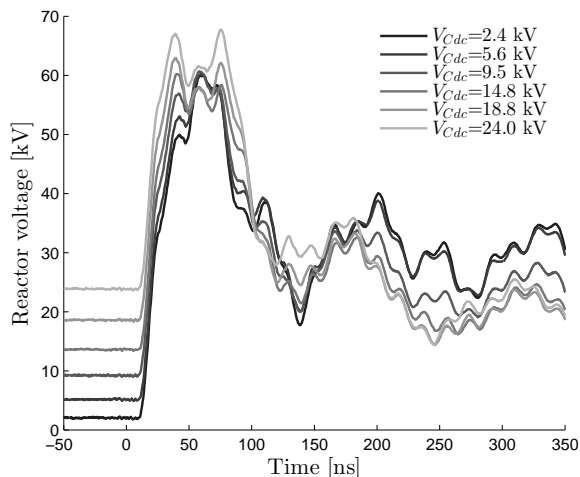
Figure 2.27: Typical reactor voltage waveforms for different DC-bias voltages.

2.4.2   Reactor pulse waveforms

Output waveforms of the pulse power modulator for different DC-bias voltages are shown in figures 2.27 and 2.28. The rise time of the reactor voltage and current are approximately 20 ns. Multiple reflections can be observed on the waveforms but the reactor voltage waveform becomes smoother and wider as the DC-bias voltage increases. The reactor acts initially as an open end with only the reactor capacitance as load for low DC-bias voltages. The resulting reflections cause the output voltage to reach 60 kV which is more than the double input voltage of the TLT. The reactor energy (Figure 2.29) increases significantly with higher DC levels due the improved energy transfer efficiency from C_h to the plasma and the additional energy which is delivered by C_{dc}.

2.4.3   TLT input waveforms

Input waveforms of the TLT for different DC-bias voltages are shown in figures 2.30 and 2.31. The spark gap fires at $t = 0$, the rise times of the cathode voltage and current are respectively 16 and 16.5 ns. The peak switching current is 3.1 kA and the peak voltage is 27.3 kV. The TLT acts as a steady input impedance during the first 35–40 ns (identical waveforms) until reflections due to the reactor–TLT impedance mismatch return. The impedance alteration of the reactor due streamer propagation is dependent on the reactor voltage which results in different reflection patterns for different DC-bias voltages. The current pulse widens and C_h is discharged further as the DC-bias voltage is increased. Matching of a DC-biased system will be discussed in more detail in Chapter 5. The energy in C_h is transferred for 97 % with 24 kV DC-bias voltage.
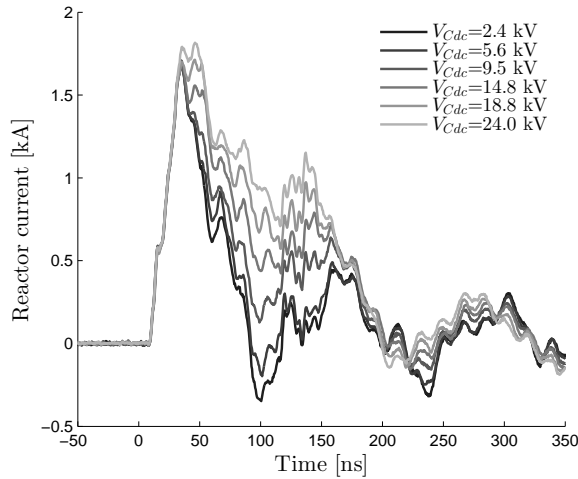
Figure 2.28: Typical reactor current waveforms for different DC-bias voltages.
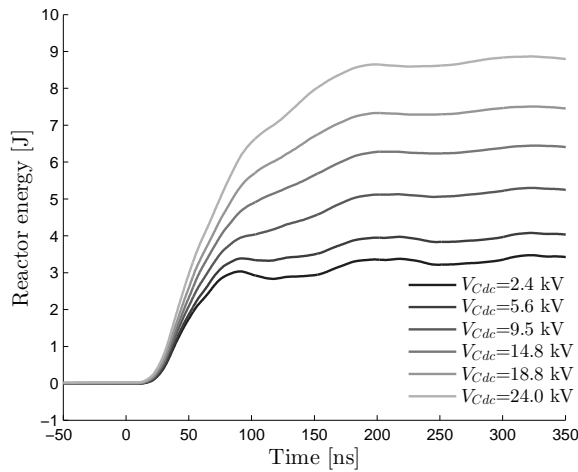
Figure 2.29: Typical reactor energy waveforms for different DC-bias voltages.

The energy transfer to the reactor stops after approximately 100-200 ns depending on the output voltage of the source and quenching behavior of the plasma.

2.4.4 TLT saturation

The energy transfer from C_h stops after 100-200 ns when the corona plasma quenches. The spark gap remains closed because Z_s provides a current path. A slow oscillation between C_h and Z_s can be observed in figures 2.32 and 2.33. A high voltage remains
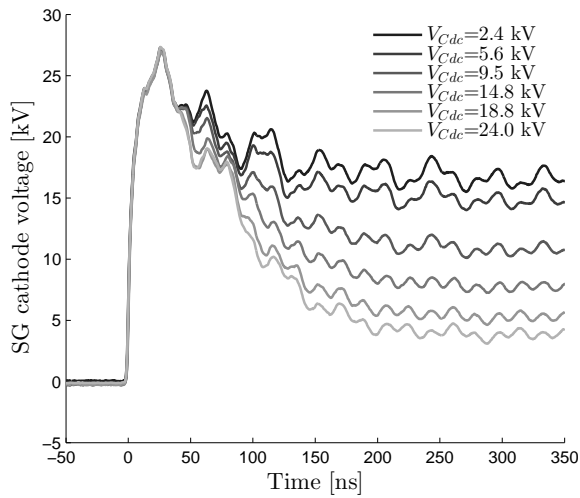
Figure 2.30: Typical spark gap voltage waveforms for different DC-bias voltages.
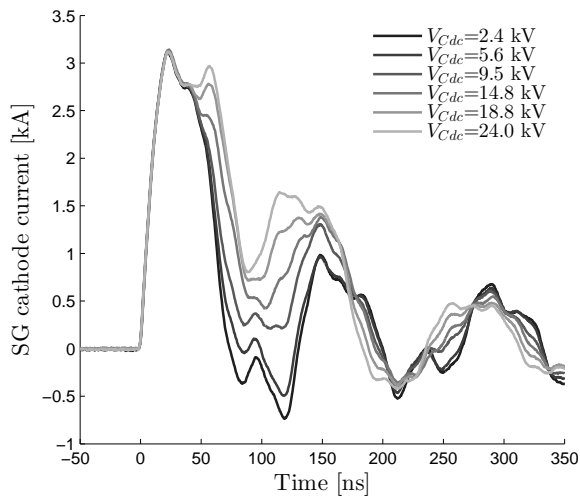
Figure 2.31: Typical spark gap current waveforms for different DC-bias voltages.

on C_h and Z_s when the energy transfer efficiency is very poor with low DC-bias levels. The magnetic cores are able to saturate which is clearly visible in Figure 2.33 at $t \approx 700$ ns. The sudden drop in permeability and impedance results in peak currents up to 1.6 kA. The magnetic cores saturate at approximately 0.32 T which is in good agreement with the specification.
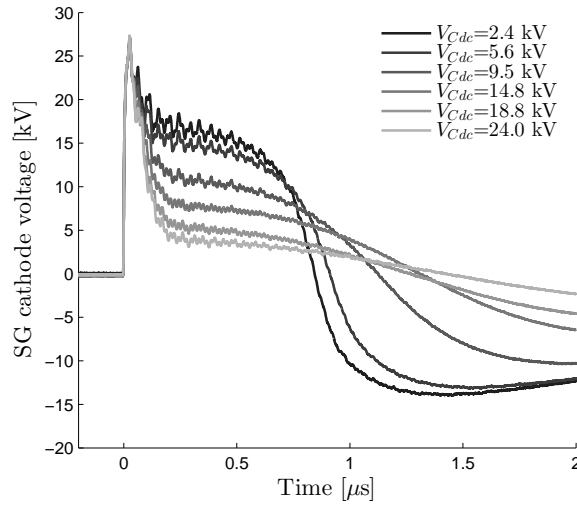
Figure 2.32: Typical spark gap voltage waveforms for different DC-bias voltages.
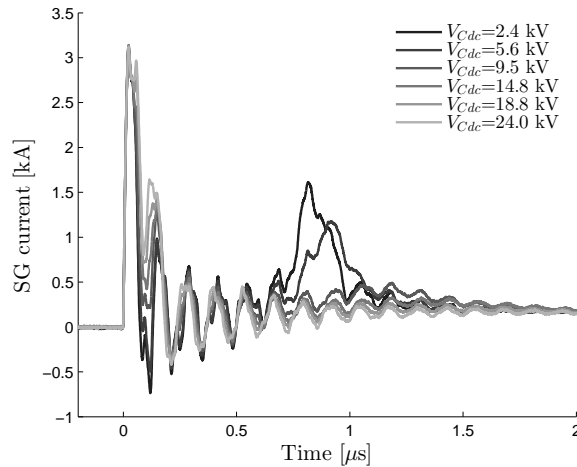
Figure 2.33: Typical spark gap current waveforms for different DC-bias voltages. The sudden increase of the current at $t \approx 700$ ns is caused by saturation of the magnetic cores. This only occurs with low DC-bias voltages because of the poor energy transfer efficiency to the reactor.

2.4.5 Spark gap quenching

The spark gap remains closed up to 20 μs until the energy in C_h is dissipated during the oscillation with Z_s, see Figure 2.34. The non linear current waveform suggests positive and negative saturation of the magnetic cores. The energy is dissipated gradually in
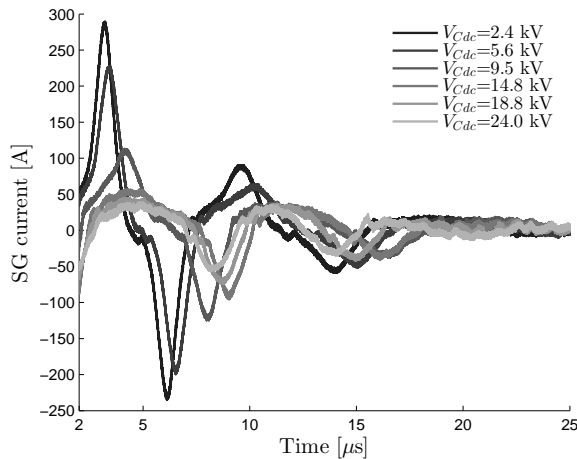
Figure 2.34: Typical spark gap turn-off current waveforms for different DC-bias voltages (2–25 μs).

the cores and spark gap. The spark gap switches off at a zero crossing as the current and voltage on C_h becomes too low to maintain the discharge. An improved energy transfer efficiency causes the spark gap to switch off earlier.

2.4.6 Modulator efficiency

An energy balance of the pulse power modulator is shown in Figure 2.35. The energy flow per pulse in the system is considered at multiple positions: 1. charging energy of capacitor C_h (pulse input energy), 2. charging energy of capacitor C_2 (DC-bias input energy), 3. spark gap–TLT interface (TLT input) and 4. TLT–reactor interface (reactor input). The energy delivered by the capacity charger (1) is 5.7 J per pulse. Between 3.7 and 5.2 J of that energy is transferred via the input of the TLT to the reactor in the first 200 ns, depending on the DC-bias level. Only the initial energy is considered because the plasma in the reactor has quenched after 200 ns, residual energy will be dissipated in the ferrites and spark gap. The reactor energy ranges from 3.4 to 9.2 J per pulse, and is able to reach 10 J when the system has warmed up and the charging voltage on C_h reaches 32.5 kV. The difference between the TLT input and reactor energy equals the energy delivered by the DC-bias circuit minus the losses in the TLT. The energy delivered to the DC buffer capacitor C_2 is very similar which means that the TLT and DC-bias circuit are highly efficient. The overall efficiency of the pulse forming circuit is shown in Figure 2.36. The transfer efficiency of C_h to the TLT is up to 90 % and the transfer efficiency of the energy in C_h and C_2 to the corona plasma is up to 92 %. The losses are primarily determined by the energy transfer efficiency to the plasma and secondly by the spark gap switching losses. Losses of the spark gap during the initial 200 ns energy transfer will be discussed in Chapter 4.
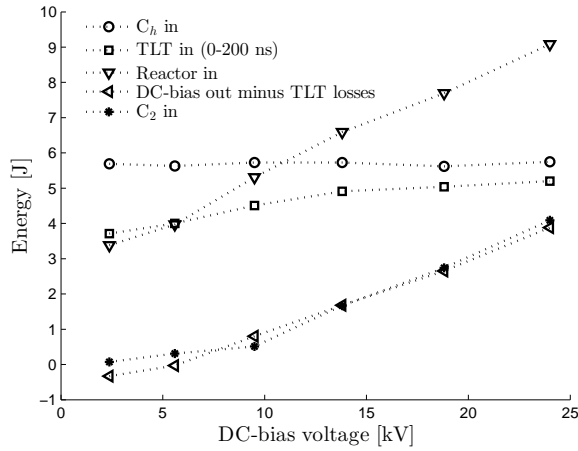
Figure 2.35: Energy transfer for different DC-bias voltages.
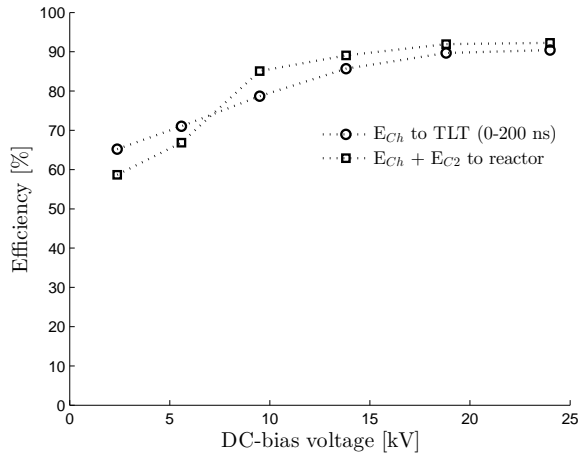
Figure 2.36: Efficiency for different DC-bias voltages.

The efficiency of the capacitor charger and DC-supply are both approximately 90 %. The overall efficiency from mains to the plasma is approximately 83 %. The required purging power for the spark gap is not included.

2.5   Electrode–plate reactor setup

The pulse power supply of the wire-plate reactor is almost identical as described in the previous section. The main differences are the use of an air purged spark gap, a TLT with higher output impedance and the lack of a DC-bias system. The schematic of

47
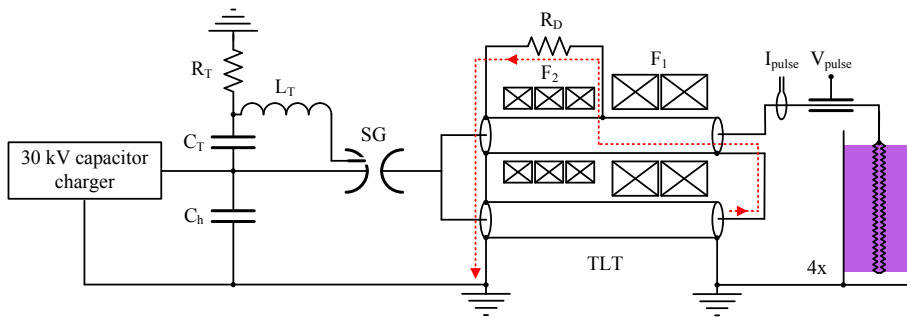
Figure 2.37: Schematic overview of the power modulator for the electrode–plate reactor.
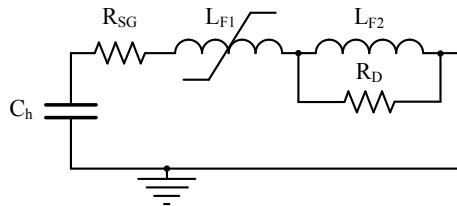
Figure 2.38: Equivalent circuit after the plasma in the reactor quenches.

the power modulator is shown in Figure 2.37. The TLT consists of two 50 Ω RG-218 high voltage coaxial cables. The spark gap is identical to the one which is used in the wire–cylinder setup. A 4 kW scroll compressor with additional drying unit to separate water from the compressed air is applied to purge the spark gap. One of the reasons we switched to the wire–cylinder reactor was the poor energy transfer efficiency of the source to the electrode–plate reactor. The magnetic cores became too hot during continuous operation because they dissipated all residual energy. The problem was patched by using two different core types and a dump resistor. The first magnetic core F_1 is a ferrite core with a high permeability and low saturation flux density. This core is designed to temper the secondary mode current during pulse generation without saturating. The energy transfer to the reactor stops after 500 ns. The residual voltage on C_h remains present and drives core F_1 eventually into saturation, acting as a magnetic switch. This effect is also shown with the wire–cylinder setup, see Figure 2.32 and 2.33. The voltage is now over the dump resistor and inductance which is introduced by the second magnetic core F_2. This Metglass core has a high saturation flux density and a low permeability. This ensures that the core takes only a small portion of the flux during pulse generation and does not saturate. The bulk of the secondary mode current is now diverted in the dump resistor R_D. An equivalent circuit of the damping circuit is shown in Figure 2.38.

The output voltage and current waveforms are shown in Figure 2.39a. Power and
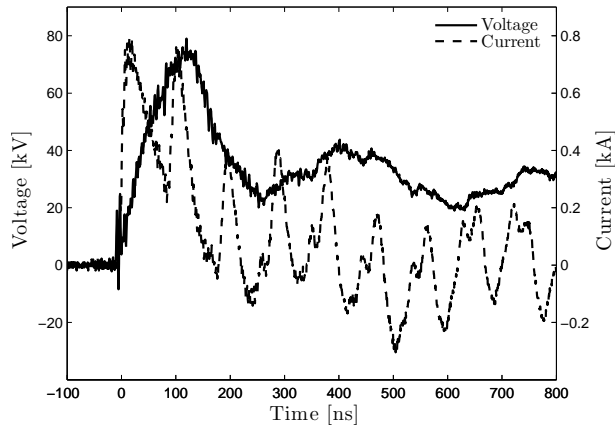
(a) Voltage and current.
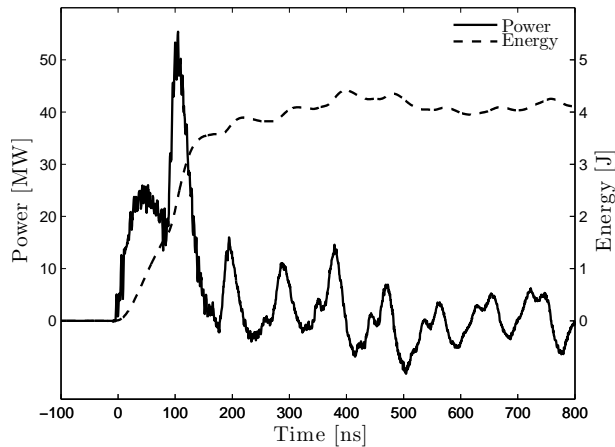
(b) Power and energy.

Figure 2.39: Typical pulse waveforms of the electrode–plate reactor.

energy waveforms are shown in Figure 2.39b. The relative long 100 ns rise time is caused by the massive reactor capacitance and limited output impedance of the source. The energy per pulse transferred to the reactor is approximately 4.1 J per pulse. Large reflections in the waveforms show poor impedance matching between source and reactor.

A schematic overview of the reactor is shown in Figure 2.40, an image is shown in Figure 2.41a. The reactor consists of four rectangular channels. The spacing between the grounded walls of the channel and the electrodes is 70 mm. Each channel is fitted with 25 saw-type electrode blades. The length of the electrodes is 80 cm. The high voltage feedthrough which connects the electrode array to the pulse source is fitted on
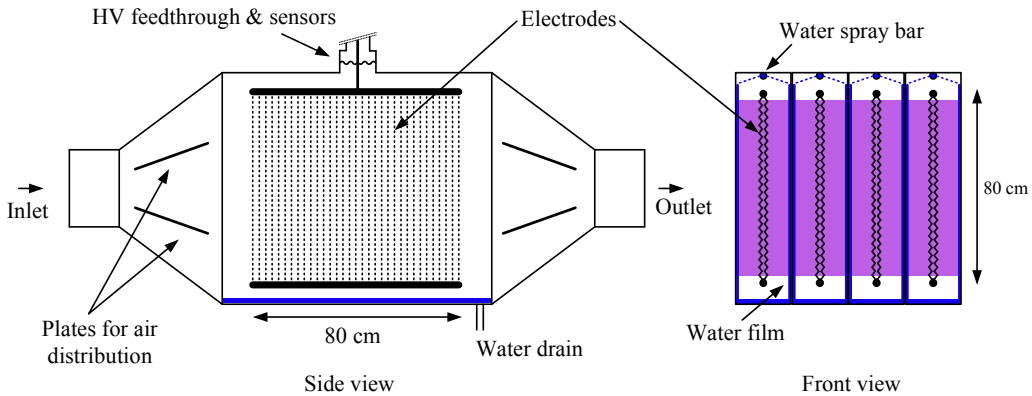
Figure 2.40: Schematic overview of the electrode–plate corona reactor.

top (in the center) of the reactor.

The in- and outlet funnel is fitted with plates which guide the air flow more evenly through the reactor. Water was injected in the reactor during a series of lab NO_x removal experiments to remove HNO_3 from the gas phase, the results will be discussed in Chapter 6.3.2.1. The reactor is fitted with four spray bar which create a water film on the walls of each channel. The fluid is drained at the bottom of the reactor and collected in a water container, the water is continuously recycled via a pump.

2.6   Conclusions

An autonomous semi-industrial scale pilot wire–cylinder type corona reactor has been constructed for on-site demonstrations and application research in the industry. The demonstrator consists of a robust sixteen fold wire-cylinder corona reactor and a spark gap based nanoseconds pulsed power supply which is designed for continuous operation. An additional DC-bias circuit increases the output power of the modulator and enables electrostatic precipitation. The power modulator is capable of generating up to 10 J per pulse with 1 kHz repetition rate. The overall efficiency is 83 %. The reactor and power supply are incorporated in a 20 feet freight container. Additional ancillary devices monitor plasma power, pulse source performance, reactor process flow, temperatures, etcetera. Multiple interrelated systems enable autonomous operation and remote control of the pilot demonstrator. The system was successfully applied for several field and lab air purification tests. The test results are discussed in Chapter 6.

Extensive testing of the corona system made it clear that the limit of the repetition rate was already in sight. As explained in the introduction of this thesis, it is desirable to increase the repetition rate as high as possible. Electrode erosion of the spark gap proved to be also a larger problem than initially anticipated. Therefore, the spark
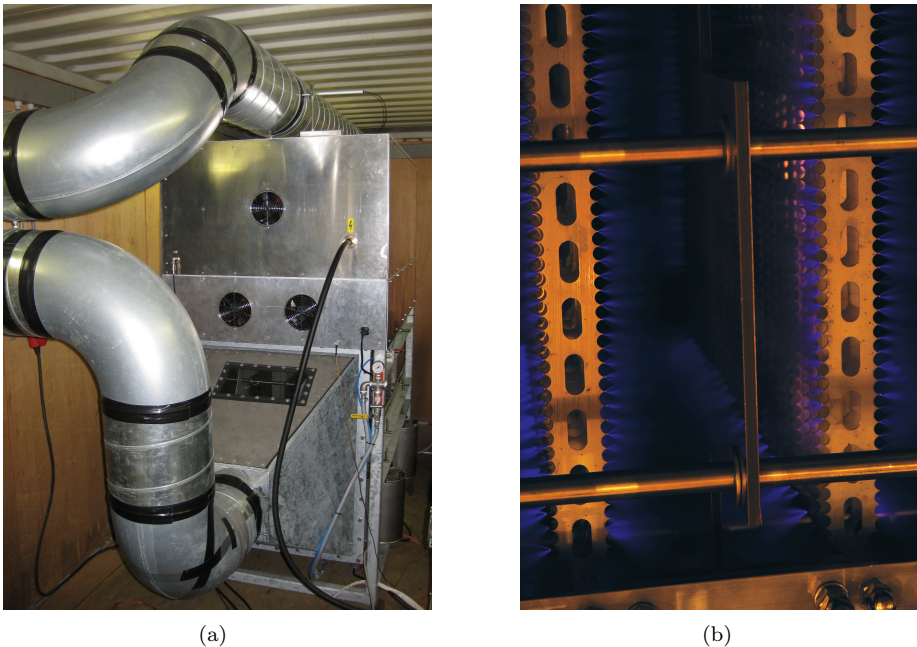
Figure 2.41: (a) Image of the electrode–plate reactor placed inside the pilot container. The TLT and other high voltage components are inside the cabinet on top of the reactor. The piping of the reactor in- and outlet is visible in the image. (b) Electrode configuration inside the reactor. Plasma is visible on the tips of the saw-type electrode blades. The grounded vertical wall of a channel is visible in the middle of the image.

gap performance will be discussed extensively in Chapter 4. Testing of the system at repetition rates exceeding 1 kHz required a new capacitor charger. The charger concept which was described in this chapter is improved at several points and the repetition rate is increased up to 5 kHz. The novel charger is described in Chapter 3.

Large multiple cylinder reactors are required for large flow handling. However, little is known about energizing large reactors with nanosecond pulses. The sixteen cylinder corona reactor enabled us to compare streamer development and energy sharing between multiple cylinders. These results are presented in Chapter 5.

High repetition rate capacitor charger

Abstract

A novel circuit topology of a fast 30 kV capacitor charger for pulsed power applications is presented in this chapter. The charger is optimized for spark gap based pulsed power modulators. A spark gap can fire spontaneously during charging (pre-firing) of a capacitor bank due to stochastic breakdown behavior. The resulting near short circuit of the output can be handled repetitively by the circuit. A 15 kW prototype has been built and the first experimental results are presented. The charger is capable of charging a 8.4 nF capacitor to 30 kV in 35 μs with 91 % efficiency. The maximum repetition rate of this 3.8 J/cycle charger is 5 kHz. An active reset circuit for resetting of the pulse transformer core has been implemented. This circuit is also capable of recovering a large part of the energy which is stored in the stray capacitance of the secondary pulse transformer winding. A numeric simulation tool based on state space modeling is used to simulate circuit behavior. Measurements and simulations are in good accordance. A control loop is implemented to regulate the output voltage. The control scheme features a look up table which is dynamically updated to smoothen instabilities generated by random pre-fire events.

3.1 Introduction

Spark gap switches offer superior switching characteristics which is ideal for efficient switching in the corona system. A large disadvantage of these switches is the recovery behavior which limits the repetition rate of the pulsed power system. Increasing the corona power and homogeneity of the plasma for enhanced plasma processing efficiency can be achieved by higher pulse repetition rates. A high repetition rate capacitor charger (> 1 kHz) is required. The voltage over the switch should be present as short as possible during high repetition rate operation to allow a large recovery time, see Figure 3.1. Fast charging of the capacitor is therefore required.

A second challenge is handling the stochastic breakdown behavior of the spark gap. Especially during high repetition rate operation, the pre-fires (premature breakdown of the gap during charging) probability caused by incomplete recovery and stochastic breakdown behavior of the gas gap becomes more unpredictable. A pre-fire results in a
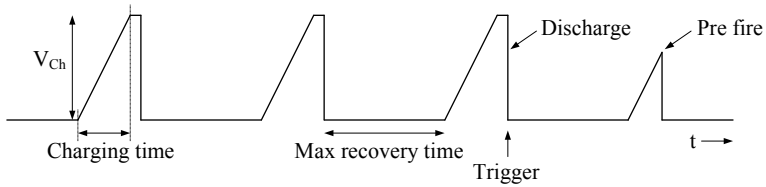
Figure 3.1: Typical C_h charging cycles in a spark gap based pulsed power system.

near short circuit load impedance of the charger circuit. The circuit should be capable of handling these events repetitively.

The charger which is introduced in Section 2.2.1 basically features the fast charging and short-circuit handling capability. However, the circuit has several drawbacks:

1. The output voltage is not stabilized and not adjustable. The output voltage will be highly unstable for several cycles after a pre-fire event. This can lead to additional unstable breakdown behavior during following cycles and is undesirable with an already high pre-fire probability during high repetition rate operation.

2. All energy which is stored in the stray capacitance of the pulse transformer is lost after each cycle. These losses will increase proportionally to the pulse repetition rate.

3. All magnetization energy of the pulse transformer is dissipated by a snubber circuit. These losses will increase proportionally to the pulse repetition rate.

4. The magnetic core of the pulse transformer only operates in the upper halve of B-H curve resulting in a large core cross-section requirement.

A novel circuit topology is presented to improve the latter drawbacks. In Section 3.2 the novel circuit topology for charging high voltage capacitors is presented. Circuit analysis is described in Section 3.3. Simulations can be found in Section 3.4. A 30 kV output, 5 kHz repetition rate implementation with 15 kW output power and a control method for stabilization of pre-fire events is presented in Section 3.5. Performance measurements can be found in Section 3.6.

3.2 Capacitor charger concept

3.2.1 Requirements

1. 30 kV stabilized charging voltage on a 8.4 nF load capacitor.

2. 1 Hz to 5 kHz repetition rate with up to 15 kW total power. We want to be able to study recovery of high power pressurized nitrogen purged spark gap switches at

high repetition rates, secondly we are interested in generation of high repetition rate pulsed plasmas.

3. <50 μs charging time. For 5 kHz operation we want to allow up to 150 μs recovery time. The main part of the energy in the capacitor will be discharged in less than 100 ns, but in practise the gap will remain closed for several micro seconds before all residual energy is dissipated.

4. Handling of up to 100 % pre-fire events. The charger should be short circuit proof, the load impedance will be several ohm when the gap fires during charging.

5. Accepting negative voltage swing of the load capacitor. Depending on the load, the load circuit can oscillate during discharging which can result in voltage reversal.

3.2.2 Circuit topology

Capacitor chargers for pulsed power operation are often series resonant type converters [39–42]. This topology is suitable for large capacitor banks (>100 nF) and can operate in current mode, enabling a linear charging voltage. A very high switching frequency would be needed for fast accurate charging of small capacitors, making it less suitable for our application. Secondly, underdamped discharging of the load capacitor could lead to excessive overload of the full-bridge high voltage rectifier due to voltage reversal.

The charger which is introduced in Chapter 2.2.1 is a proven and robust concept. Energy stored in a low voltage capacitor is resonantly transferred via a pulse transformer to the load capacitor in a single switching cycle. The charging speed and output short circuit handling capability is superior over most circuit topologies. Only the drawbacks of the basic concept need attention and improvements are incorporated in a high repetition rate concept.

3.2.3 Basic resonant charging concept

The basic circuit can be seen in Figure 3.2. Low voltage capacitor C_l is initially charged and the energy will be resonantly transferred to C_h after switch Sw is closed. The leakage inductance (L_s) of the 1:N high voltage pulse transformer is part of the resonant circuit, and a complete energy transfer will be achieved under the following condition: $C_l = N^2 C_h$, see Figure 3.3 and equations 3.3 and 3.4. T_{Sw} is the charging time and C_{tot} is the equivalent series capacitance of C_l and C_h. An additional step up or down ratio can be achieved by creating a mismatch between the capacitance values of C_l and C_h. The value of the leakage inductance is an important design constraint of the transformer. The charging time is limited by the leakage inductance and the maximum allowable current through the switch (see equations 3.1 and 3.2). The charging process of C_h will occur on a microsecond time scale while the capacitor discharges into the load on a nanosecond time scale. When firing of the spark gap already occurs during charging, the capacitor will be discharged almost instantaneously. The closed gap and
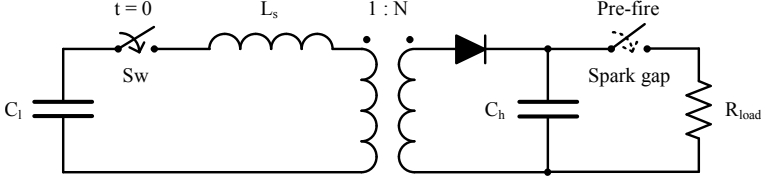
Figure 3.2: Basic resonant charging schematic.

low load impedance will subsequently act as a near short circuit for the charger circuit. C_l will still be partially charged because not all energy could be transferred to C_h. The under-damped $C_l - L_s - R_{Load}$ circuit causes the remaining voltage on C_l to reverse. This effect enables recovery of the residual energy in C_l at the time that the spark gap pre-fires. Switch Sw can still switch-off at the zero crossing of the current waveform (zero current switching) after a pre-fire event. This is required to transfer the energy in the leakage inductance of the pulse transformer back to C_l.

$$T_{Sw} = \pi\sqrt{L_s C_{tot}} \ , \quad C_{tot} = \frac{N^2 C_l C_h}{N^2 C_h + C_l} \tag{3.1}$$

$$\hat{I}_{Sw} = \frac{V_{Cl}(0)}{\sqrt{L_s/C_{tot}}} \tag{3.2}$$

$$V_{C_l}(T_{Sw}) = V_{Cl}(0)\left(1 - \frac{2C_{tot}}{C_l}\right) \tag{3.3}$$

$$V_{C_h}(T_{Sw}) = N^2 V_{Cl}(0)\left(1 + \frac{2C_{tot}}{N^2 C_h}\right) \tag{3.4}$$

3.2.4 Introduction novel circuit topology

Two circuits are added to the basic resonant charging circuit (see Figure 3.4). A charge circuit for controlled charging of capacitor C_l and a circuit for active resetting of the pulse transformer which enables symmetric flux swing. Energy in the stray capacitance of the secondary winding of the transformer (C_s) is also partially recovered by this circuit. The high output voltage and large size of the secondary coil of pulse transformers results in a significant amount of energy which is stored in the stray capacitance after a cycle. It is worthwhile recovering this energy, especially in high repetition rate applications.

C_l and C_M are uncharged at start-up but they are initially charged at the beginning of a cycle during operation as a result of the previous cycle. C_0 is the power supply buffer. Figures 3.5 and 3.6 show the simulated voltage and current waveforms under normal and pre-fire conditions. Time slots a-f correspond to a-f in Figure 3.4.
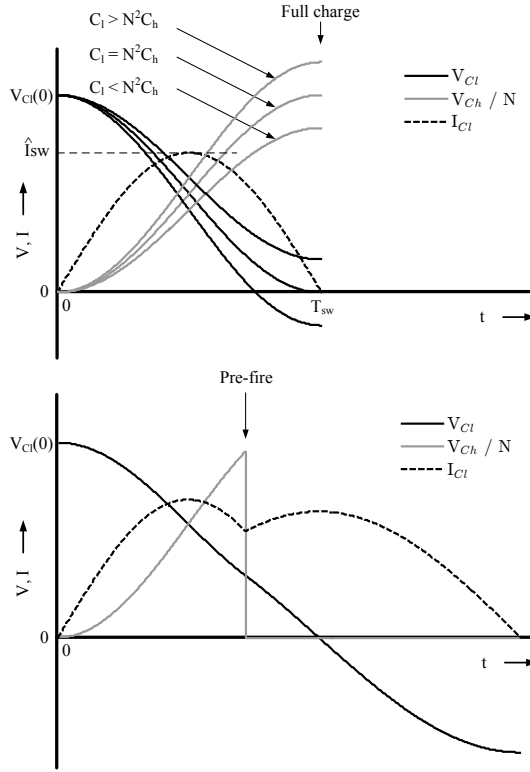
Figure 3.3: Typical resonant charging voltage and current waveforms for different capacitor value ratios and for pre-fire operation. The duration of one cycle is typically 40-80 μs.

(a) First, Sw_3 is closed to pre-magnetize the transformer core. The primary winding of the transformer is reversely biased and the magnetization current I_M builds up linearly via $C_M - R_M - Sw_3 - L_M$ until Sw_3 is opened again. C_M discharges slightly during this process. C_s is charged to $-NV_{C_M}$. R_M is included to damp the oscillation which occurs by $C_s - L_s$ at the start of the pre-magnetization step. The oscillation can be critically damped but this will result in additional losses. The oscillation is damped with an acceptable peak current through the switch.

(b) The actual charging of C_h (and C_s) is subsequently started when Sw_3 is opened and Sw_2 is simultaneously closed. The values of C_l and C_h are mismatched ($C_l < N^2C_h$) to introduce a slightly negative voltage on C_l at the end of charging. The reason for the mismatch and voltage reversal will be explained in step f. The voltage will reverse excessively when a pre-fire event occurs. In the meanwhile, the primary winding of the transformer is forward biased and the magnetization current (I_M) reverses.

57
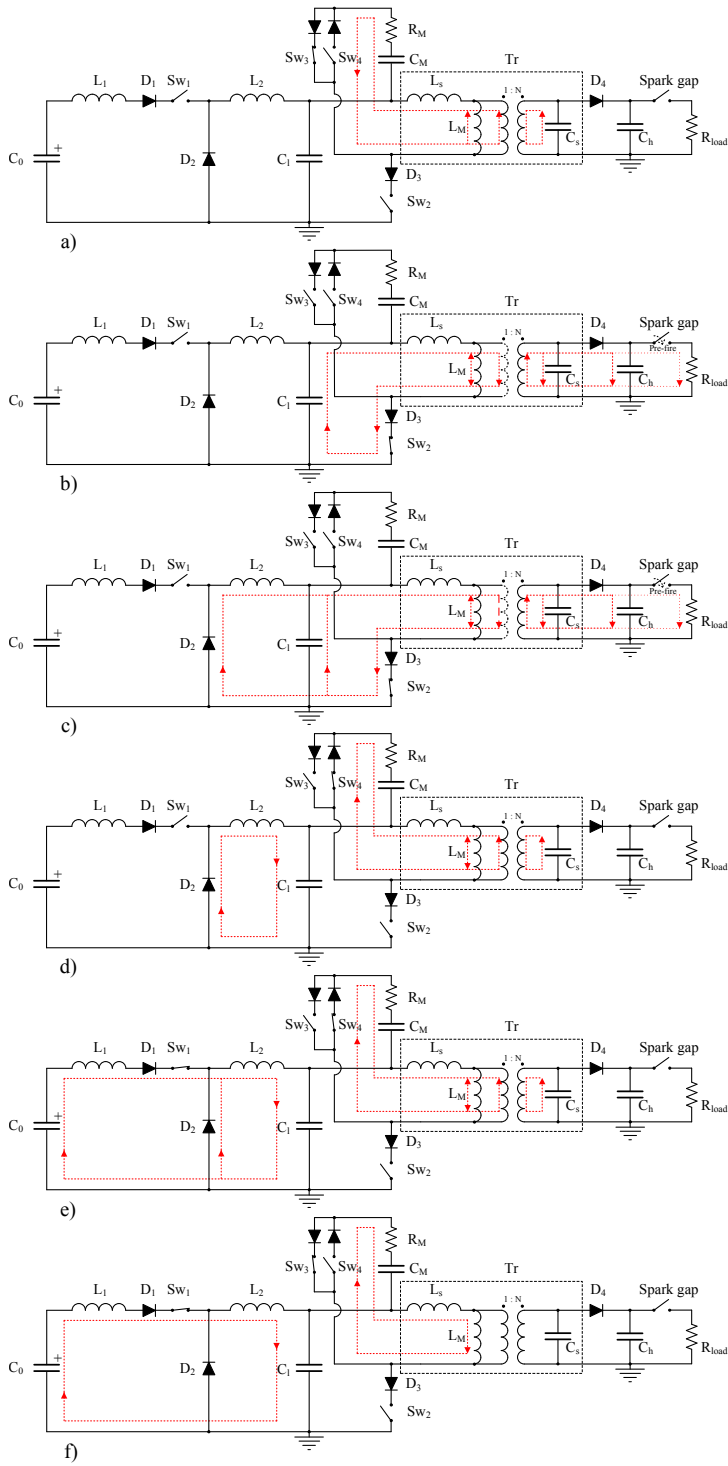
Figure 3.4: Multiple steps of a charging cycle.
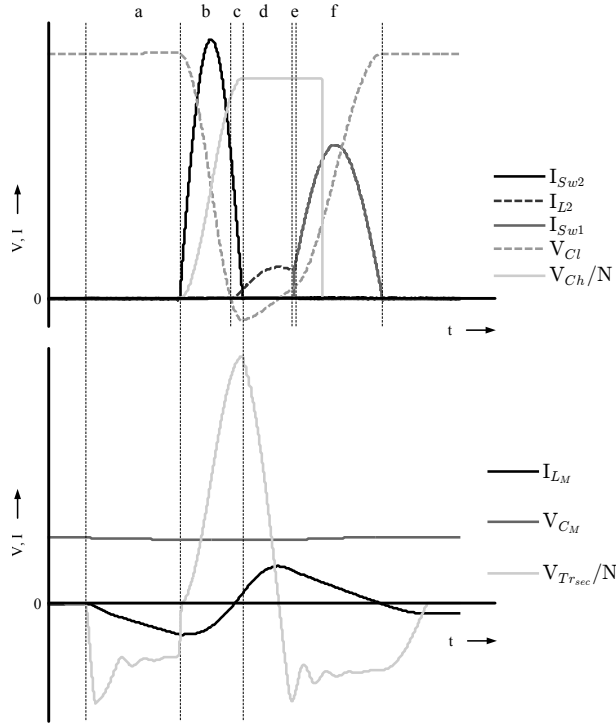
Figure 3.5: Multiple steps of a charging cycle during full charge operation. The duration of one cycle is typically 100-200 μs. Typical peak voltage and current values in the figure are respectively up to 1200 V and up to 1 kA. The magnetization current I_{L_m} is typically up to 20 A. V_{Ch} and $V_{Tr_{sec}}$ are scaled with the winding ratio of the transformer.

(c) Diode D_2 will start conducting at the moment that the voltage on C_l becomes negative. A pre-fire (according to the definition) is still possible until the current through Sw_2 becomes zero and the charge cycle is completed.

(d) Under non pre-fire operation, diode D_4 will block and the energy in C_s is transferred to L_M (oscillation $C_s - L_M$). This increases the magnetization current I_M, but the energy is not lost. Sw_4 will now be closed and the voltage over the primary winding will swing negative until C_M is able to clamp the voltage. The magnetization energy will now be transferred back to C_M. The additional switch Sw_4 is required (instead of only a diode) to prevent that energy from C_l is transferred to C_M. The voltage over the primary winding can become more negative than the quasi static voltage on C_M during a pre-fire event. The voltage level on C_M stabilizes during repetitive (normal, full charge) operation, and balances the magnetization current. C_s will be discharged immediately under
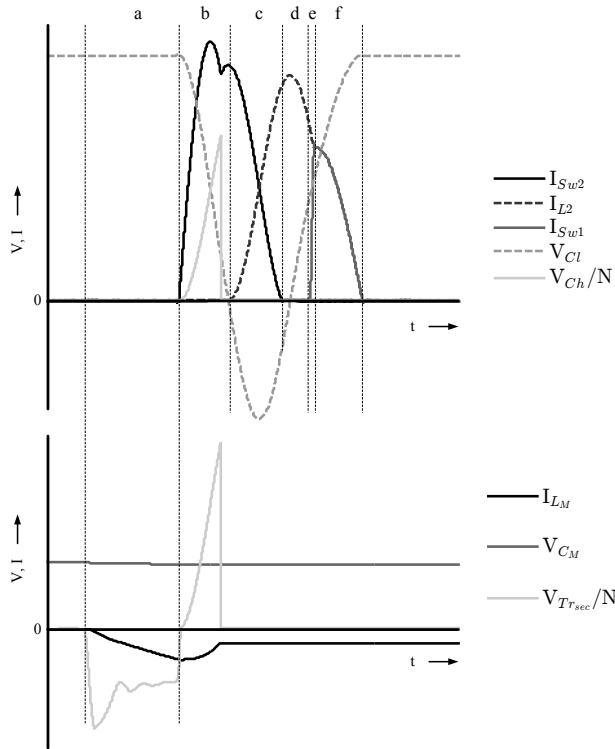
Figure 3.6: Multiple steps of a charging cycle during pre-fire operation. The duration of one cycle is typically 100-200 μs. Typical peak voltage and current values in the figure are respectively up to 1200 V and up to 1 kA. The magnetization current I_{L_m} is typically up to 20 A. V_{Ch} and $V_{Tr_{sec}}$ are scaled with the winding ratio of the transformer.

pre-fire condition, the energy in C_s will most likely be dissipated in R_{Load} and D_4. This will cause an imbalance or residual magnetization current. The residual magnetization energy will keep oscillating between $L_M - C_s$. Additionally, the residual voltage on C_l is now able to reverse positive via $C_l - D_2 - L_2$.

(e) Sw_1 is closed at a specific time to recharge C_l. Inductor L_1 is added to enable soft switching of Sw_1 which also decreases losses in D_2 by limiting the dI/dt. The diode will be able to recover at a low reverse current.

(f) Diode D_2 blocks, C_l can now be fully recharged by the buffer (C_0) to the same initial voltage (step a). More or less current can built up in L_1 and L_2 by allowing the voltage to reverse up to a certain level in step d, which eventually results in a higher or lower charging level of C_l. The closing moment of the switch (step e) controles the output voltage of the charger, the switch can be opened after the

zero crossing of the current. The closing moment of Sw_1 will be steady under normal operation but needs to be dependent on the amount of voltage reversal on C_l during a pre-fire event.

3.3 Circuit analysis

3.3.1 State space model

Additional modeling of the circuit is required to gain more insight in the circuit behavior and to enable optimal selection of component values. An analytical approach to describe sub-circuits is not attempted. Worst case, even if the magnetization current of the transformer is neglected, up to two inductors and two capacitors are part of a sub-circuit which would require solving of fourth order differential equations. Instead, a state space modeling approach is applied to create a fast numeric simulation tool [43, 44].

Direct transformation of the complete circuit to a state space representation is not possible due to the non-linearities introduced by the presence of switches and diodes. However, a sub-circuit without non-linear components (Linear Time Invariant (LTI) system) can be represented by a state space description as in equations 3.5 and 3.6.

$$\dot{\mathbf{x}} = \mathbf{A}\mathbf{x} + \mathbf{B}\mathbf{u} \tag{3.5}$$

$$\mathbf{y} = \mathbf{C}\mathbf{x} + \mathbf{D}\mathbf{u} \tag{3.6}$$

$\mathbf{x}$ is called the state vector, $\mathbf{A}$ is the state or system matrix. The input or control vector $\mathbf{u}$ is weighted by the coefficients in (input) matrix $\mathbf{B}$. Matrices $\mathbf{C}$ and $\mathbf{D}$ are respectively the output matrix and feed-through (or feed-forward) matrix. $\mathbf{y}$ is the output vector.

$$\mathbf{x} = \begin{bmatrix} V_{C_0} \\ V_{C_l} \\ V_{C_h*} \\ I_{L_1} \\ I_{L_2} \\ I_{L_s} \end{bmatrix} \tag{3.7}$$

61
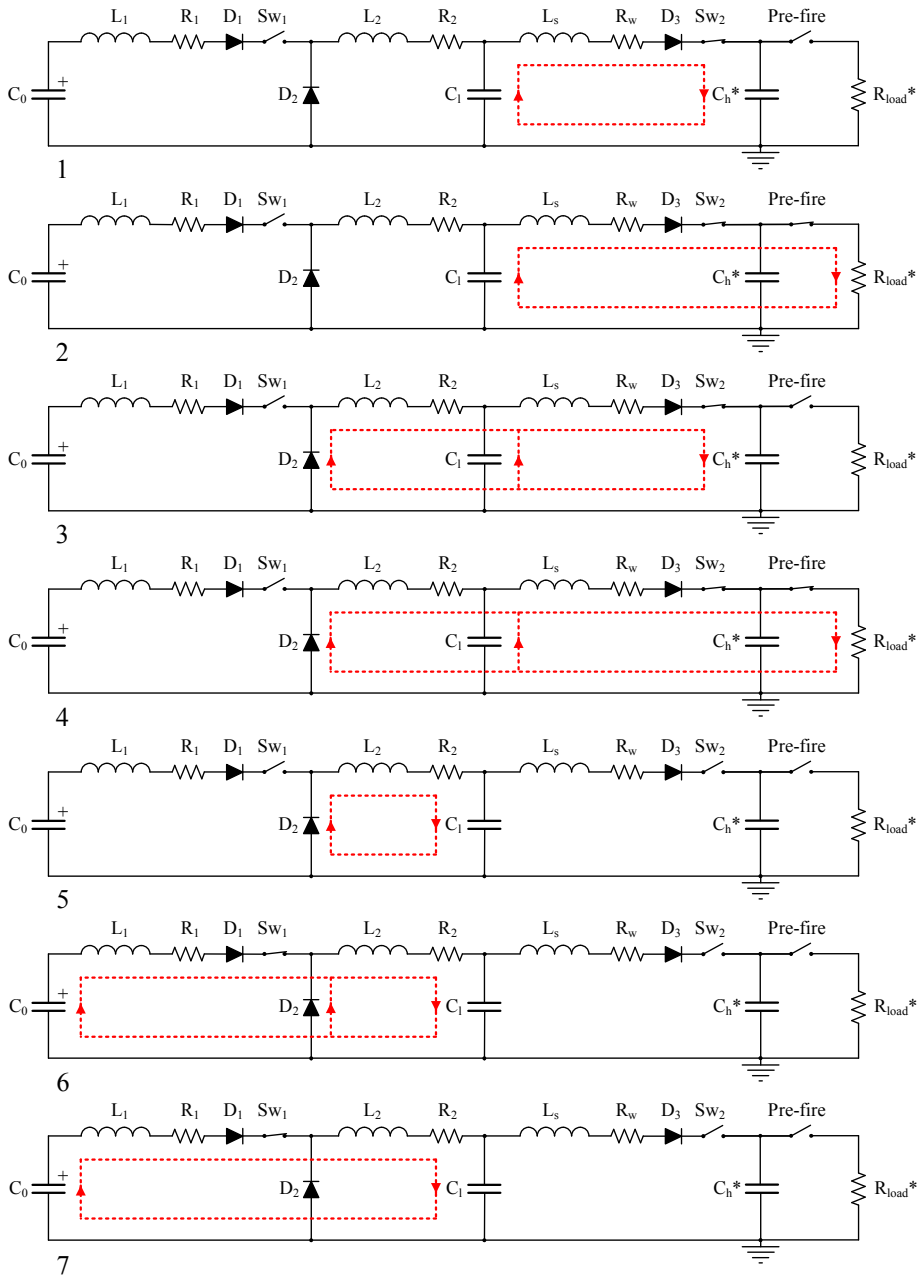
Figure 3.7: Equivalent circuit for the state space model divided into seven modes.

$$
\mathbf{A_1} =
\begin{bmatrix}
\cdot & \cdot & \cdot & \cdot & \cdot & \cdot \\
\cdot & 0 & 0 & \cdot & \cdot & -\frac{1}{C_l} \\
\cdot & 0 & 0 & \cdot & \cdot & \frac{1}{C_h} \\
\cdot & \cdot & \cdot & \cdot & \cdot & \cdot \\
\cdot & \cdot & \cdot & \cdot & \cdot & \cdot \\
\cdot & \frac{1}{L_s} & -\frac{1}{L_s} & \cdot & \cdot & -\frac{R_w}{L_s}
\end{bmatrix}
\tag{3.8}
$$

$$
\mathbf{A_2} =
\begin{bmatrix}
\cdot & \cdot & \cdot & \cdot & \cdot & \cdot \\
\cdot & 0 & \cdot & \cdot & \cdot & -\frac{1}{C_l} \\
\cdot & \cdot & \cdot & \cdot & \cdot & \cdot \\
\cdot & \cdot & \cdot & \cdot & \cdot & \cdot \\
\cdot & \cdot & \cdot & \cdot & \cdot & \cdot \\
\cdot & \frac{1}{L_s} & \cdot & \cdot & \cdot & -\frac{R_w+R_{load}{}^*}{L_s}
\end{bmatrix}
\tag{3.9}
$$

$$
\mathbf{A_3} =
\begin{bmatrix}
\cdot & \cdot & \cdot & \cdot & \cdot & \cdot \\
\cdot & 0 & 0 & \cdot & \frac{1}{C_l} & -\frac{1}{C_l} \\
\cdot & 0 & 0 & \cdot & 0 & \frac{1}{C_h^*} \\
\cdot & \cdot & \cdot & \cdot & \cdot & \cdot \\
\cdot & -\frac{1}{L_2} & 0 & \cdot & -\frac{R_2}{L_2} & 0 \\
\cdot & \frac{1}{L_s} & -\frac{1}{L_s} & \cdot & 0 & -\frac{R_w}{L_s}
\end{bmatrix}
\tag{3.10}
$$

$$
\mathbf{A_4} =
\begin{bmatrix}
\cdot & \cdot & \cdot & \cdot & \cdot & \cdot \\
\cdot & 0 & \cdot & \cdot & \frac{1}{C_l} & -\frac{1}{C_l} \\
\cdot & \cdot & \cdot & \cdot & \cdot & \cdot \\
\cdot & \cdot & \cdot & \cdot & \cdot & \cdot \\
\cdot & -\frac{1}{L_2} & \cdot & \cdot & -\frac{R_2}{L_2} & 0 \\
\cdot & \frac{1}{L_s} & \cdot & \cdot & 0 & -\frac{R_w+R_{load}{}^*}{L_s}
\end{bmatrix}
\tag{3.11}
$$

$$
\mathbf{A_5} =
\begin{bmatrix}
\cdot & \cdot & \cdot & \cdot & \cdot & \cdot \\
\cdot & 0 & \cdot & \cdot & -\frac{1}{C_l} & \cdot \\
\cdot & \cdot & \cdot & \cdot & \cdot & \cdot \\
\cdot & \cdot & \cdot & \cdot & \cdot & \cdot \\
\cdot & \frac{1}{L_2} & \cdot & \cdot & -\frac{R_2}{L_2} & \cdot \\
\cdot & \cdot & \cdot & \cdot & \cdot & \cdot
\end{bmatrix}
\tag{3.12}
$$

$$
\mathbf{A_6} =
\begin{bmatrix}
0 & 0 & \cdot & \frac{1}{C_0} & 0 & \cdot \\
0 & 0 & \cdot & 0 & -\frac{1}{C_l} & \cdot \\
\cdot & \cdot & \cdot & \cdot & \cdot & \cdot \\
-\frac{1}{L_1} & 0 & \cdot & 0 & \frac{R_1}{L_1} & \cdot \\
0 & \frac{1}{L_2} & \cdot & 0 & -\frac{R_2}{L_2} & \cdot \\
\cdot & \cdot & \cdot & \cdot & \cdot & \cdot
\end{bmatrix}
\tag{3.13}
$$

$$
\mathbf{A_7} =
\begin{bmatrix}
0 & 0 & \cdot & \frac{1}{C_0} & \cdot & \cdot \\
0 & 0 & \cdot & \frac{-1}{C_l} & \cdot & \cdot \\
\cdot & \cdot & \cdot & \cdot & \cdot & \cdot \\
\frac{-1}{L_1+L_2} & \frac{1}{L_1+L_2} & \cdot & -\frac{R_1+R_2}{L_1+L_2} & \cdot & \cdot \\
\frac{-1}{L_1+L_2} & \frac{1}{L_1+L_2} & \cdot & -\frac{R_1+R_2}{L_1+L_2} & \cdot & \cdot \\
\cdot & \cdot & \cdot & \cdot & \cdot & \cdot
\end{bmatrix}
\tag{3.14}
$$

The magnetization behavior of the transformer shouldn't have any influence on the basic operation of the circuit. Only the leakage inductance of the transformer is part of a resonant sub-circuit and should be included. The number of modes (active sub-circuits) in which the circuit operates can be limited to seven by neglecting the magnetization current and assuming that $Z_{Ch} >> R_{load}$. The approximation is valid
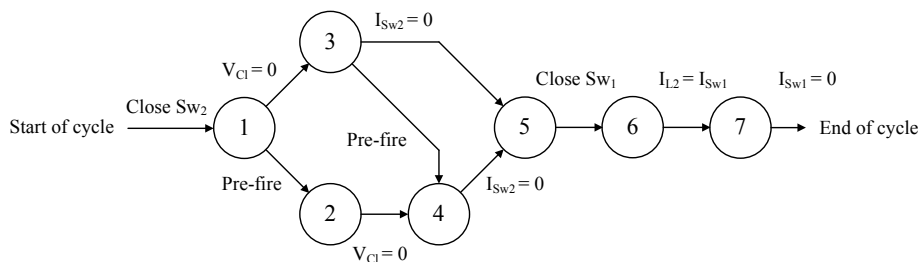
Figure 3.8: Transition diagram.

if C_h discharges very fast in a low load impedance after a pre-fire event.

Figure 3.7 is the simplified circuit which will be considered for modeling, the switches and diodes are ideal. The transformer is substituted by an equivalent circuit in which only the leakage inductance L_s and winding resistance R_w is considered, component values on the secondary side are scaled by the transformer winding ratio ($C_h{}^* = N^2 C_h$ and $R_{Load}{}^* = R_{load}/N^2$). Each mode represents one of the sub-circuits (1-7) in the figure. The model switches between modes, after events as e.g. zero-crossing of a diode current, enabling a switch or a pre-fire. The transition diagram can be observed in Figure 3.8.

Each mode can be presented by the state vector $\mathbf{x}$ and state matrix $\mathbf{A_k}$ (matrices 3.8–3.14) which changes when the model switches to a different mode. The dots are zero values and not part of a sub-circuit. There are no voltage or current sources in the circuit so $\mathbf{u}$, $\mathbf{B}$ and $\mathbf{D}$ are zero matrices. We choose the output $\mathbf{y}$ to be equal to $\mathbf{x}$ by declaring a unit matrix $\mathbf{C}$. The complete model (state space representations and transition diagram) is implemented in Matlab and can be numerically solved with initial conditions $\mathbf{x(0)}$, starting with $\mathbf{A_1}$. Initially only the capacitor voltages on C_l and power supply buffer C_0 are defined and non-zero. The output $\mathbf{y(t)}$ is solved until complied with one of the conditions in the transition diagram. Next, the model switches to the next state matrix $\mathbf{A_k}$. The model has besides the component values, four input parameters to solve a complete cycle: $V_{C_0,init}$, $V_{C_l,init}$, $T_{pre-fire}$ and Td_{Sw_1}, see Figure 3.9 for the definitions.

3.3.2 Magnetization of the pulse transformer

The active reset circuit can provide symmetric flux-swing of the transformer. The magnetization energy storage capacitor C_M oscillates with the transformer magnetization inductance L_M when Sw_3 is closed during the pre-magnetization step (see Figure 3.4a). The maximum pre-magnetization time ($T_{pm,max}$) will be reached when all energy in C_M is transferred to L_M, which can be approximated by Equation 3.15 for small R_M values. The value of damping resistor R_M should be small to limit energy dissipation, every energy loss will eventually result in an unbalanced flux-swing.
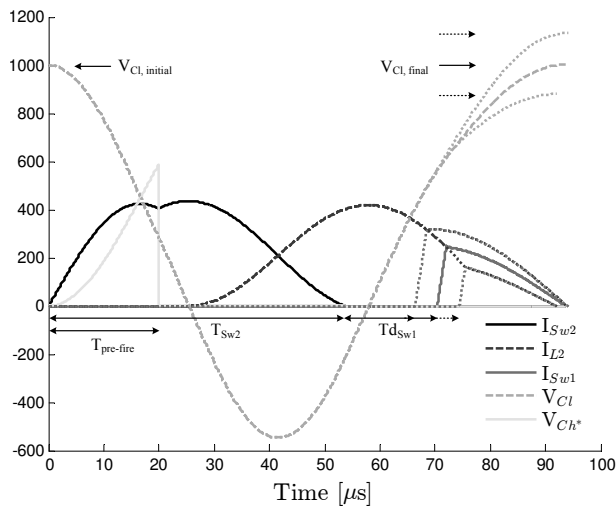
Figure 3.9: Typical model output waveforms as a function of time.

$$T_{pm,max} \approx \frac{\pi}{2}\sqrt{L_M C_M}, \quad R_M << \sqrt{\frac{L_M}{C_M}} \tag{3.15}$$

Dependent on T_{pm}, the voltage level on C_M will settle with a small ripple during operation under the condition that $T_{pm} << T_{pm,max}$. The relation between T_{pm} and V_{C_M} will be derived in this section. A detailed description and analysis of the active reset circuit can be found in [45]. In addition to this reference, we also consider the contribution of the energy in C_s. The ripple voltage on C_M caused by the pre- and demagnetization process can be minimized by choosing a large C_M value to prevent excessive discharging during the pre-magnetization step. No losses are considered to estimate an upper bound for the voltage level on C_M. The equivalent magnetization circuit that will be considered for modeling is shown in Figure 3.10. The leakage inductance L_s and damping resistor R_M are neglected. $L_M = kL_{prim}$ where k and L_{prim} are respectively the coupling coefficient and primary inductance of the transformer. A schematic V_{C_M}, V_{C_s} and magnetization current waveform of a single cycle are shown in Figure 3.11. Events which affect the magnetization current are divided into five time slots ($t_0 - t_5$) which also correspond to Figure 3.10.

($t_0 - t_1$) Initially at t_0, Sw_3 is closed to start the pre-magnetization process. V_{C_M} is applied over the primary transformer winding which charges stray capacitance C_s to $-NV_{C_M}$. A negative magnetization current is now able to increase linearly during T_{pm} (Equation 3.16).

$$I_{L_M}(t_1) = -\frac{1}{L_M}\int_{t_0}^{t_1} V_{C_M} dt \approx -\frac{T_{pm}V_{C_M}}{L_M} \tag{3.16}$$

65
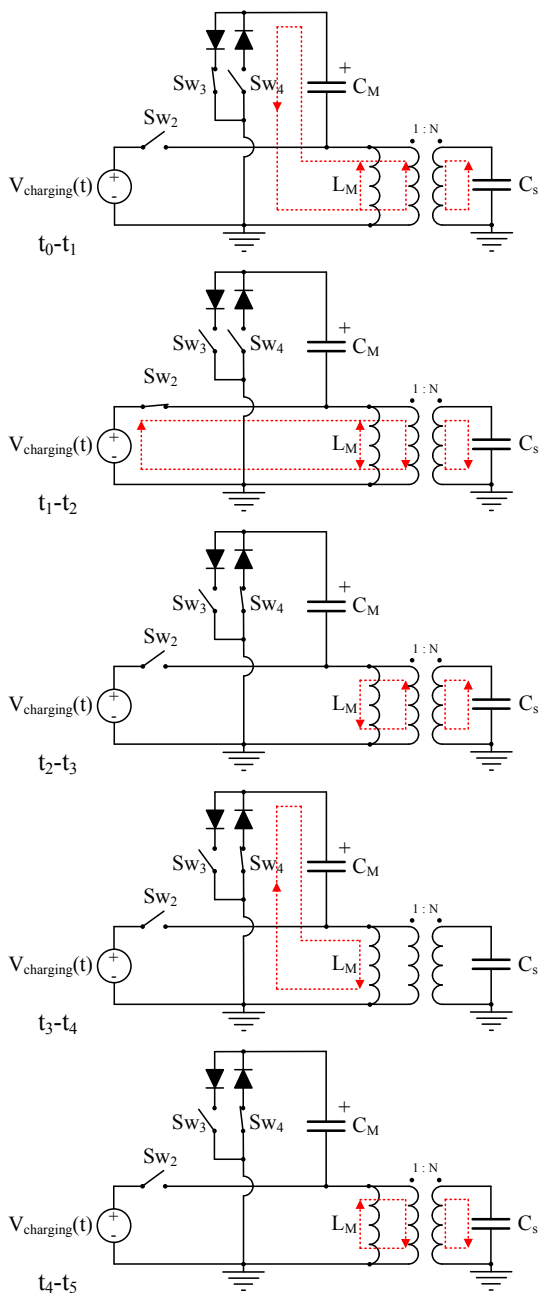
Figure 3.10: Equivalent magnetization circuit.
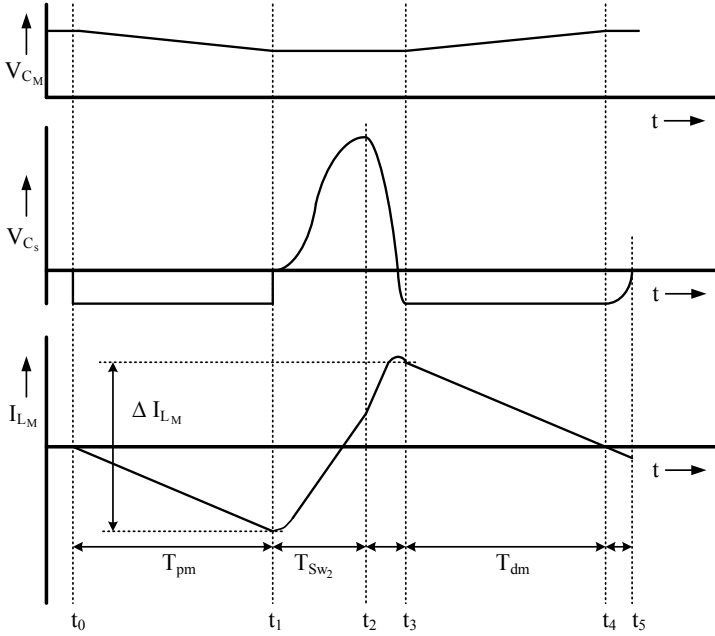
Figure 3.11: Schematic magnetization behavior of a cycle. The typical duration of a cycle is 100-200 μs.

($t_1 - t_2$) Sw_3 opens and Sw_2 closes simultaneously. An amount ΔI_{L_M} in the opposite direction is imposed by the voltage which is present over primary winding of the transformer during charging of C_h and C_s (Equation 3.17).

$$I_{L_M}(t_2) = I_{L_M}(t_1) + \frac{1}{L_M} \int_{t_1}^{t_2} V_{charging}(t)dt \qquad (3.17)$$

($t_2 - t_3$) The actual charging process is finished. Stray capacitance C_s is fully charged at t_2 and Sw_2 opens. The oscillation between $L_M - C_s$ causes an energy transfer from C_s to L_M. The voltage needs to swing negative until V_{C_M} is able to clamp the voltage on the primary winding (t_3), transferring some energy back to C_s. The difference in energy ($E_{C_s}(t_2)$-$E_{C_s}(t_3) = \frac{1}{2}C_s(\hat{V}_{C_s}^2 - (-NV_{C_M})^2)$), adds to the magnetization current, see Equation 3.18.

$$I_{L_M}(t_3) = \sqrt{I_{L_M}(t_2)^2 + \frac{C_s}{L_M}(V_{C_s}(t_2)^2 - (-NV_{C_M})^2)} \qquad (3.18)$$

67

($t_3 - t_4$) Sw_4 already closed at t_2. The energy in L_M will now be transferred back to C_M. The dI_{L_M}/dt wil be equal during pre- and demagnetization, assuming a small ripple voltage on C_M.

($t_4 - t_5$) The magnetization current becomes zero and C_s is still charged to $-NV_{C_M}$. The residual energy in C_s will now oscillate back and forth between C_s and L_M which results in a residual magnetization current, see Equation 3.19.

$$I_{L_M}(t_5) = -\sqrt{\frac{C_s}{L_M}} N V_{C_M} \tag{3.19}$$

The total swing of the magnetization current can be expressed by Equation 3.20.

$$\Delta I_{L_M} = I_{L_M}(t_3) - I_{L_M}(t_1) \tag{3.20}$$

Stability on C_M is obtained when the amount of energy flowing out of C_M during pre magnetization equals the energy flowing back into C_M during demagnetization ($E_{pm} = E_{dm}$). This is true when the magnetization current swing is symmetrical ($-I_{L_M}(t_1) = I_{L_M}(t_3) = \frac{1}{2}\Delta I_{L_M}$). Rewriting Equation 3.16 and substituting $\frac{1}{2}\Delta I_{L_M}$ results in Equation 3.21.

$$V_{C_M,stable} = \frac{L_M \Delta I_{L_M}}{2T_{pm}}, \quad -I_{L_M}(t_1) = I_{L_M}(t_3) = \frac{1}{2}\Delta I_{L_M} \tag{3.21}$$

Substituting Equation 3.20 underlaying equations in 3.21 and solving/extracting V_{C_M} results in an expression for $V_{C_M,stable}$ (Equation 3.22).

$$V_{C_M,stable} = -\frac{1}{C_s N^2} \left(T_{pm} \Delta I_{L_M} - \right.$$

$$\left. \sqrt{(C_s N \hat{V}_{C_s})^2 + (L_M C_s N^2 + T_{pm}{}^2)\Delta I_{L_M}{}^2} \right),$$

$$\Delta I_{L_M} = \frac{1}{L_M} \int_{t_1}^{t_2} V_{charging}(t)dt \tag{3.22}$$

The maximum core flux density (B) of the transformer can now be calculated by Equation 3.23. Φ is the core flux, A is the core cross-section, and N_{prim} the number of primary windings.

$$\hat{B} = \frac{\hat{\Phi}}{A}, \quad \hat{\Phi} = \frac{L_M \hat{I}_{L_M}}{N_{prim}} \tag{3.23}$$

Proper component values can now be selected using the state space model and analytical analysis of the reset circuit.

3.4 Circuit design considerations & simulations

3.4.1 Full charge operation

First, the supply voltage (V_{C0}), output voltage, load capacitance C_h and charging time T_{Sw2} have to be considered. The prototype charger has to be powered by three phase mains (400 V). After rectification, the supply voltage is estimated to be somewhere between 500 V and 540 V, depending on the load power.

The charging time T_{Sw2} is mainly determined by the oscillation frequency of $C_l - L_s - C_h$ and secondary by the value of L_2 since it only conducts current when the voltage over C_l is negative. The value of C_l should be smaller than C_h to create a certain degree of voltage reversal on C_l after a full charge cycle. This capacitor mismatch ratio is called α, $\alpha = C_h{}^*/C_l$. The α value will determine the controllability range of the output voltage but will also affect the charging time. The load capacitor C_h and α value determine subsequently the maximum allowable leakage inductance L_s of the transformer for the 50 μs charging time constraint.

Obtaining low leakage inductance in a high voltage transformer is often difficult because the winding arrangements have to comply with high voltage isolation requirements and high peak power capabilities. These factors can adversely affect compactness and coupling of the transformer. A sufficiently low L_s can be obtained by minimizing the number of primary and secondary windings which also reduces resistive losses in the windings. Reduction of the winding ratio can be achieved by applying a high primary voltage. A large core cross-section enables sufficient primary and secondary inductance, to limit the magnetization current, and to decrease flux density beneath the saturation level. These design parameters should be taken into account for an optimal design.

The winding ratio (N) of the transformer needs to be at least 30 to obtain 30 kV output voltage, depending on the chosen α value, considering 500 V supply voltage. In this case a custom made transformer which satisfies the requirements was selected for the first prototype. The specifications of the transformer are shown in Table 3.1. The winding ratio is 39, and the total leakage inductance of the transformer is 25 μH. A first estimation of the charging time can be made using Equation 3.1 if $C_l = C_h{}^*$ (no voltage reversal on C_l and no influence by L_2). The charging time would be 33.7 μs for the 8.4 nF load capacitor which is far below the charging time constraint.

The correct α value to meet a certain output voltage controllability range can be selected with simulations after the values for L_1 and L_2 have been chosen. The value of L_2 has to be larger than L_s to secure a zero-crossing of the current through Sw_2 after charging. A value of 29 μH is used in the prototype, a larger value increases the physical inductor size and extends the re-charging time of C_l.

D_2 will be conducting when Sw_1 is closed so the voltage on the anode of the diode will be zero minus the voltage drop over the device. The full supply voltage (V_{C0}) will therefore be initially over L_1 when Sw_1 is closed. L_1 has a value of 3.5 μH and limits the dI/dt through Sw_1 to 143 A/μs. This will limit the reverse recovery current in D_2

Table 3.1: Components values

Pulse transformer	
L_{prim}	5.3 mH
L_{sec}	8.1 H
L_s	25 μH
R_w	80 mΩ
C_s	26 pF
N	39
k	0.995

Charger circuit	
L_1	3.6 μH
L_2	29 μH
R_1	20 mΩ
R_2	70 mΩ
C_0	1800 μF
C_l	8.0 μF
C_M	20 μF
R_M	0.56 Ω

Load circuit	
C_h	8.4 nF
R_{Load}	<5 Ω

significantly. The dI/dt of the current can be calculated by Equation 3.24.

$$\frac{dI_{L_1}}{dt} = \frac{V_{C_3}}{L_1} \qquad (3.24)$$

The state space model can now be used to simulate the circuit behavior for different α values. All component values used as input for the model can be found in Table 3.1. The output plot of the model is shown in Figure 3.9. The control range of the output voltage (a function of Td_{Sw1}) for different mismatch ratios ($\alpha = C_h{}^*/C_l$) are shown in Figure 3.12. The associated voltages on C_l are shown in Figure 3.13. The data has been generated by setting the value for Td_{Sw1} and simulating the first cycle with $V_{Cl,\ initial} = 0$ and the following cycles with the V_{Cl} value of the previous cycle. Both figures show settled voltages, so the voltage on C_l is equal at the beginning and end of the cycle as shown in Figure 3.9. It takes typically 4–6 cycles for the voltage to settle.
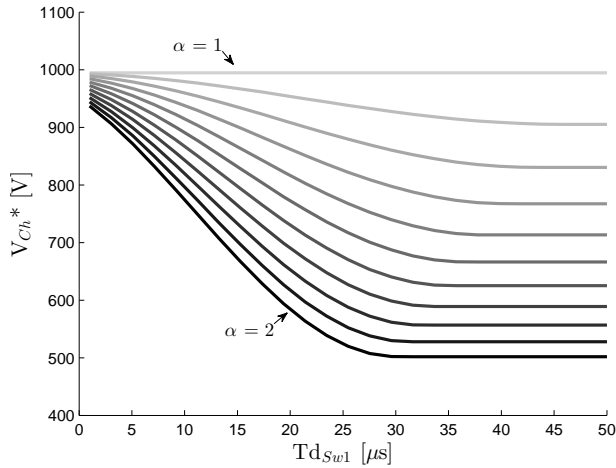
Figure 3.12: Simulated $V_{Ch, \, settled}$ as a function of Td_{Sw1} for multiple α values, step size: $\Delta\alpha = 0.1$ ($\alpha = Ch^*/Cl$)
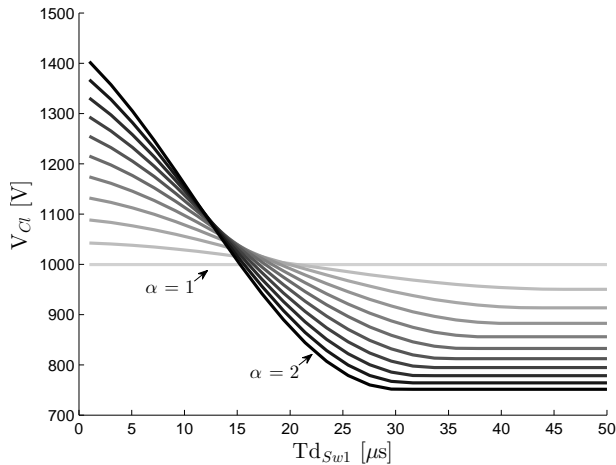
Figure 3.13: Simulated $V_{Cl, \, settled}$ as a function of Td_{Sw1} for multiple α values, step size: $\Delta\alpha = 0.1$ ($\alpha = Ch^*/Cl$)

A large α value results in high controllability of the output voltage but increases $\hat{V}_{Cl}$. A switch with higher blocking voltage is needed and the amount of reactive energy which flows through the circuit is increased. A value of $\alpha = 1.6$ provides ca. 300 V controllability which is more than sufficient for compensation of power supply voltage ripple and component value variations.

The cycle (including pre- and de-magnetization) has to be completed within 200 μs for 5 kHz operation. T_{pm} will be set to 50 μs which results in $T_{dm} = 50$ μs, 100
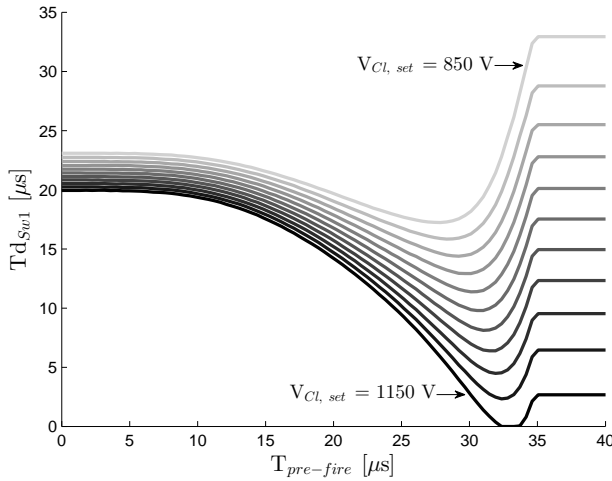
Figure 3.14: Simulated Td_{Sw1} as a function of $T_{pre-fire}$ for multiple set-values (step size: $\Delta V_{Cl,\ set} = 30V$) with $\alpha = 1.6$

µs will be left for charging C_h and discharging C_s in L_M. The magnetization current swing (ΔI_{L_M}) will be 2.6 A for a 30 kV full charge cycle. A relatively large value of 20 µF is chosen for C_M to minimize the ripple voltage. The resulting voltage level on V_{C_M} stabilizes ideally at 225 V (Equation 3.22).

The voltage over Sw_2 will be at least V_{C_l} plus V_{C_M}. A margin has to be taken into account for transient switch-off voltages.

3.4.2 Pre-fire operation

A pre-fire results in certain amount of voltage reversal on C_l. The correct switching delay (Td_{Sw1}) will result in recharging of C_l to the initial voltage level. The relation between the pre-fire time $(T_{pre-fire})$ and Td_{Sw1} is calculated for $\alpha = 1.6$ with the model. The data is generated by assigning a set-value to V_{Cl} and iteratively approximating the correct Td_{Sw1} for recharging to the same set-value with less than 1 V error. The relation between the pre-fire time $(T_{pre-fire})$ and Td_{Sw1} for multiple set-values are shown in Figure 3.14. Only a small amount of energy is transferred to C_h during an early pre-fire, the resulting Td_{Sw1} will be long and less dependent of the pre-fire time since only a small amount of energy has to be fed from C_0 to C_l at the end of the cycle. A full charge cycle is attained at t ≈ 35 µs. Td_{Sw1} saturates to 0 for a set-value of 1150 V between $T_{pre-fire} = 32–34$ µs so a lower set-value should be selected in practise. The relation between $T_{pre-fire}$ and Td_{Sw1} can be used for the control loop to stabilize pre-fire events, this will be further discussed in section 3.5.

The maximum peak current through Sw_2 will be during pre-fire operation when $T_{pre-fire} = 0$. In practise this will not occur unless a failure in the high voltage circuit
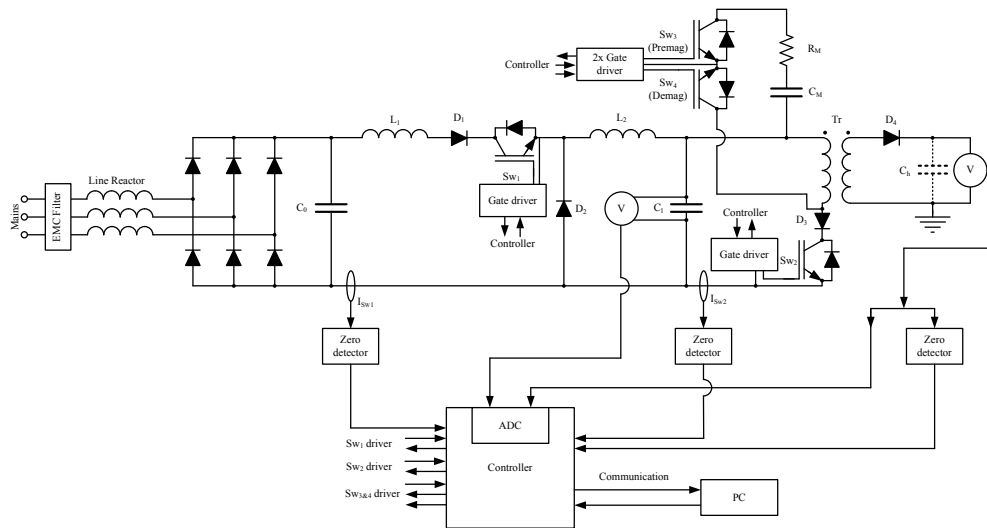
Figure 3.15: Practical implementation of the 5 kHz resonant capacitor charger.

leads to a short circuit. Up to 680 A peak current capability of Sw_2 is required if 1200 V on C_l is allowed during operation.

3.5 Implementation

3.5.1 Power electronics

The practical implementation of the circuit is illustrated in Figure 3.15. The component values of the circuit can be found in Table 3.1.

Buffer capacitor C_0 is charged via a three phase rectifier and a line reactor which improves the power quality.

The switches (Sw_1 and Sw_2) are 1700 V IGBTs (Insulated Gate Bipolar Transistor) modules with an oversized 1.2 kA peak current handling capability. Larger load capacitances can be handled optionally at reduced repetition rates. An additional series diode module enables reverse blocking. Sw_3 and Sw_4 are 1700 V IGBTs with 50 A current handling capability. The freewheeling diode of one IGBT is used to make the other one reverse blocking by connecting the devices anti-series. The IGBTs are driven by commercially available gate-drive units. Additional RC-snubbers which are omitted in the schematic are connected in parallel with the switches.

L_1 and L_2 are toroidal air core inductors which are wound from Litz wire. Inductances were calculated using the methods outlined in [38]. A toroidal coil is chosen instead of a helical coil because of the limited stray field.

All low voltage capacitors are PP film or foil (Poly Propylene) capacitors. The power supply buffer also consist of these capacitors because they have much higher

RMS ripple current handling capability than electrolytic capacitors. The high voltage capacitor C_h in the test circuit has a barium-titanate dielectric which has extreme high dV/dt capability which is required for nanosecond discharge circuits.

The high voltage diode (D_4) is a stacked 100 kV diode with 20 A peak current handling capability and 200 ns reverse recovery time.

The in-house made pulse transformer (see Figure 3.16b) has a double Metglas® 2605SA1 C-core. Each leg has 10 primary strip windings and a single layer secondary coil with 360 windings. An earth screen is placed between the primary and secondary winding to couple transient capacitive currents to ground rather than to the primary winding. Secondly, the discharge current will flow to ground in case of an insulation failure of the high voltage winding (a similar design is presented in [46]). The earth screen and secondary winding are sufficiently spaced for low electric field strengths and minimized stray capacitance. Field control rings are placed at the edges of the high voltage coils to decrease the field strength and prevent corona discharges. The windings of both legs are connected in series.

3.5.2 Control circuit

The circuit is controlled by a 16 bit Digital Signal Controller (DSC). The voltage on C_l can be sampled by a 10 bit ADC via a resistive divider and a 100 kHz bandwidth isolation amplifier. The voltage on C_h is sampled via a resistive/capacitive high voltage divider. The (pre-)fire time $(T_{pre-fire})$ is measured by a zero detector and input capture register in the DSC. The voltage on C_h will be sampled after the zero crossing of the current through Sw_2 if no pre-fire has occurred.

The zero-crossing of the current through Sw_2 needs also to be detected to switch off the IGBT and for the Td_{Sw1} reference point. The current is measured via a current sense transformer, the zero-crossing is subsequently detected by a comparator with hysteresis. The complete cycle will be finished after the zero crossing of the current through Sw_1, C_l will now be be recharged and the voltage level can be can be sampled for feedback control. The switch-off timing of both IGBT modules is not critical because they should conduct until the zero crossing and cannot conduct the reverse current due to the series diode.

A control system for the regulation of V_{Ch} would be fairly easy to implement without the pre-fire complication. The stochastic breakdown behavior of spark-gap switches and the non linear respons of the system makes implementation of a control system less straightforward. The first implementation of a test control scheme is shown in Figure 3.17. The system has a double control loop. The full charge voltage on C_h is controlled by adjusting the set-value for V_{Cl}. The voltage on C_l is subsequently controlled by adjusting Td_{Sw1}. The correct Td_{Sw1} needs to be selected when a pre-fire occurs. $T_{pre-fire}$ has a regular relation with Td_{Sw1} which can be utilized (see Figure 3.14). A Look Up Table (LUT) which is addressed by the pre-fire time $(T_{pre-fire})$ is implemented in the control system. The addressed Td_{Sw1} value is executed and the resulting voltage on C_l is sampled. The value in the addressed location in the LUT is subsequently updated with a new control value via a PI controller. The Td_{Sw1}

80 cm
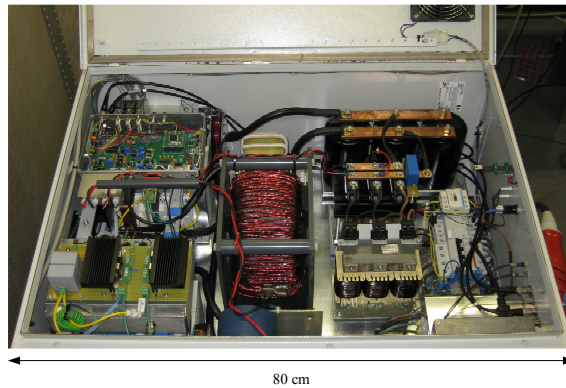
(a) Power electronics cabinet.
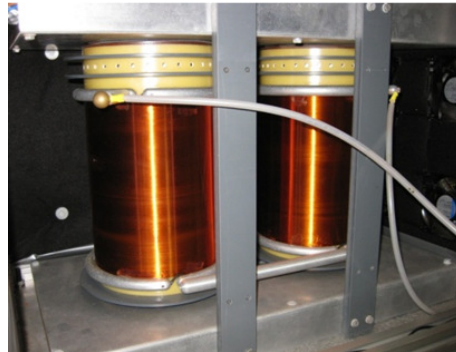
(b) High voltage pulse transformer.

Figure 3.16: The prototype capacitor charger which consists of a power electronics cabinet and an air insulated high voltage pulse transformer.

value becomes independent of the pre-fire time after a full charge cycle (see Figure 3.14, ($T_{pre-fire} > 35$ μs)). A default position in the LUT will than be addressed. The LUT values will converge to similar results as in Figure 3.14. The resolution of the LUT is 1 μs. The control loop is implemented with the state space model in Matlab for simulations. A random pre-fire voltage with Gaussian distribution is converted and applied to the input parameter $T_{pre-fire}$ to tune the control parameters for system stability. The control system still needs optimization but proof-of-concept of the system will be presented in section 3.6. Further research should include error, speed and stability analysis.
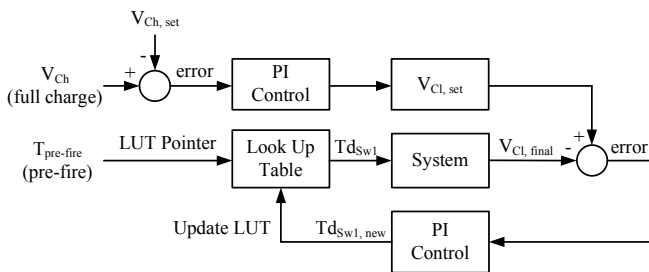
Figure 3.17: Control flow diagram for stabilization of the output voltage and stabilization of pre-fire events.

3.6 Experimental Results

3.6.1 Experimental setup

The circuit is tested by charging the capacitor of the pulsed power source for the wire-cylinder corona reactor. The pressure in the spark gap is varied to generate pre-fire events for testing purposes. The voltage in the high voltage part of the circuit is measured by a North Star PVM-2 80 MHz high voltage probe. The currents through the IGBTs are measured by Pearson 110 current monitors. The voltage on C_l and C_M is measured by a 25 MHz differential probe. The circuit is powered by a regulated 500 V DC power supply instead of three phase mains for these measurements. A well defined supply voltage enables proper comparison between modeled and measured values.

3.6.2 Full charge operation measurements

Typical voltages on C_l, C_h (scaled by winding ratio N) and current waveforms through Sw_1 and Sw_2 can be observed in Figure 3.18. The set-value of V_{Ch} is 30 kV. The pressure in the switch is set to 3 bar, and the repetition rate is 100 Hz. No pre-fire events occur with these settings, the spark gap is triggered at t = 200 μs. The voltage on C_l settles to 1051 V. The energy transfer efficiency from C_0 to C_h is 91 %. The peak output power is approximately 225 kW.

The relation between Td_{Sw1} and the charge levels on C_l, C_h are shown in Figure 3.19, including the peak currents through the switches. The figure is obtained by adjusting the set-value (V_{Ch}) and measuring Td_{Sw1} (as defined in Figure 3.9) under stable operation. The figure shows the measured and modeled controllability range which are in good agreement.

3.6.3 Pre-fire operation measurements

Typical voltages on C_l, C_h (scaled by winding ratio N) and current waveforms through Sw_1 and Sw_2 during pre-fire operation can be observed in Figure 3.20. The set-value
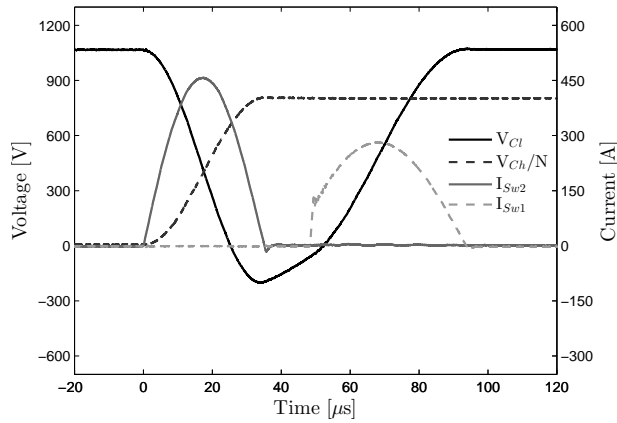
Figure 3.18: Typical measured voltage and current waveforms of a full charge cycle.
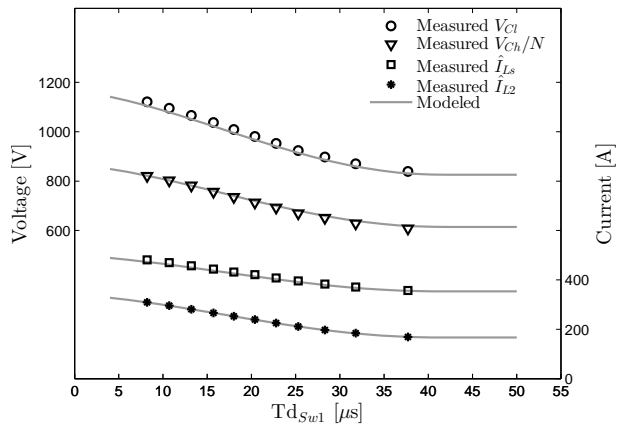
Figure 3.19: Modeled and measured settled peak voltages and currents in the circuit as a function of Td_{Sw1} during full charge operation.

of V_{Cl} is fixed at 1050 V during this measurement. The pressure in the spark gap is lowered to generate pre-fires.

The relation between $T_{pre-fire}$ and the correct Td_{Sw1} are shown in Figure 3.21. The figure is obtained by presenting the settled Td_{Sw1} values in the LUT. The figure shows the measured and modeled relation. The charging accuracy ranges of the measured V_{Cl} values is indicated in the legend. The pre-fire times are concentrated between 15 and 27 μs because C_h is charged to 88 % at $t = 27$ μs and the dV_{Ch}/dt lowers at the end of the charge cycle which increases the probability of a full charge cycle at $t = {>}35$ μs. The resolution of the LUT is also clearly visible by the collection of data points
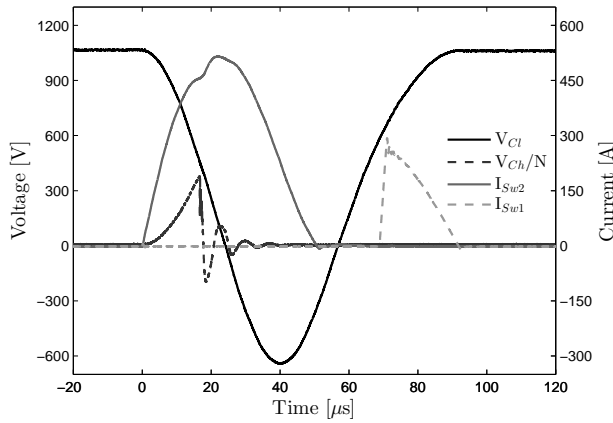
Figure 3.20: Typical voltage and current waveforms of a charge cycle with a pre-fire event.
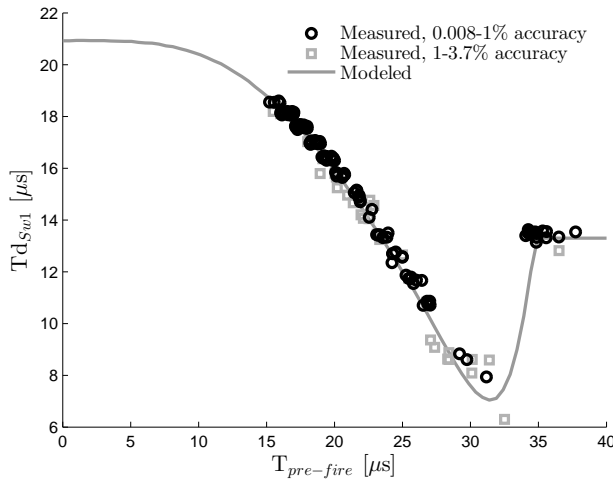
Figure 3.21: Modeled and measured Td_{Sw1} values as a function of the pre-fire time.

which are concentrated around discrete 1 μs $T_{pre-fire}$ intervals.

Figure 3.22 shows the output voltage and current of the charger at the full repetition rate and continuous pre-fire operation.

Figure 3.23 shows the measured and modeled charging efficiency as a function of the average pre-fire voltage. The input power is measured and calculated with the supply current and voltage of capacitor C_0. Losses of the three-phase rectifier and line-reactor are not included. The repetition rate of the charger is increased in steps
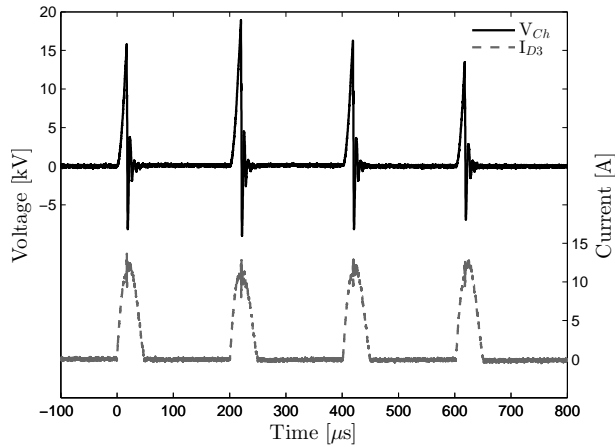
Figure 3.22: Measured output voltage and current during 5 kHz continuous pre-fire operation.
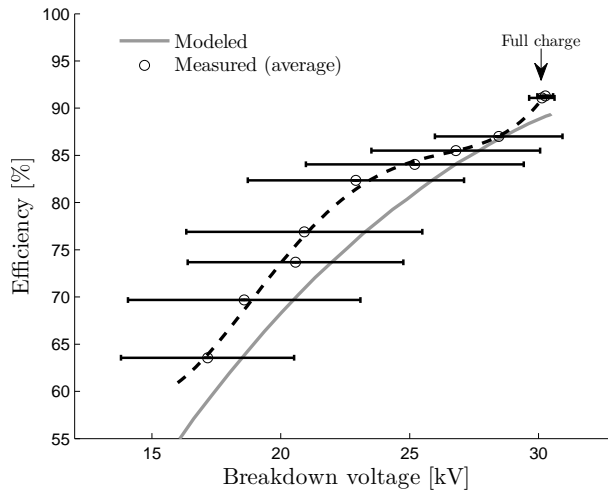
Figure 3.23: Measured charging efficiency as a function of average pre-fire breakdown voltage (the error bar represents the standard deviation of the breakdown voltage jitter).

up to 5 kHz to allow less recovery time for the spark gap, resulting in a decreasing breakdown voltage. The output energy is averaged over 100–300 charge cycles. The error bar represents the standard deviation of the breakdown voltage jitter. The state space model is applied to calculate losses per cycle and resulting efficiency as a function of the breakdown voltage.
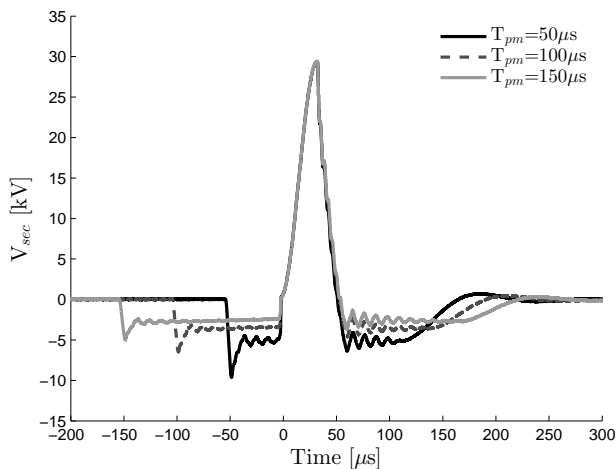
Figure 3.24: Voltage on the secondary winding of the transformer for multiple pre-magnetization times.

The efficiency decreases with lower breakdown voltages because the currents and resistive losses in the circuit increase and the energy transfer per cycle decreases. Up to 75 % of the energy circulates in the circuit if the breakdown voltage is 15 kV instead of 30 kV. The V_{C_l} set value and mismatch ratio α needs to be selected for optimal efficiency if the charger is used with continues pre-fire operation. The deviating measured values compared to the modeled values can be explained by the averaging procedure which is used for the jittering measured values.

3.6.4 Magnetization behavior

The voltage over the secondary winding of the transformer during full charge stable operation for multiple T_{pm} values can be observed in Figure 3.24. The negative voltage over the winding during pre-magnetization becomes less for larger T_{pm} values as expected. Notable is the non-sinusoidal waveform as a result of the oscillation between $L_M - C_s$ at $t = 35$–60 μs. There are several reasons. First the reverse recovery of D_3 and D_4. This will explain the sudden voltage drop after the peak of V_{sec}. Secondly, the non-linear behavior of the transformer core. The μ_r is dependent on the operating point in the B-H curve of the core material, resulting in a varying inductance. The varying inductance can be observed in Figure 3.24 between $t = 35$–60 μs, the oscillating periods ($L_M - C_s$) for the three T_{pm} values are not identical.

Figure 3.25 shows the flux swing of a single cycle which is calculated by Equation 3.25. The flux swing is increasingly non-symmetrical for shorter T_{pm} values due to increased losses in the magnetization circuit.
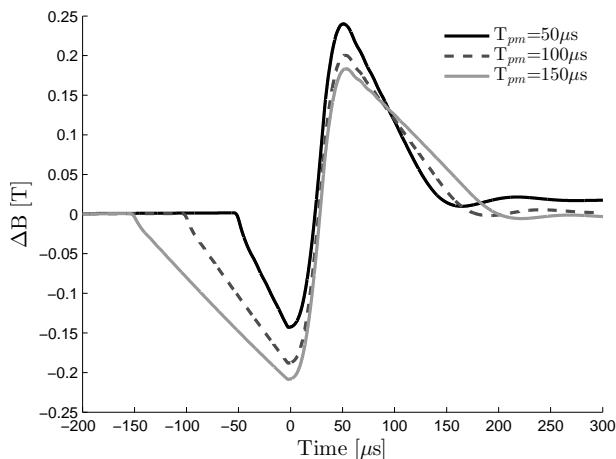
Figure 3.25: Magnetic flux density swing for for multiple pre-magnetization times.

$$\triangle B(t) = \frac{1}{N_{sec}A} \int_0^t V_{sec}(\tau)d\tau \tag{3.25}$$

T_{pm} is varied between 25 μs and 300 μs to measure the stable voltage level on V_{C_M}. The values are compared with the analytical approximation (Equation 3.22) in Figure 3.26. The approximation is only valid under condition that $-\hat{I}_{L_M} = \hat{I}_{L_M}$ or $-\hat{B} = \hat{B}$, this is only true for $T_{pm} >$125 μs. The approximation is in good accordance in this interval. Deviations can be explained by the varying inductance value of L_M, conduction losses and losses due to charging of stray capacitance C_s at the beginning of the pre-magnetization step. Also, energy can be transferred from C_h to C_M when the voltage on C_h excessively reverses ($V_{Ch}/N > V_{C_M}$) after firing of the spark gap (see Figure 3.20). This contribution will be very limited due to the fast oscillation and discharge of C_h.

Figure 3.27 shows the jitter of the voltage on C_M as result of the jitter on the breakdown voltage. The pre-magnetization time T_{pm} is set to 50 μs. The mean voltage on V_{C_M} becomes less when the average pre-fire voltage (and ΔI_{L_M}) decreases (see Equation 3.20). The energy in C_s is lost for the magnetization circuit when a pre-fire occurs because C_s is rapidly discharged. The modeled values are therefore calculated by Equation 3.22 with $\hat{V}_{Cs} = 0$. The averaging procedure and probably non-symmetrical ΔI_{L_M} causes the deviation with the measured values.
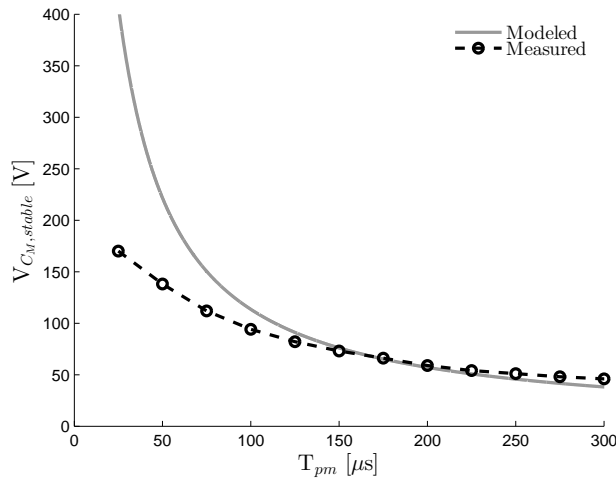
Figure 3.26: Calculated and measured settled voltage levels on C_M as function of the pre-magnetization time (full-charge operation).
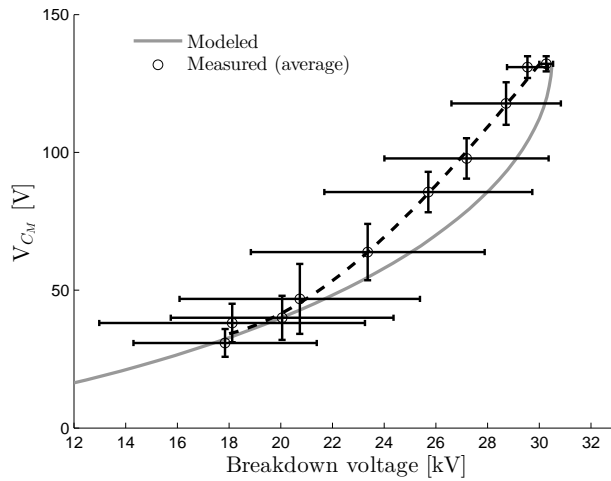
Figure 3.27: Measured and modeled voltage on C_M with $T_{pm} = 50\mu s$ as a function of average pre-fire breakdown voltage (the error bars represent the standard deviations of the voltage jitter).

3.7   Conclusions

A novel circuit topology of a fast capacitor charger for pulsed power applications is presented in this chapter. The charger is especially suitable for spark gap based power modulators, because of the repetitive near short circuit handling capability of the

output.

A 15 kW prototype has been built and the first results of measurements are presented. The charger is capable of charging a 8.4 nF capacitor to 30 kV in 35 μs with a maximum repetition rate of 5 kHz and a peak output power of more than 225 kW. The efficiency is up to 91 %.

An active reset circuit for resetting of the pulse transformer core has been implemented. This circuit is also capable of recovering a large part of the energy which is stored in the stray capacitance of the secondary transformer winding. The repetition rate of the charger is currently limited by the oscillation between stray capacitance and inductance of the secondary winding during the demagnetization process. A pulse transformer with a lower secondary stray capacitance (e.g. multi layer winding) would be desired.

A numeric simulation tool based on state space modeling is implemented to simulate the circuit behavior. Measurements and simulations are in good accordance.

A first implementation of a control loop is implemented to handle pre-fire events and to regulate the output voltage. The control system requires additional optimization, further research should include error, speed and stability analysis.

4

Spark gap characterization

Abstract

Spark gap closing switches feature superior switching characteristics in switching speed, current handling and voltage hold-off capability. Unfortunately these switches suffer from electrode erosion and the switching medium has to recover after each pulse, limiting the life-time and repetition rate of the switch. The recovery can be improved by purging the gap to remove heated and ionized gas and to cool the electrodes. The performance of the nitrogen purged spark gap system of the pulsed corona demonstrator is described in this chapter. The experimental switching performance, recovery and erosion results for multiple electrode materials are presented. An analytical and a numerical thermal erosion model is proposed to estimate electrode evaporation rates. Impedance, rise time and trigger-delay of the spark gap was measured for multiple gap distances, operating pressures and gasses (air, N_2 and N_2/H_2 95/5 mixture) to consider optimized operating points. Recovery of the N_2 switching medium in the spark gap is investigated as a function of the pulse repetition rate and purge flow, up to 800 Hz during continuous operation and up to 5 kHz in burst. Electrode erosion during continuous operation was determined for six materials after $65 \cdot 10^6$ shots. Erosion rates of the anodes were between 4 and 19.6 nL/C. By increasing quality of performance, the materials rank as follows: copper > brass > copper/tungsten > stainless steel > tungsten > aluminium. The copper cathode didn't show any erosion and gained some weight. Copper can apparently be transported from the anode and partially deposited on the cathode in a nitrogen environment. Detailed SEM images are provided of all tested electrode materials. The developed analytical and a numerical models are both based on the heat equation. The 1D analytical model assumes a static spark radius, and estimates evaporation at a boiling surface. The 2D (rz-plane) FDM (Finite Difference Method) numerical thermal model features a more realistic spark radius which expands according to the trajectory of a shockwave. Time and space resolved heating of the electrode can be simulated, including evaporation and melting. The power input of the models is the product of the measured discharge current and estimated V_{eff} (effective fall voltage) near the electrode. Comparison between modeled and experimental data give insight in the erosion behavior of the tested materials.

4.1 Introduction

Pulsed power modulators generally are equipped with high power closing switches which are used to discharge high voltage capacitors into a load. The switch should be capable of handling high voltages, high currents and should have very fast switching characteristics (typically tens of kilo Volts and tens of kilo Amperes with nanosecond closing times and micro- or nanosecond discharge times) [36]. The resulting high peak powers can be used to energize e.g. pulsed lasers, radar, ultra-strong magnetic fields, particle accelerators, fusion research and electromagnetic pulses [47–49]. A pressurized spark gap switch [50] is used in our application because of the superior switching speed (typically nano- or picosecond rise time) and low on-state impedance (typically several hundred mΩ). The erosion and recovery behavior requires specific attention when this type of switches is applied for applications where continuous robust operation is required. During switching a spark channel (thermal plasma) is created between the electrodes which heats up the gas, ionizes the switching medium and vaporizes electrode material. The switch needs to be purged to enhance the recovery and repetition rate. The electrode erosion should be minimized for long life operation.

The experimental recovery and erosion results of the spark gap switch which is described in Section 2.2.2 is presented in this chapter. Experimental recovery results for 800 Hz continuous operation and 5 kHz burst operation are shown in Section 4.2. The results include switching characteristics (e.g. rise time and spark resistance) and required gap flow as function of the repetition rate and the effect of the electrode diameter. Experimental and modeled electrode erosion results can be observed in 4.3. The section includes two developed erosion models, Scanning Electron Microscopy (SEM) images of the surfaces of the tested electrodes and comparison of modeled and measured data.

4.2 Spark gap recovery

4.2.1 Recovery mechanisms

The gap will not be able to hold off the full switching voltage for a certain time (recovery time) after switching. The recovery process can be divided into three phases [51].

The first phase is the deionization of the spark channel. This occurs primarily by recombination, de-excitation and attachment [52]. The ionization level in the spark is assumed to be reduced to background level after after tens of microseconds after the spark has quenched.

The second phase is the restoration of the gas density. The gas in the spark channel is heated to several thousand Kelvin [52] during conduction which results in a dramatic drop of the local gas density. The breakdown voltage is dependent on the E/N value, where E is the electric field (V/m) and N the concentration of neutral particles (gas density). Reducing the gas density also reduces the breakdown voltage. The breakdown voltage will be significantly lower if the voltage over the electrodes is reapplied too quickly. The gas needs to cool to ambient temperature which takes up to 10 milliseconds

dependent on the operating pressure and gas composition. The repetition rate is limited to a few hundred Hz with air or nitrogen as switching medium. Hydrogen has a much higher molecular speed and thermal diffusivity which increases the repetition rate to about 1 kHz [53]. Electrode heating during continuous operation can also limit heat transfer from the heated gas to the electrodes which affects the recovery time indirectly.

The third phase is the ability of the switch to be over-volted to a value higher than the DC breakdown voltage of the switch. Pulse charging of the gap is often applied to improve switching characteristics like jitter and rise time. This final recovery stage can take up to several hundred ms [54] and is attributed to residual ions in the gap. The breakdown voltage of the gap is affected significantly even with small amounts of residual ions [53].

The primary focus in our application is improved electrode lifetime and continuous high repetition rate operation. Recovery can be improved by purging the gap to restore density, cool the electrodes, and remove debris between switching cycles [55, 56]. The purging rate should increase proportionally to the gap volume (product of the active electrode surface and gap distance) [57] to refresh the heated gas between switching cycles. The breakdown voltage in the gap is dependent on the operating pressure and gap distance (pd_{gap}) making the purging rate theoretically proportional to the STP (Standard Temperature and Pressure) gap volume.

The pulse repetition rate of an air purged switch can be increased to 1 kHz [30]. The voltage over the switch should be present as short as possible during high repetition rate operation to allow a large recovery time. This can be achieved by charging the capacitor only just before the spark gap switches with a high power (pulse) capacitor charger [58]. Purging the spark gap with compressed air into atmospheric space is effective but costly, and produces a waste flow containing NO_x, ozone and electrode dust particles [59]. Up to 100 Nm^3/h air is required to increase the repetition rate of a 10 J per pulse system to 1 kHz [30]. The compressed air needs to be oil free and dried to prevent contamination and assure breakdown stability. Typical power requirement of a 100 Nm^3/h purging system will be at least 5–10 kW depending on the operating pressure of the switch and overal pressure drop in the system. Birx [60] reports 11 kW purging power requirement in their 1 kHz repetition rate application.

Purging the gap in a pressurized closed loop is more energy efficient, improves stability of the spark gap due reduction of impurities (e.g. moisture) and allows the use of gasses other than air. Hydrogen would be preferred because of its fast intrinsic recovery. However, fire and explosion hazards when accidently mixed with air makes it less suitable. Pressurization of the gas increases the density and heat transfer which results in faster intrinsic recovery [61]. Also the switching characteristics (jitter and rise time) and heat transfer from gas to electrodes can be improved by decreasing the gap distance. The surface roughness of the electrodes dominate the breakdown voltage of the gap for very small gap distances at high pressures. Also electrode erosion is increased for smaller gaps and complexity increases due to the high operating pressure. Trade-offs that have to be considered when designing a spark gap switch. Nitrogen has a proper breakdown strength (comparable to air) which enables design of a fast compact pulsed power spark gap at pressures up to several bars. It is also reasonably

inert which reduces electrode oxidation. Nitrogen is therefore the preferred gas for the closed loop system in our application. Addition of a safe concentration level of hydrogen (5 %) to the nitrogen is also considered to enhance the recovery time.

Recovery can also be enhanced by using an additional trigger electrode and circuit which is also used in the demonstrator. The spark gap can be triggered below the DC breakdown voltage which makes full recovery of the switching medium unnecessary. The spark gap can then be operated at a higher temperature (and lower density) of the switching medium.

4.2.2   Experimental approach

Recovery and erosion experiments were carried out with the demonstrator which was described in Chapter 2. An additional setup is used to estimate switching losses and switching speed of the spark gap. Finally, the 5 kHz capacitor charger was installed in the demonstrator setup to study recovery behavior for repetition rates exceeding 1 kHz.

4.2.2.1   Switching characteristics setup

Determining switching losses in a spark gap can be quite challenging. Measurement of the switching current is relative easy compared to the differential voltage measurement (which would be needed to determine the voltage over the resistive gap). The resistance of the spark is typically several hundred mΩ resulting in an estimated voltage drop over the gap of less than 1 kV. The induction voltage in the spark gap structure is (in most cases) larger than the resistive voltage. The inductance cannot be neglected because we have a high dI/dt of the switching current and small spark diameter [62]. Calculation of the gap voltage would be possible by applying a model with estimated parameters. A different approach is chosen in order to keep the measurements accurate and simple. The switching characteristics of the spark gap are investigated by placing the spark gap in a RLC circuit. The experimental setup is shown in figure 4.1.

Capacitor C_h (= 8 nF) is charged in approximately 35 μs to 30 kV by the 5 kHz resonant capacitor charger. The charging current and voltage are measured by a Pearson 6600 current monitor and North Star PVM-2 high voltage probe and the stored energy in C_h is subsequently calculated. The spark gap is subsequently triggered by the solid state trigger unit. The trigger voltage is negative to limit the isolation voltage requirement of the trigger transformer to 30 kV instead of 45–60 kV. The coaxial load consists of a disc-type low inductance resistor of 1.13 Ω. The spark gap switching characteristics are monitored using a voltage and current sensor which are incorporated in the spark gap housing (see sections 2.2.6 and 2.2.2). The capacitor input energy and load energy can subsequently be calculated for each shot. The switching losses can be estimated by considering the difference in energy. A low load resistance value and resulting high discharge current proved to be needed to observe significant distinction in results between spark gap settings. The impedance of the spark gap needs to be reasonably significant compared to the 1.13 Ω load. The spark gap is too efficient
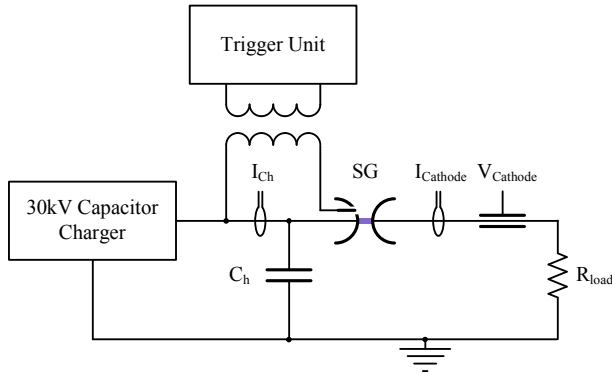
Figure 4.1: Schematic experimental setup to evaluate the SG performance.
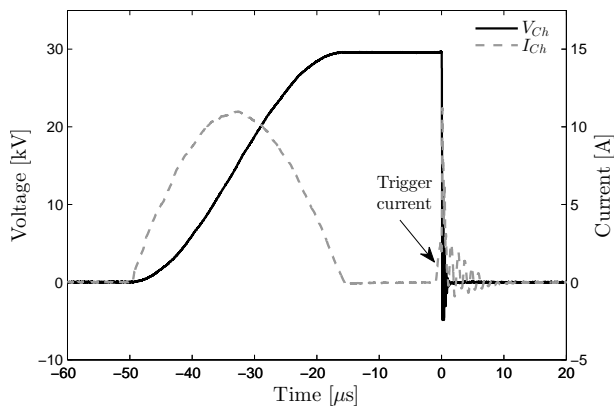
Figure 4.2: Typical charging voltage and current waveforms of capacitor C_h. The spark gap is triggered at t=0, the current delivered by the trigger circuit can be observed just before the spark gap fires. C_h discharges rapidly in the load after triggering.

at a higher impedance load which would not reveal difference in switching efficiency. The trigger unit is applied to fire the spark gap shortly and accurately after charging which enables capturing of charging and discharging waveforms simultaneously on one oscilloscope with a sample rate of 2 Gs/s. A typical charging cycle is shown in Figure 4.2. The spark gap is triggered at $t = 0$. The trigger current which charges the stray capacitance of the electrode and connection rod can be observed just before the spark gap fires. The anode current and voltage are shown in Figure 4.3. The 200 ns long noisy voltage waveform before the actual closing of the gap at $t = 0$ is caused by the discharge activity in the trigger gap. It takes a certain time before the main gap fires after the trigger gap has been fired. This trigger delay time will also be considered
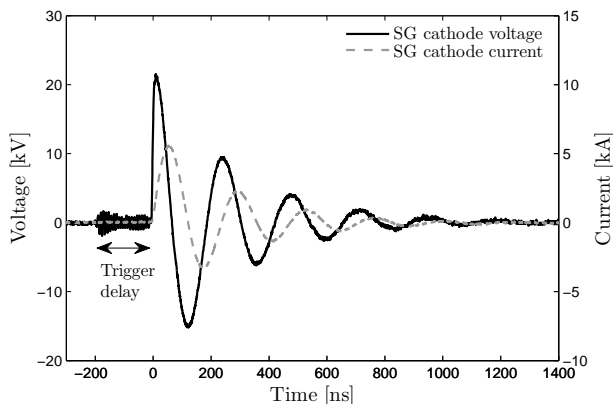
Figure 4.3: Typical spark gap cathode (R_{load}) voltage and current waveforms. The noisy cathode voltage waveform before t=0 is caused by the discharge in the trigger gap.

because it provides insight in the trigger behavior of the spark gap. A long trigger time suggests an arduously triggering, and an increased probability of not firing at al. The low value of the needed load resistor results in an underdamped oscillation of the voltage and current. The peak voltage at the anode is only 20 kV due the large dI/dt of the current and inductance in the spark gap.

A pseudo spark resistance is introduced by considering the energy balance of the setup. The real impedance of the spark alters during the discharge period, so the static pseudo resistance can only be used to compare results and to obtain some sense of the spark resistance. It is assumed that all losses in the circuit are in the spark, so the energy stored in the capacitor (E_{in}) minus the energy delivered to the load (E_{out}) is equal to the energy dissipated in the spark (E_{spark}). The spark resistance is assumed to be static so the total dissipated energy per pulse is equal to: $R_{spark} \int I_{cathode}(t)^2 dt$. The current is measured accurately so the pseudo spark resistance can be derived, see Equation 4.1 and 4.2.

$$E_{spark} = E_{in} - E_{out} = R_{spark} \int I_{cathode}(t)^2 dt \tag{4.1}$$

$$R_{spark} = \frac{\int V_{C_h}(t) I_{C_h}(t) dt - \int V_{cathode}(t) I_{cathode}(t) dt}{\int I_{cathode}(t)^2 dt} \tag{4.2}$$

The obtained resistance value can be validated by applying RLC circuit analysis [63]. The current in an RLC circuit can be described by Equations 4.3, 4.4 and 4.5. Where L is the (parasitic) inductance in the circuit. L is unknown and can be fitted with actual measurements to obtain the correct oscillation frequency. Figure 4.4 is obtained by substitution of the calculated 0.13 Ω value from Equation 4.2 in Equation 4.3. L is fitted and has a value of 175 nH. Although the actual resistance is time dependent, the calculated and actual waveform are
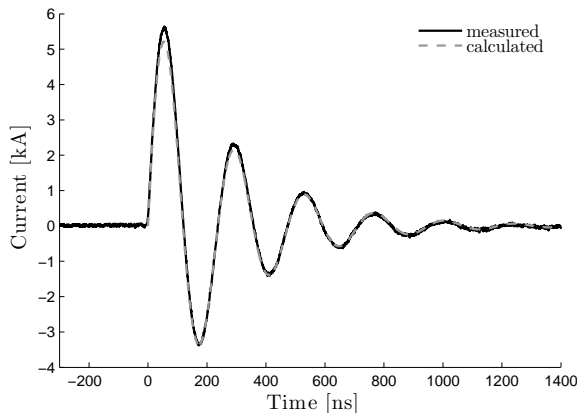
Figure 4.4: Measured and calculated spark gap cathode current as a function of time. The pressure of the N_2 in the spark gap is 2 bar.

very similar. The actual peak current is slightly higher because the resistance of the spark is reversely proportional to some function of the current [64].

$$I(t) = \frac{V_{Ch}(0)}{\omega_d L} e^{-\alpha t} sin(\omega_d t) \tag{4.3}$$

$$\alpha = \frac{R_{load} + R_{spark}}{2L} \tag{4.4}$$

$$\omega_d = \sqrt{\frac{1}{LC_h} - \left(\frac{R_{load} + R_{spark}}{2L}\right)^2} \tag{4.5}$$

4.2.2.2 Continuous 800 Hz operation recovery

The demonstrator setup with the 1 kHz capacitor charger, RLC trigger and 20 kV DC-bias is used during these experiments. The pressure in the spark gap is 3.4 bar, results will later show that this is a well-considered choice. Several electrode materials are tested using the following procedure. The spark gap housing is only vented for mounting of a new set of electrodes at a start of a series. The spark gap housing is subsequently purged to expel any air out of the system. At least 10^6 shots are executed to erode the surfaces of the electrodes evenly. Preferential discharge areas introduced by slight misalignments of the electrodes will now be eliminated. Recovery of the gap is investigated up to 800 Hz. Although the capacitor charger is capable of operating at 1 kHz, thermal limitations in some system components prevent continuous operation above 800 Hz. The switching current is shown in Figure 2.31 and 2.34 (Chapter 2).

The recovery experiment is started by setting the power of the rootsblower to 5 % of the maximum power. The corresponding absolute flow will be 0.5–1.5 m^3/h (at 3.4 bar). Although the spark gap is able to recover fully at low repetition rates (1-200 Hz), some flow is needed to cool the electrodes and provide transportation of particles originating from the

discharges during continuous operation. The spark gap is now able to recover at a repetition rate of 250 Hz and will be used as a start value for the recovery experiment. The repetition rate is subsequently automatically increased with 25 or 50 Hz every 10 or 20 minutes (50 Hz per 20 min.). An increasing repetition rate will inevitably result in a growing amount of pre-fires which are detected by the control circuit. The power of the rootsblower is increased automatically with 1 % when the average number of pre-fires exceeds 5 % of the total number of fires. This ensures a stable operation of the spark gap over the repetition rate sweep up to 800 Hz. The 20 minutes between repetition rate steps are needed to obtain thermal equilibriums of the gas flow and electrode temperatures. The flow though the spark gap will be settled to a stable value during the 20 minute interval. The settled flow value is subsequently captured together with the corresponding repetition rate. The following materials are tested: stainless steel (ss 316 grade), brass (CuZn 60/40), aluminium (Al), copper (Cu) and copper tungsten alloy (WCu 75/25) [65].

4.2.2.3 5 kHz burst recovery

The demonstrator setup with the 5 kHz capacitor charger, RLC trigger and 0 kV DC-bias is used during these experiments. The DC-bias circuit was not designed to recharge C_{dc} with these high repetition rates. The absence of the DC-bias voltage decreases the energy transfer efficiency between between the power source and the reactor which result in increased dissipation in the spark gap.

Recovery of the switch is tested using the rootsblower to purge the spark gap with flows up to 10 m^3/h. We are primarily interested in the effect of the flow on the recovery behavior of the spark gap so only the 3.2 mm gap distance is considered at an operating pressure of 3 bar. The gap volume and flow determine the refreshing rate of the gap. Multiple flows and gap volumes are applied to investigate the recovery behavior of N_2 with and without addition of 5 % H_2. The volume of the gap is varied by using three electrode diameters (d_o): 29.5, 34.5 and 40 mm. The recovery voltage of the spark gap is measured with repetition rates up to 5 kHz by applying bursts of 100 charge cycles to the spark gap (example Figure 4.5).

The voltage on C_h is measured using a long record length on the oscilloscope to capture the complete burst. Individual charge cycles are extracted and the peak voltages which are equal to the breakdown or to the recovery voltage are subsequently averaged. The spark gap will always operate in the triggered mode during the first charge cycle of the burst. Depending on the flow, gap volume and repetition rate, the spark gap is able to recover fully before the next charge cycle and remains to operate in the triggered mode. Otherwise, the spark gap will operate in the pre-fire mode for the remaining cycles of the burst. The breakdown voltage of the first cycle of the burst will be discarded for the average recovery voltage calculation because it is not representative for the recovery voltage during pre-fire operation.

4.2.3 Experimental results

4.2.3.1 Trigger delay, rise time and spark resistance

Figures 4.8a-c shows the spark resistance measurements as a function of operating pressure for three gap distances (d_g) and three gasses: air, pure N_2 and N_2/H_2 mix (95/5). The closed-loop system is not used in this setup so it was possible to use air for comparison with the other gasses. First the spark gap is purged, then pressurized and sealed for each experiment. The gas was periodically refreshed. Measurements were performed at a repetition rate of 5
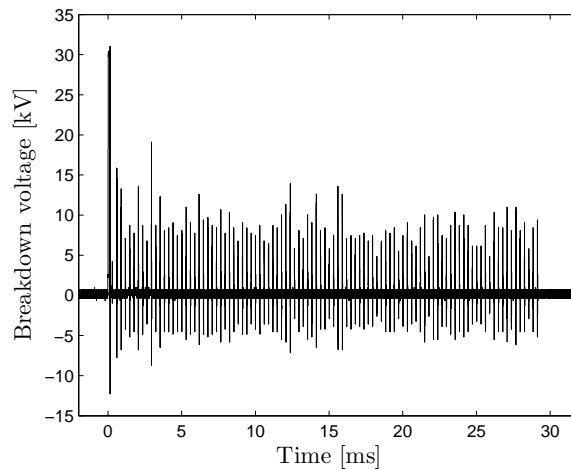
Figure 4.5: Typical break down voltage waveform of a 100 charge cycles burst. The gap is able to hold off 30 kV charging voltage and operates in the triggered mode during the first charge cycle. The spark gap pre-fires during the following cycles.

pulses per second. Up to 20 cycles were captured and processed individually. The results are averaged, the error bars represent the standard deviation. Voltage rise time measurements are shown in figures 4.7a-c and the trigger delay times are shown in figures 4.6a-c. The pressure in the spark gap was varied during these measurements and data points were collected if the gap was able to hold the 30 kV charging voltage and if the trigger unit was able to fire the gap. This pressure window will be referred to as the operating range. The following observations are made from these measurements.

Trigger delay:

- The operating pressure range of air is much more limited compared to the other gasses. At a fixed voltage and gap setting only a Δ 500 mbar window was usable for air, the N_2 and N_2/H_2 can have a window up to Δ 2.75 bar. The reason for this limited operating range is the presence of oxygen which is an electronegative gas. The oxygen molecules are tended to attract electrons which impedes the avalanche which is needed to initiate the spark.

- Trigger delays are similar for al gasses if the gap is able to fire. The delay is always present and increases with higher operating pressures. The jitter on the trigger delay is low and only increases in the upper region of the operating range. The delay can be up to 2500 ns with N_2 or N_2/H_2.

Rise time:

- The air gap is fast switching under al conditions. The voltage rise time in N_2 and N_2/H_2 primarily dependents on the operating pressure and gap distance. The rise

93

time decreases always with increasing pressure because the discharge transit time is dominated by the electron avalanche time which decreases with a higher initial gas density. A decreasing rise time can also be observed for smaller gap distances due to the increased E-field in the gap which also decreases the avalanche time. [66] [67].

- The addition of 5 % H_2 seems to improve the switching speed for the 2.2 and 3.2 mm gap distance in the lower region of the operating range. This is possibly related to the very low molecular weight of hydrogen which allows fast channel expansion resulting in faster rise times [68]. Apparently even with low concentration levels hydrogen.

- The rise time saturates at a minimum value for all gasses in the upper region of the operating range. The minimum rise times for gap distances 2.2, 3.2 and 4.2 mm are respectively 3 ns, 3.7 ns and 5 ns. Inductance of the spark is related to the gap distance (or length of the spark) [69] [62] which limits the rise time of the switch.

Spark gap resistance:

- The spark gap resistance is typically between 0.1 and 0.25 Ω for all gases and electrode distances. A smaller gap (or shorter spark) results in a lower resistance value.

- The expansion of the plasma channel is more limited at higher pressures which results in a higher spark resistance for the 2.2 and 3.2 mm gap distance in the upper region of the operating range.

- The lowest resistance is obtained with N_2/H_2 followed by N_2 and air. The resistance decreases for decreasing average molecular weight of the gas mixture [68]. The fast channel expansion of hydrogen also reduces the on state conduction losses.

A more optimized operating point for the closed-loop purging system can be chosen by considering these results. Air cannot be used because of accumulation of ozone and NO_x in the system. The effect of low percentages hydrogen is not yet known, the gas composition in the system could change due to continuous recycling. N_2/H_2 mix was considered for burst recovery experiments to investigate added value. For long term erosion experiments only pure nitrogen was considered.

A high operating pressure decreases the voltage rise time and decreases the spark resistance. An optimal pressure from a switching efficiency point of view would be 3-3.5 bar for the 3.2 mm N_2 gap (see figures 4.7b and 4.8b). The rise time reaches almost the minimum plateau (caused by the spark inductance), while the spark resistance increases from 3.5 bar onwards. Also the trigger delay is relative low with minimal jitter which enables stable triggering of the gap. An even better switching performance is obtained with the 2.2 mm gap at an operating pressure of 5 bar. Increased erosion is expected with smaller gap distances [70, 71], also more energy is required to purge the gap at higher operating pressures. The 3.2 mm gap at 3-3.5 bar is eventually chosen for recovery and erosion experiments with the demonstrator (TLT load). The switching performance is good enough because the current pulse rise time is limited to 20 ns by another effect: the parasitic inductance in the TLT and the connections. This operating setting proved to be a very stable for the system which is essential for endurance testing of electrode materials.
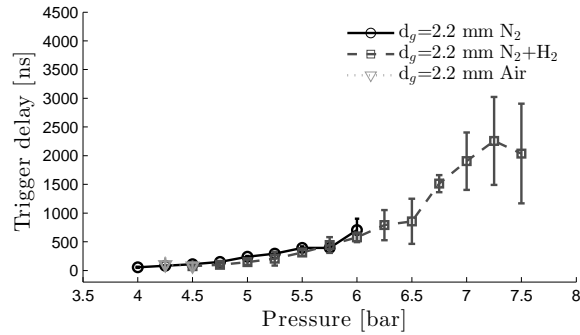
(a) 2.2 mm gap distance.
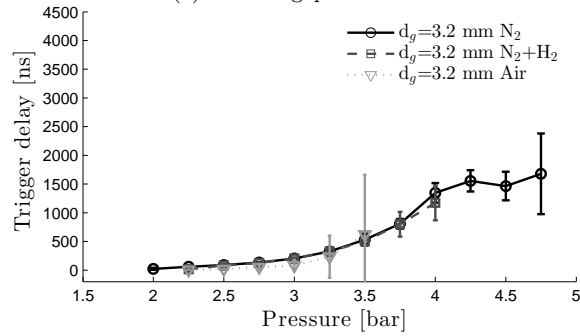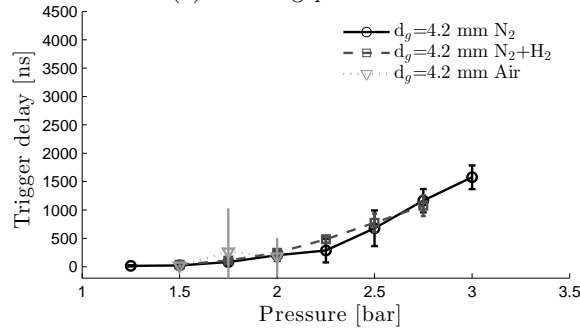
(b) 3.2 mm gap distance.

(c) 4.2 mm gap distance.

Figure 4.6: Spark gap trigger delay time as a function of pressure for multiple gasses and gap distances

4.2.3.2 Continuous 800 Hz operation recovery

The results are shown in Figure 4.9 for the following five electrode materials: stainless steel (SS 316 grade), brass (CuZn 60/40), aluminium (Al), copper (Cu) and copper tungsten alloy (WCu 75/25) [65]. Two diameters of the copper electrodes are tested (40 mm and 34.5 mm), see Figure 2.9.

(a) 2.2 mm gap distance.

(b) 3.2 mm gap distance.
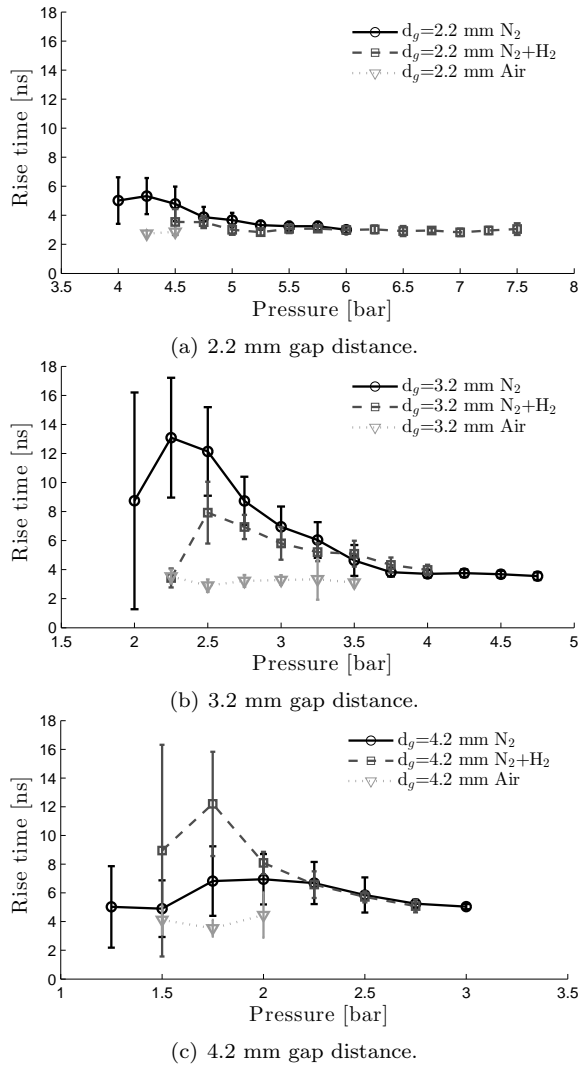
(c) 4.2 mm gap distance.

Figure 4.7: Spark gap voltage rise time as a function of pressure for multiple gasses and gap distances

Recovery experiments with tungsten (W) electrodes proved to be difficult. Often flakes of poorly sintered material crumbled off the surface of the electrode causing local electric field enhancement. Recovery fails subsequently completely because the sparks will tend to strike the same spot on the electrode surface.

The materials containing copper show similar flow requirements. A slightly higher flow is needed for the recovery of the gap with aluminium electrodes compared to the copper alloys.
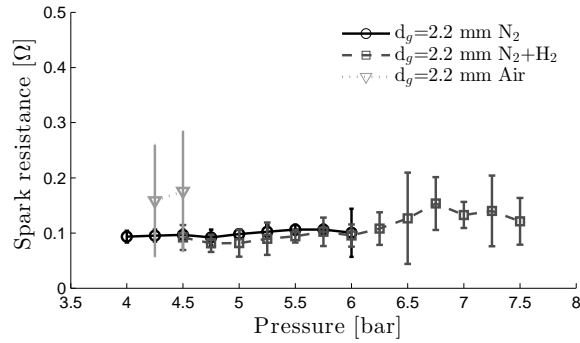
(a) 2.2 mm gap distance.
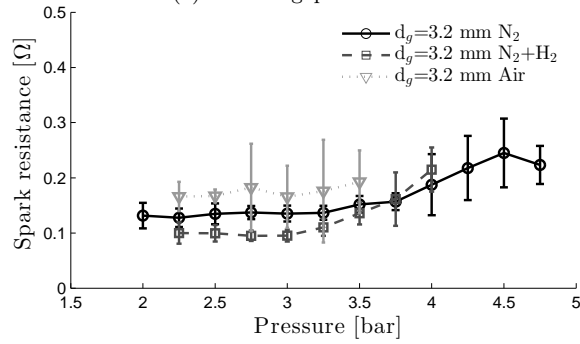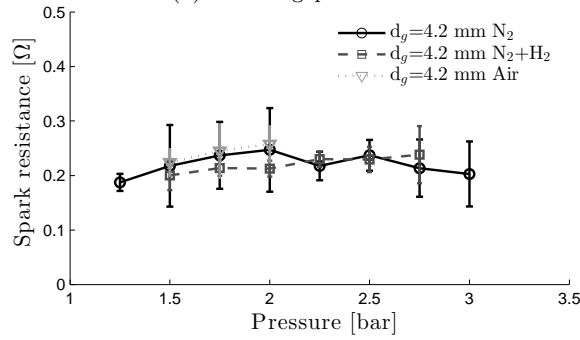
(b) 3.2 mm gap distance.

(c) 4.2 mm gap distance.

Figure 4.8: Pseudo spark gap resistance as a function of pressure for multiple gasses and gap distances

Aluminium has a slightly lower work function than the other materials which could affect the breakdown strength of the gap. Aluminium has also the highest erosion rate in volume which will be shown in Section 4.3.3. The higher amount of vaporized material in the gap could also effect the breakdown voltage.

Significantly deviating recovery behavior was only observed with tungsten and stainless
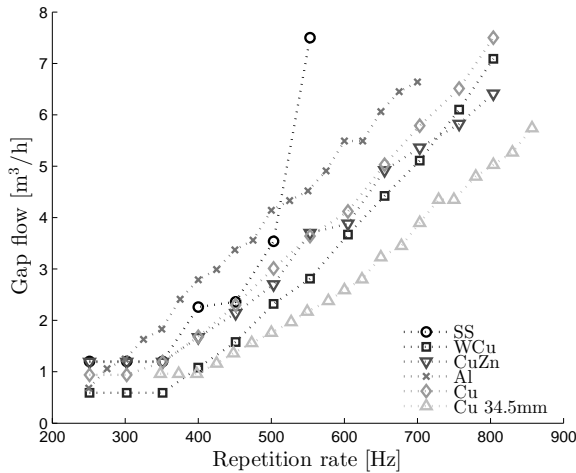
Figure 4.9: Required flow (at 3.4 bar) through the spark gap for different electrode materials and 5 % prefire operation.

steel. Although the stainless steel electrodes perform similar as the copper alloys up to 500 Hz, the flow requirement increases significantly above this repetition rate. The erosion pattern of all materials shows the highest erosion near the trigger disc and the lowest erosion at the outer rim. Although it is obvious that the strike probability is higher near the trigger-gap of the spark gap, the sparks should strike randomly around the trigger disc for proper recovery. Sparks will tend to strike one spot for several sequential pulses if insufficient purging is applied [57]. The recovery fails completely if the spark location remains the same for all consecutive pulses. Stainless steel has a very poor thermal conductivity compared to the other materials (17 W/(m·K) for stainless steel and 110–385 W/(m·K) for the other materials) which could explain the poor recovery behavior at higher repetition rates, see Table 4.1. The surface temperature will rise due to poor heat transport of from the surface (where the spark root attaches) to the bulk of the electrode. The resulting hot-spot is less capable of holding of the voltage with as result that the spark strikes the same spot over and over again. This explains the abrupt recovery failure beyond 500 Hz. It is reported in literature that the electrode surface is also responsible for conducting a part of the heat of the gas in the gap [72,73]. So a second less dominant explanation could be the lack of heat conduction (poor for stainless) from the heated gas to the electrode which increases the recovery time.

Figure 4.10 shows the required flow as a function of the recovery time of the gap for 5 % pre-fire operation. The recovery time is in this case defined as the time that the spark gap is open and there is no voltage present over the spark gap (no voltage over C_h). It is calculated by the following equation $T_{Recovery} = (1/f) - T_{Charge} - T_{Trigger} - T_{SG_{on}}$, where f is the repetition rate, T_{Charge} is the charging time of C_h, $T_{Trigger}$ is the average time before the spark gap triggers and $T_{SG_{on}}$ is the time that the spark gap remains on.

The 34.5-mm Cu electrodes have a reduced flow requirement compared to the 40-mm electrodes due the smaller gap volume which can be purged with less gas flow. The volume of the gap is 1.8× smaller, the flow requirement is at 1.2, 1.5 and 2 ms recovery time respectively 1.5×, 1.6×, and 1.5× smaller. The erosion is much more severe at the inner edge of the anode
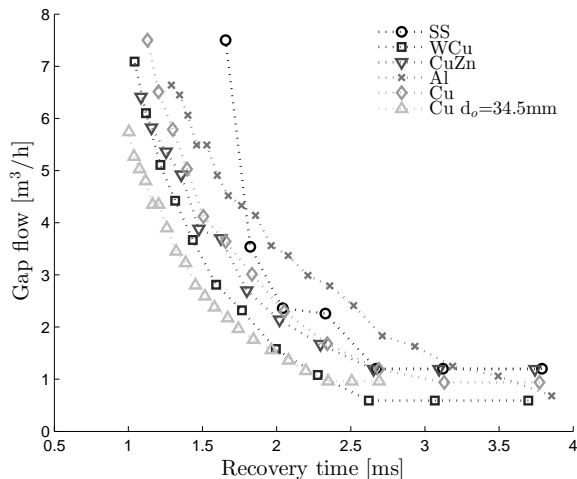
Figure 4.10: Required flow (at 3.4 bar) through the spark gap as function of the recovery time for different electrode materials and 5 % prefire operation.

near the trigger electrode. Discharge activity is concentrated here because of the triggering process. Reducing the outer electrode radius has therefore probably less effect as expected on the recovery behavior. Heated gas in the outer radius region of the gap which reduces the breakdown strength of the gap can however be removed from the gap volume with less flow requirement.

Efficiency of a pulsed power system becomes more important in commercial application as i.e. air purification. The electrical switching efficiency of the spark gap is very high ($>$ 95 %) but the energy consumption of the purging system should also be considered. Figure 4.12 shows the power requirement of the compressor as a function of the repetition rate for the copper electrodes in this system. The pressure drop in the system dominates the power consumption and is primarily caused by the particle filter which saturates within 40 operating hours.

Approximately 0.5 kW is needed to increase the repetition rate to 600 Hz. More than double the power (1.1 kW) is needed for 800 Hz repetition rate. Figure 4.12 shows the repetition rate limitation of purged spark gap switches. Power consumption can probably be reduced by minimizing the pressure drop in the system, but the non-linear trend of the graph will be similar. Faltens [74] concluded that the purging power requirement is proportional to the cube of gas velocity in the gap.

$$\eta_{SG}(f) = \frac{E_{Ch}f - E_{spark}f}{E_{Ch}f + P_{purge}(f)} \tag{4.6}$$

The overall switching efficiency as a function of the repetition rate can now be estimated by Equation 4.6, where f is the repetition rate, E_{Ch} the input energy in capacitor C_h, E_{SG} the energy which is lost per pulse due to switching losses, and $P_{purge}(f)$ the required compressor power as a function of the repetition rate (Figure 4.12). E_{SG} is estimated from the spark
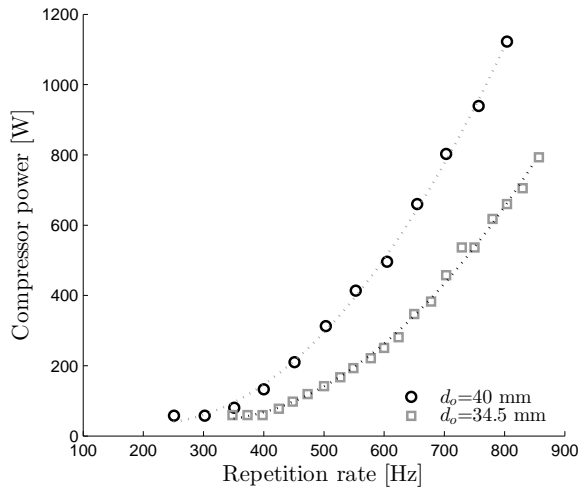
Figure 4.11: Input compressor power as a function of the repetition rate for 34.5 and 40-mm copper electrodes (3.4 bar operating pressure and 500 mbar maximum pressure drop).
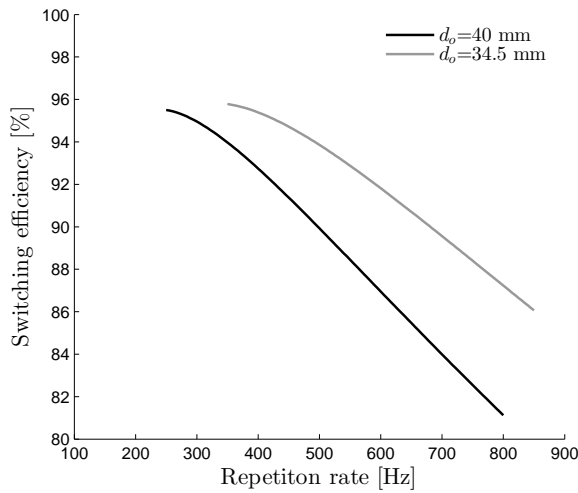
Figure 4.12: Spark gap switching efficiency (including purging power) as a function of the repetition rate for 34.5 and 40-mm copper electrodes (3.4 bar operating pressure and 500 mbar maximum pressure drop).

resistance measurements, approximately 0.15 Ω which results in 0.1 J per pulse E_{spark} (see Equation 4.1).

A maximum efficiency of 96 % can be achieved at low repetition rates. The efficiency

is then primarily limited by the switching losses. The purging power dominates at higher repetition rates resulting in 81 % efficiency at 800 Hz for the 40-mm electrode and 87 % efficiency for the 43 mm electrode.

4.2.3.3   5 kHz burst recovery

Figure 4.13a-c show the relative (to 30 kV) mean recovery voltage as a function of the repetition rate for 1, 5 and 10 m^3/h flow (N$_2$ and N$_2$/H$_2$ mixture) and the three electrode diameters. The following observations can be summarized with respect to the recovery voltage:

- Generally, the recovery voltage is enhanced with increasing gap flow. Except for the 40 mm diameter electrode, the spark gap is only able to remain in the triggered mode up to 600 Hz with 5 m^3/h gap flow. Although doubling the flow does not increase the recovery voltage below 1600 Hz, it remarkably has an effect above this repetition rate (the tipping point is marked by the gray arrow in Figure 4.13a).

- A smaller electrode diameter increases the recovery voltage with the same gap flow under all circumstances. The gap volume is equal to $V_{gap} = d_g\pi(d_o^2 - d_i^2)/4$ so the refreshing rate of the gas in the gap increases with decreasing d_o at the same flow, explaining the improved recovery voltage. A smaller electrode diameter would also increases the amount of discharges per unit area, assuming a random distribution of discharge locations on the electrode surface (during pre-fire operation). Although this effect should be disadvantageous, it does not seem to affect the recovery. The gas velocity at the outer rim of electrode is proportional to the outer radius of the electrode. Cooling of the small electrode by the purging flow is apparently very effective.

- The addition of 5 % hydrogen increases the recovery voltage at repetition rates beyond 2500 Hz for the 40 and 34.5 mm electrode, the tipping point is marked by the black arrows in figures 4.13a and 4.13b. The effect is noticeable over the complete repetition rate range for the 29.5 mm electrode. The spark resistance and energy dissipation is lowered by the addition of H$_2$, also the heat conduction of the gas is slightly increased. The gas density is restored faster which could explain the improved recovery. The tipping points beyond 2500 Hz for the larger electrode diameters are not completely understood. Repetition rates beyond the tipping point are accompanied by large jitter in the breakdown voltage (see figures 4.14a and 4.14b). There is possibly a relation to sparks which strike the same spot for consecutive pulses. A similar abrupt alteration was also seen for the stainless steel electrode during the 800 Hz contentious operation experiment.

- Multiple plateaus can be observed in figures 4.13b and 4.13c which are marked by the dashed horizontal lines. The start of these plateaus is primarily dependent on the repetition rate, in these experiments near 3000 and 4500 Hz. Small intermediate plateaus also seem to be present. The height of the plateaus can be lifted by increasing the flow. Figure 4.13b shows that three settings (1 m^3/h N$_2$, 1 m^3/h N$_2$/H$_2$ and 5 m^3/h N$_2$) eventually reach the lowest plateau. Apparently some parameter in the recovery process becomes dominant, for instance the electrode temperature.

- The overall best recovery result was obtained with 10 m^3/h N$_2$/H$_2$ and the 29.5 mm electrode. The spark gap was able to operate up 1 kHz in the triggered mode and the recovery voltage was 62 % at 5 kHz repetition rate during pre-fire operation.

(a) d_o=40 mm

(b) d_o=34.5 mm

(c) d_o=29.5 mm
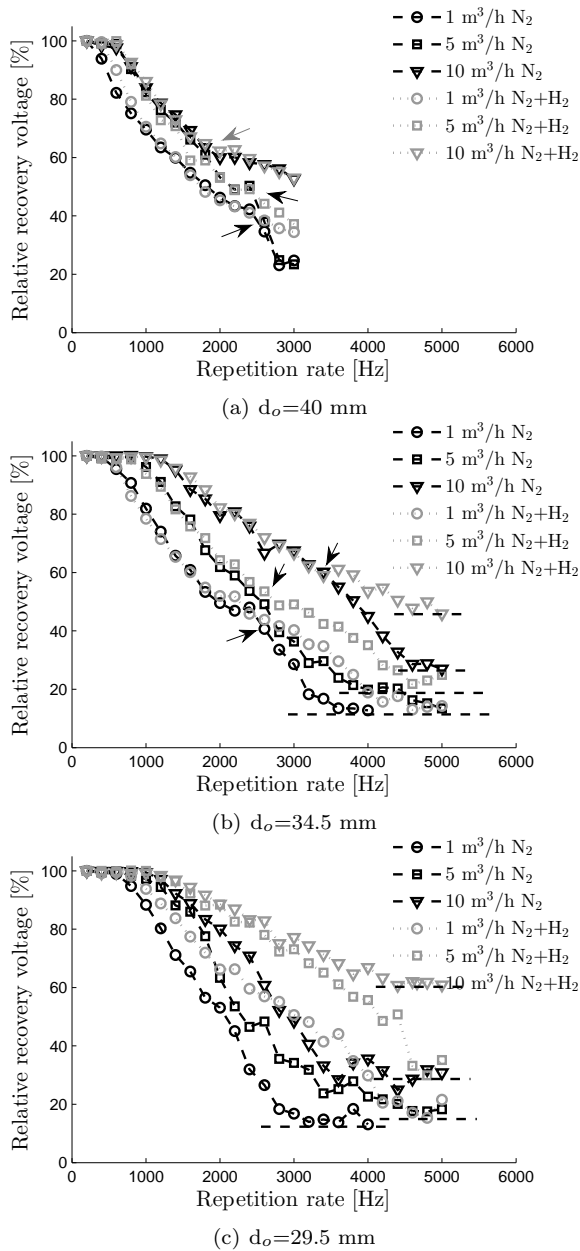
Figure 4.13: Relative mean recovery voltage as a function of the repetition rate. The grey arrow marks the tipping point where the 10 m^3/h flow has effect on the recovery voltage. The black arrows mark the tipping points where the addition of 5 % H$_2$ affects the recovery voltage. The dashed horizontal lines mark the plateaus where the recovery voltage is more or less independent of the repetition rate.
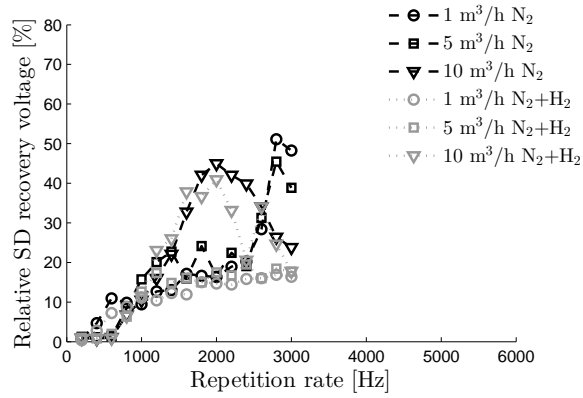
(a) d_o=40 mm
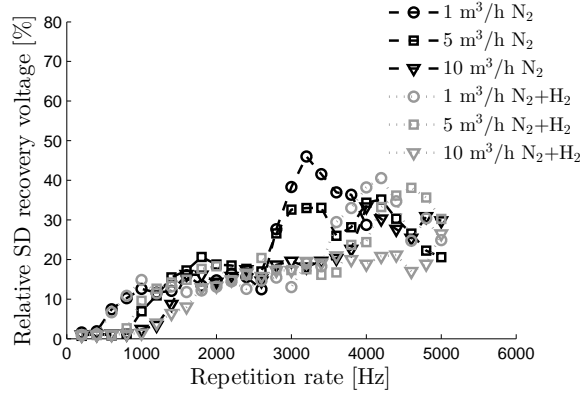
(b) d_o=34.5 mm
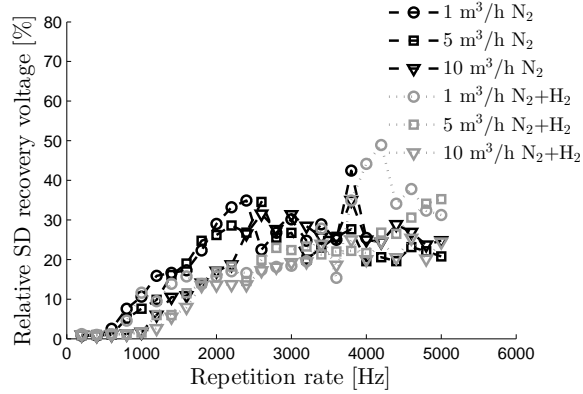
(c) d_o=29.5 mm

Figure 4.14: Relative standard deviation of the recovery voltage as a function of the repetition rate.

Figure 4.14a-c shows the relative (to the mean recovery voltage) standard deviation (SD) of the recovery voltage as a function of the repetition rate for 1, 5 and 10 m^3/h flow and three different electrode diameters. The following observations can be summarized with respect to the jitter of the recovery voltage:

- The jitter is near zero for low repetition rates where the spark gap operates in the triggered mode. The relative SD increases on average up to 15-25 % for repetition rates beyond 2000 Hz.

- Unstable areas can be observed where the relative SD increases up to 50 %. For instance in Figure 4.14a, these unstable areas seem to be related to the recovery voltage tipping points marked by the arrows in Figure 4.13a. The same observation can be made from Figure 4.13b and 4.14b, the tipping points at 2500 Hz in both figures are related. The system is able to enter in a sort of alternating mode, a cycle with a high breakdown voltage is followed by a cycle with a low breakdown voltage. A larger amount of energy is dissipated in the gap with the high breakdown voltage resulting in a poorer recovery and lower breakdown voltage during the following cycle.

4.3 Electrode erosion

4.3.1 Erosion mechanisms

The lifetime of the spark gap switch is limited by the erosion rate of the electrodes [57,75–77]. Erosion occurs when sufficient energy from the discharge is applied to the surface of the electrode material which raises the temperature to the boiling point. Several processes affect the erosion, i.e. ablation (vaporization or chipping), sputtering by particle bombardment and oxidation [78]. Liquified electrode materials can be ejected out of the surface by shockwaves produced by the transient discharge. The erosion processes are complex and poorly covered by theory. There are multiple parameters which affect the erosion such as: electrode material, gap distance, gas composition, gas pressure, peak current and total charge transfer of the pulse.

The energy sources which initiate these processes include electron impact, Joule heating, exothermic chemical reactions and jet impact. Energy input to the electrode surface is often related to the electrode fall voltage. Fall regions exist near the cathode and anode surface, see figure 4.15. The fall voltage is typically 10–50 V. The discharge channel needs to make the transition from gas to metal. Conditions and self maintaining mechanisms exist in these regions which allow these transitions [79]. Electrons are emitted at the cathode by the high electric field in the fall region and as a result of ion impact. Electrons accelerate in the electric field of the fall region, producing ions and electrons near the boundary of the discharge column upon collision. The ions are then accelerated back to the cathode where they bombard the cathode surface. When the surface of the electrode heats up (by ion impact) to several thousand Kelvin, thermionic emission will become significant and the fall voltage decreases [80]. At the cathode the current has an ionic and electronic component. Current continuity in the anode fall region is mainly achieved by electrons being fed into the anode because positive ion emission from the anode can be neglected.

Joule heating (resistive heating) occurs in the spark (gas) and in the electrode. The region of interest for Joule heating in the gas phase is near the electrode surface. The power input at the electrode surface is determined by a combination of various mechanisms. Significant are:
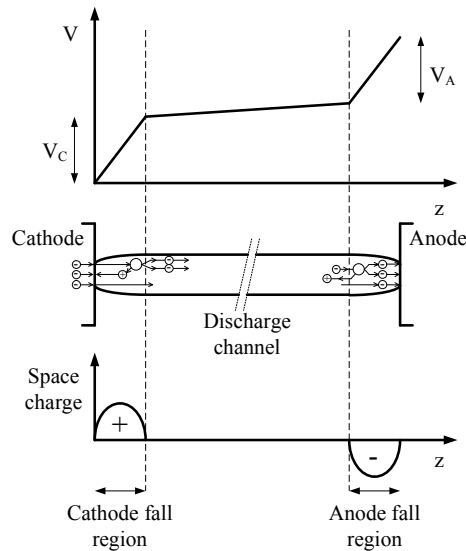
Figure 4.15: Schematic representation of the space charges and fall voltages near the surfaces of the anode and cathode.

E-field determined fall voltage, electron and ion impact, electron field emission and thermal electron emission, metal work function, ion recombination and enthalpies of the particle fluxes. A convenient way to formulate the power input is the introduction of an effective fall voltage at the electrodes, see the work by Tepper [81]. Along these lines we can equate the power input as current times effective fall voltage. The expression for the effective fall voltages, adapted from [81] is:

$$V_{eff_C} = V_C - F - 2.5 \frac{kT_C}{e} \qquad (4.7)$$

$$V_{eff_A} = V_A + F + 2.5 \frac{kT_A}{e} \qquad (4.8)$$

Where V_C and V_A are the E-field determined fall voltages at the cathode and anode, F is the work function expressed in volts, T_A or T_C is a temperature determined by the temperature of the spark, the electrons and the surface. Note that 2.5 kT/e is an expression in volts. Filling in numbers to have a crude estimate of magnitudes shows that the anode has a significantly higher effective fall voltage than the cathode, e.g. 16 V versus 4 V (we used $V_C=V_A=10$ V, $F=4.5$ V, $2.5kT/e=1.5$ V).

Other forms of energy delivered by the spark are radiation, convection and conduction. The high current densities in the spark (kA amperes vs. μm-mm spark radius) results in high current densities and Joule heating in the electrode at the spark-root attachment point. The skin effect can play a reinforcing role during transient discharges. An erosion mechanism which can occur during high current pulsed discharges is jet production [70, 82, 83]. High speed (10^4 m/s) directed streams of ionized electrode vapor are produced in the space near the electrode surfaces. These jets are super heated up to 4×10^4 K as they pass through the

spark plasma and create crater like erosion upon collision with the opposite electrode. The jet production results in an electrode-separation dependent erosion rate [70, 71].

4.3.2 Electrode erosion modeling

Analytical and numerical thermal models are developed to investigate and estimate the electrode erosion behavior and to gain insight in the effect of material properties. The actual power input to the surface is difficult to estimate and depends on multiple factors as described in Section 4.3.1). Therefore we apply a basic approach, the power input is proportional to the product of the effective fall voltage and discharge current. The power dissipated in the fall region is transferred to the electrode surface resulting in: $P_{in} = V_{eff_A}|I_{SG}(t)|$ for the anode and $P_{in} = V_{eff_C}|I_{SG}(t)|$ where V_{eff_A}, V_{eff_C} the effective anode and cathode fall voltage. Electrode erosion can be estimated by considering the energy balance between heat conduction and power input at the electrode surface. The difference of the input power and conducted power is converted into evaporation of the electrode material. The radius of the discharge at the electrode-spark attachment affects the current density in the discharge and thus the power density (W/m^2) on the electrode surface. The analytical model assumes a static spark radius and thus a static power density to the electrode surface, while the numerical model features a more realistic spark radius which follows the trajectory of a shockwave. The numerical model also enables estimation of the melted electrode volume which is rather important. The total volume erosion actually consists of the sum of the vaporized material and ejected molten material [57, 84], see Equation 4.9. V_e is the total eroded volume, V_v and V_l are respectively the vaporized and molten volume. k_v and k_l are the coefficients of removal, where e.g. $k_v = 1$ means that all molten material is removed from the surface. Estimation of these coefficients is challenging because they depend on various parameters.

$$V_e = k_v V_v + k_l V_l \qquad (4.9)$$

4.3.2.1 Analytical model

Starting point of the analytical model is Fourier's law which describes the rate of flow of heat energy Q through a surface A which is proportional to the negative temperature gradient normal to the surface, where λ is the thermal conductivity ($W/m^2 \cdot K$).

$$Q = -\lambda A \nabla T \qquad (4.10)$$

An approach comparable to our model is followed by Tepper [81]. However, he assumes $T_B >> T_{amb}$ where T_B is the boiling temperature of the electrode material and T_{amb} is the temperature of the bulk of the electrode. It is also assumed in this reference that the contact area A equals the entire electrode surface. In our present case we assume a much smaller area A. A schematic representation of the problem can be observed in Figure 4.16. Our analytical 1D model which describes the evaporated volume per pulse as a function of the heat flux (power) on the electrode surface can be derived as follows. The heat flux (P_{in}) delivered by the spark column to the electrode surface is assumed to be circular with surface area A. Evaporation of the surface layer will occur if the surface layer reaches the boiling point and if the heat conduction into the surface (P_c) is smaller than the heat flux (P_{in}). The difference in power is assumed to be dissipated by material evaporation.
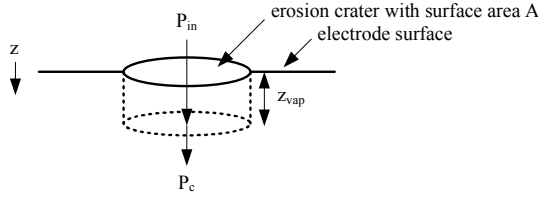
Figure 4.16: Schematic representation of the 1D thermal erosion model.

The conduction of the incident heat into the body is governed by the heat diffusion equation where α is the diffusivity of the given by Equation 4.12.

$$\frac{\partial T}{\partial z} = \alpha \frac{\partial^2 T}{\partial z^2} \tag{4.11}$$

$$\alpha = \frac{\lambda}{\rho c_p} \tag{4.12}$$

ρ in Equation 4.12 is the mass density of the electrode material and c_p the heat capacity. The solution of the diffusion equation is given by the complementary error function $erfc(x)$ where the argument x is given by $z/(2\sqrt{\alpha t})$:

$$T(z,t) = A\lambda(T_B - T_{amb})erfc\left(\frac{z}{2\sqrt{\alpha t}}\right), \quad erfc(x) = \frac{2}{\sqrt{\pi}}\int_x^\infty e^{-t^2}dt \tag{4.13}$$

This solution for T in Equation 4.13 is used to evaluate the heat conduction P_c (Equation 4.14) into the body

$$P_c(t) = A\lambda \frac{\partial T}{\partial z}\bigg|_{z=0} \tag{4.14}$$

The result is subsequently given by Equation 4.15

$$P_c(t) = A\lambda(T_B - T_{amb})\frac{\partial}{\partial z}erfc\left(\frac{z}{2\sqrt{\alpha t}}\right) = \frac{A\lambda(T_B - T_{amb})}{\sqrt{\pi \alpha t}} \tag{4.15}$$

The power which is converted into evaporation of electrode material is equal to the following equation assuming that the input power is larger than the conduction power.

$$P_{vap}(t) = P_{in}(t) - P_c(t), \quad P_{in}(t) > P_c(t) \tag{4.16}$$

The enthalpy (or latent heat) of evaporation ΔH_{vap} (J/kg) is applied to calculate the evaporated volume in the z-direction per unit of time dt. ρ and $d_{z_{vap}}$ are respectively the density of the electrode material and the per unit time thickness of the evaporated layer.

$$P_{vap}(t) = \rho \Delta H_{vap} A \frac{d_{z_{vap}}}{dt} \tag{4.17}$$

Determining the enthalpy of evaporation for alloys is not completely straightforward. One can argue that the metal with the lower boiling point in the alloy first needs to evaporate from the surface before the temperature can rise to the boiling point of the second metal. We choose to use the following approach in Equation 4.18 [81] where x_a and x_b are the volume

107

Table 4.1: Thermal electrode material properties

Material	λ [W/(m K)]	c_p [J/(kg K)]	ρ [kg/m^3]	α [m^2/s]
Cu	385	385	$8.96 \cdot 10^3$	$11.16 \cdot 10^5$
W	173	134	$19.25 \cdot 10^3$	$6.70 \cdot 10^5$
CuZn	110	380	$8.40 \cdot 10^3$	$3.45 \cdot 10^5$
Al	205	897	$2.70 \cdot 10^3$	$8.46 \cdot 10^5$
SS	17	500	$7.99 \cdot 10^3$	$0.43 \cdot 10^5$
WCu	164	130	$16.68 \cdot 10^3$	$7.56 \cdot 10^5$

Table 4.2: Melting and evaporation material properties

Material	ΔH_{vap} [J/kg]	ΔH_{melt} [J/kg]	T_b [K]	T_m [K]
Cu	$4.73 \cdot 10^6$	$2.05 \cdot 10^5$	2835	1358
W	$4.48 \cdot 10^6$	$1.93 \cdot 10^5$	6203	3695
CuZn	$3.54 \cdot 10^6$	$1.68 \cdot 10^5$	2022	1203
Al	$10.87 \cdot 10^6$	$3.98 \cdot 10^5$	2743	933
SS	$6.32 \cdot 10^6$	$0.28 \cdot 10^3$	3000	1650
WCu	$4.54 \cdot 10^6$	$1.96 \cdot 10^5$	6173	3693

ratios of the metals in the alloy, ΔH_{vap_a} and ΔH_{vap_b} are the enthalpy of evaporation values for the metals.

$$\Delta H_{vap} = x_a \Delta H_{vap_a} + x_b \Delta H_{vap_b} \tag{4.18}$$

Substitution of previous equations, reordering and integration over time leads to the integral evaporation distance (z_{vap}) after time τ.

$$z_{vap}(\tau) = \int_0^\tau \frac{P_{in}(\tau) - P_c(\tau)}{A\rho\Delta H_{vap}} \tag{4.19}$$

The volume can subsequently be calculated by:

$$V_{vap}(\tau) = Az_{vap}(\tau) \tag{4.20}$$

The final solution for the evaporated volume per pulse of duration τ is described by following equation.

$$V_{vap}(\tau) = \int_0^\tau \left(\frac{P_{in}(\tau)}{\rho\Delta H_{vap}} - \frac{A\lambda(T_B - T_{amb})}{\rho\Delta H_{vap}\sqrt{\pi\alpha\tau}} \right) d\tau \tag{4.21}$$

4.3.2.2 Finite Difference Method model

The basic analytical model includes only heat conduction in the z-direction, assumes an instantaneous boiling electrode surface and static spark radius. Especially during nanosecond spark discharges, the spark radius expands violently, typically following the trajectory of a blast wave [85, 86]. The electrode erosion will be affected by this varying radius since a smaller spark surface (A) increases the electrode erosion (see Equation 4.21) because the current density in the spark at the spark-electrode attachment will be inversely proportional to the square of the spark radius.

A numerical Finite Difference Method (FDM) [87] model is applied which facilitates the addition of a spark radius which varies as a function of time. Also, evaporation onset moment, heat penetration into the surface and melted electrode volume can be investigated.

The adiabatic spark expansion model proposed by Zhang [88] is applied to calculate the spark radius as a function of time. The model is described as follows. A cylindrical spark channel rapidly develops between the electrodes after the gap breaks down. A finite amount of energy is deposited in the initial spark volume which results in rapid heating of the gas column before it starts expanding [89]. Homogenous temperature of the gas column and behavior which follows the state equation of a real gas is assumed. The gas pressure, temperature and flow velocity outside the column remain unaffected. The temperature of the gas column increases rapidly during energy deposition while the gas density (ρ_0) in- and outside the column remains constant. The initial volume of the gas column (V_1) can be estimated by the latter assumption.

$$V_1 = \frac{E}{c_v \rho_0 (T_1 - T_0)} \tag{4.22}$$

E is the energy which is instantaneously deposited in the gas column, c_v is the heat capacity of the gas, T_0 is the gas temperature before energy deposition (in- and outside the column) and T_1 is the temperature in the gas column after heating. A temperature limit exists for specific gases in strong discharges [90], typically 41000 K for N_2. Energy deposited in the gas column beyond the temperature limit does not result in a higher gas temperature but in an increased gas volume. The bulk of the energy in our application is deposited in the spark during the first 100 ns of the discharge and can be estimated from measurements. Assuming constant gas density (ρ_0), the initial spark volume can now be calculated by Equation 4.22. The initial spark follows from: $R_1 = \sqrt{V_1/(\pi d_g)}$, where d_g is the distance between the electrodes. The gas column will now expand and follow the trajectory of a strong cylindrical shock wave [85, 86]. A solution for the radius of a strong cylindrical shock wave as a function of time is described by:

$$r(t) = \sqrt{CR_c t + C^2 t^2} \tag{4.23}$$

Where C is the velocity of sound in the gas outside the column, $C = \sqrt{\gamma p_0 / \rho_0}$. The relaxation radius R_c is described by:

$$R_c = \sqrt{\frac{4E}{d_g B \gamma p_0}} \tag{4.24}$$

Where B is a constant (3.37 for N_2), $\gamma = c_p/c_v$ is the ratio of specific heats and p_0 the pressure inside the column before energy deposition. Following the shock wave trajectory, some time after energy deposition is needed before the initial radius R_1 would be reached.

The gas column expands due to the instantaneously introduced pressure difference between the in- and outside of the column. During expansion, zero heat transfer between the gas column and the surrounding gas is considered (adiabatic expansion). The pressure change due to the adiabatic expansion is then described by Equation 4.25.

$$\frac{p_2}{p_1} = \left(\frac{V_1}{V_2}\right)^{\gamma} \tag{4.25}$$

The expansion stops when the pressure inside the column equals the pressure outside the column, $p_2 = p_0$. The volume change due to the pressure equalization is subsequently used to calculate the radius (R_2) of the expanded gas column;

$$R_2 = \sqrt{\frac{V_1}{\pi d_g (p_1/p_0)^{\frac{1}{\gamma}}}} \tag{4.26}$$

The power input to the electrode surface in the FDM model can now be implemented since the spark radius trajectory can be estimated. The following assumptions are made for the FDM model:

- The radius of the spark $r_Q(t)$ has initially the value of R_1 and follows the trajectory of the shockwave as a function of time $r(t)$ until radius R_2 is reached. The radius remains constant afterwards.

- The energy input from the spark root to the electrode surface is proportional to the discharge current ($P_{in}(t) = V_{eff}I_{SG}(t)$). The location of the spark on the electrode is assumed to be static during the discharge.

- No heat conduction from the electrode surface to the gas above.

- The temperature in the surface layer of the electrode is limited to the boiling temperature of the electrode material.

Starting point for the numerical FDM model is the heat equation with internal heat generation per unit volume (Q). Equation 4.27 contains a diffusion equation which expresses the heat conduction and the internal heat generation part which is used as power input at the spark-electrode attachment point.

$$\frac{\partial T}{\partial t} = \alpha \nabla^2 T + \frac{Q}{\rho c_p} \tag{4.27}$$

The equation is converted into cylindrical coordinates. We assume cylindrical symmetry. The simulation grid can therefore be limited to a 2D rz-plane, see Figure 4.17.

$$\frac{\partial T}{\partial t} = \frac{\alpha}{r}\left[\frac{\partial}{\partial r}\left(r\frac{\partial T}{\partial r}\right)\right] + \alpha\frac{\partial}{\partial z}\left(\frac{\partial T}{\partial z}\right) + \frac{Q}{\rho c_p} \tag{4.28}$$

The source layer of the grid consists of nodes $Q_{i,1}$ which lie directly under the spark-electrode attachment. Instead of introducing a heat flux through the surface, all power (P_{in}) which is fed to the grid is deposited in this top layer of nodes, $Q_{i,1}$ ($1 < i \leq N_Q$). Equation 4.28 is subsequently converted into a forward time, central space (FTCS) scheme:

$$\frac{T_{i,j}^{n+1} - T_{i,j}^n}{\Delta t} = \alpha(\varphi + \gamma) + \zeta \tag{4.29}$$
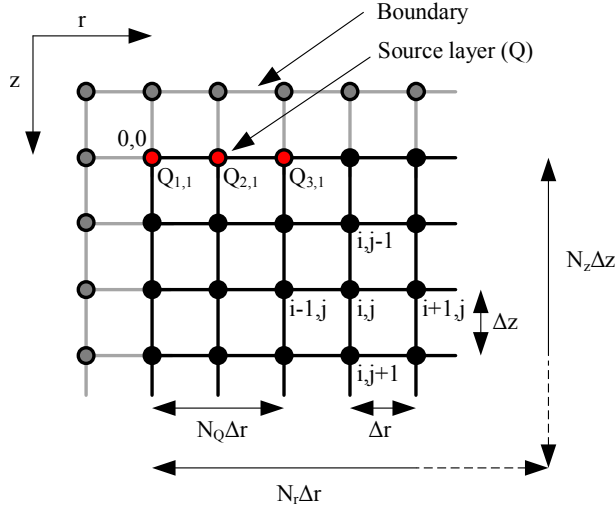
Figure 4.17: Finite difference discretization grid in the 2D rz plane. Energy is fed to the grid via heat generation Q at the top layer where the spark root attaches.

$$\varphi = \frac{T_{i+1,j}^n - 2T_{i,j}^n + T_{i-1,j}^n}{(\Delta r)^2} + \frac{1}{r_i}\frac{T_{i+1,j}^n - T_{i-1,j}^n}{2\Delta r} \qquad 0 < i < N_r \qquad (4.30)$$

$$\gamma = \frac{T_{i,j+1}^n - 2T_{i,j}^n + T_{i,j-1}^n}{(\Delta z)^2} \qquad 0 < j < N_z \qquad (4.31)$$

$$\zeta = \begin{cases} \frac{Q_{i,j}^n}{\rho c_p} & j = 1 \ \ and \ \ i \le N_Q \\ 0 & j > 1 \ \ or \ \ N_Q < i < N_z \end{cases} \qquad (4.32)$$

One layer of extra nodes is added at the virtual position $z = -\Delta z$ and similarly one at $r = -\Delta r$ to avoid numerical issues. The central space scheme requires a layer of nodes above the source layer and at the inner axis in the r-direction. We assume no heat conduction above the source layer and there is only axial heat conduction at the r-axis. The heat conduction at $z = 0$ and $r = 0$ is prevented by the following boundary conditions:

$$\left.\frac{\partial T}{\partial r}\right|_{r=0} = 0 \qquad\qquad T_{0,j}^{n+1} = T_{1,j}^{n+1} \qquad (4.33)$$

$$\left.\frac{\partial T}{\partial z}\right|_{z=0} = 0 \qquad\qquad T_{i,0}^{n+1} = T_{i,1}^{n+1} \qquad (4.34)$$

Generally the grid needs to be large enough to avoid heat reaching the end of the grid ($N_r\Delta r$ and $N_z\Delta z$). These node temperatures will then remain at the initial value (T_{amb}), 300 K during our simulations. Heat flux through the grid boundaries is however allowed by setting the following conditions:

111

$$\left.\frac{\partial T}{\partial r}\right|_{r=N_r\Delta r} \geq 0 \qquad\qquad T_{N_r,j}^{n+1} = T_{amb} \tag{4.35}$$

$$\left.\frac{\partial T}{\partial z}\right|_{z=N_z\Delta z} \geq 0 \qquad\qquad T_{i,N_r}^{n+1} = T_{amb} \tag{4.36}$$

Stability is always an issue for FDM simulations. The explicit solution which we are applying is only stable below a maximum time step (Δt) which depends on the minimum spatial step size in the grid. According to literature, the following criterion applies for this numerical scheme [91]:

$$\frac{\alpha\Delta t}{\Delta r^2 + \Delta z^2} \leq 0.25 \tag{4.37}$$

The flowchart in Figure 4.18 describes the program which consists of a triple nested loop to calculate the temperatures of the nodes in the grid space ($i\Delta r, j\Delta z$) and time ($n\Delta t$) resolved.

The following steps are sequentially processed:

1. The radius of the spark is set and quantized per time step. Define the internal heat generation in the source layer Q (W/m^3). The instantaneous power $P_{in}^n = P_{in}(n\Delta t)$ is put into the source layer (Q) with thickness Δz and spark area $A_Q^n = \pi[r_Q(n\Delta t)]^2$.

$$Q_{i,j}^n = \frac{P_{in}^n}{A_Q^n\Delta z} \tag{4.38}$$

2. Calculate values $T_{i,j}^{n+1}$ in the grid by applying Equation 4.29 in a double nested loop (r and z direction).

3. Set the boundary conditions (Equations 4.33–4.36)

4. Calculate the melting energy of all the nodes in the grid. The temperature of a node is not allowed to rise further than the melting temperature until the enthalpy of melting is equal to the melting energy of the concerning node.

   In our approach, energy is converted into melting when a node temperature reaches the melting point. A small temperature overshoot (ΔT) per time step (Δt) of a node can be present if sufficient heat is conducted from the surrounding nodes. The overshoot $\Delta T = T_{i,j}^{n+1} - T_M$ represents an amount of surplus thermal energy Q_{melt} that is available for melting, see Equation 4.39.

$$Q_{melt} = mc_p\Delta T \tag{4.39}$$

   In more detail, this surplus of thermal energy per node is calculated and integrated in a separate variable $Q_{melt_{i,j}}$ during each time step Δt.

$$Q_{melt_{i,j}}^{n+1} = Q_{melt_{i,j}}^n + V_i\rho c_p(T_{i,j}^{n+1} - T_M) \tag{4.40}$$

   Where V_i is the volume of the node (or ring in the rz-plane) and T_M is the boiling point, see Equation 4.41.
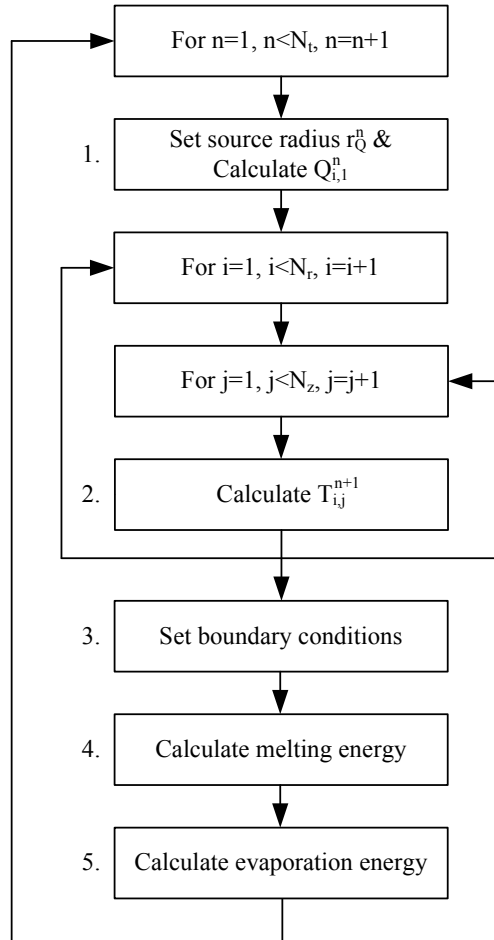
Figure 4.18: Flowchart of the FDM erosion model

$$V_i = \begin{cases} \pi \Delta z (0.5 \Delta r)^2 & i = 0 \\ \pi \Delta z \left((i\Delta r + 0.5\Delta r)^2 - (i\Delta r - 0.5\Delta r)^2 \right) & 0 < i < N_r \end{cases} \quad (4.41)$$

The temperature of the node is subsequently set back to the melting temperature $(T_{i,j}^{n+1} = T_M)$. The temperature is allowed to rise further if the melting energy per node is equal or larger than the energy required to melt the entire node, $Q_{melt_{i,j}}^{n+1} \geq V_i \rho H_{melt}$. Due to this procedure, all melting energy has been removed form the heat flow and stored in the node.

The process reverses when the temperature of the node eventually falls below the melting temperature. The undershoot of the temperature per time step is again converted and integrated in $Q_{melt_{i,j}}^{n+1}$ according to Equation 4.40. Because ΔT is now negative, $Q_{melt_{i,j}}^{n+1}$ will approach zero after a number of time steps. The temperature of the node is set to T_M while $Q_{melt_{i,j}}^{n+1}$ is larger than zero. Due to this procedure the previously stored melting energy has been delivered back to the node when $Q_{melt_{i,j}}^{n+1}$ is zero. The temperature of the node is subsequently allowed to decrease below the melting point.

The melted volume is calculated after each time step by checking which nodes exceed the melting temperature and subsequently summing the volume of "melted" nodes using Equation 4.41.

5. Calculate the evaporation energy per node in the source layer (Q_i). Energy is converted into evaporation when the temperature of a source node reaches the boiling point. A small temperature overshoot (ΔT) per time step (Δt) of one or multiple source nodes is always present when the boiling point is reached. The overshoot $\Delta T = T_{i,j}^{n+1} - T_B$ represents an amount of surplus thermal energy Q_{vap} that is available for evaporation ($Q_{vap} = mc_p\Delta T$). This surplus of thermal energy per node is calculated and integrated in a separate variable Q_{vap_i} during each time step Δt, see Equation 4.42. Where T_B is the boiling point.

$$Q_{vap_i}^{n+1} = Q_{vap_i}^n + \rho V_i c_p (T_{i,1}^{n+1} - T_B), \quad T_i^{n+1} > T_B \tag{4.42}$$

The temperature in the source nodes can overshoot again during the following time step, depending on the power input and heat conduction. In our approach only the source layer is allowed to reach the boiling temperature. The "boiling" nodes are subsequently set to the boiling temperature before the next time step starts ($T_{i,1}^{n+1} = T_B$). Underlying nodes are therefore not able to exceed the boiling temperature.

The total volume which has been evaporated after time step n can subsequently be calculated by equation 4.43. Where ΔH_{vap} is the enthalpy of evaporation of the electrode material.

$$V_{vap}^n = \frac{\sum_{i=1}^{N_Q} Q_{vap_i}^n}{\rho \Delta H_{vap}} \tag{4.43}$$

Typical simulation results are illustrated by Figure 4.19. The effective fall voltage was chosen relative high (50 V) to demonstrate evaporation and melting of all materials. The melted pool develops during the first 200 ns, the switching current reduces subsequently drastically. Depending on material properties, the pool solidifies again within 2 μs. The enthalpy of melting is often discarded in erosion models because it is nearly impossible to implement analytically. The error introduced by assuming zero latent heat of melting is shown in Figure 4.19 for aluminium. The maximum melted volume increases substantially and the cooling down time of the pool is shorter when the heat of melting is set to zero. This can be explained by the temperature limitation and energy storage when a node reaches the melting temperature. The melting energy is subsequently released again, resulting in a longer tail of the solidification process. Evaporation is mainly limited to the first 70 ns of the switching current, the poor thermal conduction (and thus power conduction into the surface) of stainless steel allows evaporation up to 170 ns.
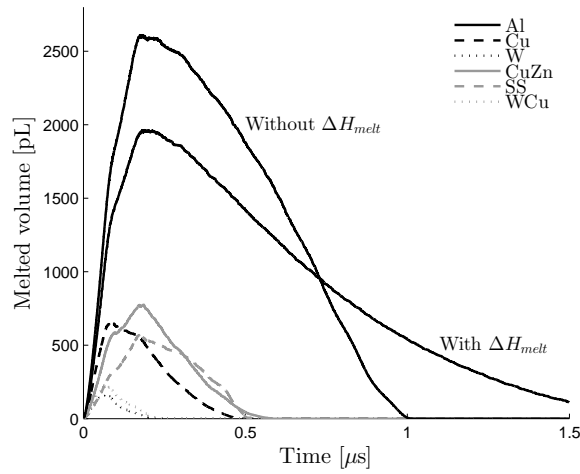
(a) Melted electrode volume as a function of time.
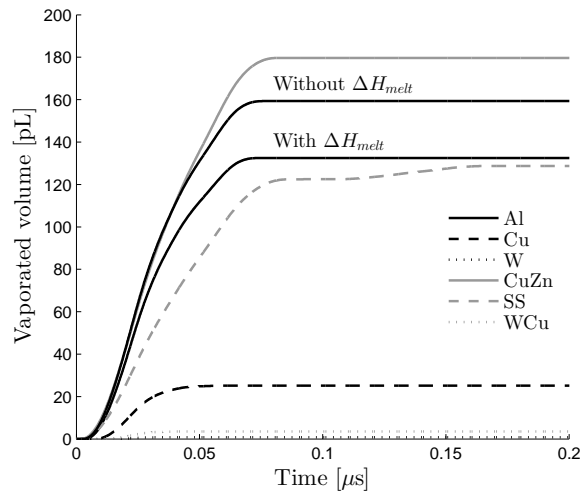
(b) Evaporated electrode volume as a function of time.

Figure 4.19: Typical output of the numerical erosion model. The melted and evaporated volume as a function of time for six electrode materials is shown. The effective fall voltage was chosen relative high (50 V) to demonstrate evaporation and melting of all materials. Simulations are performed with the enthalpy of melting incorporated in the model. The effect of discarding the enthalpy of melting is shown for aluminium.
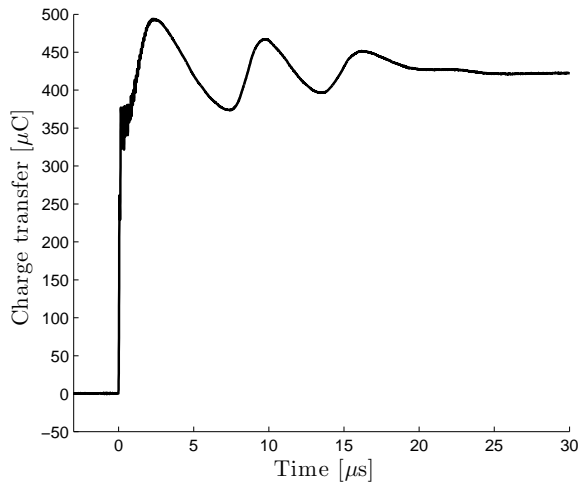
Figure 4.20: Typical spark gap charge transfer per pulse as a function of time.
The spark gap quenches after 25 μs

4.3.3 Experimental results

Erosion and continuous recovery experiments were performed simultaneously so the experimental details are described previously in Section 4.2.2.2. The electrode materials have been tested with $65 \cdot 10^6$ discharges to obtain accurate mass erosion measurements. This corresponds to an equivalent of 40 hours operation at 450 pulses per second for each material. The results are shown graphically in Figure 4.21 for the cathode and anode normalized with the transported charge. The charge transfer through the spark gap is calculated by integration of the current and is shown in Figure 4.20. 320 μC is transferred in the first 500 ns. The residual charge in the capacitor passes the spark gap multiple times during the remaining on-time of the switch (approximately 25 μs). On average, 425 μC is transferred each pulse via the spark gap.

The volume erosion is of main interest sinds it determines the lifetime of the electrodes. The anodes have higher overall erosion rates than the cathodes. Aluminium shows the poorest performance as expected sinds it has a low melting point and low density. Surprisingly tungsten does not perform much better. The high melting point of 3695 K compared to 933 K for aluminium has minimum effect on the erosion rate. Even stainless steel electrodes outperform tungsten. The ratio between anode and cathode erosion is similar for the three mentioned materials. Interesting results can be observed from the materials containing copper. Although the anode erosion of CuZn and WCu is higher than SS and W, the cathode erosion is much lower. The copper cathode didn't erode at all but gained some weight. The copper anode had substantially less erosion than the copper alloy anodes. Copper can apparently be transported from the anode and partially deposited (by sputtering or splashing) on the cathode in a nitrogen environment.

Images of the electrodes are shown in Figure 4.22. Remarkable are the dark discolorations on the copper and brass cathode surfaces. This possibly indicates copper deposition from the anode on the cathode surface. Although the erosion rate of the copper anode is low, the
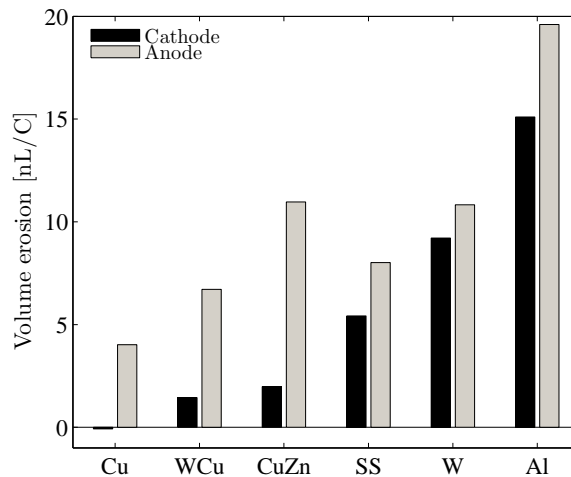
Figure 4.21: Measured volume electrode erosion rates normalized to the transferred charge for six materials.

Table 4.3: Measured electrode erosion rates normalized to the transferred charge for six materials.

Material	Electrode	nL/C	μg/C	pL/pulse
Cu	C	-0.08	-0.71	-0.03
WCu	C	1.44	23.98	0.62
CuZn	C	1.97	16.23	0.85
SS	C	5.42	43.28	2.33
W	C	9.21	177.35	3.96
Al	C	15.10	40.77	6.49
Cu	A	4.02	36.03	1.73
WCu	A	6.72	112.00	2.89
SS	A	8.01	64.02	3.45
W	A	10.83	208.41	4.66
CuZn	A	10.97	90.27	4.72
Al	A	19.60	52.93	8.43

surface is extremely ablated (by e.g. droplet ejection) compared to the other materials. The surface of the brass anode is on the other hand very smooth. The other materials have similar surfaces, when comparing the anode and cathode. Spots related to spark attachment points are visible on almost all electrodes. Obvious large spots were observed on the brass cathode, copper anode and both stainless steel electrodes, typical spot diameters are between 0.5–1.5 mm.

Scanning Electron Microscope (SEM) images of the electrode surfaces are made with a FEI Quanta 600F to study the electrode surfaces. An image of a copper electrode which is

(a) Copper (Cu)   (b) Brass (CuZn)   (c) Tungsten/copper (WCu)

(d) Alumnium (Al)   (e) Stainless steel (SS)   (f) Tungsten (W)
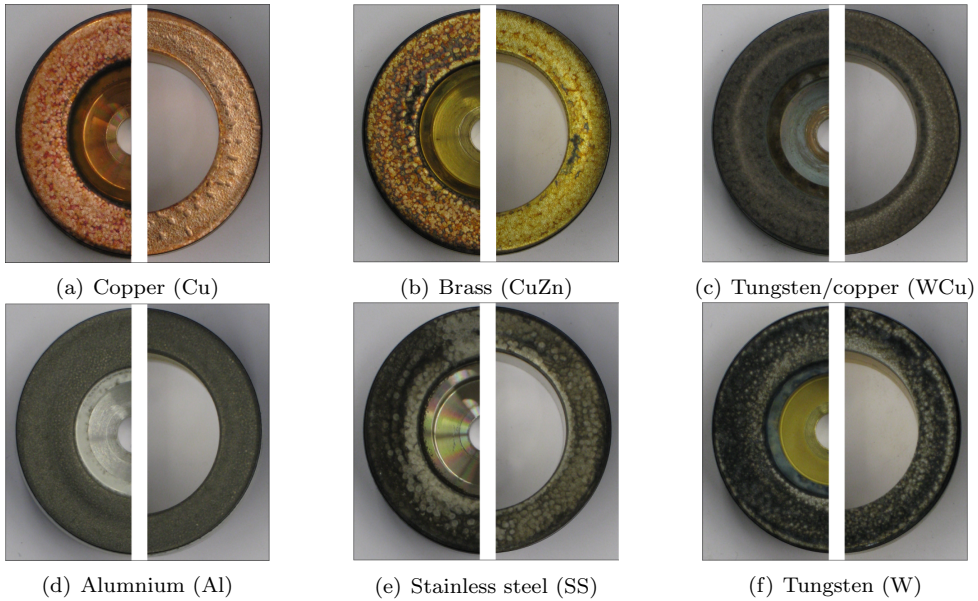
Figure 4.22: Images of the electrodes after $>65 \cdot 10^6$ shots. The left half of the images is the cathode. The anode is shown in the right halve. The outer diameter of the electrodes is 40 mm.

not exposed to any discharges can be observed in Figure 4.23. Only surface defects as a result of the machining process are visible and similar for all electrode materials. Overview images of the electrodes of the tested materials are shown in Figure 4.24. Detail images are shown in Figure 4.25. The copper has a molten surface and a small amount of punctures. The layered molten surface of the Cu electrodes suggests the ability to merge earlier formed surface defects. The puncture formation is probably much higher than can be seen on the SEM images. Sizes of punctures are typically in the range of 1–4 μm which corresponds to a volume in the range of $2.6 \cdot 10^{-4}$–$1.7 \cdot 10^{-2}$pL, assuming a hemi-spherical puncture shape. Although the number of punctures formed per discharge is unknown, ejection of liquid material does not seem to be the main erosion mechanism due the limited volume of the punctures.

Puncture formation seems to be more severe along the grain boundaries of the brass electrodes while the surface in the middle of the grains appears to be smooth. Grain boundaries are known to reduce electrical and thermal conductivity [92]. The temperature on the boundary will possibly rise faster by Joule heating in combination with lack of thermal conduction. The puncture is subsequently formed by explosive evaporation of the material near the grain boundary. The defects on the anode seem to be more severe compared with the cathode which agrees with the erosion rate results.

The aluminium cathode and anode surfaces look very similar. Clear marks of surface melting are visible. Puncture formation seems to be very limited with this material and less compared to brass and copper. The low melting point possibly enables easy merging or melting of surface defects as seen with the copper electrodes.
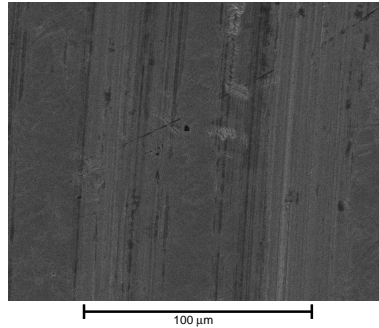
Figure 4.23: Typical surface surface imperfections of a new electrode.

The stainless steel anode has also small punctures along the grain boundaries and a molten surface, while the cathode has high concentrations of punctures over the complete surface. Concluding from the erosion results, more energy is deposited on the anode, explaining the molten surface of this electrode.

Only the tungsten and copper/tungsten alloy electrodes have a entire different surface. The overall surface seems to be much rougher. Small protrusions grow on the surface of the electrodes with a typical size of 5–10 μm. They are probably formed in a similar less violent manner as the punctures. The high melting and boiling point of tungsten tempers explosive evaporation of the surface material. Liquid surface material seems to be inflated by vapor into bubble like protrusions. A small hole in the side the protrusion enables the hot gasses to escape.

4.3.4   Comparison between experimental and model data

Accurate erosion estimations are not expected from the models because of composite material effects which were observed in the previous section. The anodes show increased erosion rates compared to the cathodes which suggests a higher effective fall voltage near the anode according to the assumptions in the models and according to the estimates in Section 4.3.1. Energy delivered to the electrode surface by electron impact seems to be the dominant mechanism. The good performance of copper may also suggest that the erosion in this application is strongly related to Joule heating in the electrode surface. Copper has the highest electrical and thermal conductivity.

The models with the effective fall voltage as input power parameter can however be used to gain insight in the behavior of different electrode materials. First we start with the analytical model. The evaporated volume per pulse as a function of the (static) spark radius is shown in Figure 4.26. The input power is calculated with $V_{eff} = 10$ V as a first estimation, $P_{in} = 10|I_{SG}(t)|$. Where $I_{SG}(t)$ is the actual current waveform of the spark gap during the erosion experiments, see Figure 2.31 and 2.34 (Chapter 2) (20 kV DC-bias). According to the model, there's no evaporation for spark radiuses exceeding 396 μm. The power conduction is proportional to the spark area and exceeds the input power for large radiuses. Clearly visible are the effects of the material parameters. E.g. CuZn and Al perform initially better than stainless steel for small radiuses because of low boiling temperatures and low ΔH_{vap} values.

119
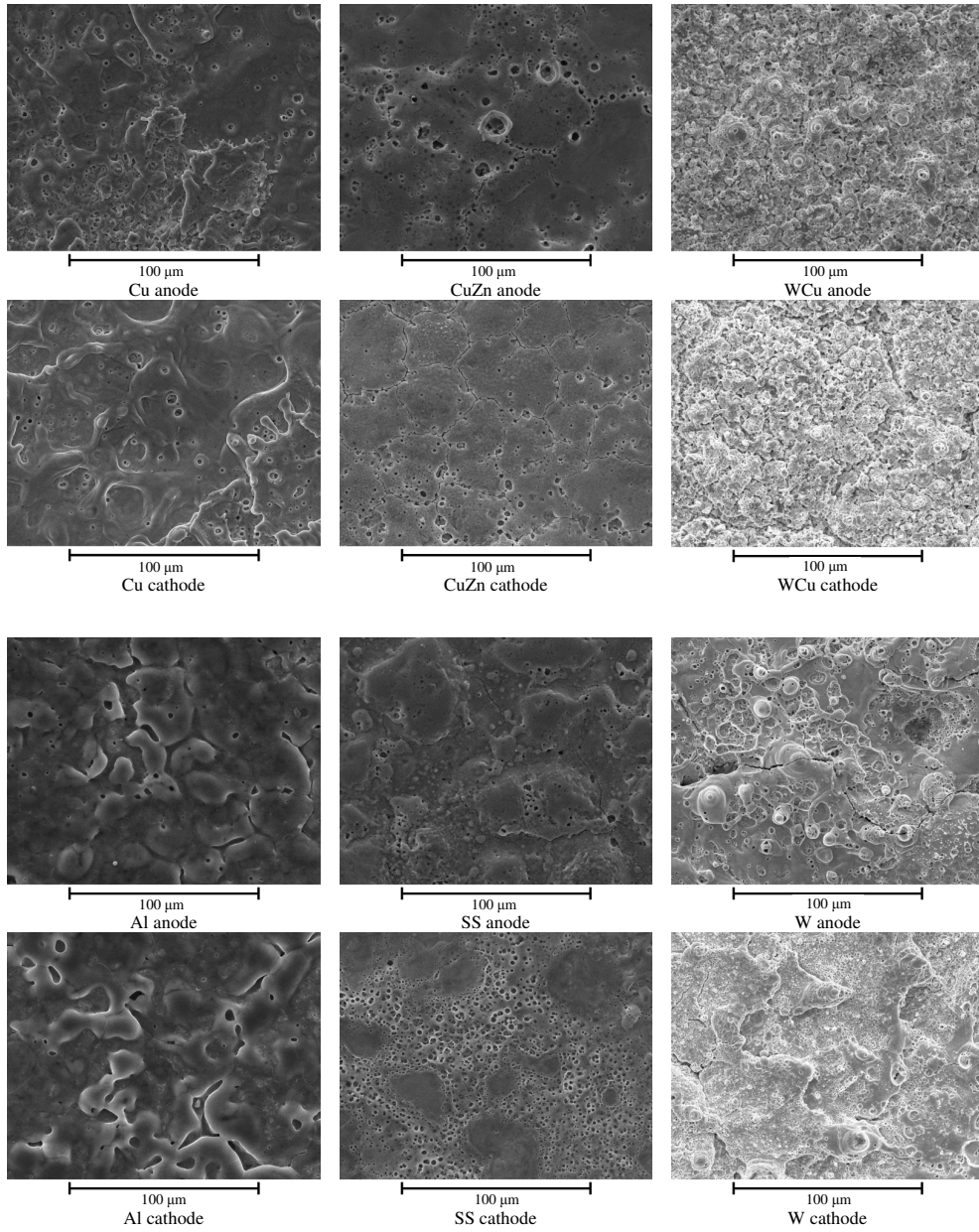
Figure 4.24: Overview SEM images of the anode and cathode surfaces after $65 \cdot 10^6$ shots (SEM imaging facilitated by Multi-scale lab TU/e).
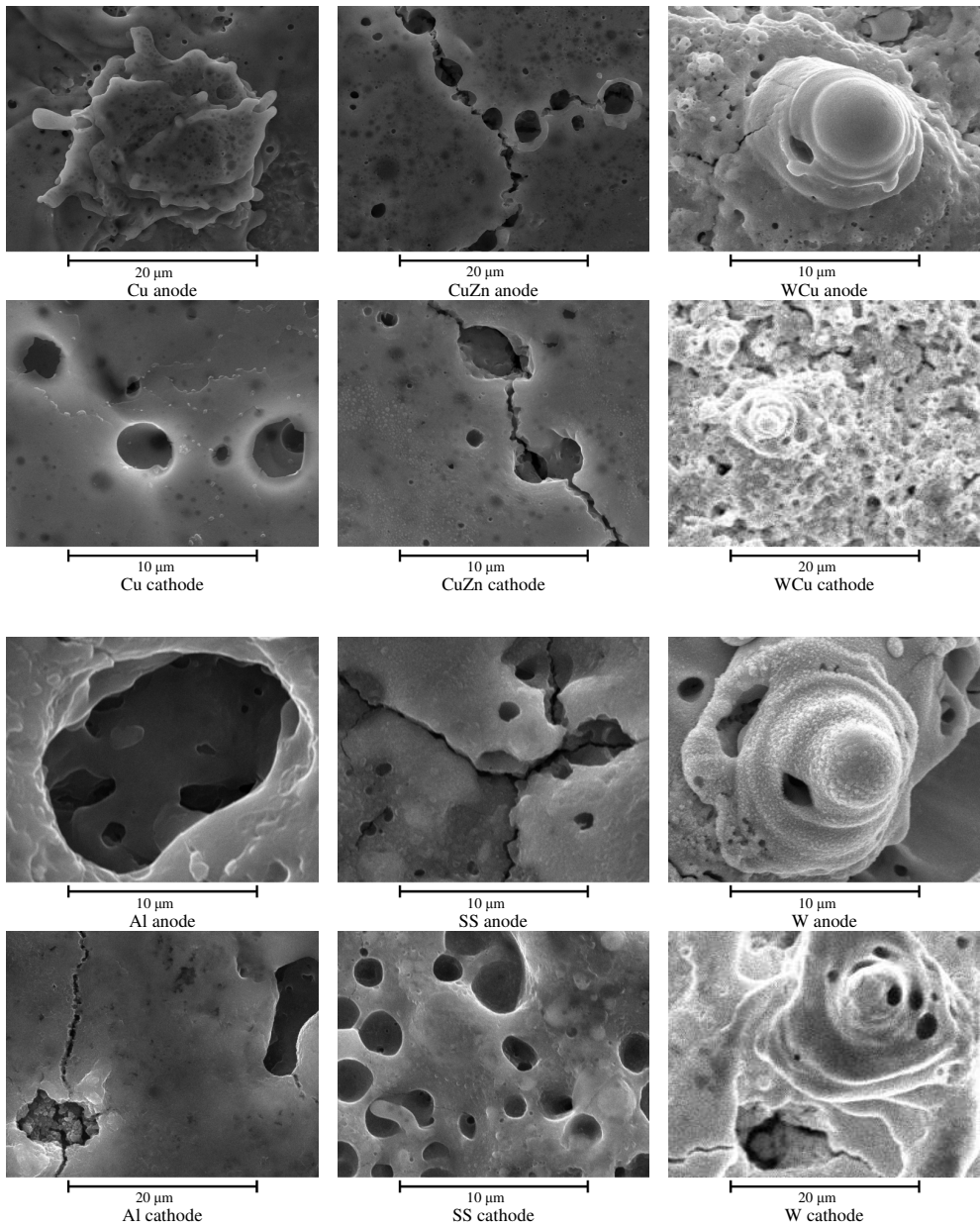
Figure 4.25: Detail SEM images of the anode and cathode surfaces after $65 \cdot 10^6$ shots (SEM imaging facilitated by Multi-scale lab TU/e).

Figure 4.26: Modeled (analytical) evaporated volume per pulse as a function of the spark radius for multiple electrode materials. V_{eff} is assumed to be 10 V.

The poor thermal conductivity of stainless steel seems to dominate for larger radiuses, resulting then in higher erosion rates for this material. W and WCu should perform the best according to the model. The spark quenches after 25 μs, Figure 4.27 shows the time that the vaporization occurs as a function of the spark diameter. The plateaus are caused by the oscillations in the current between 200 ns and 25 μs. The conduction power is larger than the input power at some point during the damped oscillation of the current, resulting in material dependent vaporization times. This Figure suggests that it is not always required to quench the spark gap as fast as possible to limit electrode erosion.

Now we apply the numerical model to estimate more accurate erosion rates. The initial spark volume V_1 according to Equation 4.22 is calculated with following parameters, d_g=3.2 mm, and $p_0 = 3.4 \cdot 10^5$ Pa. The energy which is deposited in the spark is estimated from spark resistance measurements (see Figure 4.8b) and the measured current waveform, 0.15 Ω results in approximately E=0.1 J energy deposition. Taking into account the fast expanding radius (Equation 4.23), the initial spark radius of 273 μm is already too large to obtain any erosion compared to the results in Figure 4.26. Obviously there is an error in the initial radius calculation because not all energy is injected in the spark at t=0 in reality. Therefore we choose the radius to be initially zero. The radius expands according to Equation 4.23, and stops expanding when the radius is 1.6 mm (Equation 4.26) after 852 ns. The evaporated volume per pulse (calculated with the numerical model) is calculated as a function of the power input factor V_{eff} [V]. The results of the total evaporated volume per pulse is shown in Figure 4.28. If we assume that vaporization is the main erosion mechanism and would assume that V_{eff} is approximately equal for all materials, than we can attempt fitting of the experimental data. The actual measured total erosion volume per pulse (for anode and cathode) is indicated in Figure 4.28 on top of the lines of the corresponding materials. According to the model, it is immediately clear that evaporation cannot be the only mechanism. Evaporation of 4-6 pL
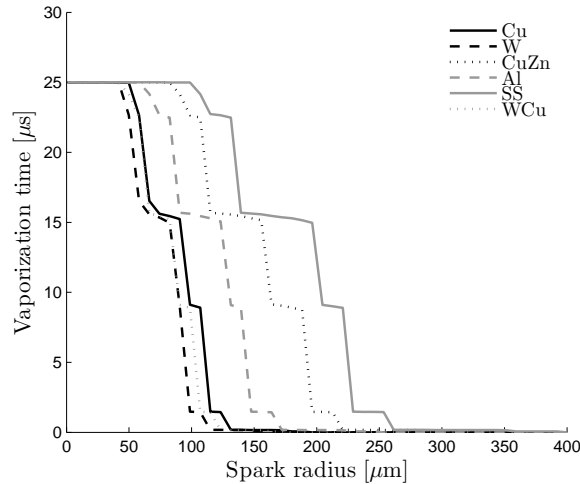
Figure 4.27: Modeled (analytical) vaporization time as a function of the spark radius for multiple electrode materials. V_{eff} is assumed to be 10 V.

Tungsten (W) (V_{eff}=55–60V) would lead to massive erosion of stainless steel, Al and CuZn. A deviation of a factor of five in the effective fall voltage is also unlikely.

A second approach is to consider the ejected volume per pulse. The maximum molten volume per pulse as a function of V_{eff} is shown in Figure 4.29. At least V_{eff}=22–25 V is required to obtain surface melting of W and WCu. This would still lead to massive erosion of stainless steel, Al and CuZn. The SEM images show obvious surface melting of Cu and only puncture formation (localized melting/boiling) for WCu and W. According to the model V_{eff} should be between 13 and 22 to explain these images.

Surface melting of an aluminium electrode is illustrated by Figure 4.30 (V_{eff}=11.4 V). The images show the heat conduction into an aluminium electrode surface for multiple moments in time. The magenta lines in images 4.30a–h represent the interface between molten and solid material. The molten pool develops rapidly, making liquid ejection likely during the strong initial channel expansion. The molten material is solidified again after 200 ns according to the model.

Since erosion is apparently composed of evaporation and ejection we consider Equation 4.9 to fit the erosion results. The coefficients of rem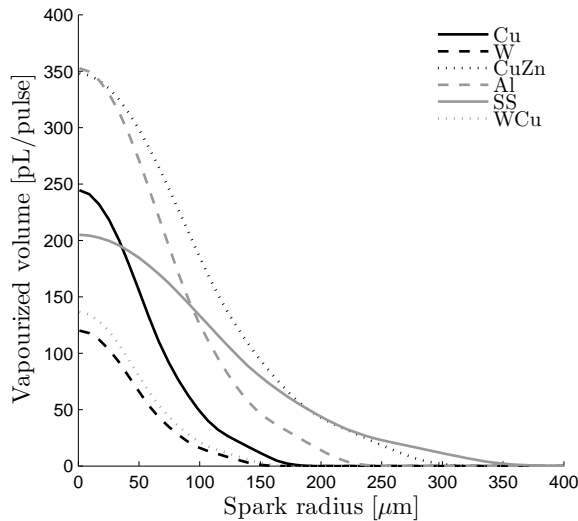oval k_v is assumed to be 1 (the evaporated volume is completely removed) and k_l is a fit factor which is equal for all materials. A least squares fit procedure according to Equation 4.44 is applied to minimize the error with the measured data, where i is an index for the electrode material, 6 in total.

$$E(k_l, V_{eff}) = \sum_{i=1}^{6} \left(V_v(V_{eff}, i) + k_l \widehat{V}_l(V_{eff}, i) - V_{measured}(i) \right)^2 \tag{4.44}$$

The minimum error results in V_{eff}=11.4 V and k_l= 3 % for the anode and V_{eff}=10.1 V and k_l= 3 % for the cathode. The modeled and measured results are shown in Table 4.4.

The model apparently contains deficiencies since large errors can be observed for W and WCu. A reason for the superior performance of copper electrodes can however be explained
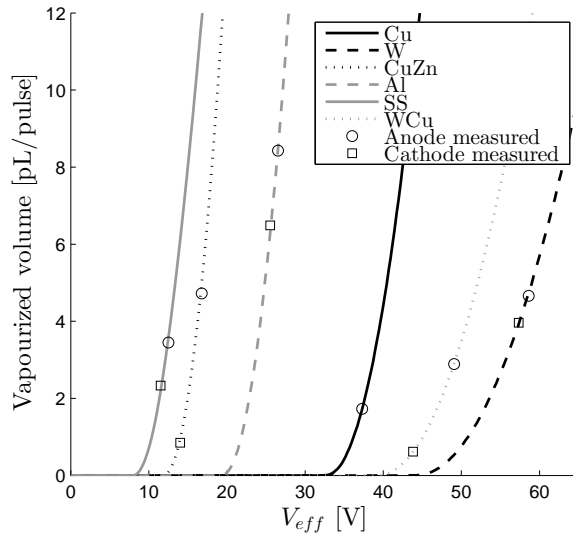
Figure 4.28: Modeled (numerical) evaporated volume per pulse as a function of V_{fall} for multiple electrode materials. The actual measured total erosion volume per pulse (for anode and cathode) is indicated in the figure to estimate the V_{eff} value for each material.
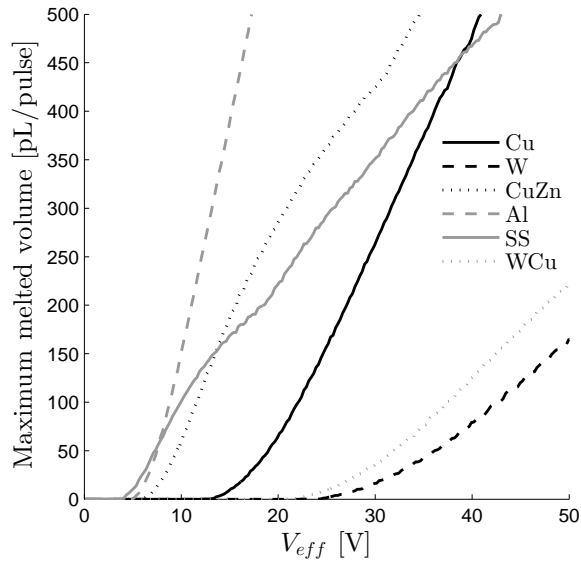
Figure 4.29: Modeled (numerical) maximum molten volume per pulse as a function of V_{eff} for multiple electrode materials.
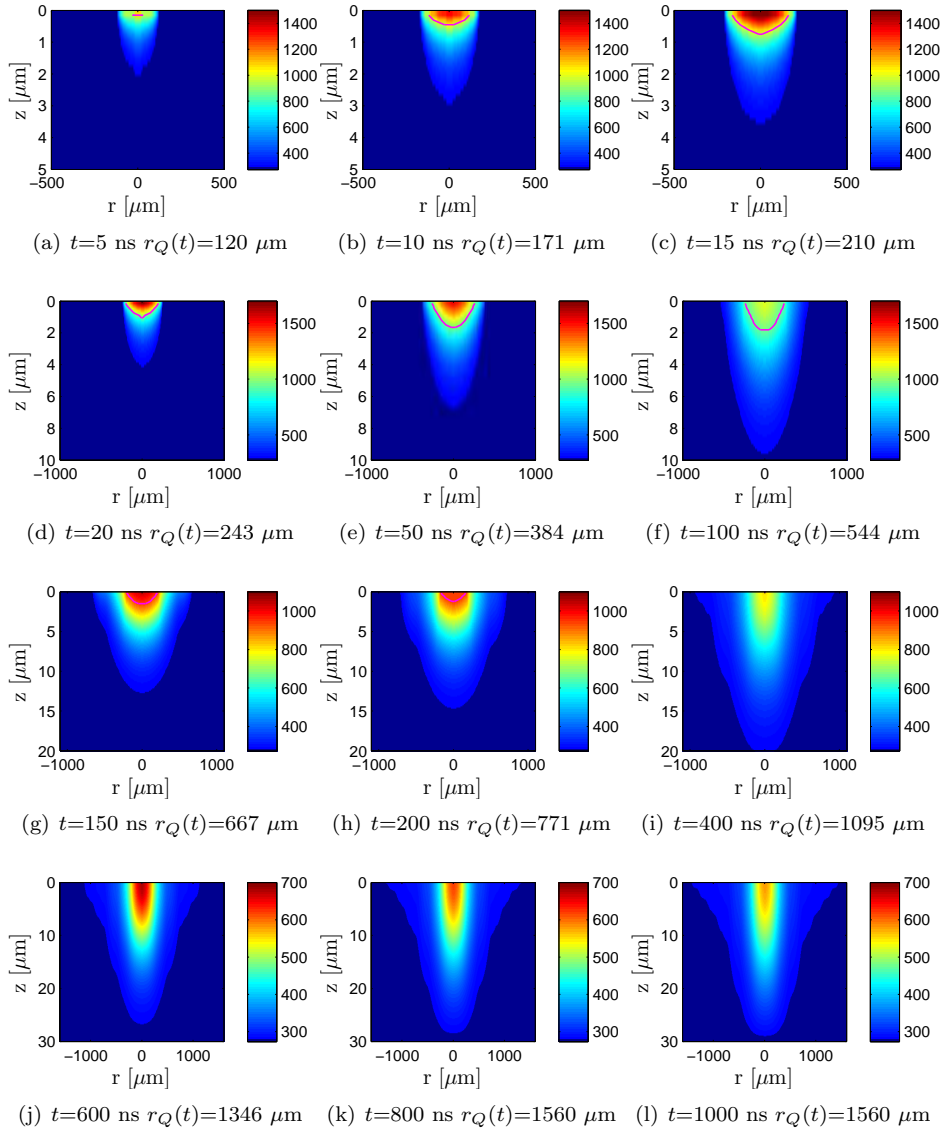
Figure 4.30: Numerical calculated thermal images (rz–plane) of an aluminium electrode with $V_{eff} = 11.4$ V. The bar on the right of the images relates colors to temperatures. The magenta lines in a–h represents the interface between molten and solid material.

Table 4.4: Modeled (numerical) and measured electrode erosion. V_{eff}=11.4 V and k_l= 3 % for the anode and V_{eff}=10.1 V and k_l= 3 % for the cathode

Material		Measured	Modeled V_v	Modeled k_lV_l	Error
Cu	A	1.73	0	0	-1.73
W	A	4.66	0	0	-4.66
CuZn	A	4.72	0	2.9	-1.82
Al	A	8.43	0	6.4	-2.03
SS	A	3.45	2.0	3.7	2.25
WCu	A	2.89	0	0	-2.89
Cu	C	-0.03	0	0	0.03
W	C	3.96	0	0	-3.96
CuZn	C	0.85	0	1.9	1.05
Al	C	6.49	0	4.7	-1.79
SS	C	2.33	0.8	3.1	-1.57
WCu	C	0.62	0	0	-0.62

by the model results. W and WCu are sintered materials which are more brittle (also shown by surface cracks in the SEM images). They possibly behave differently and suffer from solid ejection due the strong shockwaves in the discharge. This was also proven during recovery experiments when flakes of tungsten crumbled from the surface resulting in total recovery failure. These effects cannot be incorporated in the thermal model.

4.4   Conclusions

The required flow through the spark gap as a function of pulse repetition rate is similar for brass, copper and copper/tungsten electrodes. Approximately 20.1 Nm^3/h (7 m^3/h, 3.4 bar) is needed to fully recover 95 % of all switching cycles at a repetition rate of 800 Hz. Slightly more flow is required with the aluminium electrodes. The stainless steel electrode spark gap had a poor recovery above 500 Hz. Possibly the poor heat conduction of the material affects cooling down of the electrode surface and gas in the gap. Reduction of the gap volume by a factor of 1.8 reduces the flow requirement by a factor of 1.5-1.6 due to the this reduced diameter. The reduced diameter reduces the power consumption by the purging system to 14 % of the transferred power by the spark gap at a repetition rate of 800 Hz.

The spark gap resistance is typically between 0.1 and 0.25 Ω for air, N$_2$ and N$_2$/H$_2$ (95/5) mixture with electrode distances varying between 2.2 and 4.2 mm. The lowest resistance is obtained with N$_2$/H$_2$ followed by N$_2$ and air. The minimum voltage rise times for gap distances 2.2, 3.2 and 4.2 mm are respectively 3 ns, 3.7 ns and 5 ns. The addition of the H$_2$ seems to improve the switching speed for the 2.2 and 3.2 mm gap distance. A smaller electrode diameter increases the recovery voltage with the same gap flow under all circumstances. The addition of hydrogen increases the recovery voltage at repetition rates beyond 2500 Hz for the 40 and 34.5 mm electrode. Generally, tipping points can be observed where the recovery voltage suddenly decreases rapidly for higher repetition rates. Repetition rates beyond the tipping point are accompanied by large jitter in the breakdown voltage. Also, plateaus can be

observed where the recovery voltage becomes independent of the repetition rate. The height of the plateaus can be lifted by the increasing the flow. The overall best recovery result was obtained with 10 m^3/h N$_2$/H$_2$ and the 29.5 mm electrode. The spark gap was able to operate up to 1 kHz in the triggered mode and the recovery voltage was 62 % at 5 kHz repetition rate during pre-fire operation.

Erosion rates of the cathodes were between -0.08 and 15.1 nL/C after 65·10^6 shots. Erosion rates of the anodes were between 4 and 19.6 nL/C. The materials performance ranks as follows: copper > brass > copper/tungsten > stainless steel > tungsten > aluminium. Although the anode erosion of brass and copper/tungsten is higher than stainless steel and tungsten, the cathode erosion is much lower. The pure copper cathode became slightly heavier and the copper anode had substantial less erosion than the other copper alloy anodes. Copper can apparently be transported from the anode and partially deposited on cathode in a nitrogen environment and is therefore the preferred electrode material in this application. Erosion of the length of the anode is estimated to be 165 μm per day at 800 Hz pulse repetition rate. SEM images show similar molten surfaces for aluminium and copper. The copper electrodes seem to have more surface punctures than the aluminium electrodes. Sizes of punctures are in the range of several μm for all materials. Brass electrodes show surface punctures mainly along the grain boundaries, the remaining surface appears to be smooth. The overal surface of the tungsten and copper/tungsten electrodes is rough. Protrusions which grow on the surface have typical sizes of 5-10 μm.

An analytical and numerical model both based on the heat equation have been developed. The 1D analytical model assumes a static spark radius, and estimates evaporation at a boiling surface. The 2D (rz-plane) numerical thermal model features a more realistic spark radius which expands according to the trajectory of a shockwave. Time and space resolved heating of the electrode can be simulated, including evaporation and melting. The power input of the models is the product of the measured discharge current and estimated V_{eff} (effective fall voltage) near the electrode. Comparison between modeled and experimental data showed that the spark radius should be initially very small. A radius larger than 396 μm with 10 V effective fall voltage results in zero erosion. The analytical model indicates that evaporation cannot be the main erosion mechanism and that ejection of liquid material is likely. A liquid pool in the surface rapidly (nanoseconds) develops and solidifies after 200 ns for aluminium. A least square fit of modeled an measured data results in V_{eff}=11.4 V and k_l= 3 % for the anode and V_{eff}=10.1 V and k_l= 3 % for the cathode, where k_l is the liquid ejection coefficient. Zero erosion is then estimated for Cu, W and WCu. The model apparently contains deficiencies since large errors can be observed. The superior performance of copper can however be explained by the model results. W and WCu are sintered materials which are more brittle (also shown by surface cracks in the SEM images). They possibly behave differently and suffer from solid ejection due the strong shockwaves in the discharge.

Energizing large corona reactors

Abstract

Industrial application of nanosecond (ns) pulsed corona technology for air purification requires high volume, high power plasma reactors. Cylinder-wire type reactors require multiple cylinders to meet these demands. Variations in pulse waveforms per cylinder, misalignment of wires and jitter in streamer inception could lead to an uneven energy distribution over the cylinders. Nanosecond ICCD imaging is applied to the demonstrator reactor to study streamer inception and propagation of the streamer plasma simultaneously in sixteen cylinders.

The reactor cylinders act like coaxial transmission lines wherein high voltage pulses propagate with the speed of light. Interactions between plasma generation and reflection behavior inside the reactor are expected and therefore investigated. A 4.5 m long corona reactor is constructed and equipped with voltage and current sensors at multiple positions along the reactor length. A lumped element SPICE model is developed to simulate the reflection behavior. Strong reflections at the end of the reactor are observed for pulse rise times which are shorter than the transient time of the reactor. Plasma generation and energy distribution in the reactor, as well as impedance matching between source and reactor is affected by these reflections. The role of cylinder length, input voltage and rise time is investigated.

5.1 Introduction

Typically two reactor shapes are suitable to create pulsed corona plasma in a large volume, wire-plate or wire-cylinder. Wire-plate reactors consist of rectangular duct channels with multiple wires or electrodes which are suspended side by side and equally spaced towards the wall of the duct [94] [95]. They can be applied for large scale systems but they have large (dead) volume areas where there is no discharge activity. Strong turbulent mixing in the

---

reactor should be present to ensure proper plasma processing. Cylinder-wire type reactors with axial flow are preferred because they have no dead spaces and offer a more uniform electric field and streamer plasma field than wire plate reactors [96] [97]. A design trade-off has to be made between the diameter of the reactor cylinder, diameter of the wire and pulse parameters (peak voltage, width, rise time) produced by the pulse source. Also the reactor should have a large plasma volume for large flow handling and a low pressure drop to reduce ventilation power. Multiple parallel wire-cylinders with axial gas flow can be used for industrial applications to meet these requirements. The length of the reactor cylinders is an interesting design parameter from an electrical engineering point of view. Electric pulses propagate with the speed of light through the reactor. Interesting interactions are expected when the rise time and width of the pulse are in the same order of magnitude as the transient time of the reactor. In such situations inception of the plasma in the reactor will be space and time dependent. But because propagation of the streamers from the wire to the cylinder causes an impedance alteration, the reflection behavior and energy distribution in the reactor will be affected. In addition problems can arise when multiple cylinders have to be powered by a single nanosecond pulse source. It is a challenge to create a compact connection from the source to all cylinders. Misalignment of wires, jitter in streamer inception and asymmetric connections could possibly result in an uneven energy distribution inside the cylinder and between multiple cylinders.

Experimental investigations are performed to gain insight in the pulse reflection behavior in large scale systems. ICCD imaging is applied to study propagation of the discharges simultaneously in the sixteen cylinder DC-biased pulsed corona reactor of the demonstrator. A separate setup was designed and built for investigation of the pulse reflection behavior and energy distribution inside a 4.5 m long corona reactor. A lumped element SPICE model is developed to simulate the reflection behavior. The effect on source–reactor impedance matching and energy transfer efficiency from the source to the reactor is also investigated.

5.2 Experimental setups

5.2.1 Optical characterization of the multiple cylinder reactor setup

ICCD (Intensified Charge Coupled Device) imaging enables capturing of images with sub-nanosecond gating time. Development of the streamers can be studied time and space resolved. A micro channel plate photo multiplier (MCP) in the camera creates an optical amplification up to 10^6 to enable these extreme gating times. The reactor and pulse source of the demonstrator setup are used for the optical characterization experiments. System characteristics are available in Chapter 2.

Accurate triggering of the camera in advance is required because the camera has an internal delay of 60 ns before the gate opens. Usually there is a large jitter on the fire moment of the spark gap due to the stochastic breakdown behavior and low dV/dt on the trigger electrode delivered by the RLC trigger circuit. The RLC trigger circuit is replaced by the 30 kV trigger unit (see Section 2.2.3.2) to trigger the spark gap for accurate synchronization of the actual pulse generation and enabling the gate of the ICCD camera. The reactor voltage and current waveforms are simultaneously captured with the gating signal of the camera (see Figure 5.1).

The camera is a 4Picos-DIG from Stanford Optics [98]. It has a resolution of 780x580 pixels, and a minimum exposure time of 200 ps. A Sigma 70-300 F4-5.6 DG MACRO lens is
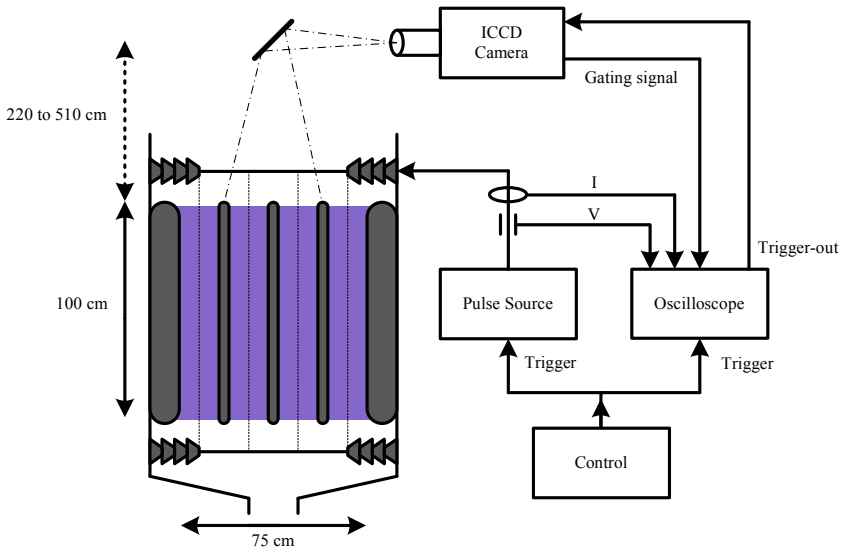
Figure 5.1: Schematic overview of the 1 m multiple cylinder reactor setup for optical characterization.

mounted to the device. The camera is placed horizontally in an EMC cabinet and mounted on top of a frame which is placed on the edge of the corona reactor, see Figure 5.1. The camera is able to view vertically in the reactor via a 45 angled mirror. The total optical path from the camera to the edge of the cylinders is 260 cm (four cylinder view), and 550 cm (sixteen cylinder view).

5.2.1.1 Camera synchronization

After triggering the camera, it has a minimum internal delay of 60 ns before the Micro Channel Plate (MCP) detector of the device is energized and the gate is opened. The streamer discharges in the reactor develop in less than 80 ns after the voltage pulse reaches the reactor so the camera needs to be triggered well in advance of that. The whole sequence starts at the control circuit. This unit triggers simultaneously the spark gap trigger-unit and oscilloscope (via trigger input), see Figure 5.1. The camera is directly triggered by the oscilloscope with an additional delay of less than 50 ns. It then takes up to 300–500 ns randomly before the spark gap fires. There is some jitter in the moment that the spark gap fires because the voltage rate of rise on the trigger pin is limited. The internal delay of the camera is set to a desired value to enable the gate at the desired moment. The V&I waveforms and actual gating signal of the camera are captured simultaneously by the oscilloscope. The setup is operated in burst mode to obtain 50 images of 50 successive pulses. This enables selection of images which are captured at the desired moment. The frame rate of the camera is much faster than the triggering rate and data storage speed of the oscilloscope. So the slower unit needs to be the master, the camera is slave. This will ensure synchronization of data at all time.
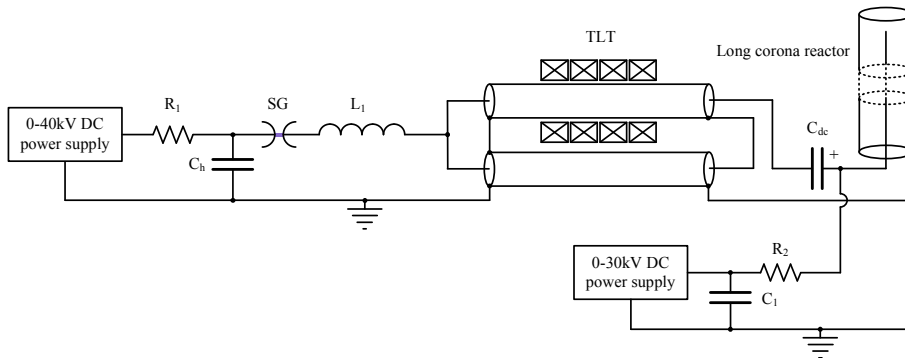
Figure 5.2: Power modulator of the long corona reactor. L_1 is optionally installed to adjust the rise time, C_{dc} (and C_{dc} charging circuit) is optionally installed to provide a DC-bias.

5.2.2   4.5 m single cylinder reactor

The experimental setup consists of a 4.5 m long corona reactor and a power modulator which is a very basic version of the unit in the demonstrator. The objective was to build a single tube reactor which is as long as possible within the practical limits. It should have the same cylinder diameter as in the demonstrator so the streamer propagation will be comparable in the 4.5 m reactor.

5.2.2.1   Pulse generation

The schematics of the power modulator are shown in Figure 5.2. A DC high voltage supply charges high voltage capacitor C_h via a 12 MΩ resistor to 10-35 kV. The spark gap has an adjustable electrode distance and can be set to fire without triggering at a certain voltage. The repetition rate is limited to approximately 10 Hz. C_h (typical value between 2 and 8 nF) is discharged via a two stage TLT into the reactor. The TLT consists of two 50 Ω RG-218 high voltage coaxial cables. Metglass magnetic cores are stacked around the upper cable to increase the secondary mode impedance. The input and output of the TLT are respectively 25 and 100 Ω. The rise time of the pulse can be adjusted by using different inductance values for L_1. The parasitic circuit inductance is approximately 275 nH which limits the pulse rise time to 11.5 ns.

5.2.2.2   DC-bias circuit

An additional coupling capacitor C_{dc} and power supply can be installed to create a DC-bias voltage on the corona wire. The DC-bias improves the energy transfer efficiency between source and reactor, increases pulse energy and enables electrostatic precipitation of particulate matter in the process gas [99] [100] [101]. C_{dc} is charged via resistor R_1 (12 MΩ) which forms a low pass filter with C_1 (2 nF) to protect the DC power supply for the high voltage pulse. A DC charging path to ground is available via the inner conductors of the upper and lower line and outer conductor of the upper line. The coupling capacitor should have a minimum

value depending on the DC-bias voltage level and the amount of charge which is injected by the TLT during pulse generation. The charge in C_{dc} at the beginning of the pulse should be larger than the total charge which is transferred via the TLT ($Q_{TLT_{out}}$) to prevent negative undershoot of the voltage on C_{dc} (already discussed in Section 2.2.5). $Q_{TLT_{out}} = C_h V_{Ch}/2$ since the output current is halved by the TLT. The minimum value of C_{dc} can be calculated by Equation 5.1 [33].

$$C_{dc} > \frac{C_h}{2V_{Cdc}}V_{Ch} \tag{5.1}$$

This criterion prevents that energy from C_h is transferred to C_{dc} but a secondary consideration is the output impedance of the source. The coupling capacitor discharges as the pulse current flows resulting in a decreasing voltage on C_{dc}. It behaves like a time-dependent impedance which affects the output impedance of the source. Equation 5.2 describes the series impedance of capacitor C_{dc}, where V_{Cdc} is the initial charge voltage and I_{out} the output current of the TLT.

$$Z_{Cdc}(t) = \frac{-V_{Cdc}(0) + \frac{1}{C_{dc}}\int_0^t I_{out}(\tau)d\tau}{I_{out}(t)} \tag{5.2}$$

The output current of a matched TLT which discharges C_h can be described by Equation 5.3 (already discussed in Section 2.2.4), where Z_{TLT} is the output impedance of the TLT. The input impedance of the TLT is 4 times lower than the output impedance.

$$I_{out}(t) = \frac{2V_{Ch}(0)}{Z_{TLT}}e^{(\frac{-4t}{Z_{TLT}C_h})} \tag{5.3}$$

Z_{Cdc} is connected in series with the reactor. Equation 5.4 is valid under the assumption of a matched TLT ($Z_{TLT} = Z_{Cdc} + R_{reactor}$). An unmatched reactor will result in reflections which makes Equation 5.3 invalid. Z_{Cdc} will have a constant value under the condition that $C_{dc} = \frac{V_{Ch}C_h}{2V_{Cdc}}$, see Equation 5.5. The impedance is negative because the coupling capacitor delivers energy if $C_{dc} \geq \frac{V_{Ch}C_h}{2V_{Cdc}}$.

$$Z_{Cdc}(t) = \left(\frac{C_h Z_{TLT}}{4C_{dc}} - \frac{V_{Cdc}(0)Z_{TLT}}{2V_{Ch}(0)}\right)e^{(\frac{4t}{Z_{TLT}C_h})} - \frac{C_h Z_{TLT}}{4C_{dc}} \tag{5.4}$$

$$Z_{Cdc} = -\frac{C_h Z_{TLT}}{4C_{dc}}, \quad C_{dc} = \frac{V_{Ch}(0)C_h}{2V_{Cdc}(0)} \tag{5.5}$$

Z_{TLT} and Z_{Cdc} are part of the source circuit. The reactor impedance (or output impedance of the source) can be described by Equation 5.6. Note that the reactor impedance should vary in time under the condition that $C_{dc} \neq \frac{V_{Ch}C_h}{2V_{Cdc}}$ to keep the TLT matched.

$$R_{reactor}(t) = Z_{TLT} - Z_{Cdc}(t) \tag{5.6}$$

The value of C_h and charging voltage during the DC-bias experiments are respectively 4 nF and 30 kV. The inception voltage in the reactor is designed to be 18 kV (will be discussed later on) so DC-bias voltages near this value are interesting for investigation. 6 nF capacitance is initially chosen for C_{dc} to allow DC-bias voltages as low as 10 kV without negative undershoot.
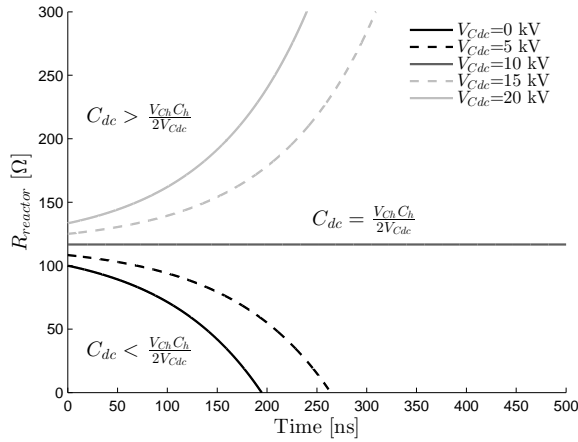
Figure 5.3: Matched source output impedance as a function of time for multiple DC-bias levels.

The theocratical effect on the source/reactor impedance $R_{reactor}$ (Equation 5.6) is shown in Figure 5.3 (with Z_{TLT}=100 Ω). The output impedance is shown to increase for DC-bias voltages higher than 10 kV.

The amount of energy per pulse delivered by C_h and C_{dc} to the reactor can be calculated by equations 5.7 and 5.8 (already discussed in Chapter 2). C_{dc} is discharged by the charge which is injected by the TLT: $Q_{Cdc} = Q_{Cdc} - Q_{TLT_{out}} = C_{Cdc}V_{Cdc} - C_hV_{Ch}/2$. The residual voltage and energy in C_{dc} after the pulse can thus be calculated. The difference with the initial energy in $C_{dc}(0)$ results in Equation 5.8.

$$E_{Ch} = \frac{1}{2}C_hV_{Ch}{}^2 \tag{5.7}$$

$$E_{Cdc} = V_{Cdc}\frac{C_hV_{Ch}}{2} - \frac{C_h{}^2V_{Ch}{}^2}{8C_{dc}} \tag{5.8}$$

The amount of energy delivered by C_{dc} scales linearly with the DC-bias voltage C_{Cdc} and will be negative (C_{dc} will be charged) if Equation 5.1 is not satisfied.

5.2.2.3 Long corona reactor

The outside diameter of the reactor was chosen to be the same as in the demonstrator (150 mm). Streamer propagation will be comparable as in the imaging experiments. A schematic overview of the reactor is shown in figure 5.4. The reactor consists of three 1.5 m sections, and a small 30 cm section at the end. Flanges equipped with sensors are installed between each interface of two sections to measure the voltage on and current in the corona wire. The flanges have holes to allow some gas flow through the reactor. A field control element is connected to the wire at the end of the reactor. An additional load resistor can be installed at the end of the field control element during the calibration procedure of the sensors. The coupling capacitor
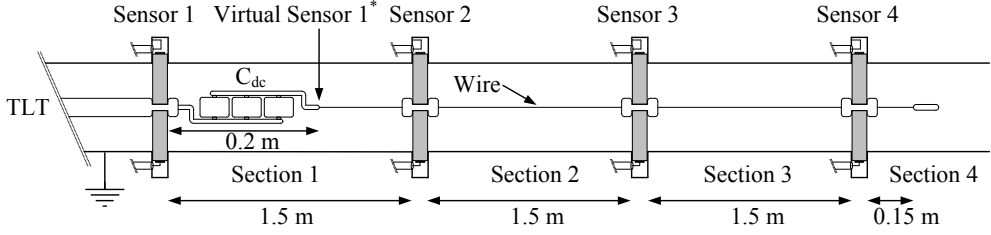
Figure 5.4: Schematic overview of the 4.5 m long corona reactor. Sensor 1^* is virtual sensor position which is used to indicate the (calculated) voltage on the reactor wire when C_{dc} is installed.

C_{dc} is placed inside the reactor behind the first sensor flange during DC-bias experiments. The corona wire will then be 20 cm shorter in the first reactor section.

The diameter of the wire needs to be chosen wisely because it affects not only the field strength in te reactor but also the characteristic impedance and attenuation if the reactor is considered as a transmission line. For long reactors where the transient time of the reactor is similar to the rise time or width of the pulse is the transmission line behavior interesting to investigate. The transient time of a 4.65 meter reactor would be 15.5 ns (in air, 3.33 m/s). The vacuum impedance of this system will affect the initial impedance matching with the output of the source. The wire of the reactor needs to be stainless steel for proper chemical corrosion resistance. Drawback of this material is the poor conductivity, approximately 40 times less than copper. Attenuation can be significant for high frequencies. The field strength around the wire needs to be as large as possible to reach the inception field strength of the plasma (typically 30 kV/cm) with a relative low voltage on the wire. A compromise has to be made to dimension the wire diameter.

The vacuum impedance of the reactor can be calculated by Equation 5.9, where d_{wire} and d_{cyl} are the wire and reactor cylinder diameter. The maximum electric field at the edge of the wire (E_{max}) can be calculated by Equation 5.10, where $V_{reactor}$ is the voltage on the wire.

$$Z_{reactor} = \frac{1}{2\pi} \sqrt{\frac{\mu_0}{\epsilon_0}} \ln \left(\frac{d_{cyl}}{d_{wire}} \right) \tag{5.9}$$

$$E_{max} = \frac{2V_{reactor}}{d_{wire} ln(\frac{d_{cyl}}{d_{wire}})} \tag{5.10}$$

The attenuation of the reactor as a transmission line (no corona discharges) for high frequencies can be calculated by Equation 5.11 [102] (frequency domain), where L_e is the distributed external inductance (Equation 5.14), C the distributed capacitance (Equation 5.13) and l the length. The distributed conductance G of the dielectric (air) is negligible and omitted in the equation.

$$V_{out} = V_{in} e^{-l\sqrt{((1+j)\lambda\sqrt{\omega}+j\omega L_e)j\omega C}} \tag{5.11}$$

$$\lambda = \frac{1}{\pi} \left(\frac{1}{d_{cyl}} + \frac{1}{d_{wire}} \right) \sqrt{\frac{\mu}{2\sigma}} \tag{5.12}$$

135
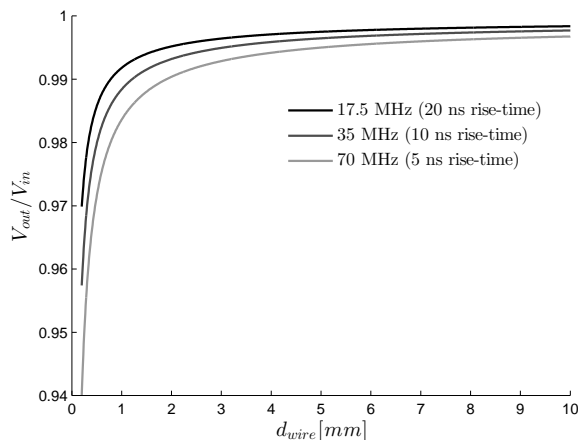
Figure 5.5: Reactor attenuation at 4.5 m for multiple wire diameters and frequencies (calculated using Equation 5.11).

$$C = 2\pi\epsilon_0 ln\left(\frac{d_{cyl}}{d_{wire}}\right) \tag{5.13}$$

$$L_e = \frac{\mu_0}{2\pi} ln\left(\frac{d_{cyl}}{d_{wire}}\right) \tag{5.14}$$

The attenuation at the end of the 4.5 m reactor for multiple wire diameters and frequencies is shown in Figure 5.5. The bandwidth for a pulse with rise time t_r can be approximated by: $BW = 0.35/t_r$. Only the attenuation for very small wire diameters appears to be significant.

In the following section, the impedance and maximum E-field will be considered. The minimum voltage needed to initiate discharges ($E_{max} =$30 kV/cm) as a function of the wire diameter is shown in Figure 5.6. The reactor impedance is plotted in the same figure. The pulse source used for the setup has an output impedance of 100 Ω and maximum output voltage of approximately 70 kV. It is clear that the reactor impedance cannot be matched with this pulse source. The inception voltage would be too high to create corona discharges. A 3 mm wire is finally chosen because it has a reasonably low impedance (238 Ω) and 18 kV inception voltage. The primary objective of the experiment is characterizing the energy distribution of the plasma in the reactor and secondary optimal impedance matching and energy transfer efficiency.

5.2.2.4 Corona reactor sensors

The DI measurement system [33,37] is again preferred because it can be completely integrated in the reactor (see Figure 5.7) without interrupting the coaxial structure. Capacitive voltage sensors (D-dot sensors) as well as a single winding B-dot sensors are installed in the interfaces of the corona reactor sections. The functioning of the measurement system is already described in detail in Section 2.2.6. The voltage and current cannot be measured on the wire directly because of the corona discharge activity. The capacitance between wire and sensor is not
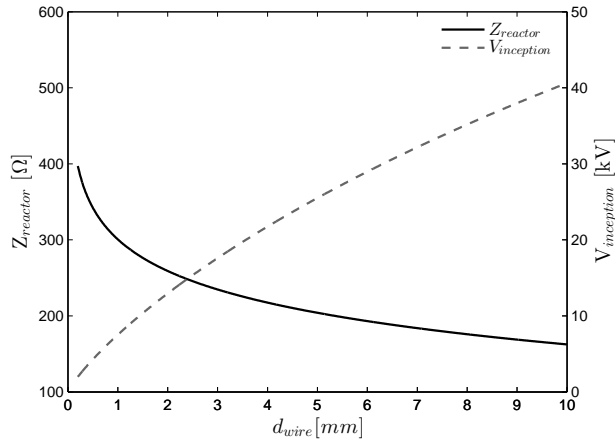
Figure 5.6: Reactor impedance and inception voltage as a function of wire diameter (calculated using Equation 5.9 and 5.10).
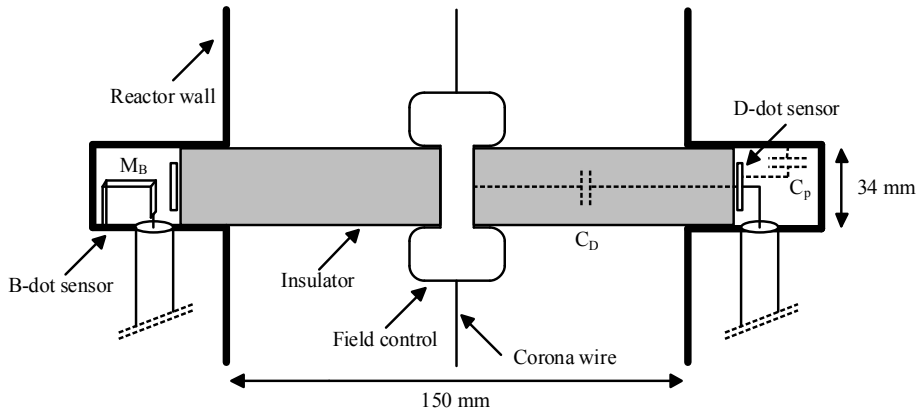
Figure 5.7: Schematic sensor flange design.

constant as the streamers propagate towards the sensor. Once crossed, streamer currents will add up to the sensor signals which would distort the actual waveform completely. In addition, a spark towards the sensor in case of reactor breakdown could damage measurement equipment. The B-field generated by the discharges would possibly have a small contribution to the sensor signal because of the small streamer currents. Plastic (PVC) insulator flanges with centered field control elements are installed at the section interfaces to create a corona discharge free area where the sensors can be installed. The D-dot sensor consists of a 2.5 cm high ring which is concentrically placed around the insulator flange which has a diameter of 220 mm. The B-dot sensor is square loop which is constructed from a copper strip. Four passive integrators are used to measure the voltage of current waveforms of two flanges simultaneously.
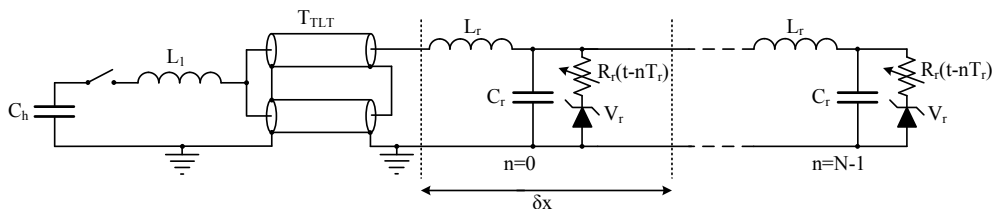
Figure 5.8: SPICE simulation model for the reactor and power supply. The lumped element reactor model consisting of N=16 sections.

Calibration of the sensor flanges is performed as follows. The attenuation of the reactor as a transmission line is negligible, so all sensors should have an equal response if the reactor is terminated with the correct load impedance (238 Ω) and if the voltage is below the inception voltage of the plasma. The voltage on and current through the load was measured with a North Star PVM-2 high voltage probe and a Pearson 6600 current monitor to calibrate all DI sensors. The amplitude of the pulse injected by the TLT needs to be as high as possible but below inception for sufficient sensor signal strength. Injection of a 12 kV 10 ns rise time pulse showed some minor reflections in the reactor, introducing some uncertainty in accuracy of the calibration. The rise time of the pulse was decreased to 50 ns to eliminate waveform distortion.

The DI measurement system is incapable of measuring DC voltages. The DC-bias voltage has to be added to the measured transient voltage when the DC-bias capacitor is installed, see Section 2.2.6. Capacitor C_{dc} is charged by a stabilized DC power supply so the charging voltage is known if the repetition rate is low enough to allow C_{dc} to be fully charged. The actual voltage on the wire at the TLT side of the reactor is calculated by equation 5.15, see Figure 5.4 where this position is indicated as "Virtual sensor 1". The real sensor 1 is in front of the coupling capacitor. This virtual sensor is referred to as $V_{sensor1}^{*}$ during DC-bias measurements.

$$V_{Sensor1}^{*}(t) = V_{Sensor1}(t) + V_{Cdc}(0) - \frac{1}{C_{dc}} \int_{0}^{t} I_{Sensor1}(\tau)d\tau \qquad (5.15)$$

5.3 Reactor SPICE model

A SPICE model has been developed to gain insight in the reflection behavior inside the reactor. Especially time and space resolved voltage gain and pulse edge distortion are interesting to estimate because they affect streamer development [2,4]. Huiskamp [4] developed a lumped element reactor model but only provided electrical measurements of the reactor input to compare modeled and measured data. The model has been adapted to obtain a better agreement between the theoretically predicted and the experimentally obtained data. The circuit model is shown in Figure 5.8.

The reactor model consists of N identical sections. Each section is composed of a distributed capacitance C_r, inductance L_r and resistance R_r. C_r-L_r form the coaxial transmission line of the reactor and R_r the resistance of the streamers in a section. According to Figure 5.5, the attenuation of the coaxial reactor structure is neglectable for the 3 mm reactor wire.

Lumped damping resistors are therefore omitted in the model. C_r and L_r can be calculated by Equation 5.16 and 5.17, where d_{cyl}, d_{wire} and l are respectively the diameter of the reactor cylinder, diameter of the reactor wire and length of the reactor. The inception voltage of the plasma is implemented by a series Zener diode with the distributed plasma resistance R_r. A plasma current can only flow through R_r if the voltage over the Zener diode is higher than the breakdown or Zener voltage of the device. The real plasma resistance is initially high but decreases as the streamers propagate towards the wall of the reactor cylinder. To simulate this effect, $R_r(t)$ is incorporated in the model as a time variable resistor (see Equation 5.18). A basic exponential function is chosen with an initial resistance R_0 which decays with time constant τ_r. R_0 is chosen an order of magnitude higher than the vacuum impedance of the reactor to prevent disturbance of this impedance. τ_r is a fit parameter, proper results were obtained with τ_r= 10 ns. The resistance saturates at the R_1 as the streamers cross the gap between the wire and the cylinder wall. The pulse reaches the reactor at $t = 0$ in the model, so the plasma resistance only starts decaying when the pulse reaches the corresponding section.

The section delay time T_r is defined as $T_r = T_d/N$, where T_d is the transient time of the reactor. The pulse propagation speed in the reactor (air) is 3.33 m/s resulting in T_d=15.5 ns. The rise time of the fastest pulse during our experiment was 11.5 ns. This is an order of magnitude longer than the section delay T_r if we choose N=16 sections. Therefore the model is sufficiently accurate, a larger number of sections only increases the accuracy slightly. The physical length of one model section corresponds to δx=0.29 m. The sensor positions in our long reactor setup correspond to sections n=0, n=5, n=10 and n=15 for respectively sensor 1, 2, 3 and 4.

Inductor L_1 limits the rise time and needs to be approximately 275 nH to simulate the 11.5 ns rise time pulse. The output impedance of the TLT is 100 Ω and the transient time of the TLT (T_{TLT}) is chosen equal to the TLT delay in the setup, approximately 20 ns.

$$C_r = \frac{2\pi\epsilon_0 l}{Nln(\frac{d_{cyl}}{d_{wire}})} \tag{5.16}$$

$$L_r = \frac{\mu_0 l}{2\pi N}ln\left(\frac{d_{cyl}}{d_{wire}}\right) \tag{5.17}$$

$$R_r(t) = \begin{cases} \frac{R_0}{N} & t < 0 \\ R_r(t) = \frac{1}{N}\left(R_1 + (R_0 - R_1)e^{\frac{-t}{\tau_r}}\right) & t \geq 0 \end{cases} \tag{5.18}$$

5.4   Results & discussion

5.4.1   Streamer inception and propagation

Images 2 to 9 of Figure 5.9 show images of streamer inception and propagation in the sixteen cylinders. An increasing view angle from the center outward causes some image and intensity distortion. The numbers with the vertical bars to the right of each picture relate colors to intensity. The black bars crossing the picture are the image of the wire suspension rack. V_{mcp} sets the gain of the cameras micro-channel plate detector. Experimental settings: lens 70 mm F/8, 10 Hz pulse repetition rate, (image 13) 0 kV DC-bias 4.1 J per pulse, (image 14) 10 kV

DC 5.7 J per pulse, (images 2-10, 12, 15 and 16) 20 kV DC 7.8 J per pulse, no flow through the reactor. Each image (2-9) is captured with an exposure time of 5 ns, the start time of the exposure is relative to the discharge inception of the first cylinders. Figure 5.10 shows the voltage and current waveforms which are linked to the images. The first images show inception in all cylinders within 9 ns. The streamers propagate to the wall of the cylinders within 80 ns without any significant deviations in the intensity and length of the discharges when comparing the cylinders mutually. The relatively slow initial streamer propagation (compared to the 9 ns inception window) ensures comparable streamer development of all reactor cylinders. Image 12 shows the center four cylinders near inception with 500 ps exposure. The inception of the discharges in these cylinders seems to be very synchronous. Misalignment of wires is believed to be the main cause of the inception window, also because the sequence of inception in the cylinders is reproducible. Image 11 shows the very weak DC corona discharges (no pulse) on four wires in the center. The last four images and image 10 are the result of exposures of the full pulse with different DC-bias levels. Although the intensities near the wall of the cylinder are weaker with lower DC-bias voltages, the discharges appear to be very similar when comparing the four cylinders mutually. The streamers do not seem to cross to the reactor wall fully with 0 kV DC-bias.

5.4.2 Electrical characterization of the 4.5 m corona reactor

Problems concerning proper energy distribution are expected when the rise time and width of the pulse are of the same order of magnitude as the transient time of the reactor. Inception of the plasma in the reactor will be space an time dependent. Propagation of the streamers from the wire to the cylinder causes an impedance alteration which affects the reflection behavior in the reactor. Local streamer propagation and number of streamers are dependent on local field strength and rate of rise of the pulse. The reflection behavior and impedance alteration are coupled making it difficult to predict the energy distribution for short pulses.

5.4.2.1 Comparison of modeled and measured data

Measured voltage waveforms of a fast rise time pulse with severe reflection behavior will first be shown. Comparison of modeled and measured data will subsequently clarify the consequences of the reflection behavior in the reactor. The minimum rise time of the voltage pulse which could be achieved with the setup was 11.5 ns (10-90%). Typical voltage and current waveform plots of the various sensors along the axial coordinate are shown in figures 5.11 and 5.12. The charging voltage of C_h is set to 31.2 kV and the additional inductor L_1 is omitted in the setup.

The transient time of the electromagnetic pulse traveling in the axial direction the reactor is 15.5 ns for three sections. The 5 ns transient time per section is clearly visible. The input voltage of the reactor is more than $2V_{Ch}$ due to the mismatch between TLT and reactor impedance. Voltage gain is also observed at the other sensors. The pulse is reflected at the end of the reactor causing a peak voltage of approximately 100 kV at sensor 3 and 4. The transient time of each section (5 ns) is initially clearly visible from the signals. The current at the end of the reactor (section 4) is relatively high for the 15 cm corona wire indicating high discharge activity due the high electric field at the end of the reactor. Reflections appearing at sensors 1,2 and 3 make the observed rise time seem longer. Only sensor 4 (last position) sees an almost undisturbed rise time, see figure 5.13 for a schematic overview of the reflection behavior.
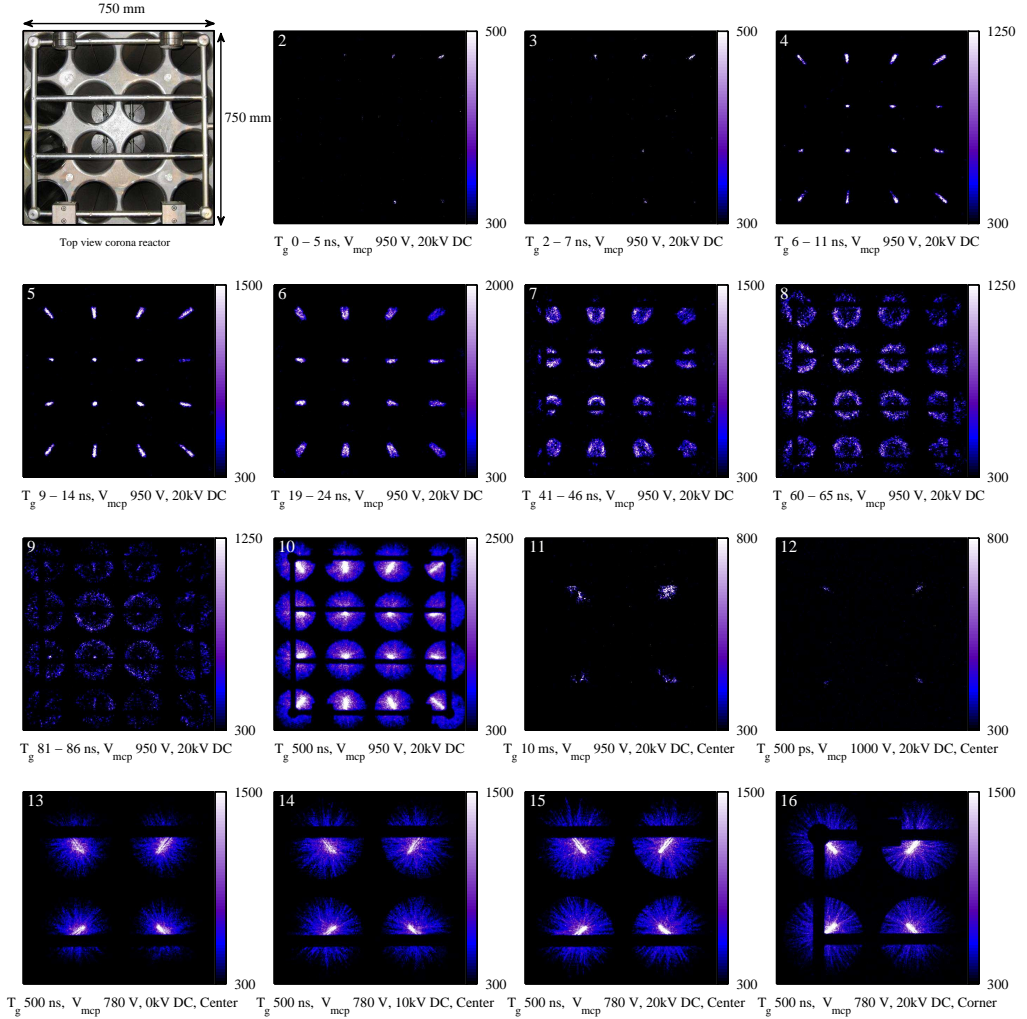
Figure 5.9: ICCD images of the sixteen cylinder pulsed corona reactor. The numbers with the vertical bars to the right of each picture relate colors to intensity. The black bars crossing the picture are the image of the wire suspension rack. Vmcp sets the gain of the cameras micro-channel plate detector. Experimental settings: lens 70 mm F/8, 10 Hz pulse repetition rate, (image 13) 0 kV DC 4.1 J per pulse, (image 14) 10kV DC 5.7 J per pulse, (images 2-10, 12, 15 and 16) 20 kV DC 7.8 J per pulse, no flow through the reactor.
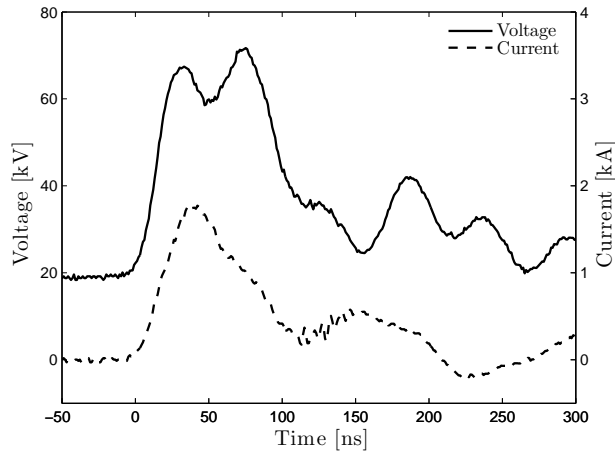
Figure 5.10: Demonstrator reactor voltage and current waveforms which are related to images 2–10 of Figure 5.9

The measured and modeled voltages and current waveforms for three R_1 values are shown in Figure 5.14 and 5.15. The rise time of the pulse is 11.5 ns. The modeled and measured voltage waveforms look quite similar. The rise time distortion, peak voltages and general shape of the pulse in the reactor can be estimated reasonably accurate. Even the quenching behavior of the plasma after 100–150 ns is predicted by model. Distinct reflections can still be observed at places where the modeled and measured waveforms deviate from each other. The peak voltage is best estimated with R_1=50 Ω, the falling edge of the pulse is better estimated with a higher value. The current waveforms in Figure 5.15 are less accurate but peak current and pulse rise time distortion are still similar.

The energy distribution in the reactor is defined as the energy dissipated per reactor section (between two sensor flanges) divided by the wire length of the section. Energy distribution simulations with the model show minor deviations of the energy distribution in the reactor, see Table 5.1. Only the last section shows a significant increased energy consumption due to the high voltage gain. The measured energy distribution is completely completely uneven. Apparently is streamer development and propagation significantly affected by the reflection behavior. The model is therefore not suitable for energy distribution estimations because the rise time and voltage dependant development of the streamers is not incorporated in the model.

Although the model is accurate for voltage waveform estimations, refitting of parameters (e.g. R_1 and τ_r) is required if the source voltage is increased because the streamer development also affects the impedance of the reactor significantly as will be shown in the following sections.

5.4.2.2 Effect of the rise time

Energy distribution in the reactor can possibly be improved if the reflection behavior is reduced by a slower rising pulse. The rise time of the pulse can be increased by choosing higher values

Figure 5.11: Typical voltage waveforms at multiple sensor positions of a 11.5 ns rise time pulse (3 sections, V_{Ch}=31.2 kV, C_h=4 nF).
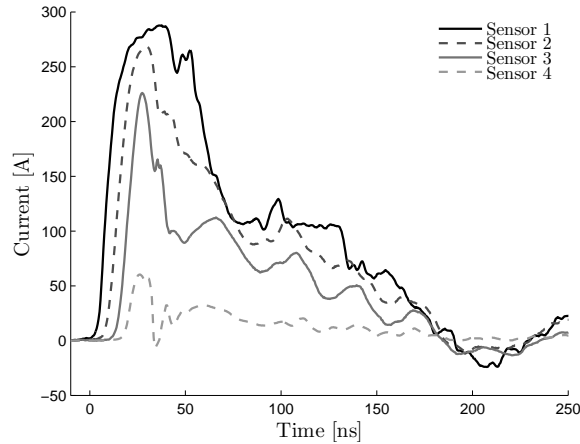
Figure 5.12: Typical current waveforms at multiple sensor positions of a 11.5 ns rise time pulse (3 sections, V_{Ch}=31.2 kV, C_h=4 nF).

for L_1. The resulting voltage waveforms at the four sensor positions are shown in Figure 5.16. The rise time of the pulse corresponds to sensor 4.

Peak voltages on sensor 2 to 4 decrease as the rise time increases. Clearly visible is also the variation in the rise time for the different sensor positions, slow at the beginning of the reactor and fast at the end. The rise times and peak voltages as a function of the rise time (sensor 4) are summarized in Figure 5.17. As already explained by Figure 5.13, the reflections result in an increase of the apparent rise time. Also the voltage increases after reflection due to a high impedance mismatch. The transition from TLT to reactor impedance complicates the reflection behavior apparently even more. Reflections in the TLT due to mismatch between

143
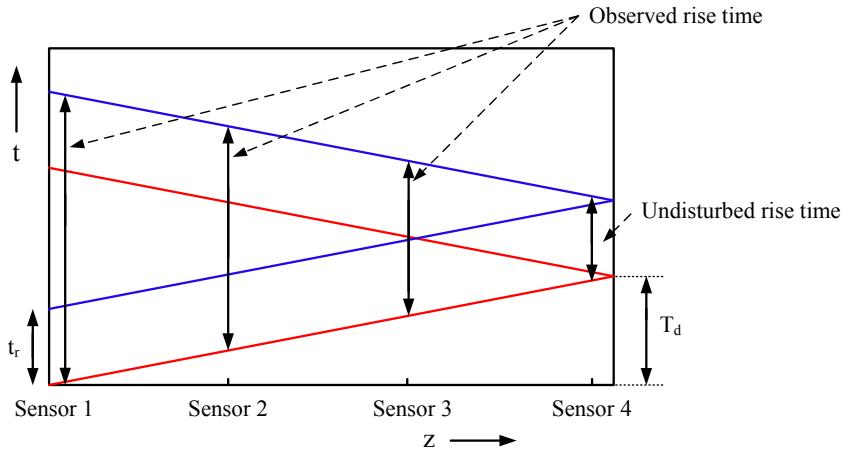
Figure 5.13: Schematic overview of the reflections in the reactor which result into the slower observed rise times. The red and blue lines represent respectively the start and stop in time of the rising edge of the pulse. t_r and T_d are respectively the rise time of the pulse ad the transient time of the reactor.

reactor and TLT impedance are an issue which will be discussed later on.

The effect on the energy distribution is shown in Figure 5.17c. A more equal distribution was obtained with a slower rise time. Multiple interrelated mechanisms are responsible:

- The rise time is long compared to the transient time of the reactor. Reflections add-up/blend together in the rising edge of the pulse.

- It was reported in literature that increased rate of rise and peak voltage, increase the propagation speed of the primary streamers [103]. Higher peak voltages also increases the number streamers leaving the wire [2]. Both effects alter the impedance of the streamer discharge resulting in an impedance alteration of the reactor which is space and time dependent.

- The rate of rise effect on streamer development weakens for long rise times.

5.4.2.3 Effect of the source voltage

Damping in the reactor by the resistive nature of the discharges will be place dependant if the streamers develop differently. Streamer development will also be influenced by the source voltage amplitude which affects the damping and reflection behavior indirectly. The effect of the source voltage is studied by varying the the charging voltage V_{Ch} of the pulse modulator. Inductance L_1 was omitted for the shortest possible rise time. Results of the rise time and peak voltage as a function of V_{Ch} are shown in Figure 5.20.

A higher source voltage affects streamer development significantly which in turn affects the rise time. Although the rise time becomes more similar for high charging voltages, the peak voltages on the various sensor locations remain highest towards the end.
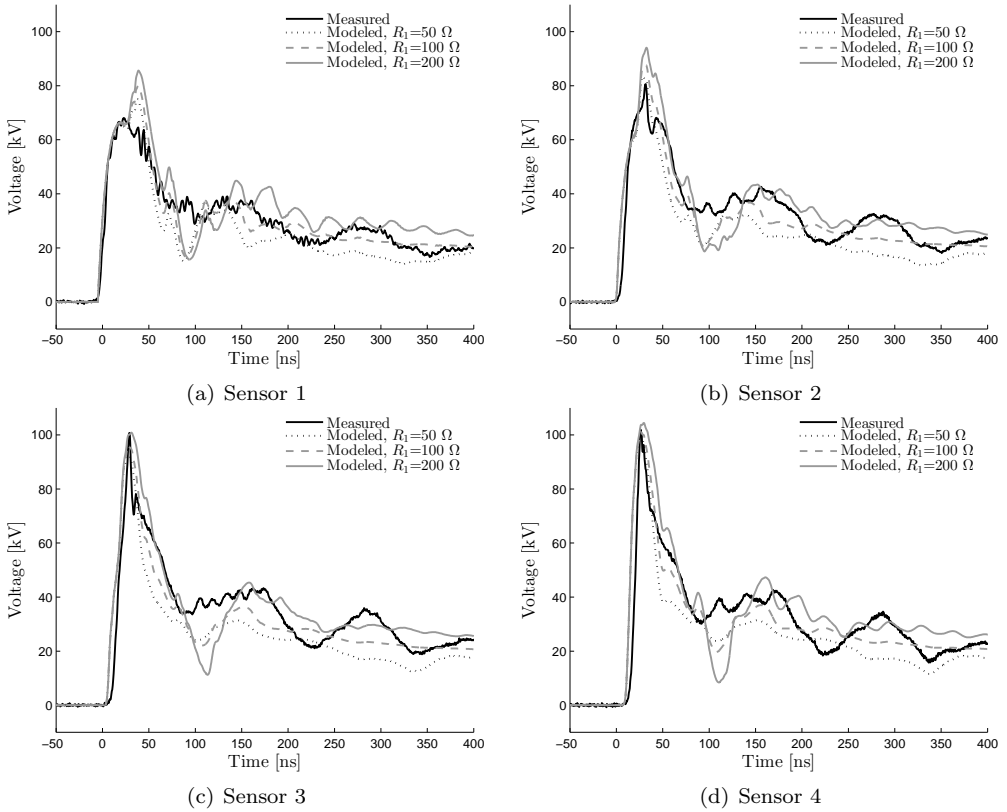
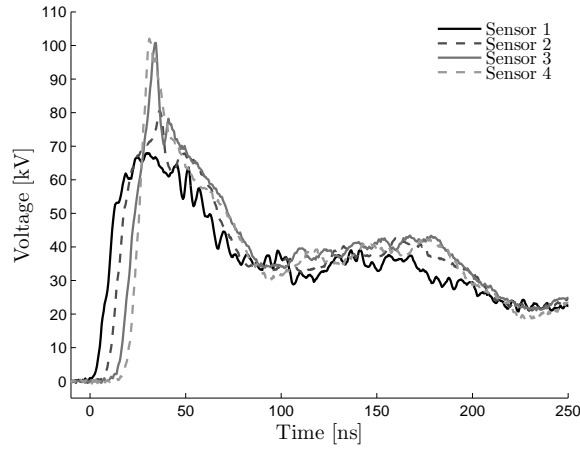Figure 5.14: Modeled and measured voltage waveforms at multiple sensor positions of a 11.5 ns rise time pulse (3 sections, V_{Ch}=31.2 kV, C_h=4 nF). The voltage waveforms are simulated for three R_1 values.

The effect on energy distribution is shown in Figure 5.20c. The distribution is very uneven as could be as expected from the observations in earlier sections. The energy total delivery to the reactor increases with higher charging voltages because more energy is stored in C_h. Sections 1 and 2 consume an equal amount of energy for all charging voltages. The consumption increases again near the end of the reactor up to a factor 4.7 for section 4 (1.4 J/m, V_{Ch}=36 kV) compared to sensor 1 (0.3 J/m, V_{Ch}=36 kV).

Coupling capacitor C_{dc} and the DC power supply are now installed to provide a DC-bias and higher source voltage to the reactor. Figure 5.21 shows the peak voltages and rise times as a function of the DC-bias voltage (up to 25 kV). The rise time of the pulse at the four sensor positions seems to level as the DC-bias voltage rises. They are between 9.5 ns and 15 ns at 25 kV DC-bias. The voltage on Sensor 1[*] increases up to 89 kV because of the addition of the DC-bias voltage (note that Sensor 1[*] is a virtual sensor which is previously described in Section 5.2.2.4). Remarkable is the decreasing voltage at sensor 4. It decreases from 110 kV (with 0 kV DC-bias) to 92 kV (with 25 kV DC-bias). The voltage at beginning and end of the

145

(a) Sensor 1

(b) Sensor 2

(c) Sensor 3

(d) Sensor 4

Figure 5.15: Modeled and measured current waveforms at multiple sensor positions of a 11.5 ns rise time pulse (3 sections, V_{Ch}=31.2 kV, C_h=4 nF). The current waveforms are simulated for three R_1 values.

Table 5.1: Measured and modeled energy distribution in the reactor. The energy distribution [J/m] is the energy dissipated in each section divided by the wire length of the section.

	Section 1 [J/m]	Section 2 [J/m]	Section 3 [J/m]	Section 4 [J/m]
Measured	0.13	0.23	0.33	1.0
Modeled R_1=50 Ω	0.29	0.36	0.29	0.6
Modeled R_1=100 Ω	0.34	0.33	0.31	0.6
Modeled R_1=200 Ω	0.29	0.36	0.29	0.6

(a) Sensor 1

(b) Sensor 2
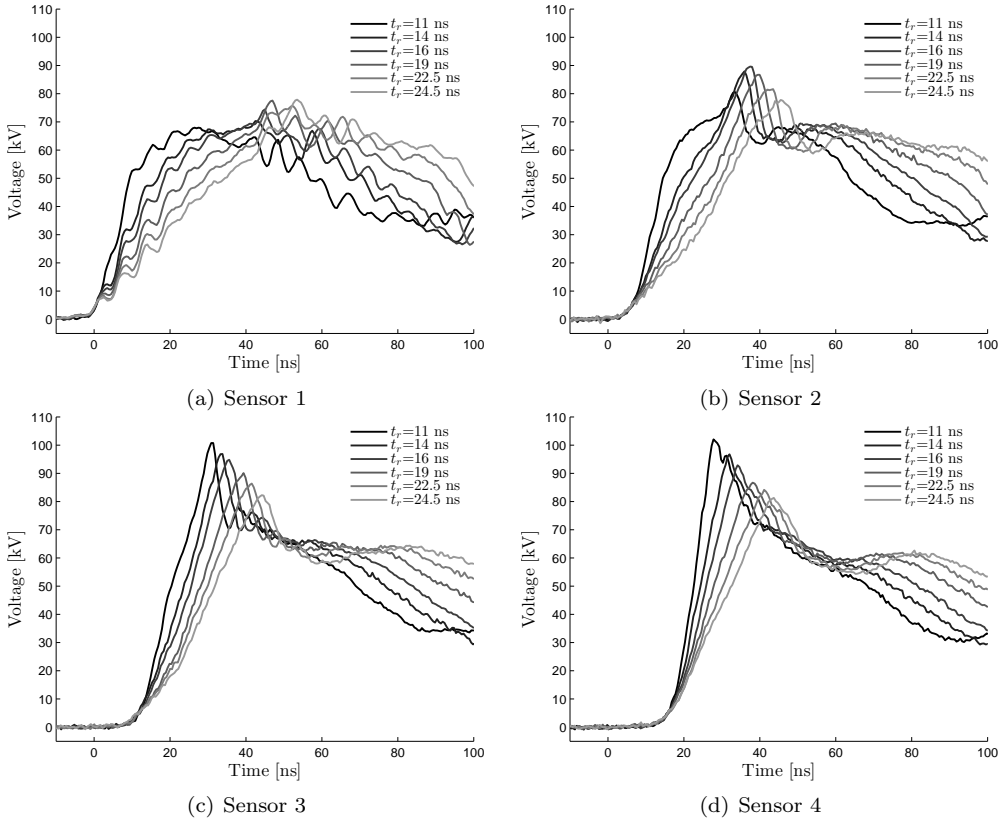
(c) Sensor 3

(d) Sensor 4

Figure 5.16: Voltage waveforms at multiple sensor positions for different rise times (3 sections, V_{Ch}=31.2 kV, C_h=4 nF). The rise time of the pulse which is mentioned in the legend corresponds to the voltage rise time measured at sensor 4.

reactor becomes almost equal while the voltages at the intermediate sensor positions are near 78 kV. Theoretically is the inception voltage of the plasma 18 kV so there's already some DC corona discharge activity with 20 kV and 25 kV DC-bias voltage. The inception voltage will be reached faster during pulse generation with increasing DC-bias level. This seems to advance the damping in the reactor significantly because the voltage at sensors 2-4 becomes lower with increasing DC-bias levels, while the voltages generally increase with increasing charge voltage V_{Ch} (see Figure 5.20b). Also the rise time at the four sensor positions is leveled within 5.5 ns difference, indicating significant damping of reflections in the reactor.

Effect on energy distribution is shown in Figure 5.21c. More energy is delivered to the reactor with an increased DC-bias voltage because energy is delivered by C_{dc} (see Equation 5.8). Only the energy consumption in the small top section (section 4) is significantly affected with an increasing DC-bias voltage, it decreases from 1.6 J/m to 1.1 J/m. The energy distribution for sections 1 to 4 are respectively 0.8, 0.6, 0.4 and 1.1 J/m at 25 kV DC-bias

(a) Rise time

(b) Peak voltage

(c) Energy distribution.
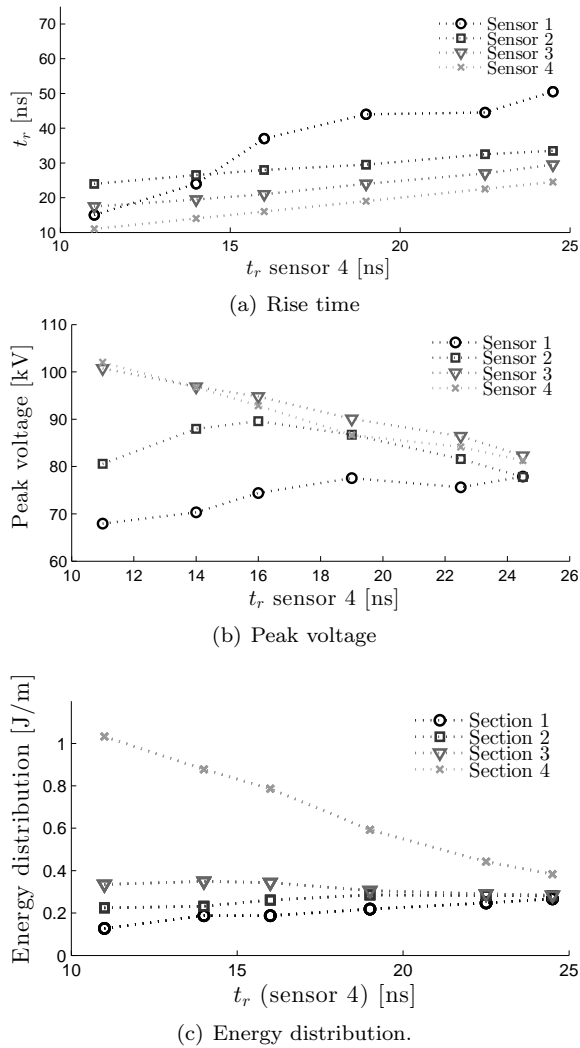
Figure 5.17: Measurements at multiple sensor positions as a function of the rise time at sensor 4 (3 sections, V_{Ch}=31.2 kV, C_h=4 nF).

voltage. The discharge activity in the section 4 is significantly reduced and the overall energy distribution improves slightly for higher DC-bias voltages.

5.4.2.4   Effect of the pulse width

A wider pulse causes more energy consumption in the secondary streamer regime which could level the energy consumption per section. The pulse width and energy per pulse is enlarged
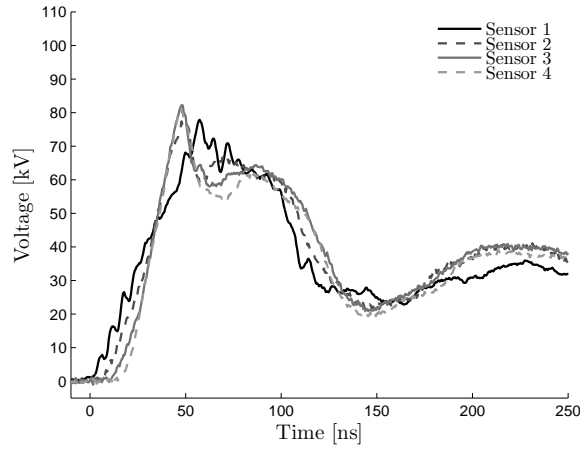
Figure 5.18: Typical voltage waveforms at multiple sensor positions of a 24.5 ns rise time pulse (3 sections, V_{Ch}=31.2 kV, C_h=4 nF).
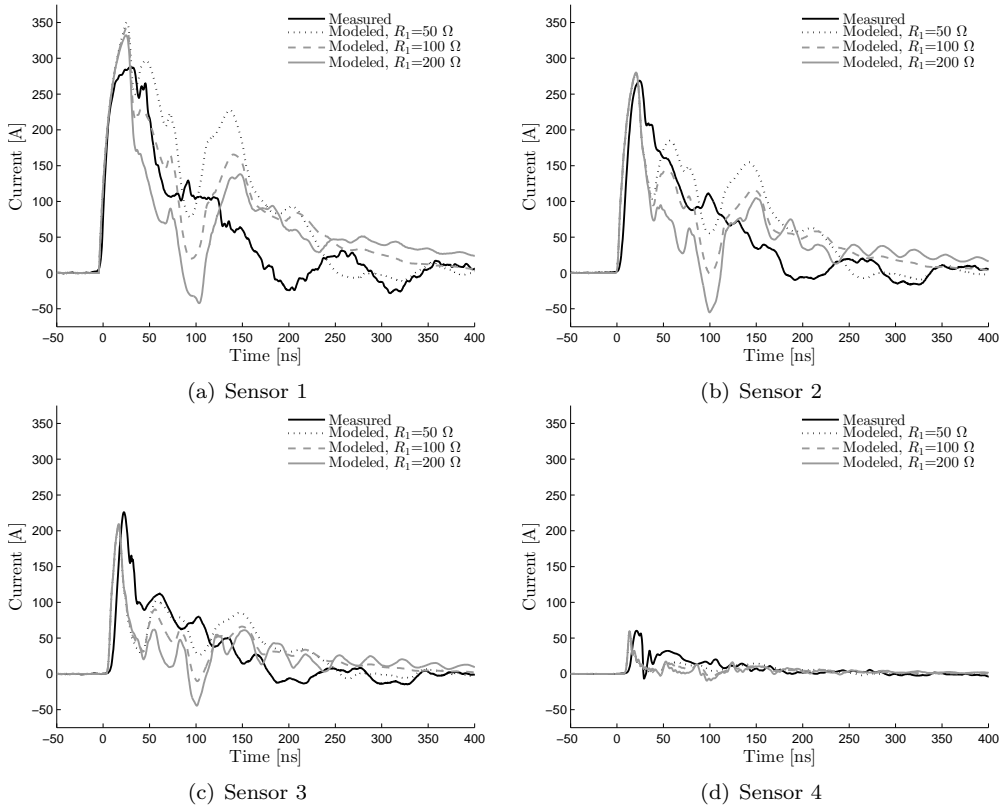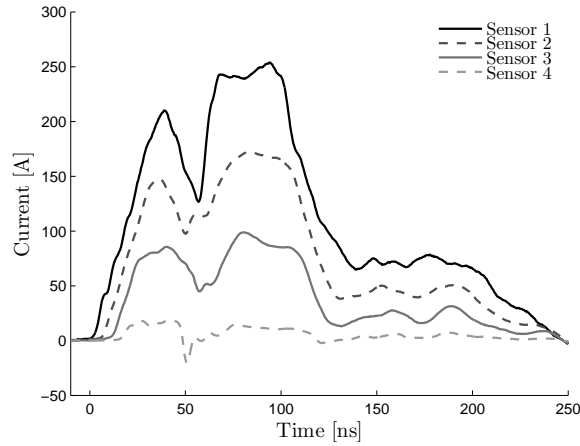

Figure 5.19: Typical current waveforms at multiple sensor positions of a 24.5 ns rise time pulse (3 sections, V_{Ch}=31.2 kV, C_h=4 nF).

by larger C_h values to investigate the effect of the secondary streamer regime. The initial reflection behavior in the reactor should be similar for the same charge voltage, in this case 31.2 kV. The results are shown in Figure 5.22 for different C_h and resulting energy per pulse values.

The pulse-width of the power waveform for the 2 nF, 0.55 J per pulse setting is only 45 ns wide and too short to feed energy to the secondary streamer regime. For 1.2 J per puls or higher, energy is fed to secondary streamers. The relative consumption per section remains then more or less equal. A secondary streamer is actually a re-illumination of a primary streamer filament which explains the result. The local development of primary streamers

149

(a) Rise time

(b) Peak voltage

(c) Energy distribution.
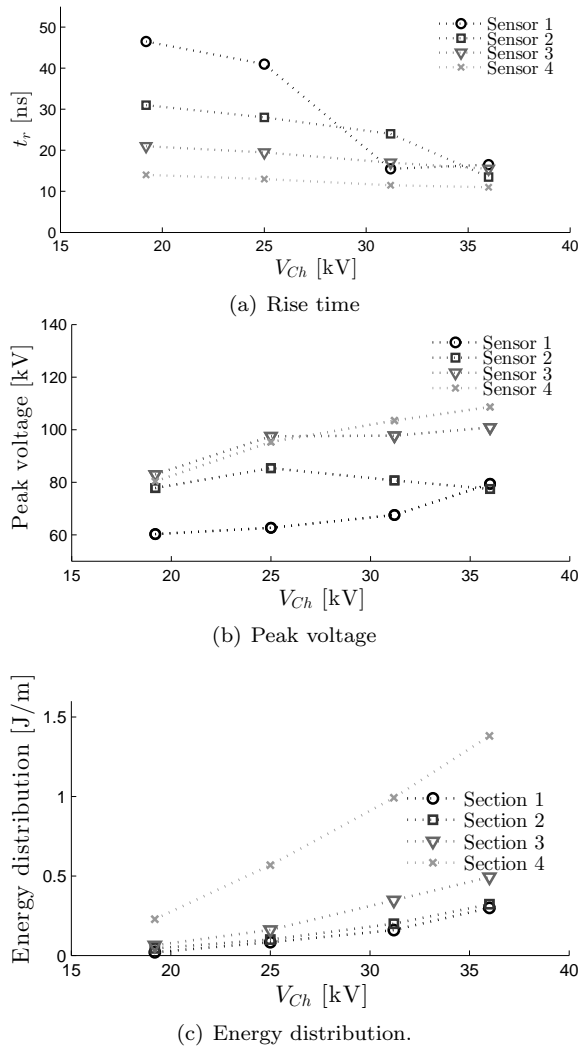
Figure 5.20: Measurements at multiple sensor positions as a function of V_{Ch} (3 sections, t_r=11.5 ns, C_h=4 nF)

outlines the discharge behavior and energy consumption during the secondary streamer phase.

5.4.3 Impedance characterization

The reactor impedance should be more or less equal to the source impedance to prevent reflections at the TLT-reactor interface and to transfer all energy in C_h to the plasma. The transmission line behavior of the reactor and streamer propagation affects the impedance of

(a) Rise time

(b) Peak voltage

(c) Energy distribution.
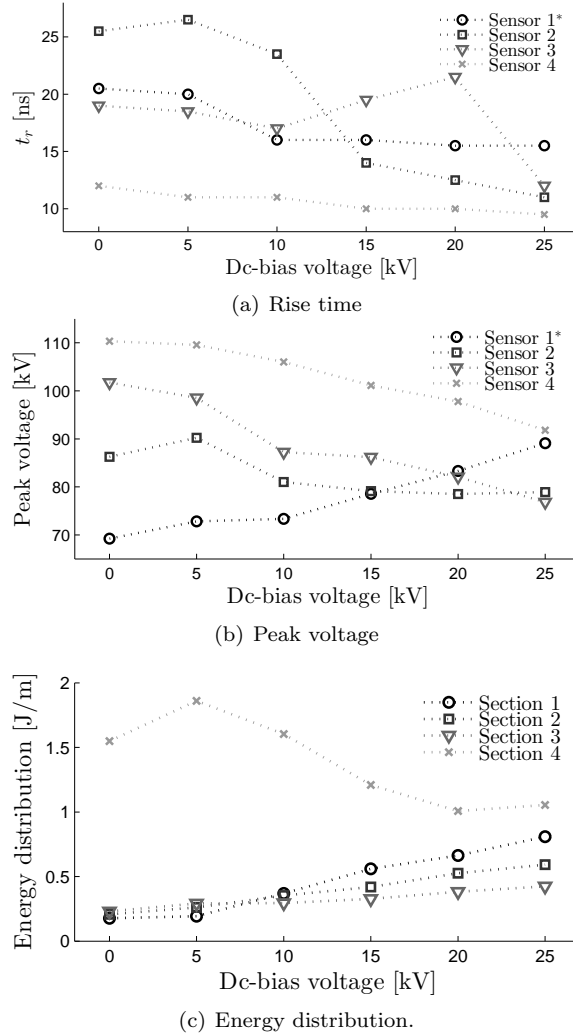
Figure 5.21: Measurements at multiple sensor positions as a function of V_{Cdc} (3 sections, t_r=11.5 ns, C_h=4 nF).

the reactor and thus the impedance matching. Reactor impedances from the data in the previous section were calculated and studied to find relevant mechanisms which affect the impedance of the reactor. The time dependent apparent reactor impedance as a function of time can be calculated from the measured voltage and current waveforms at multiple sensor positions $Z(t) = \frac{V_{Sensor\ x}(t)}{I_{Sensor\ x}(t)}$. Multiple interrelated mechanisms are found that affect the apparent impedance:

- The apparent impedance is initially equal to the vacuum impedance of the reactor.

151
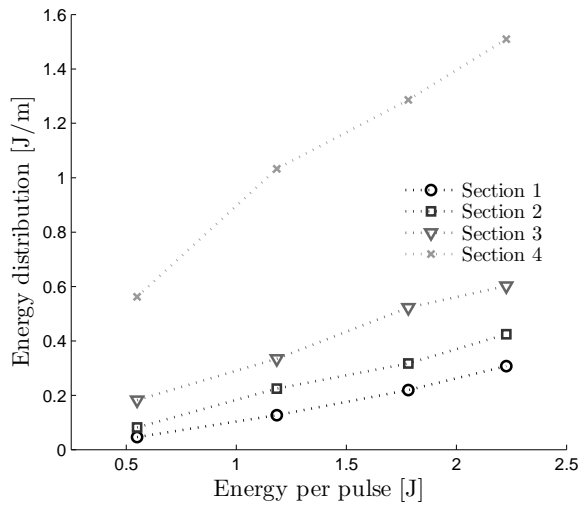
Figure 5.22: Energy distribution as a function of energy per pulse (3 sections, V_{Ch}=31.2 kV, t_r=11.5 ns, C_h = 2,4,6 or 8 nF).

Figure 5.23 shows the impedance at sensor 1 for different pulse rise times and 31.2 kV charge voltage. Although the inception voltage of the plasma is reached in 10 ns to 25 ns (depending on the position) in the reactor, the vacuum impedance of the reactor (238 Ω) does not seem to be initially affected. The pulse propagates to the end of the reactor in 15.5 ns and is reflected back in 31 ns, explaining the perfect initial impedance. The reactor capacitance increases as the distance between the heads of the conducting streamer filaments and reactor wall decreases during propagation [104] [2]. Although the characteristic impedance of the reactor is expected to be effectively lowered, early development of streamers does not seem to result in impedance that differs from the vacuum impedance.

- Reflections at the end of the reactor coming back to the reactor/TLT interface distort the initial steady impedance. Damping of the reflections is enhanced due to streamer currents.

  Large reflections in the system can be observed after 30 ns if the rise time of the pulse is increased (see Figure 5.23). The longer rise time slows down the plasma development and therefore the damping of the reflected pulse in the reactor. The fastest 11.5 ns rise time pulse results in sufficient plasma generation so that the reflected pulse is damped almost completely. The reactor/plasma impedance also remains near 238 Ω beyond 30 ns, this seems to be a coincidence as will be showed later on. The impedance at multiple sensor positions for the 11.5 ns rise time pulse is shown in Figure 5.24. These impedances are initially also near the vacuum impedance as expected. The back and forth transient time is shorter for sensors located nearer the end of the reactor.

- Lowering of apparent impedance and streamer currents directly by higher pulse voltage and/or DC-bias voltage.

  Discharge intensity (and apparent impedance) is related to the applied reactor voltage.
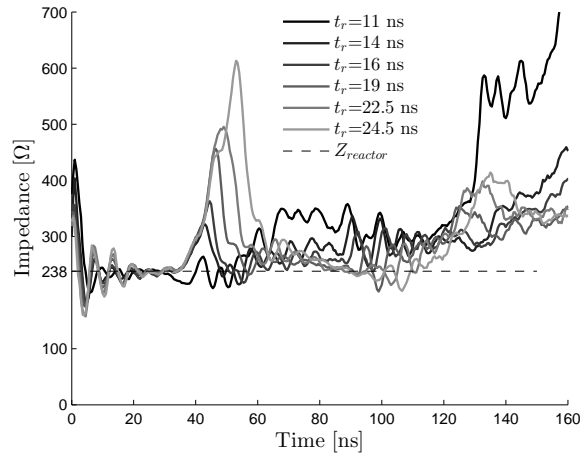
Figure 5.23: Reactor input impedance as a function of the rise time (3 sections, V_{Ch}=31.2 kV, C_h=4 nF).
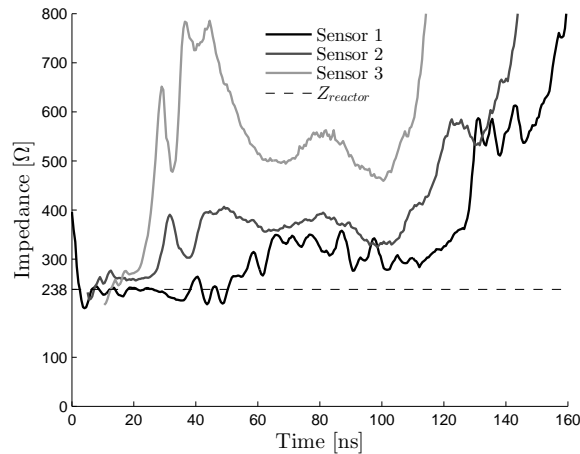
Figure 5.24: Reactor impedance at multiple sensor positions (3 sections, t_r=11.5 ns, V_{Ch}=31.2 kV, C_h=4 nF).

Figure 5.25 shows the reactor impedance as a function of the charging voltage. For low voltages (almost no plasma) and high voltages the measured impedance is still equal to the vacuum reactor impedance during 30 ns. After 40 ns the impedance increases rapidly for less than 25 kV charge voltage because the reactor voltage is too low to maintain the plasma. The impedance becomes eventually lower than 238 Ω for 36 kV charging voltage as the streamers propagate towards the wall of the reactor. Winands [2] concluded using ICCD imaging that more streamers are generated at higher source voltages. More parallel streamer filaments results in a lower total reactor impedance.

153
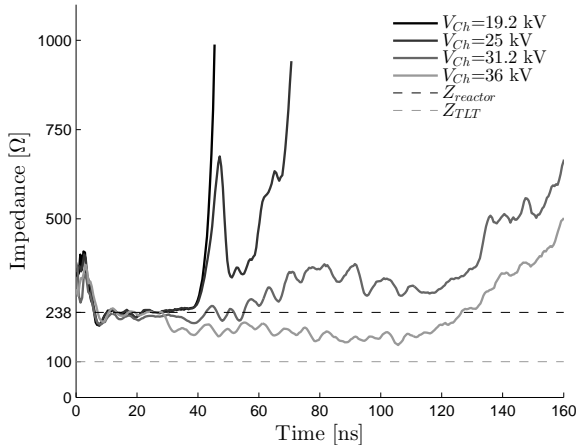
Figure 5.25: Reactor impedance at sensor 1 as a function of the charging voltage (3 sections, t_r=11.5 ns, C_h=4 nF).

A similar result is seen when adding a DC-bias voltage. The reactor impedance measured with DC-bias ($Z = V_{Sensor1*}/I_{Sensor1}$, where $V_{Sensor1*}$ should be calculated according to Equation 5.15) is shown in Figure 5.26. The initial impedance of the reactor seems to deviate from the vacuum impedance while it is actually similar. The reactor is already charged to the DC-bias voltage at the beginning of the pulse. This has to be considered when interpreting the impedance measurement. The vacuum impedance would only apply for transient waveforms or a correctly (resistively) terminated reactor. Also the coupling capacitor disturbs the impedance at the beginning of the reactor slightly. With increasing time, the impedance of the reactor lowers as the streamers propagate. Transition to the secondary streamer regime is estimated to be after 80–110 ns and is shown to result in a minimum impedance value which is reached earlier for higher voltages. The impedance saturates at a minimum value of 100 Ω (which is equal to the TLT impedance) at DC-bias levels above 20 kV. Saturation of the plasma impedance near the TLT output impedance after the primary–secondary steamer transition at high source voltages was also observed by Yan [30] and Winands [2]. An explanation for this observation was however not found.

Figure 5.27 shows the same data set but for now the load impedance of the TLT ($Z = V_{Sensor1}/I_{Sensor1}$), the load equals the reactor plus the series impedance of the coupling capacitor C_{dc}. The impedance for DC-bias levels above 15 kV is capable to become significantly lower than the output impedance of the TLT. It is remarkable that the reactor impedance saturates at exactly the TLT impedance while the total load impedance (reactor + C_{dc} series impedance) of the TLT is significantly lower.

- The apparent impedance of a longer reactor is lower during the secondary streamer phase (due to larger streamer volume) compared to a shorter reactor. Reflections in a longer reactor cylinders are also damped more strongly.

Figure 5.28 shows the TLT load impedance (sensor 1) for 10 kV and 29.5 kV DC-bias voltage and the three reactor sizes (1.65 m, 3.15 m and 4.65 m). A longer reactor
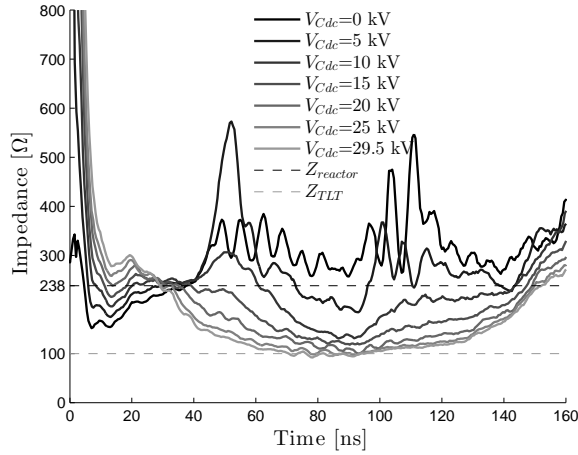
Figure 5.26: Reactor impedance as a function of DC-bias voltage (3 sections, t_r=11.5 ns, C_h=4 nF, V_{Ch}=31.9 kV). The reactor impedance is high at t=0 because the the DC-bias voltage is already present while current pulse still needs to rise.
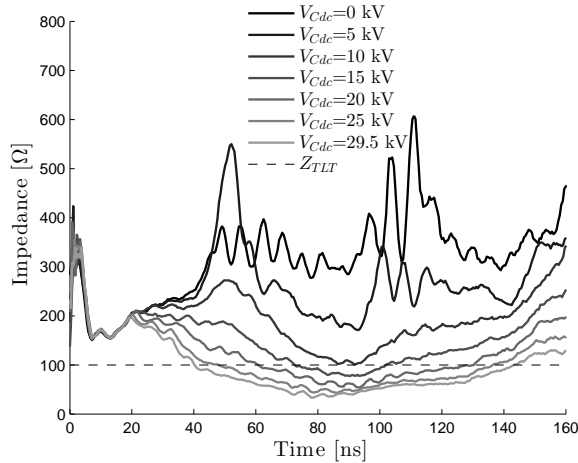
Figure 5.27: TLT load impedance (reactor impedance + C_{dc} series impedance) as a function of time for multiple DC-bias voltages (3 sections, t_r=11.5 ns, C_h=4 nF, V_{Ch}=31.9 kV).

improves the initial impedance matching because the reflection at the end of the reactor is damped more before it returns to the TLT-reactor interface. This is illustrated in Figure 5.28 by a decreasing impedance peak for a longer reactor after 18–40 ns (10 kV DC-bias voltage). This advantage seems to be redundant for high DC-bias voltages. The impedance during the secondary streamer regime (expected after the minimum at 70–80
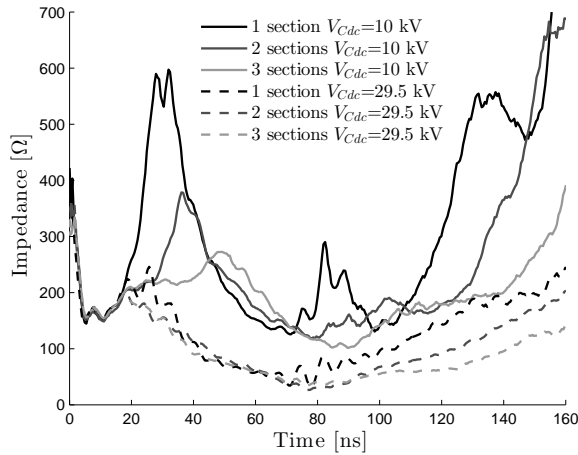
Figure 5.28: TLT load impedance as a function of time for two DC-bias voltages and three different reactor lengths (t_r=11.5 ns, C_h=4 nF, V_{Ch}=31.9 kV).

ns for 29.5 kV DC) is lower for longer reactors due to the larger plasma volume. The fact that shorter reactors have similar apparent impedances confirms strong interaction between plasma generation and source impedance.

5.4.4 Energy transfer efficiency

The apparent reactor impedance has initially a value close to the vacuum of the reactor and converges to a lower impedance level as the streamers propagate. The saturation level of the impedance is dependent on the applied reactor voltage. Impedance matching between source and reactor, and proper energy transfer from C_h to the reactor can therefore be optimized by choosing the amplitude of the reactor voltage. Figure 5.29 shows the transfer efficiency (energy transfer efficiency from C_h to the reactor) as a function of the applied peak reactor voltage. The Figure consists of two data sets wherein the peak voltage is varied. The first set is without DC-bias (no C_{dc} installed), V_{Ch} is varied. The second set is with DC-bias and contant V_{Ch}, V_{Cdc} is varied.

A higher peak reactor voltage results clearly in improved energy transfer efficiency, up to 85 % at 85 kV. The data sets seem to follow the same trend above 77 kV. The transfer efficiency is initially less with low DC-bias voltages compared to the data without DC-bias because C_{dc} affects the output impedance of the source. Additionally, C_{dc} can be charged by the pulse for very low DC-bias voltages. This effect is illustrated in Figure 5.30.

The energy transfer from C_h and C_{dc} to the reactor as a function of the DC-bias voltage is shown for a reactor consisting of one, two or three sections (1.8 m, 3.3 m or 4.8 m). The negative energy values for C_{dc} indicate charging of this capacitor by the TLT (and thus by C_h which reduces the transfer efficiency). The modeled values can be calculated by Equation 5.8.

The impedance mismatch after 40–70 ns for DC-bias levels above 10 kV (see Figure 5.27) does not seem to disadvantage the transfer efficiency. The current at the input side of the
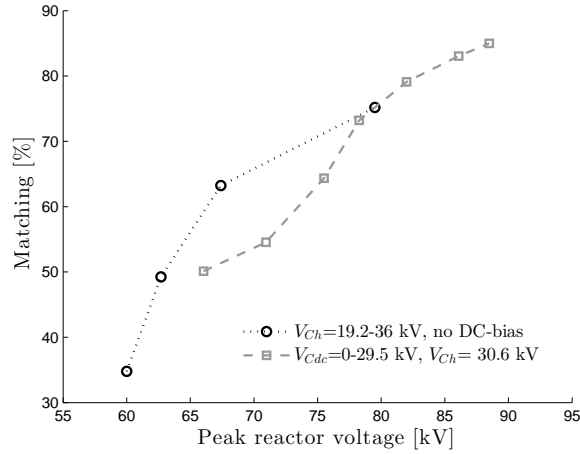
Figure 5.29: Energy transfer from C_h to the reactor as a function of the peak reactor voltage (3 sections, t_r=11.5 ns, C_h=4 nF). The results are obtained by varying the voltage on C_h without the DC-bias capacitor installed, and by varying the voltage on C_{dc} with DC-bias capacitor and V_{Ch}=30.6 kV.
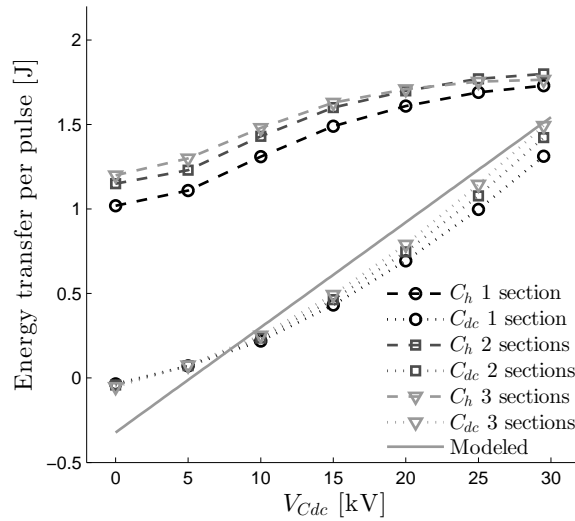
Figure 5.30: Measured and modeled energy transfer of C_h and C_{dc} to the reactor (1, 2 and 3 sections) as a function of the DC-bias voltage (t_r=11.5 ns, C_h=4 nF), V_{Ch}=30.6 kV. The modeled energy transfer from C_{dc} to the reactor is calculated by Equation 5.8.

TLT (I_{Ch}) is measured to explain this observation. I_{Ch} is shown in Figure 5.31 for multiple DC-bias voltages. The reactor impedance is initially higher than the TLT impedance and a negative current pulse is reflected back towards the input of the TLT. The first reflection arrives at $t = 22$ ns and causes the dip in the current waveform (observable at e.g. 55 ns for V_{Cdc}=29.5 kV). The transient impedance of the reactor decreases faster for higher DC-bias voltages which results in less reflection (visible at $t > 55$ ns in Figure 5.31 and the higher reactor peak current in Figure 5.32). A positive current reflection can be observed as the impedance of the reactor becomes lower than the output impedance of the TLT. The pulse is reflected again at the input of the TLT, resulting in a back and forth reflections which add-up and shape the distorted reactor pulse. C_{dc} is only partially discharged which keeps the reactor voltage above inception level so that these reflections can be consumed by the plasma, see Figure 5.33 (reactor voltage). The plasma quenches as the voltage becomes lower than 30–40 kV. Although perfect impedance matching of the reactor as in Figure 5.3 seems to be impossible, the DC-bias maintains the plasma and enables reflections to be consumed more easily. The modeled values according to equations 5.7 and 5.8 appear to be a correct approximation. Full energy transfer is not possible due to the losses in the TLT and spark gap.

Another observation in Figure 5.29 is that the transfer efficiency differences between reactor lengths are remarkably small. A longer reactor only improves the transfer efficiency slightly. The apparent reactor impedances for multiple reactor lengths appear to be very similar for high DC-bias voltages as can be seen in Figure 5.28.

5.5 Conclusions

The ICCD images show streamer plasma inception of all cylinders within 9 ns in the sixteen cylinder corona reactor. The streamers propagate to the wall of the cylinders within 80 ns without any significant deviations in the intensity and length of the discharges when comparing the cylinders mutually. The relatively slow initial streamer propagation (compared to the 9 ns inception window) ensures comparable streamer development in all reactor cylinders. Misalignment of wires is believed to be the main cause of the inception window because the order in which the individual reactor cylinders ignite is reproducible. The intensities in the images near the wall of the cylinder are weaker with lower DC-bias voltages, primary streamers do not seem to fully cross the gap. The discharges appear to be very similar when comparing the cylinders mutually, even with low DC-bias voltages.

The voltage and current waveform which are measured at the interface of the TLT and reactor are often not giving the correct details of the pulse which propagates initially through the long reactor. For energy measurements this is not a problem, for statements about rate of rise of the reactor voltage it is.

Due to overlap of the reflected pulse with the rising edge of the incoming pulse, the rise time at the input of the reactor appears to be longer than the rise time at the end. The energy distribution in the reactor should be more or less equal according to the SPICE model. The measured energy distribution is completely completely uneven. Apparently is local development of the streamers (number of streamers and/or speed) affected by the reflection behavior resulting in an uneven energy distribution along the reactor. The model is therefore not suitable for energy distribution estimations. The measured energy consumption [J/m] at the end of the reactor is higher than near the input connection. Decreasing the rise time of
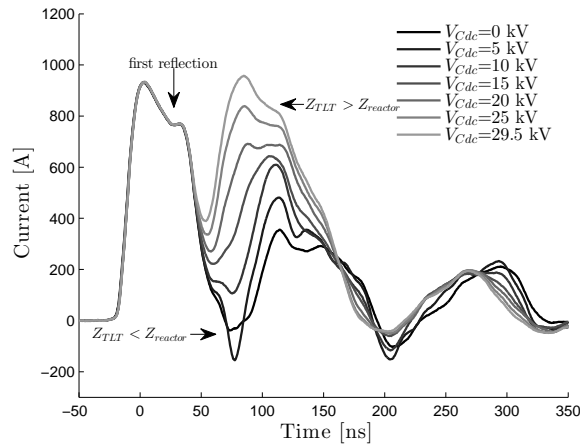
Figure 5.31: I_{Ch} as a function of time for multiple DC-bias voltages (3 sections, t_r=11.5 ns, C_h=4 nF, V_{Ch}=31.9 kV).
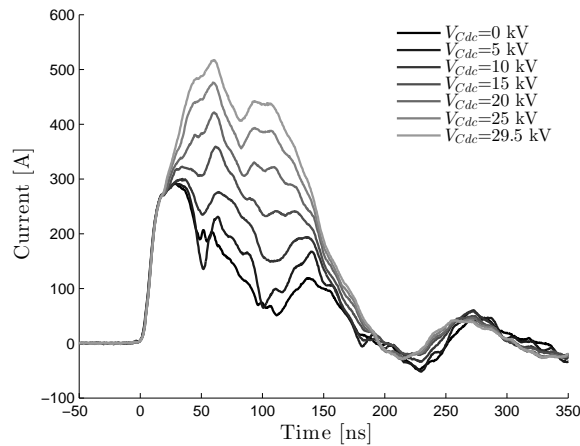
Figure 5.32: Reactor input current as a function of time for multiple DC-bias voltages (3 sections, t_r=11.5 ns, C_h=4 nF, V_{Ch}=31.9 kV).

the pulse improves the energy distribution. The input voltage level has little effect on the energy distribution.

The impedance of the reactor is initially equal to the vacuum impedance of the coaxial structure during the back and forth transient time of the reactor. Streamer development during this time interval does not seem to affect the total impedance.

Higher source voltages (including DC-bias) result in an impedance which alters towards and below the output impedance of the TLT. Improved energy transfer efficiency from C_h to the reactor can be obtained this way. The energy transfer efficiency can be up to 85 % even with reactor impedances which alter below the output impedance of the TLT. Resulting reflections at the TLT-reactor interface (into the TLT) are reflected back again at the input
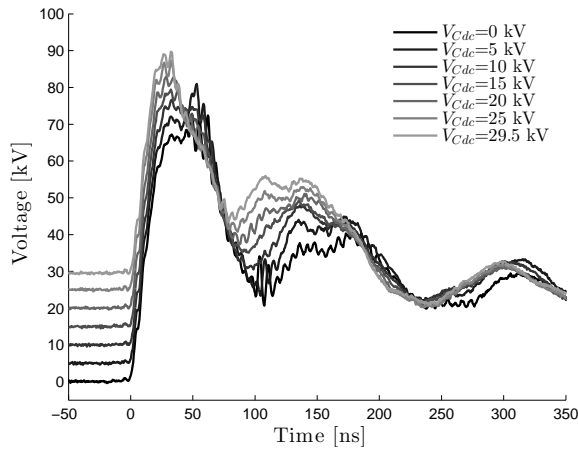
Figure 5.33: Reactor input voltage as a function of time for multiple DC-bias voltages (3 sections, t_r=11.5 ns, C_h=4 nF, V_{Ch}=31.9 kV).

of the TLT. The DC-bias voltage keeps the reactor voltage above the inception level which enables these reflections to be consumed by the plasma.

The reactor length has a minimum effect on the energy transfer efficiency. The pulse reflected from the end of the reactor is damped by the plasma load more for longer reactors. This advantage is redundant for high reactor voltages because damping is already enhanced with higher voltages. A longer reactor improves the energy transfer efficiency slightly because the larger plasma volume causes a lower impedance during the secondary streamer phase.

The impedance matching can possibly be improved even further with less pulse distortion if the vacuum impedance of the reactor is chosen near the TLT output impedance. Multiple reactor cylinders can be placed in parallel like in the demonstrator. The output impedance of the TLT can also be adapted to obtain a matched system. The source output voltage can subsequently be used to tune the reactor impedance to minimize reflections back into the TLT.

Calculations show that the wire diameter should be at least 1 mm for negligible damping (skin effect) of the coaxial reactor structure. Boosting of energy transfer to the reactor could likely be achieved by using a larger corona wire diameter which decreases the reactor vacuum impedance. The increased inception voltage (due to smaller E-field around the wire) can be compensated with a higher DC-bias voltage. This will also increase the energy per pulse because the energy delivered by the coupling capacitor scales linearly with the DC-bias voltage.

From a plasma chemical processing point of view the non-equal energy sharing in the reactor possibly be an advantage. A multiple stage conversion process can be created by exposing pollutants and products to different plasma intensities.

6

Plasma processing

Abstract

Potential industrial applications of pulsed corona technology for air purification are investigated by a series of field and lab experiments. Corona technology has a wide range of applications but performs generally optimal for target pollutant concentration levels in the 10-1000 ppm range. Investment costs, the amount of energy required to convert target compounds and competition with conventional technologies will determine if applications are viable. To investigate the span of possibilities, conversion of a selection of compounds of concern is attempted. The required input energy which is needed to convert the target compound to an acceptable level is established together with the product spectrum. The following applications are investigated: NO_x (flue gas emissions), VOCs (hydrocarbon/solvent emissions), H_2S and NH_3 (factory farming) and fine dust removal (general problem).

6.1 Introduction

Pulsed corona technology for air purification has a wide range of applications. Depending on the concentration level, each compound has its own energy density level which is required to convert the compound and intermediate product spectrum to an acceptable level. The investment cost and energy consumption of the installation will ultimately determine if the technology is able to compete with conventional technologies. Therefore, conversion by pulsed

Part of the content in this chapter has been published previously in [14, 105, 106]:

- F.J.C.M. Beckers, W.F.L.M. Hoeben, T. Huiskamp, A.J.M. Pemen, and E.J.M. van Heesch. Pulsed corona demonstrator for semi-industrial scale air purification. *IEEE Transactions on Plasma Science*, 41(10):2920–2925, 2013

- F.J.C.M. Beckers, W.F.L.M. Hoeben, A.J.M. Pemen, and E.J.M. van Heesch. Low-level NO_x removal in ambient air by pulsed corona technology. *Journal of Physics D: Applied Physics*, 46, 2013

- W.F.L.M. Hoeben, F.J.C.M. Beckers, A.J.M. Pemen, E.J.M. van Heesch, and W.L. Kling. Oxidative degradation of toluene and limonene in air by pulsed corona technology. *Journal of Physics D: Applied Physics*, 45(5):1–14, 2012

corona technology of a selection of compounds is attempted during a series of field and lab experiments. The required specific input energy and product spectrum are investigated. The obtained data could provide a base for cost calculations of specific applications. Also, insight is provided for additional required after treatment (e.g. scrubbers, catalysts, active carbon). The following selection of applications will be discussed:

NOx NOx is a generic term for the total concentration of NO and NO$_2$ (nitric oxide and nitrogen dioxide respectively). These compounds are produced during high temperature combustion from the reaction between oxygen and nitrogen. Especially diesel engines generate NO$_x$ due to their high internal combustion temperature. Air pollution caused by NO$_x$ emission in the atmosphere can be significant in crowded cities with large numbers of motorized vehicles. Other NO$_x$ sources are waste incineration or combustion of fuels (e.g. coal and oil in powerplants and furnaces). The nitrogen for NO$_x$ formation can originate not only from the air but also from nitrogen containing fuel. NO is also produced by lightning during thunderstorms. The intense heat of the discharge facilitates the endothermic oxidation of nitrogen. NO$_x$ gases in the atmosphere form acid rain and smog. The specific applications which will be reviewed are NO$_x$ removal from flue gas and traffic tunnel air. Flue gas typically contains 50-1000 ppm NO$_x$. Tunnel traffic emissions typically comprise sub–ppm level NO$_x$, which does not affect the traffic participants during their tunnel passage. In contrast, these emission levels are not acceptable for long term exposure in residential areas close to the tunnel portals.

VOCs   VOC removal has a wide range of applications in the (petrochemical) industry. Two Volatile Organic Compounds were chosen as model compounds. Toluene is an important solvent and building block in organic synthesis. Limonene is a volatile organic compound which is present in domestic waste (e.g. fruit peels, soap) and is used as solvent in cleaning products. This compound is for instance responsible for odor and VOC emissions from household waste processing facilities.

H$_2$S & NH$_3$ ppb–ppm Levels of H$_2$S and NH$_3$ are often emitted by factory farming (e.g. feces and urea), waste water treatment, and food processing [107] [108] [109] [110]. In practise these compounds cause major stench problems, even emitted in low concentration levels. Very low levels are perceivable by the human sense of smell, 0.47 ppb for H$_2$S and 5 ppb for NH$_3$. In high concentration levels (>100 ppm) they are extremely toxic and corrosive. H$_2$S is also present in natural gas, biogas and liquid petroleum gas (LPG). It often needs to be removed from the fuel gases to avoid corrosion in gas lines and combustion engines. Commercial use of natural gas demands desulphurization up to 10 ppm [111]. Our main application focus is on odor control for factory farming.

Particulate matter   Fine dust or particulate matter (PM) are microscopic liquid/solid particles which are suspended in the atmosphere. These particles can be composed of multiple chemicals and materials and exist in a variety of sizes. The particle size is directly linked to their hazardousness for public health. Particles smaller than 10 μm in diameter can be inhaled and have the potential to cause health effects. Exposure to these particles can affect both lungs and heart [112]. Particulate matter can be directly emitted from sources such as forest fires, or formed during fuel combustion in power plants, industry and motorized vehicles.
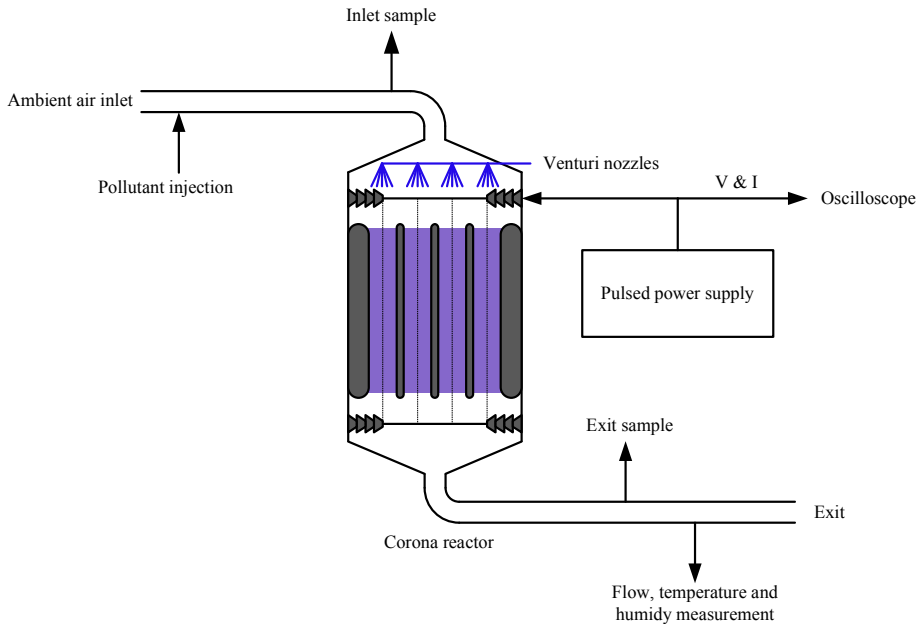
Figure 6.1: Schematic setup overview

The lab and field experimental setups are introduced in Section 6.2. Chemical diagnostics and analytical methods for measuring the conversion of the target pollutant and the resulting product spectrum are discussed. The results are shown in Section 6.3.

6.2 Experimental setups

The basic setup is shown in Figure 6.1. A pollutant is injected in the ambient air stream of the reactor during lab experiments. Two types of reactors were used, the demonstrator (wire-cylinder) and the electrode plate-reactor. An overview of the used diagnostics and reactors during lab experiments is shown in Table 6.1. The gas is only sampled in the reactor exit during lab experiments. First a sample is taken with the plasma disabled, the plasma is subsequently enabled and a second measurement is acquired. During field testing the reactor was continuously enabled and the gas had to be sampled in the reactor inlet and exit. Two equal gas analyzers were mostly available for simultaneous sampling. Venturi nozzles were optionally installed during high level NO_x tests to provide water aerosols in the reactor.

6.2.1 Pollutant injection

The following methods and compounds were used to inject pollutants in the reactor inlet:

NO_x   The exhaust gases of a diesel generator were used as a NO_x source during this study. The exhaust gases contains typically two times more NO than NO_2. A part of the

Table 6.1: Overview experiments

Compound	Reactor	Diagnostics	Pollutant source
Low level NO_x	Wire-cylinder	Recordum Airpointer	Diesel generator & Tunnel air
High level NO_x	Electrode-plate	Testo 350S	Diesel generator & Incinerator flue gas
VOCs	Wire-cylinder	Schimadzu QP2010P	Liquid evaporation
NH_3 & H_2S	Electrode-plate	Testo 350S & Dräger gas detection tubes	Gas cylinders
Particulate matter	Wire-cylinder	Grimm EDM 365	Tunnel air
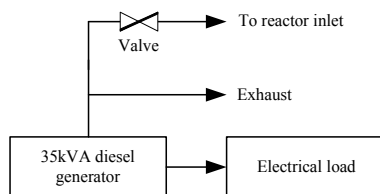
Figure 6.2: NO_x injection setup.

exhaust flow was mixed with the ambient air flow of the reactor to create a desired NO_x concentration level, see Figure 6.2. A valve controls the amount of exhaust flow which is injected into the reactor inlet duct. The remaining exhaust gases exit the generator directly. A 10 kW heater is used as an electrical load for the generator which results in higher NO_x concentrations in the exhaust. An additional compressed air fed venturi nozzle enables injection of liquids (e.g. dissolved NH_3 mist) in the gas flow to enhance the chemical conversion process.

VOCs Toluene and limonene are both liquids at room temperature. An evaporation setup is needed to apply a ppm concentration level in the ambient air flow through the reactor. The setup is shown in Figure 6.3. A few L/min nitrogen (bottle 3.0 grade) is fed via a mass flow controller (MFC) to a bubble flask which is partially filled with the liquid to be evaporated. Toluene (>99%, FW = 92.14 g/mol) or R(+) Limonene (97%, FW = 136.24 g/mol). The liquid in the flask is heated to temperatures up to 80 °C. The temperature and flow rate of the nitrogen control the evaporation rate of the liquid which eventually controls the concentration level in the ambient reactor stream. The line between bubbler and reactor was not traced resulting in some condensation in the line. Droplets eject from the line-end in the ambient air stream resulted in unstable concentration levels. An additional condensation trap was added to solve this problem.

H_2S and NH_3 Gaseous H_2S and NH_3 originating from gas cylinders was injected directly into the reactor inlet. Both gases are highly corrosive, dedicated stainless steel reducing valves and needle valves were used.
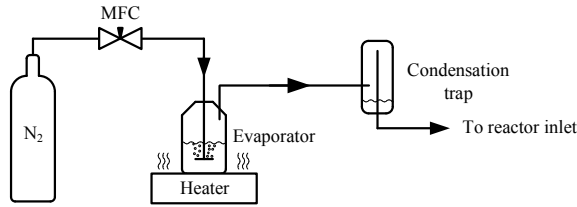
Figure 6.3: Toluene/Limonene evaporation setup
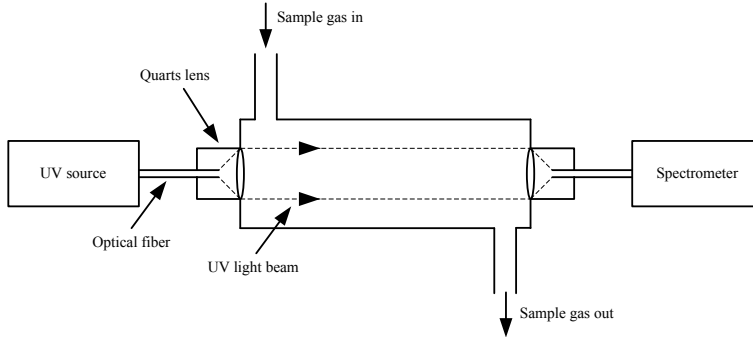
Figure 6.4: UV absorption spectrometry setup for measuring the ozone concentration.

6.2.2 Chemical diagnostics

Several diagnostic tools were used to observe conversion levels of compounds and the oxidation product spectrum.

Ozone Ozone which is produced by the plasma is measured quantitatively by UV absorption spectrometry, see Figure 6.4. Absorption of ozone is the strongest in the Hartley band (230-290 nm). A Mikropack D-2000 UV source is connected via an optical fiber to a gas cell. Two collimating quarts lenses focus the light beam in the gas cell. An Ocean Optics HR2000 UV spectrometer (wavelength 200-400 nm, resolution 0.1 mm) is connected via a second optical fibre to the lens on the opposite side. The sample gas passes through the gas cell (and light beam). The ozone yield is determined by Lambert-Beer's absorption law, see Equation 6.1.

$$-ln\left(\frac{I(\lambda)}{I_0(\lambda)}\right) = c_{O_3}\epsilon(\lambda)d \tag{6.1}$$

$I(\lambda)$ is the absorption spectrum, $I_0(\lambda)$ is the background spectrum (sample gas contains no ozone), c_{O_3} is the ozone concentration (molecules/m^3), $\epsilon(\lambda)$ is the absorption cross-section (m^2/molecule) and d is the optical path of the gas cell (distance between the lenses, d=111 mm). Multiple ozone cross-sections for different wavelengths are known in literature [2]. c_{O_3} is calculated for 17 different wavelengths and subsequently averaged for improved accuracy.
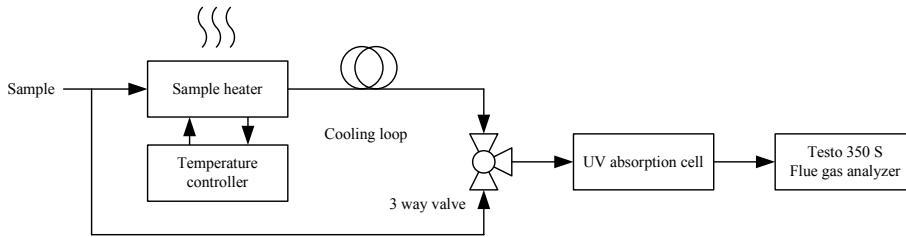
Figure 6.5: NO_x sample conditioning setup for ozone removal.

The measurement procedure is as follows. A background spectrum is recorded ($I_0(\lambda)$) with the plasma is switched off (no ozone in the reactor and gas cell). The plasma is subsequently switched on, ozone will be produced. The absorption spectrum ($I(\lambda)$) is recorded when the spectrum (and ozone concentration) has stabilized. The ozone concentration is subsequently calculated by Equation 6.1. The temperature of the gas which passes the gas cell is also measured by a K-type thermocouple. The molar gas volume (which is temperature dependent) is required to convert c_{O_3} in molecules/m^3 to ppm concentrations, see Equation 6.2.

$$c_{O_3, \, ppm} = 10^6 \frac{c_{O_3}}{nNa}, \quad n = \frac{PV}{RT} \tag{6.2}$$

Where Na is Avogadro's constant, n the molar volume, P the absolute pressure, V volume, R the gas constant and T the temperature of the gas.

High level NO_x (> 10 ppm)   The NO_x concentration levels in the reactor inlet and exit are measured with a Testo 350S flue-gas analyzer. The electrochemical NO_2 measurement cell of the analyzer appeared to be cross sensitive for O_3. Ozone produced by the reactor distorts the NO_2 measurement. The sample gas has been pre-heated to 250 °C in a metal tube to thermally decompose the ozone before entering the analyzer, see Figure 6.5. The temperature is controlled by a control unit with feedback. A part of the NO_2 is unfortunately decomposed to NO due to the pre-heating operation. Therefore, only the measured total NO_x value is valid. Separate NO and NO_2 are however determined by an additional step in the measurement procedure: first, the sample gas is guided directly to the flue-gas analyzer via a 3-way valve. Only the NO values is now valid because of the cross sensitivity of the NO_2 cell. The ozone concentration in the sample gas is measured simultaneously by the UV-absorption cell. Then the flue gas is guided via the sample heater to the flue-gas analyzer. The UV-absorption cell is used to confirm that all ozone is decomposed. Now only the total NO_x (NO+NO_2) value is valid. The difference with the previously measured NO value results now in the actual NO_2 value.

Low level NO_x (0.4–10000 ppb)   Two chemiluminescence [113] based Recordum Airpointer NO_x analyzers were used during experiments to measure NO_x levels simultaneously at reactor inlet and exit. The lower detection limit is 0.4 ppb, the upper limit is 20 ppm. A UV absorption based O_3 measurement cell with an upper detection limit of 20 ppm is available in the Recordum Airpointer as a secondary detector. The sample gas, principally containing NO and NO_2, is analyzed via two analytical pathways, as follows (Figure 6.6). Ozone is generated (by the Airpointer) and mixed with sample gas in the reaction cell. Ozone-induced oxidation

(a) Schematic overview (NO/NC, normally open/closed)

$$\alpha NO + \beta NO_2 \underset{Mo}{\overset{O_3}{<}} \quad \begin{array}{l} \xrightarrow{} \alpha NO_2^{*} + \beta NO_2 \Rightarrow \alpha NO \\ (\alpha + \beta) NO \xrightarrow{O_3} (\alpha + \beta) NO_2^{*} \Rightarrow (\alpha + \beta) NO \end{array} \quad \Rightarrow \alpha, \beta$$

(b) Diagnostics chemistry
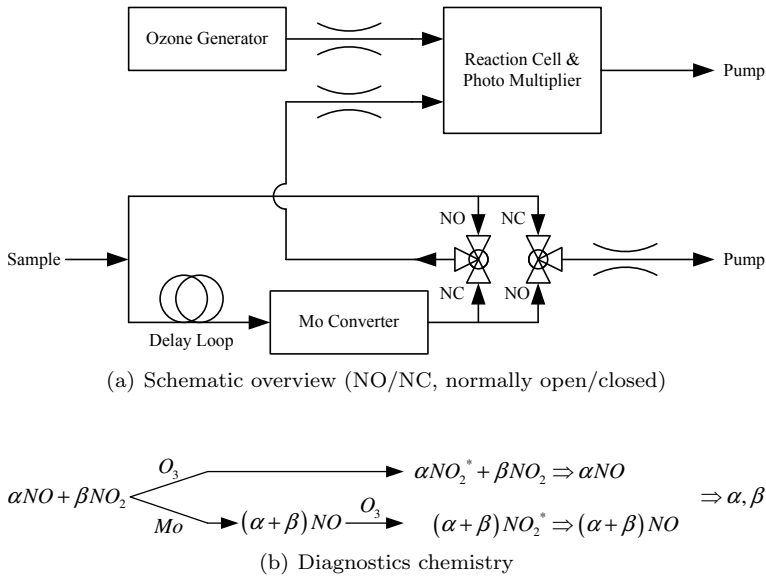
Figure 6.6: Chemiluminescence based NO_x detection (Airpointer)

of NO to excited nitrogen dioxide (NO_2^*) will result in emission of wavelengths in the range 0.6-3.0 μm. The chemiluminescence intensity measured by a photomultiplier is proportional to the NO concentration in the sample. The second path comprises the first path, preceded by reduction of NO_2 to NO by a molybdenum converter which is heated to 325°C, yielding a NO signal based on both NO and NO_2. A delay loop in the second path ensures gas sampling at the same moment as is in the first path. The NO_2 concentration is then calculated from the NO signal differences of path 2 and path 1.

Application of ppb level NO_x chemiluminescence analyzers for plasma reactors involves specific attention. Electric discharges in air are known to produce ozone concentrations at several hundred ppm level, depending on the energy density [2]. Clean ambient air does not contain ozone. Although ozone generation in the chemiluminescence-based NO_x detector is needed for NO detection, high levels of ozone in the sample gas showed significant deviations in sub ppm NO_2 measurement values. Therefore sample conditioning was applied to the analyzer at the reactor outlet. The sample gas flow has been preheated to thermally decompose ozone into oxygen (see Figure 6.7). The sample heater consists of a one meter long borosilicate glass tube wrapped with an insulated heating ribbon. Glass was used because adhesion and releasing of ppb levels NO_x were observed in the metal tube. A temperature controller is applied to control the temperature on the outside of the tube. The residence time of the sample gas in the heater is approximately 6 seconds. Although the NO-NO_2 equilibrium is temperature dependent, preheating has no effect on the sum of both oxides. The threshold for instantaneous ozone decomposition in the heater is 300-350°C. A significant increase of the calculated NO_2 signal has been observed after turning on the sample heater. This means that the Mo converter in the Airpointer device is overloaded by ozone and incapable of removing all ozone out of the sample gas. Consequently the Mo Converter is not able to convert all
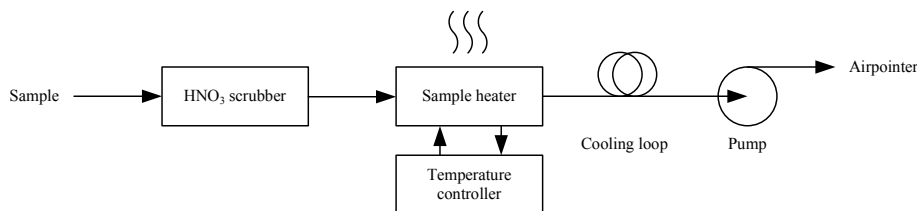
Figure 6.7: Reactor outlet sample conditioning

NO_2 into NO, resulting in a negative contribution to the NO_2 readings.

Another issue is sensitivity for other NO_y species like HNO_3 which is known to be produced in the corona reactor. Thermal decomposition of HNO_3 at ambient pressure requires temperatures over $500°C$ [114], so decomposition in sample heater likely is no issue. However, the Mo converter converts HNO_3 into NO [115], resulting in a positive contribution to the NO_2 reading. There are NO-O_3 chemiluminescence based techniques which use this effect to quantify gaseous HNO_3 [116] [117]. Detecting HNO_3 is very difficult due the extremely high sticking probability of nitric acid for e.g. metallic surfaces [118]. The sample gas should only be exposed to suitable inert materials like PFA tubing before entering the converter. The sample gas is filtered and dried before entering the Mo converter in the Recordum Airpointer, resulting in an uncertain amount of gaseous HNO_3 entering the converter and contributing to the NO_2 value. An additional HNO_3 scrubber has been added in the sample line to rule out possible HNO_3 cross-sensitivity. The scrubber consists of a bubbler flask filled with 350 mg NaCl crystals with a typical particle size of 300 μm. HNO_3 is removed from the sample gas by reaction with NaCl [119], see Equation 6.3. The residence time of the sample gas in the crystals is approximately 3 seconds. Increased residence times showed no additional uptake of HNO_3.

$$HNO_{3\ (g)} + NaCl_{(s)} \rightarrow HCl_{(g)} + NaNO_{3\ (s)} \tag{6.3}$$
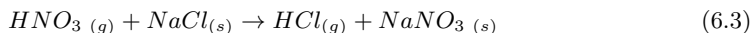
The NO_x diagnostics are cross sensitive for O_3 and HNO_3 to a certain degree as explained. To show the effect of O_3 removal by thermal decomposition on the detected NO_x values, an experiment has been carried out as follows. First a 10 sL/min mass flow controller is applied to inject NO from a gas cilinder (NO/N_2 0.1/99.9 %) into the ambient gas flow through the reactor (407 m^3/h). The diesel generator is in this case not used. A very stable NO level of approximately 1000 ppb is applied Only the sample heater and membrane pump are placed in the sample line of the reactor outlet. The temperature of the heater is initially at room temperature, and the power source of the corona reactor is enabled with an energy density of 3.8 J/L. The NO is fully oxidized in the reactor and the NO_2 value approaches 850 ppb after the plasma is enabled (figure 6.8); this would (wrongly) suggest a removal of 150 ppb NO_x by the corona reactor. The O_3 concentration in the lower temperature range remains at 19.9 ppm. The heater temperature is subsequently increased in steps of 100 °C, the NO_x value takes up to 15 minutes to stabilize between steps. For no obvious reasons a further decreasing NO_x value can be observed as the temperature is increased to 200 °C. Significant ozone decomposition can be observed as the temperature reaches 300 °C. An increase of the NO_x value can be observed simultaneously, confirming the O_3 cross sensitivity. Intrinsic NO_x production of the plasma apparently results in a true total NO_x concentration of more than
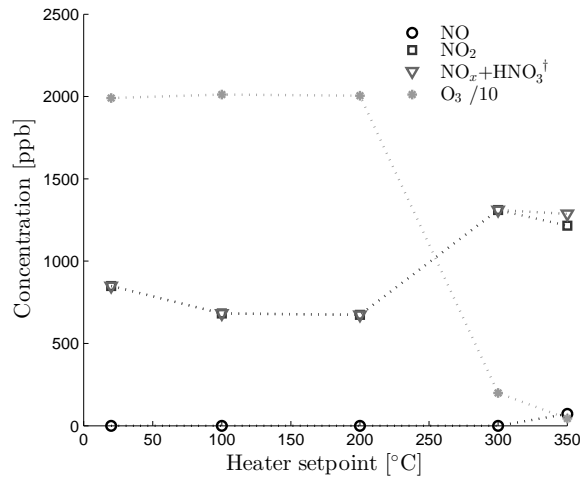
Figure 6.8: Effect of O_3 removal on NO_x measurement values († gas phase detected)

1000 ppb. The NO_2 decomposes as the temperature is increased further. The presence of NO suggests that ozone should be completely removed to ppb level at this point. Any residual O_3 would directly react with NO to NO_2.

The cross sensitivity for HNO_3 can be observed in figure 6.9. A gas flow through the reactor containing 10-11 ppm NO_x (69-71% NO) is obtained by mixing exhaust gases with ambient air. The reactor inlet NO_x concentration is measured directly without any sample conditioning. The reactor outlet sample is preheated to decompose O_3, and measured with and without HNO_3 scrubber as function of the energy density. The difference of these measurement values corresponds to the amount of HNO_3 which is detected by the Airpointer as NO_2. A part of the HNO_3 produced by the corona discharges is apparently able to enter the Mo converter of the Airpointer and is measured as NO_2. This amount of detected HNO_3 is defined as $HNO_3^†$.

VOCs   The concentration levels at the reactor inlet and outlet were monitored by a standalone-calibrated flame ionization detector (ABB AO2000-MultiFID14 analyser). The toluene and limonene concentration levels were far beneath explosion limits during experiments and could be monitored continuously. Flame ionization detection is based on detection of ions which are formed during combustion of organic compounds in a hydrogen flame [120]. The detector response is proportional to the concentration of organic components in the sample gas. The response of hydrocarbons scales with the number of carbon atoms in their molecule. Molecules containing oxygen tend to have a lower detector response [121, 122]. The detector is not sensitive for CO and CO_2. Quantization of concentration levels is possible when calibrated for the concerning component. FID measures hydrocarbons integrally, making simultaneous quantization of mixed hydrocarbon concentration levels impossible. The device is extremely suitable to monitor the inlet concentration level of the reactor during lab experiments (only one hydrocarbon in the gas flow). Target compound concentration levels can be converted into mass densities by Equation 6.4. At a temperature $T = 25\ °C$ and pres-
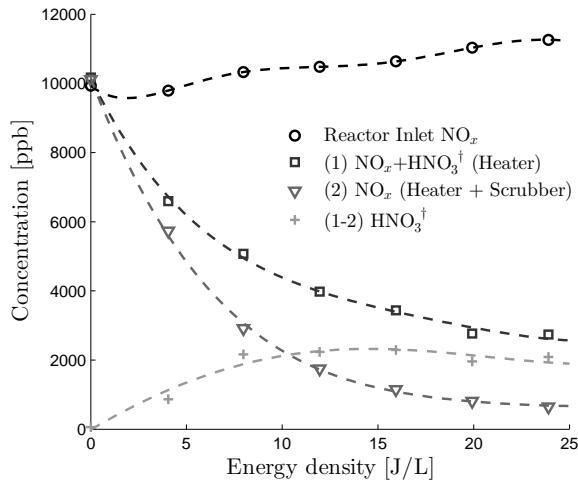
Figure 6.9: HNO$_3$ cross sensitivity Airpointer († gas phase detected)
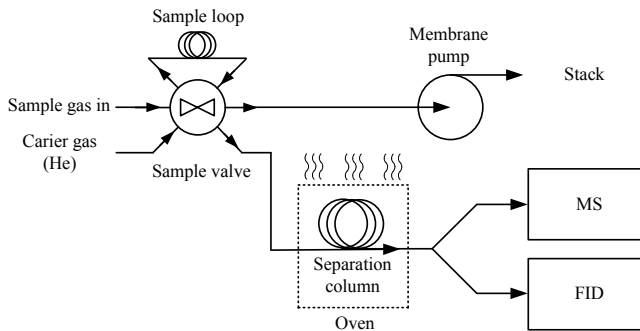
Figure 6.10: Gas chromatography-mass spectrometry setup

sure $p = 1$ atm, 1.0 ppm toluene corresponds to 3.8 mg/m^3 toluene, while 1.0 ppm limonene corresponds to 5.6 mg/m^3 limonene. Vm (L/mol) equals the (ideal) gas molar volume under the mentioned standard conditions, i.e. 24.47 L/mol, FW (g/mol) is the formula weight.

$$C(mg/m^3) = C(ppm)\frac{FW}{V_m} \tag{6.4}$$

The corona plasma oxidizes the hydrocarbon resulting in a wide component spectrum. FID is not suitable to analyze these components. These components were analyzed by a Shimadzu QP2010 Plus gas chromatograph mass spectrometer with a separate parallel FID. It can be used for qualitative detection of oxidative degradation products and determination of conversion levels. GC-MS consists of two separate parts, the gas chromatograph and the mass spectrometer. A schematic overview of the gas analyze setup is shown in Figure 6.10.

The sample gas is guided via the sample valve through a fixed volume sample loop by a

membrane pump. The sample loop holds the sample gas which will be used for the actual analysis. An analysis starts by switching the sample valve. The carrier gas now flows via the sample loop and separation column to the detectors. The film on the inner wall of this capillary column has certain phase properties which enables separation of molecules in the sample gas as the sample travels along the column. These molecules are adhered, other molecules which have no interaction and exit the column right away to the detectors. The dimensions (e.g. length, thickness) and film properties makes the column suitable for separation of a certain range of molecules. The oven is now switched on and a controlled temperature gradient is applied to the separation column. The adhered molecules release again from the columns inner wall depending on the component, temperature and time. Injection of separate components at separate moments in time in the detectors is hereby achieved. The time it takes before a certain component releases is called the retention time. The column heating program ensures the eventual desorption of all components from the separation column. The individual components enter the FID which gives a response which is proportional to the number of molecules and number of carbon atoms in the molecule as explained before. Simultaneous identification of the components occurs by the mass-spectrometer (MS). Molecules are ionized and partially fragmented by a 70 eV E-beam in the MS. These fragments are subsequently detected by using their mass to charge ratio. Each molecule has a unique fragmentation spectrum which allows matching to a library in the software to identify the component. A FFAP BP21, 30 m, 0.25 mm ID, 0.25 μm GC separation column (SGE Analytical Science) has been utilized, with specific retention behavior towards polar organic compounds. Applied instrument settings have been column flow $F = 1.3$–2.0 mL/min, injection loop volume 60 μL, temperature gradient program 50–230 $^{\circ}$C at a rate $= 20$ $^{\circ}$ C/min. The GCMS software has been equipped with NIST08 and Wiley229 mass spectral libraries.

NH_3 & H_2S   The H_2S concentration levels were measured with the Testo 350 S flue-gas analyzer by an electrochemical cell. No cross sensitivities were observed, additional sample conditioning was not required. NH_3 was measured with gas detection tubes from Dräger.

Particulate matter   Two Grimm EDM 365 fine dust analyzers [123] were simultaneously applied to sample the in- and outlet air of the reactor. The measurement principle is based on laser light scattering which enables continues monitoring with a resolution of several seconds. Three particle matters are distinguished: PM10 (all particles <10 μm), PM2.5 (<2.5 μm) and PM1 (<1 μm). The minimum detection limit of the grimm EDM 365 is 250 nm, the measured value of PM1 is therefore all particles between 250 nm and 1 μm in diameter.

6.2.3   Conversion calculations

Equation 6.5 is applied to express the removal efficiency G [g/kWh] of the target compound, according to [106]. C_0 equals the inlet target compound concentration [ppm] and X [-] is the conversion level, molar volume V_m [L/mol] and energy density E_d [J/L]. The conversion level is expressed by Equation 6.6 where C_{exit} is the concentration level of the target compound in the reactor exit. The energy density is calculated by Equations 6.7 and 6.8, where F [L/s] is the volumetric reactor flow rate.

The Specific Energy Input (SEI) value is equal to the energy density which is required to convert the target compound to $(1 - (1/e)) \cdot 100 \approx 63$ %

$$G = \frac{10^{-6} \cdot C_0 \cdot X}{V_m \cdot E_d} \qquad (6.5)$$

$$X = 1 - \frac{C_{exit}}{C_0} \qquad (6.6)$$

$$E_p = \int \left(V_{pulse}(t) + V_{dc}(t=0)\right) I_{pulse}(t) dt \qquad (6.7)$$

$$E_d = \frac{f \overline{E_p}}{F} \qquad (6.8)$$

Table 6.2: Interconversion of the G-value [124].

	mol/J	$(100\text{ eV})^{-1}$	g/kWh
mol/J	1	$\frac{1}{100 N_a e}$	$\frac{1}{3.6 \cdot 10^6 FW}$
$(100\text{ eV})^{-1}$	$100 N_a e$	1	$\frac{100 N_a e}{3.6 \cdot 10^6 FW}$
g/kWh	$3.6 \cdot 10^6 FW$	$\frac{3.6 \cdot 10^6 FW}{100 N_a e}$	1

6.3 Results & discussion

6.3.1 Low level NO_x

Oxidation proceeds by reactive oxygen species like e.g. the hydroxyl radical OH, O, ozone O_3, singlet oxygen (lowest excitation state of O_2), produced by the electrical discharges in oxygen and water vapor enriched gas phases. Oxidation of NO_x by these corona induced radicals proceeds as follows. NO is oxidized by the OH radicals and yields nitrous acid HNO_2, oxidation of NO by ozone yields NO_2. Further oxidation of NO_2 by OH yields nitric acid HNO_3 [125] [126]. Further oxidation of NO_2 by ozone yields NO_3, which can react with NO_2 to dinitrogen pentoxide N_2O_5, the anhydride to HNO_3. On the other hand, thermal or photochemical action can decompose the species back to their precursors. The corona technology facilitates the conversion of NO_x in waste/flue gas flows to HNO_2 and HNO_3, these acids are water soluble thus removable from the gas phase by conventional scrubbing technology. The low level NO_x results have been published in [127]

6.3.1.1 Lab NO_x conversion results

Figure 6.11 shows the NO_x removal rate as a function of energy density for 10-11 ppm NO_x (69-71% NO). The experimental conditions were as follows: initial NO_x concentration C_0 = 10 ppm, the reactor gas temperature T = 25.9 °C, the relative humidity RH = 68 %, reactor flow F = 506 m^3/h. The SEI value is approximately 7 J/L. Energy levels of >20 J/L are required to reduce the NO_x levels to approximately 500 ppb (95% removal), the sum of residual nitrogen oxides ($NO_x + HNO_3^\dagger$) is however >2000 ppb. It is expected that a large part of HNO_3 adheres to the approximately 8.0 m^3 stainless steel inner surface area of the reactor.
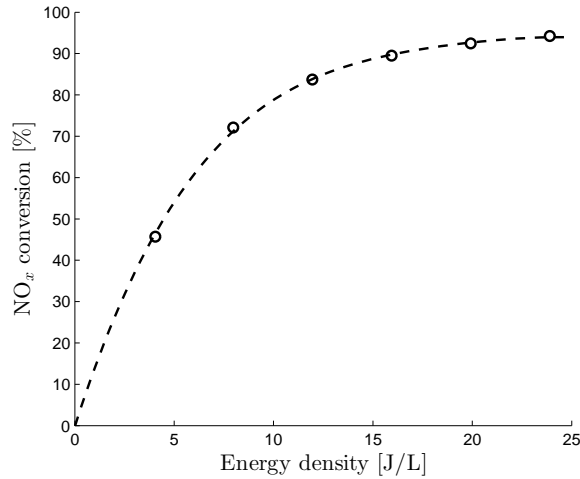
Figure 6.11: 10 ppm NO$_x$ removal
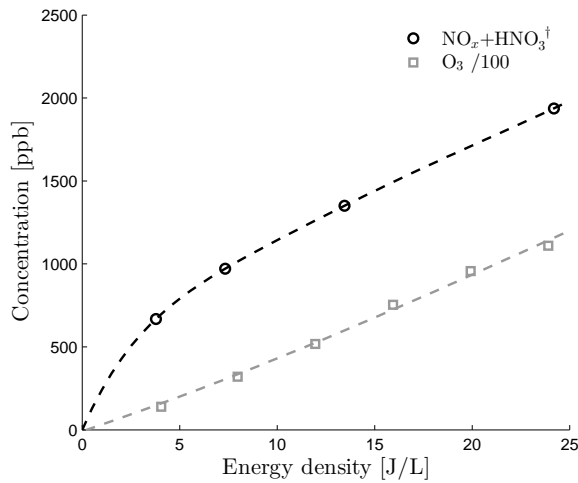
Figure 6.12: Intrinsic NO$_x$ and O$_3$ production († gas phase detected)

ppb Level NO$_x$ production by DC corona discharges was earlier observed [128] [129]. Pulsed corona experiments showed also ppm level intrinsic NO$_x$ production for high energy densities, see figure 6.12. The experimental conditions were as follows: the reactor gas temperature $T = 22.5$ °C, the relative humidity $RH = 33$ %, reactor flow $F = 414$ m^3/h. The HNO$_3$ scrubber wasn't applied so the measurement values contain also an amount of HNO$_3$, the total is referred to as NO$_x$+HNO$_3$†. Figure 6.12 shows also the amount of ozone which the corona discharges is able to produce. It is expected that there will be interaction between intrinsic production of NO$_x$ and removal of injected NO$_x$.

6.3.1.2 Field NO_x conversion results (traffic tunnel)

Field tests were carried out at a 130x6x3 m bicycle/pedestrian tunnel in the city of Eindhoven. The inlet of the reactor was extended 1/3-way into the tunnel. Additional exhaust gases of the diesel generator were emitted in the tunnel to simulate traffic emissions. Conversion of 0-10 ppm NO_x levels have been monitored in sessions of several hours. A typical measurement session of inlet and exit levels is shown in Figure 6.13. The experimental conditions were as follows: reactor flow $F = 528$ m^3/h and the energy density $E_d = 10.5$ J/L. The concentration levels are monitored over a period of 300 minutes, the concentrations are sampled every 6 seconds and averaged to obtain a resolution of 1 min. The unsteady inlet and exit concentrations are initially equal since the plasma is disabled. Removal can be observed at t = 60 minutes as the plasma is enabled with an average energy density of 10.5 J/L. Intrinsic NO_x production can be observed at t = 80 minutes when the inlet level drops below 800 ppb. The plasma is disabled at t = 190 minutes. The results of conversion level as a function of inlet NO_x levels for two energy density levels are shown in Figure 6.14. Intrinsic NO_x production is indicated as a negative removal fraction. The conversion level increases only by 10% if the energy density is increased a factor of two (for inlet concentrations over 4000 ppb). For inlet concentrations below 4000 ppb the removal rate is significantly higher for 10.5 J/L. Since at higher energy densities the intrinsic NO_x production is also higher, the exit gas is assumed to contain a higher amount of HNO_3 (more oxidation of NO_x by higher OH radical production).

The conversion efficiency (G-value) is shown in Figure 6.15. These NO_x removal efficiency results show a clear dependency on inlet concentration and energy density. For high concentrations (>3000 ppb) the G-yield is better with the lower energy density of 5.2 J/L. The influence of energy density at low NO concentrations (<3000 ppb, encircled area) is remarkable: The higher energy density $E_d = 10.5$ J/L gives a better G-yield than $E_d = 5.2$ J/L. Please note that the apparently low data point density at 5.2 J/L below 1000 ppb is due to overlap of many data markers in Figure 6.15. The better G-yield can be reasoned by considering the NO_x mass balance over the corona reactor (Equation 6.9) and the definition for G.

$$Rate\ Of\ Change = In - Out + Production - Conversion \tag{6.9}$$

In and Out are the mass flows NO_x of reactor inlet and outlet respectively, Production = source term due to plasma-induced intrinsic production of NO_x and Conversion = NO_x consumption by OH radicals and other reactive oxygen species. The Rate Of Change will be 0 for steady state conditions. At low energy density indeed we have a low intrinsic NO_x production, but at the same time a low conversion. At high energy density we have more intrinsic NO_x production, but also a higher conversion. It is the balancing of the production and conversion divided by the energy density that causes the typical observed behavior of the G-value.

6.3.2 High level NO_x

Figure 6.16 shows the NO, NO_2 and O_3 levels as a function of the energy density for an initial NO_x concentration of 29 ppm. The initial NO and NO_2 level are respectively 7 and 22 ppm. Almost all NO is converted to NO_2 at 5 J/L. No ozone is detected in the reactor outlet up to this energy density. Oxygen atoms react directly with NO or forms O_3 which reacts with NO to NO_2 in the reactor volume. Approximately 20 J/L is required to convert all NO_2 to 90 %.
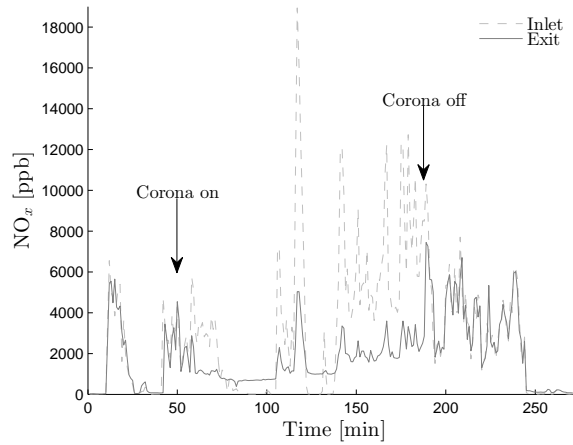
Figure 6.13: Typical in- and output NO_x levels during field experiment
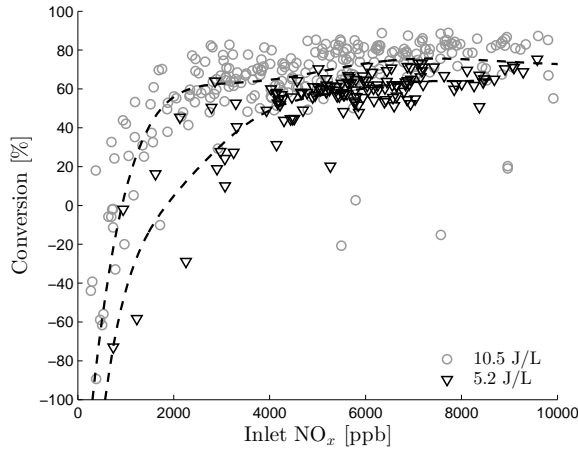
Figure 6.14: NO_x as a function of inlet concentration level

The NO_x conversion rate as a function of energy density for three levels (14, 29 and 59 ppm) is shown in figure 6.17. The experimental conditions are shown in Table 6.3. The SEI values for converting 14, 29 and 59 ppm are respectively 6.2, 11.5 and 20.5 J/L. A similar result, SEI = 7 J/L, was obtained with 10 ppm inlet concentration level in the wire-cylinder reactor (see Figure 6.11). The conversion efficiencies (G-values) as a function of the energy density are shown in Figure 6.18. The 10 ppm conversion efficiency result was also added for comparison. The conversion efficiencies for the SEI values are 6.5, 9.7, 10.7 and 12.3 g/kWh. Maximum G-values are 7.8, 10.3, 11.1, and 12.3 g/kWh for respectively 10, 14, 29 and 59 ppm NO_x. The efficiency increases with higher inlet concentration levels. There are two explanations for this observation. First, the conversion limitations by the intrinsic NO_x

175

Figure 6.15: NO_x removal yield as a function of inlet concentration level

Figure 6.16: NO, NO_2 conversion and O_3 production as a function of energy density. The NO_x inlet level is 29 ppm.

Table 6.3: Experimental conditions NO_x removal

C_0 [ppm]	F [m^3/h]	T [°C]	RH [%]
14	310	28.0	57.0
29	310	28.0	61.5
59	310	32.2	60.3

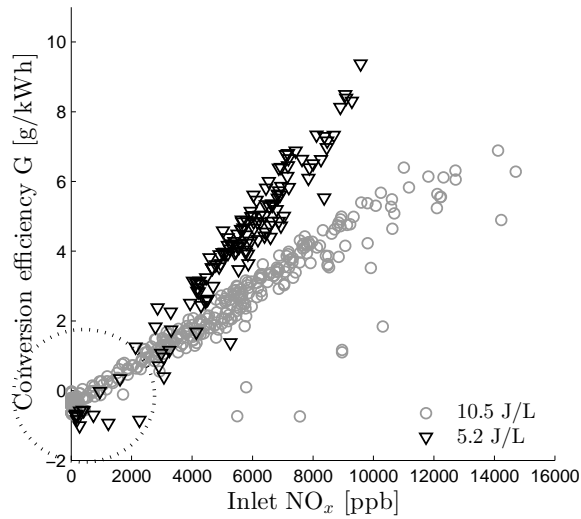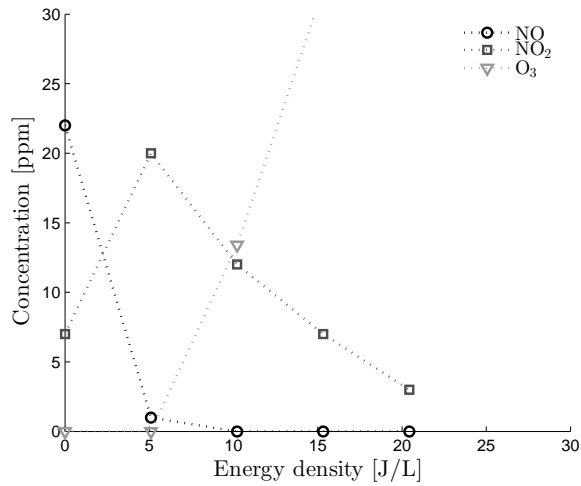production becomes less dominant with higher inlet concentration levels. Secondly, radicals (e.g. OH) are used more efficiently. The probability that active species meet during their lifetime becomes higher with higher inlet concentration levels, less active species and thus energy is required to obtain the same conversion. This also explains the maximum values in Figure 6.18. Relatively more active species are required to convert remaining molecules as the conversion level increases.

The ozone production as a function of the energy density during the 14, 29 and 59 ppm NO_x removal experiments is shown in Figure 6.19. Produced ozone reacts directly with NO resulting in no ozone in the reactor outlet as long as not all NO is oxidized. Ozone is produced proportionally to the energy density when al NO is converted to NO_2. The production rate (slope) is similar for 14, 29 ppm NO_x but decreases for the 59 ppm NO_x measurement. Multiple factors are responsible for this observation. First, a much larger flow of the diesel exhaust had to be mixed with the reactor inlet air which effectively lowers the reactor inlet oxygen level. Flue gas contains typically 11–13 % oxygen (compared to 21 % in ambient air) which is the source for the ozone production. Secondly, the reactor inlet flow contains higher CO_2 and water vapor levels (the relative humidity is similar but the temperature is higher) which affects ozone production.

6.3.2.1 HNO_3 scrubbing in the reactor

Conversion efficiencies could possibly be enhanced by removing gaseous HNO_3 from the gas phase in the reactor. The resulting lower HNO_3 levels shifts the reaction equilibrium towards HNO_3 formation which increases the reaction rate and conversion efficiency. The following methods are attempted to remove HNO_3 from the gas phase and to investigate the effect on conversion efficiency.

- HNO_3 can be removed from the gas phase by conventional wet scrubbing technology [130]. Wet scrubbing in the reactor volume is applied by a nozzle in the reactor inlet. A mist of water aerosols is created in the process gas which dissolves HNO_3 in the reactor volume. NaOH (caustic soda) is optionally added to the scrubbing water to bind/neutralize HNO_3 [131].

- HNO_3 can possibly be scrubbed out the gas phase by a water film on the reactor wall. Process gas which is ionized by the corona discharges is accelerated by the electrical field, resulting in movement of the gas (called corona or electrical wind). Gaseous HNO_3 in or near the discharges could be transferred to the wall and dissolved in the water film.

- Gaseous HNO_3 reacts with gaseous NH_3 which forms NH_4NO_3 (a component of fertilizer) particles [132]. These particles are subsequently electrostatically precipitated in the reactor.

Several experiments have been performed to attempt conversion efficiency enhancement by scrubbing HNO_3 in the reactor. The NO_x reactor inlet level was approximately 30 ppm and the liquid flow of the nozzle was limited to 13 mL/min. Five experiments were performed: no mist, mist, mist with dissolved NH_3, mist with NaOH and a waterfilm on the reactor wall. The experimental conditions are shown in Figure 6.4. NH_3 was dosed using a concentrated aqueous solution. NH_3 should be stoichiometrically dosed with the HNO_3 production to avoid remaining NH_3 leaving the reactor. Two settings were chosen, the NH_3 concentration reactor
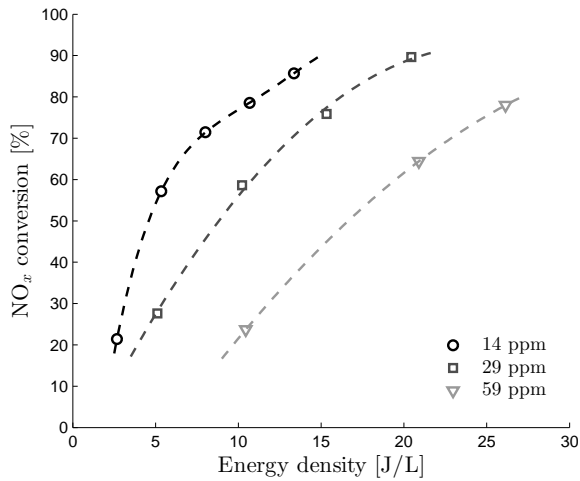
Figure 6.17: NO$_x$ conversion as a function of energy density for multiple inlet concentration levels.
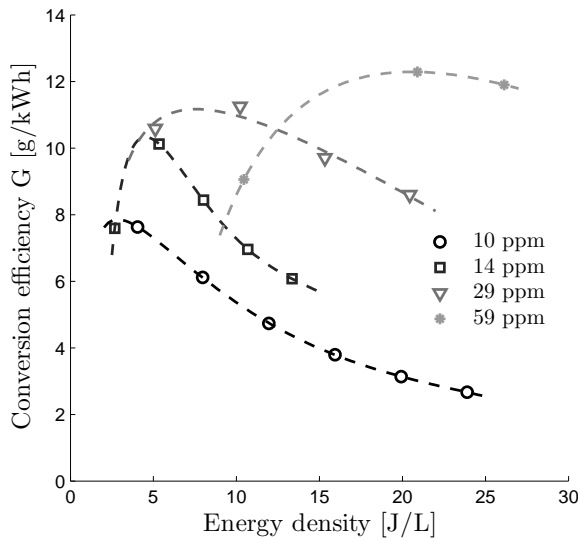
Figure 6.18: NO$_x$ conversion efficiency as a function of energy density for multiple inlet concentration levels.

inlet level was approximately 38 ppm and 132 ppm assumed that all NH$_3$ was evaporated from the spraying water.

The conversion results as a function of the energy density are shown in Figure 6.20. No significant effect could be observed from these experiments. Although differences are minimal, the conversion seems to be highest for no spraying at all. The effluent water of the reactor

178
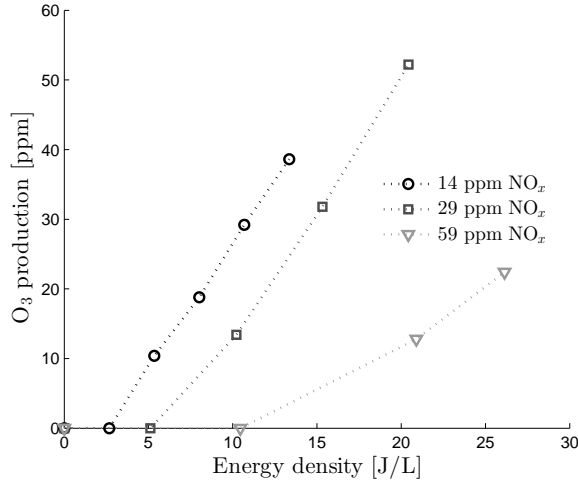
Figure 6.19: O_3 production as a function of energy density for multiple inlet NO_x concentration levels.

Table 6.4: Experimental conditions HNO_3 scrubbing.

Experiment	C_{liq} [g/L]	F_{liq} [mL/min]	C_0 NO_x [ppm]	F [m^3/h]	T [°C]	RH [%]
None	-	-	29	310	27.5	61.5
Water	-	13	29	320	24.4	100
Water+NH$_3$	25	6	34	330	29.0	52
Water+NH$_3$	250	2	31	320	24.4	74.4
Water+NaOH	6.25	13	29	320	24.7	100
Water film	-	-	31	320	23.4	100

(only water spay experiment) was pH 1.8, indicating significant dissolved HNO_3. Addition of NaOH resulted in effluent water with PH 10.7. A complication during these experiments could be precipitation of the water mist. The water aerosols are charged by the corona discharges and transported to the reactor wall by the electric field. Precipitation will be limited in the used reactor. Because it doesn't feature the DC-bias circuit, the electric field is only present during the pulses. Possibly much more intense contact between water and gas is needed for effective scrubbing. To investigate this process, additional research is needed as well as a better way to measure the reactor outlet HNO_3 level. Although quantitative measurement of HNO_3 is difficult, several diagnostic techniques are available [117, 118, 133].

NH_3 injection didn't show any conversion enhancement. A large fraction of the NH_3 remains probably dissolved in the spray aerosol which is only partially precipitated in the reactor. Also the provision of an excess amount of NH_3 (250 g/L, 2 mL/min, 132 ppm gaseous) into the reactor plasma didn't show any conversion enhancement.

Although the conversion efficiency was not improved by the waterfilm, lowering of the pH (during the experiment) of the recycled film water was observed. This is an indication
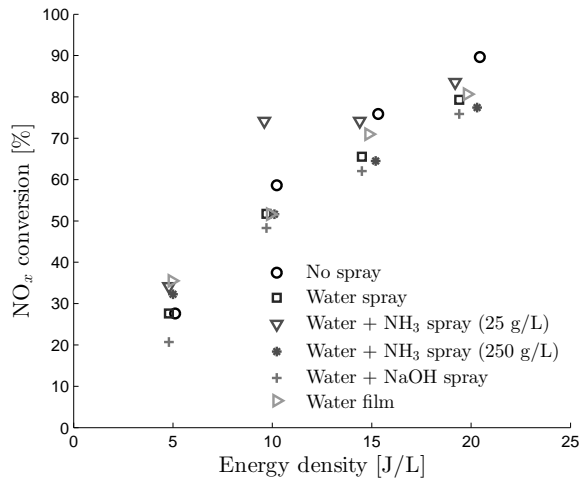
Figure 6.20: NO_x conversion as a function of energy density for multiple water spraying experiments. The additives NH_3 and $NaOH$ are dissolved in the spraying water.

that HNO_3 is dissolved. Hydrogen peroxide (H_2O_2) is a weak acid which is also formed and dissolved at the water–gas interface [134, 135]. The major contribution to the acidity will be by HNO_3.

There isn't any indication that shifting the reaction equilibrium of HNO_3 is achieved by scrubbing in the reactor at 30 ppm inlet level NO_x. Enhancement of conversion efficiencies with scrubbing is possibly noticeable with NO_x reactor inlet levels which are an order of magnitude higher. The acidity of spray water indicates removal of HNO_3 from the gas phase. Further investigations are needed to determine the effectiveness of scrubbing and HNO_3 removal rate. Qualitative measurement of gaseous HNO_3 is hereby needed. An additional conventional wet-scrubber will be needed if scrubbing in the reactor proves to be insufficient. Some form of scrubbing wil always be needed in the reactor to prevent corrosion of the reactor interior by acidic oxidation products. A water film would be preferred because it causes minimal high voltage problems and also removes precipitated dust from the reactor walls. Water mist increases the arcing probability in the reactor, especially with high DC-bias voltages.

6.3.2.2 Field NO_x conversion results (incineration plant)

A field test was performed at an incineration plant. The plant already uses selective catalytic reduction (SCR) with ammonia [136] to reduce NO_x emissions. NO_x emissions are reduced to 60–70 ppm with the SCR. Experiments with the demonstrator were performed to reduce the remaining NO_x. The demonstrator corona reactor was placed near the plant and connected via a 30 m pipe to the smokestack. The flow through the corona reactor was only 485 m^3/h of the total 100.0000 m^3/h in the smokestack. The temperature of the process gas was 50–60°C in the smokestack. The oxygen content was 13 %. The water-saturated gas cooled down to 31.5°C before entering the reactor. An additional condensation trap was placed between connection pipe and reactor inlet to prevent condensation from seeping into the reactor. Four
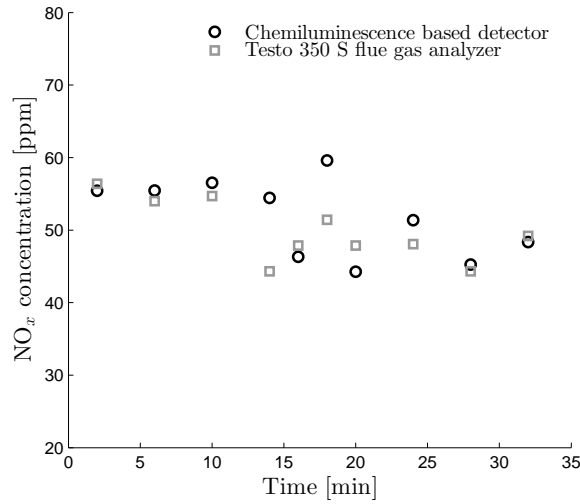
Figure 6.21: Comparison of the NO_x concentration measured in the smokestack and reactor inlet at a incineration plant.
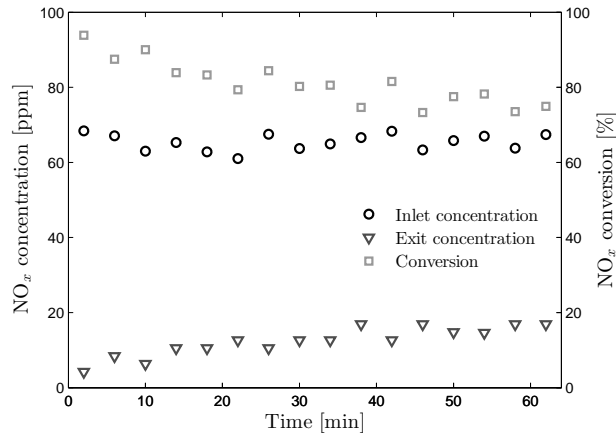
Figure 6.22: NO_x concentration and conversion level during a 60 minute run at a incineration plant.

venturi nozzles provided a mist with a flow of 20.6 L/h in the reactor inlet. The plant was equipped with a chemiluminescence based NO_x detector for permanent process control. Only the exit concentration levels of the corona reactor were measured with the Testo 350 S flue gas analyzer (with additional sample conditioning for ozone removal). A comparison between measurement values of both analyzers with the plasma off is shown in Figure 6.21. The values were measured with 4 minute intervals appear to be very similar.

The results of a 60 min run at 13.1 J/L are shown in Figure 6.22. Approximately 80 % conversion was achieved, resulting in a reactor exit concentration of less than 20 ppm. The

spraying water was pH 8 and the condensation water in the inlet pipe was pH 7. Effluent water of the reactor was pH 4.0, indicating scrubbing of HNO_3. Another observation was presence of CO levels up to 11 ppm in the reactor exit, while the smoke stack CO level was only a few ppm. Flue gases contain high concentration levels CO_2 which can be partially dissociated to CO by the plasma [137].

6.3.3 VOCs

6.3.3.1 Toluene conversion results

The results have been published by Hoeben et al. in [106]. Table 6.5 presents conversion levels of toluene as a function of the energy density (E_d). X_{GCMS} is the conversion level of (only) toluene, detected by the GCMS. $X_{Integral}$ is the integral hydrocarbon conversion level detected by the ABB FID. The experimental conditions were as follows: initial toluene concentration $C_0 = 70$ ppm, the reactor gas temperature $T = 25$ °C, the relative humidity $RH = 57$ %, reactor flow $F = 150$ m^3/h. It appears that a toluene conversion level of 74 % can be reached with an energy density of 92 J/L, the observed oxidation product spectrum still contains 26 % of non-oxidized toluene. The conversion efficiency G corresponds to G = 7.6 g/kWh.

Comparable toluene degradation efficiencies have been reported for dielectric barrier discharges [138,139] and DC positive corona [140], where it should be noted that large differences under experimental conditions apply (flow rate, reactor dimensions and reactor temperature). The toluene conversion determined by the ABB FID is obviously biased because the device measures all hydrocarbons integrally. Oxidation lowers the FID response of hydrocarbons depending on the degree of oxidation [121, 122]. Measured conversion levels will therefore represent lower limit values.

Figures 6.23(a) and 6.23(b) show the oxidation product spectrum as a function of the energy density. The output signal of the MS is the total ion current (TIC), the retention time of the eluting compounds is on x-axis of the figures. Each peak represents a different compound and the surface area of the peak is ideally proportional to the concentration level of that compound. The sensitivity of the MS is different for each component, separate calibration of each compound would be required for qualitative analysis. During this study only the MS is used for compound identification and determination of conversion levels.

Spectra recorded at zero energy density ($E_d = 0$ J/L) represent the gas composition without corona treatment. Figure 6.24 shows the GC-TIC spectrum recorded at the highest energy density (92 J/L), the identified peaks are numbered and declared in the table. The GC-TIC spectrum is explained as follows. The first very broad and intense peak at $t_R = 2.50$ min in Figure 6.23a represents the unseparated species e.g. ambient air background (containing nitrogen, oxygen, argon, carbon dioxide) and other unretained gaseous products released from toluene oxidation also elute here, including the nitrogen oxides produced by the electrical discharges in air. The applied SGE FFAPBP21 GC-column is not able to separate all compounds as explained before. Toluene elutes subsequently after 4.25 min. The detector gain is now increased at 4.80 min to detect the oxidation compounds which are present in lower concentration levels. The enhanced sensitivity also introduces an increased base. It is remarkable that the observed oxidation product spectrum is relatively simple. The largest peaks originate from acetic acid CH_3COOH, formic acid $HCOOH$ and benzaldehyde C_6H_5CHO. With oxidation progress, the carboxylic acid signal increases, while the benzaldehyde signal seems to remain constant. This is explained by the fact that as long as toluene conversion is incomplete, partial
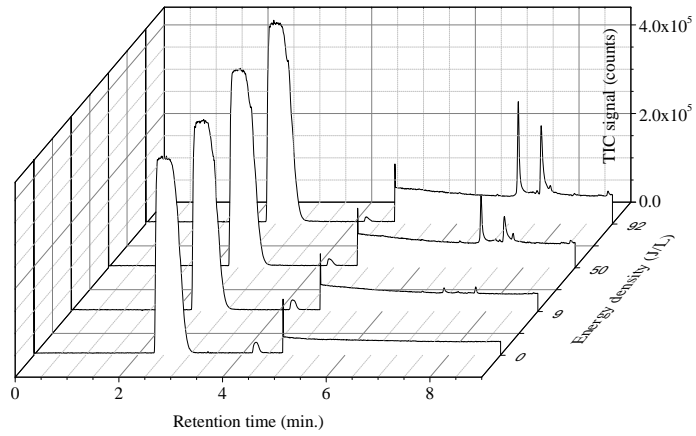
(a) GC-MS data
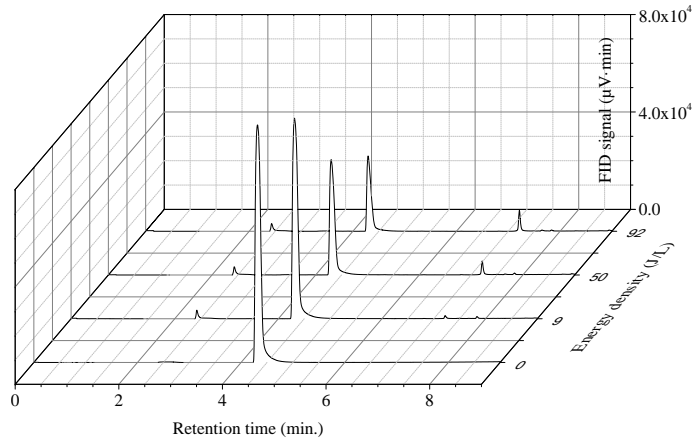
(b) GC-FID data

Figure 6.23: Toluene GC-MS and GC-FID conversion results. It should be noted that the detector gain of the MS is increased after 4.8 minutes

Table 6.5: Toluene conversion results

E_d [J/L]	X GCMS [%]	X Integral C [%]	G [g/kWh]
9	17	10	17.6
50	55	41	10.6
92	74	55	7.6

183

Peak	Compound name
1	Acetic acid
2	Ethanediol diformate
3	Formic acid
4	Benzaldehyde
5	3-Methyl-2,5-furandione
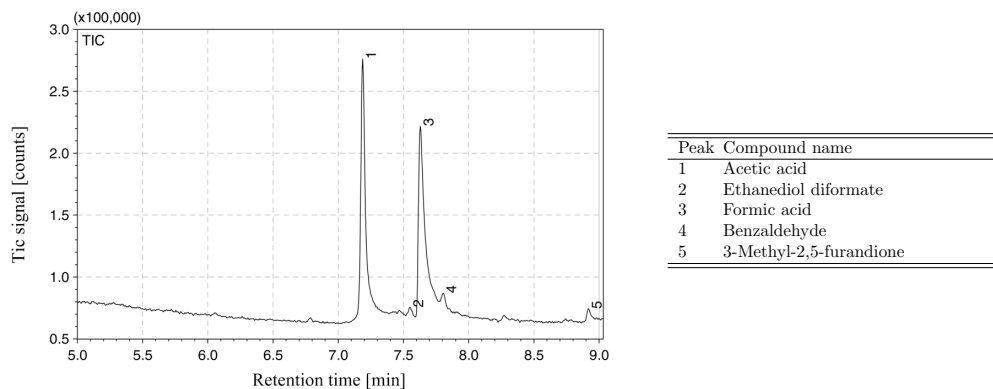
Figure 6.24: Detailed GC-MS spectrum of the toluene oxidation products at 92 J/L. The numbers at the identified peaks in the left figure correspond to the number in the table.

oxidation to benzaldehyde is possible. Sufficient organic carbon is simultaneously available to produce simple carboxylic acids.

Accurate determination of the toluene conversion is enabled by the GC-FID spectrum. Formic acid cannot be properly detected by the FID because the equivalent carbon response ranges from insignificant to very weak [141]. This can be observed in Figure 6.23, the evolution of the acetic acid signal runs parallel to the mass spectrometer TIC signal but is almost invisible in the GC-FID spectrum.

Formation of the observed oxidation compounds is explained in detail in [106]. Hydroxyl radical, oxygen and ozone are key reactive oxygen species in the corona-induced degradation of toluene in air. Additional degradation reactions will occur due to electrical discharge-induced UV photons and collisional impact of excited and metastable species, energetic electrons and ions. For instance, ring cleavage by excited nitrogen species is a known degradation mechanism in cracking of hydrocarbons [138, 142].

6.3.3.2 Limonene conversion results

Table 6.6 presents conversion levels of limonene as a function of the energy density (E_d). The experimental conditions were as follows: initial limonene concentration $C_0 = 10$ ppm, the reactor gas temperature $T = 24$ °C, the relative humidity $RH = 41.7$ %, reactor flow $F = 150$ m^3/h. It appears that limonene is very easily oxidized, conversion is complete at an energy density of 11 J/L. The conversion efficiency is 18.5 g/kWh at this energy density. Increasing the energy density beyond 11 J/L actually lowers the conversion efficiency because it is based on the energy input relative to the conversion level (which is already 100 %). The oxidation state of the product spectrum is naturally increased at these higher energy densities. Plasma-induced limonene conversion efficiencies are not present in literature. Only data on conversion of the limonene isomer α-pinene have been reported, once [143]. The conversion efficiency of 400 ppm α-pinene was reported to be 39 g/kWh.

Figures 6.25(a) and 6.25(b) present the GC-TIC and GC-FID chromatograms as a function of the energy density. All GC-TIC chromatograms have been presented with peak identifi-

cation (see figures 6.26(a)-(c)) because the product spectrum significantly changes with the applied energy density. Again, the broad peak at $t_R = 1.80$ min represents the unseparated compounds. Limonene elutes after $t_R = 4.55$ min and the detector gain is increased at $t_R = 5.00$ min. The limonene conversion has been determined from the GC-FID chromatogram. Limonene oxidation is characterized by the appearance and disappearance of a complex spectrum of species. Intermediate products from partial oxidation are typically epoxides such as limonene oxide and limonene dioxide. Epoxides generally have strong tissue sensitizing and allergenic properties [144] and have often been linked to carcinogenic, mutagenic and cytotoxic potential [145]. Therefore, sufficiently high-energy densities should be applied to avoid formation of intermediate oxidation products which possess a higher level of harmfulness than the target compound. Figures 6.26(a)-(c) confirm that the epoxides are not present at the highest applied energy density.

Similar to toluene oxidation, limonene oxidation also shows typical acetic acid and formic acid signal appearance and increase as a function of the energy density. A wide variety of saturated and unsaturated hydrocarbons with single or multiple oxygen functionality appear, e.g. ketones, esters, epoxides and carboxylic acids. Applying energy density levels beyond mentioned values will result in further oxidation and, finally mineralization. Compared with the degradation of toluene, limonene oxidation is more complex, because the molecule has a more complex structure. The resulting product spectrum is therefore much more diverse. Formation of the observed oxidation compounds is discussed in detail in [106].

6.3.4 H_2S and NH_3

6.3.4.1 H_2S conversion results

The conversion results for three reactor inlet concentration levels are shown in Figure 6.27. The experimental conditions were as follows: initial H_2S concentrations $C_0 = 9$, 19 and 31 ppm, the reactor gas temperature $T = -4$ °C (outdoor experiment in the winter), the relative humidity $RH = 68$ %, reactor flow $F = 420$ m^3/h. A conversion rate near 100 % was achieved. The SEI values are 3.4, 5.1 and 8.0 J/L for respectively 9, 19 and 31 ppm. The linear conversion trend results in conversion efficiencies which are almost independent of the energy density. The G-values were 7.4, 10.4, and 10.8 g/kWh for respectively 9, 19 and 31 ppm inlet concentration. Liang [146] reports 1.8–7.3 g/kWh conversion efficiency in their DBD reactor.

Reduction to elementary sulfur and hydrogen gas is possible in oxygen free conditions [111]. H_2S in ambient air is oxidized by O and OH radicals to SO_2, SO_3 H_2SO_3, (sulfurous acid) and H_2SO_4 (sulfuric acid) [147]. These compounds can be removed by conventional scrubbing technology or possibly by scrubbing in the reactor. The detection limit of sulfuric acid for the human sense of smell is 1 mg/m^3 or 232 ppb [148, 149], The odor threshold will be increased by a factor of 494 if H_2S is converted up to 100 %. Conversion of H_2S by pulsed corona could be sufficient to solve the odor problem if allowable sulfuric acid emissions are not violated. Effective scrubbing should else be applied.

6.3.4.2 NH_3 conversion results

The experimental conditions were as follows: initial NH_3 concentration $C_0 = 13.5$ ppm, the reactor gas temperature $T = 9$ °C, the relative humidity $RH = 83$ %, reactor flow $F = 420$ m^3/h.
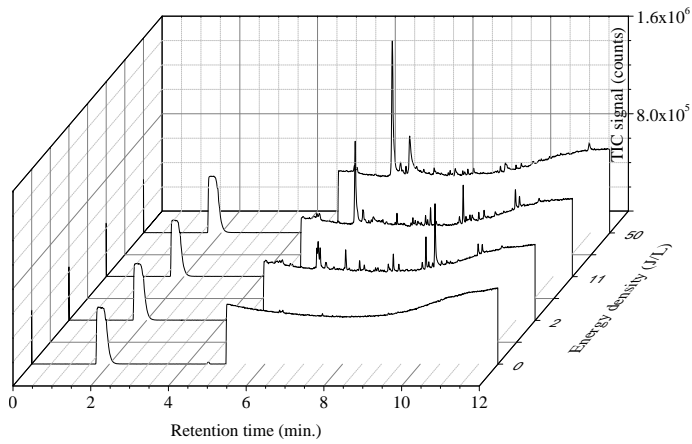
(a) GC-MS data
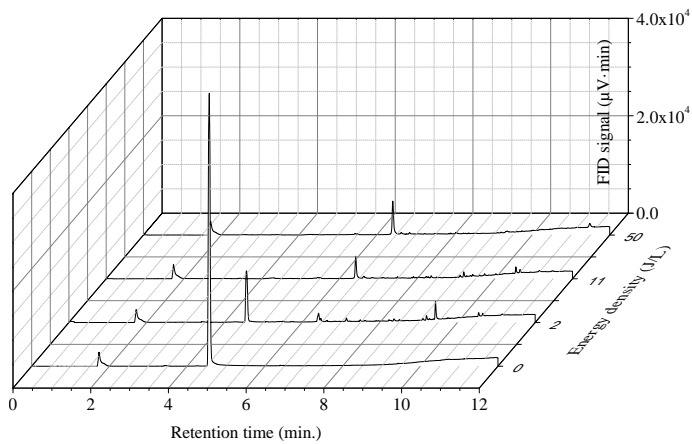
(b) GC-FID data

Figure 6.25: Limonene GC-MS and GC-FID conversion results.

Table 6.6: R(+) Limonene conversion results

E_d [J/L]	X GCMS [%]	X Integral C [%]	G [g/kWh]
2	81	67	88.7
11	100	90	18.6
50	100	96	3.9
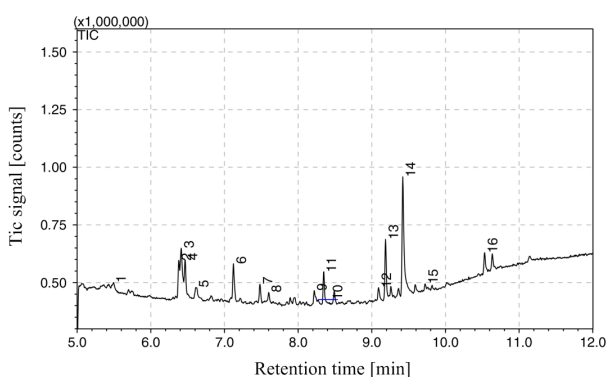
Peak	Compound name
1	1-Hydroxy-2-propanone
2	Trans-p-menta-1 (7),8-dien-2-ol
3	Acetic acid
4	Trans-lirnonene oxide
5	2-Butanone
6	4-Acetyl-1-methylcyclohexene
7	2-Aceionylcyclopentanone
8	Cis-dihydrocarvone
9	3-A ceton ylcyclopentanone
10	3-Methylene-2,6-heptanedione
11	(E)-2-hexen-1-ol acetate
12,14	Limonene dioxide isomers
13	Trans-2-dodecen-1-ol acetate
15	Trans-2-methy1-5-(1-methylethyl)-cyclohexanone
16	Menthyl acetate

(a) $E_d = 2$ J/L
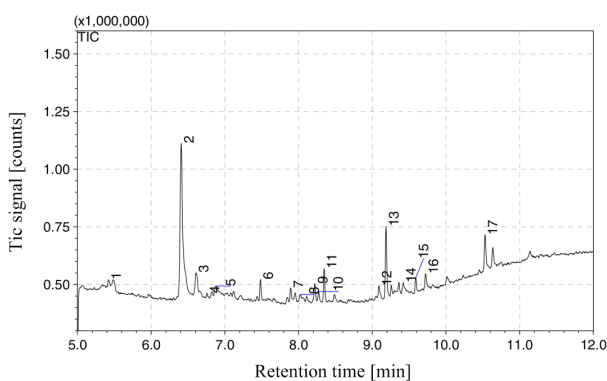
Peak	Compound name
1	1-1-1ydroxy-2-propanone
2	Acetic acid
3	2-Butanone
4	1,2-Ethanediol diformate
5	Formic acid
6	2-Acetonylcyclopentanone
7	3,4-Dimethy1-2,5-hexanedione
8	2,5-Hexanedione
9	3-Acetonylcyclopentanone
10	3-Methylene-2,6-heptanedione
11	(Z)-2-hexen-1-n1 acetate
12,14	Limonene dioxide isomer
13	Trans-2-dodecen-1-ol acetate
15	1,5-Dimethy1-7-oxabicyclo[4.1.0]heptane
16	Trans-2-methyl-5-(1-methylethyl)-cyclohexanone
17	Menthyl acetate
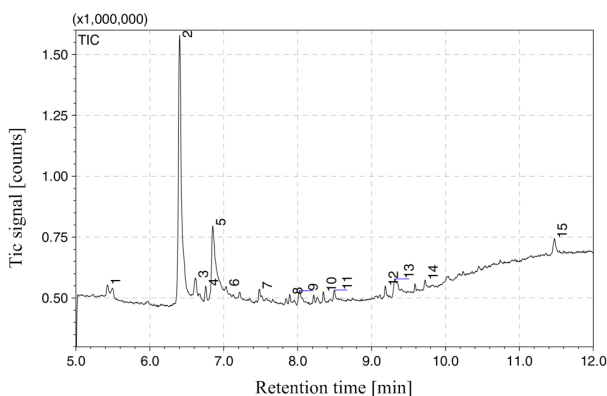
(b) $E_d = 11$ J/L

Peak	Compound name
1	1-Hydroxy-2-propanone
2	Acetic acid
3	2-Butanone
4	1,2-Ethanediol diformate
5	Formic acid
6	4-Hydroxypentenoic acid
7	2,3-Dihydroxypropenal?
8	1-Propen-2-al acetate
9	2,5-Hexanedione
10	(E)-2-hexen-1-ol acetate
11	Formamide
12	Trans-2-dodecen-1-ol acetate
13	2-Methoxy-1,3-dioxolane
14	Trans-2-methyl-5-(1-methylethyl)-cyclohexanone
15	2-Methyl-1 ,3-dioxolane

(c) $E_d = 50$ J/L

Figure 6.26: Detailed GC-MS spectrum of the limonene oxidation products at multiple energy densities. The numbers at the identified peaks in the left figures corresponds to the numbers in the tables.
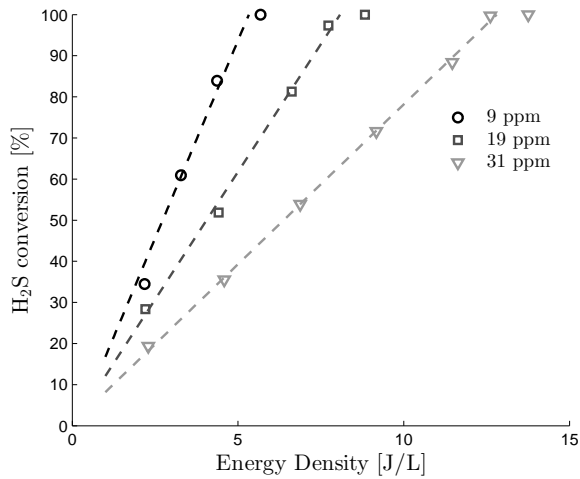
Figure 6.27: H_2S conversion as a function of the energy density for multiple inlet concentration levels.
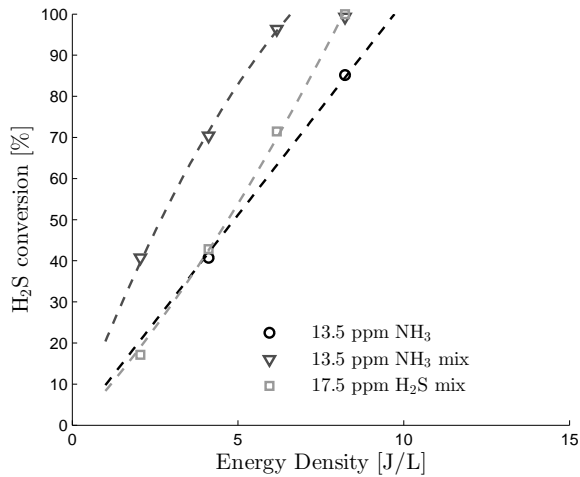
Figure 6.28: NH_3 and H_2S conversion as a function of the energy density. The second and third line plot are the conversion results of 13.5 ppm NH_3 and 17.5 ppm H_2S mixed together.

The conversion result of 13.5 ppm NH_3 is shown in Figure 6.28. The second and third line plot are the conversion results of 13.5 ppm NH_3 and 17.5 ppm H_2S mixed together. The SEI value for (only) 13.5 ppm NH_3 conversion is 6.2 J/L. The conversion efficiency is 3.7 g/kWh at the SEI value. Literature reports comparable results. Xia [110] reports a conversion efficiency of 2 g/kWh ($C_0 = 40$ ppm) with a DBD reactor and Ruan [150] reports 3 g/kWh ($C_0 = 147$ ppm) with a pulsed corona reactor. NH_3 reacts with O_3 and

forms NH_4NO_3 aerosols, intermediate products are NH_4NO_2 and H_2O_2 (hydrogen peroxide) [151–153]. Another conversion path is via the plasmas intrinsic NO_x production which is is oxidized to HNO_3 and reacts subsequently with NH_3 [110, 132, 150] which is also results in NH_4NO_3 aerosol formation.

An interesting result is revealed when 13.5 ppm NH_3 is mixed with 17.5 ppm H_2S. The SEI value for NH_3 conversion drops from 6.2 J/L to 3.2 J/L and the conversion efficiency increases from 3.7 g/kWh to 6.7 g/kWh. Clearly there is synergy between the reaction paths of these compounds. The SEI value for the H_2S conversion is 5.7 J/L with 10.2 g/kWh conversion efficiency. This result is slightly less efficient than the conversion of 19 ppm H_2S in Figure 6.27.

6.3.5 Particulate matter removal

Multiple conventional technologies are available which can reduce particulate matter e.g. cyclonic separators, fabric filter collectors (baghouses), wet scrubbers, and electrostatic precipitators (ESP) [154]. The corona reactor is with respect to dust removal no more than the latter ESP. The corona discharges ionize the air and charge particles in the reactor. The DC-bias voltage on the reactor wires generates an electrostatic field in which the charged particles deflect and migrate towards the wall as they pass through the reactor. The particles are collected on the wall and will build up a layer if they are not constantly removed. Pulsed corona for air purification does not focus on dust removal but it is seen as a beneficial feature of the technology. Collection efficiencies of ESPs heavily depend on the electric field strength, reactor residence time, resistivity and size of the particles. ESPs with high flow throughput and high collection efficiencies (e.g. 99.9 %) are enormous in size. The corona reactor should have similar sizes to achieve the same collection efficiency. The size of a pulsed corona reactor is limited by electrical characteristics as discussed in Chapter 5 and does not need to be large for efficient plasma processing. High particle collection efficiencies are not expected since the reactor is build for plasma processing.

The collection efficiency of the reactor was tested during the NO_x field test at the traffic tunnel. Early exploratory measurements showed no effect of the energy density on particle collection, even with very low repetition rates (a few Hz). Significant effect was naturally observed from the DC-bias voltage. The higher the voltage, the higher the collection efficiency.

The removal as function of inlet dust concentration of a 5 hour measurement can be observed in figures 6.29–6.31, 3 hours with the corona reactor enabled (pulse and DC-bias) and 2 hours with the power source disabled. The DC-bias voltage was 20.1 kV and the energy density 10.5 J/L. The PM values have been reported in ranges of particle sizes: 0.25–1 μm, 1–2.5 μm and 2.5–10 μm.

The reactor is able to collect particles even when the power source is disabled. During this experiment, the air flow through the reactor was from bottom to top. The air velocity in the reactor is much lower than in the piping due to the large volume of the reactor. Especially large particles do not seem to remain suspended in the slow moving gas stream. Except for very low concentration levels (<20 μg/m^3) of the 0.25–1 μm particle range, less than 10 % was collected by the reactor. The average dust collection with the power source disabled is 59 %, 40 % and 18 % for respectively the 2.5–10 μm, 1–2.5 μm and 0.25–1 μm particle size range. This result is directly related to the observed inlet concentration levels of the different particle sizes. Smaller particles are more likely to stay suspended in the air. The 2.5–10 μm
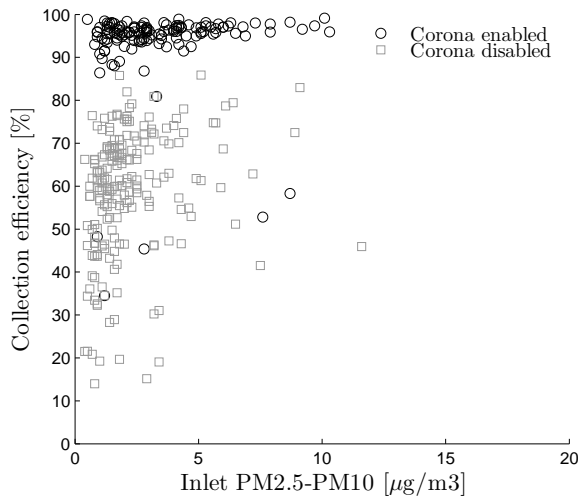
Figure 6.29: Collection efficiency of particle sizes between 2.5 μm and 10 μm as a function of reactor inlet concentration level, 10.5 J/L & 20.1 kV DC.
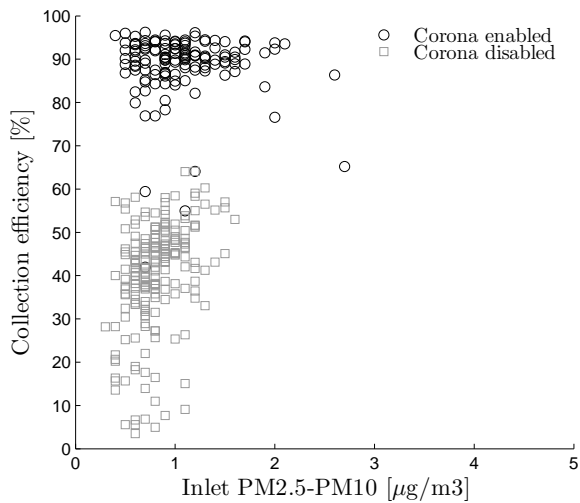
Figure 6.30: Collection efficiency of particle sizes between 1 μm and 2.5 μm as a function of reactor inlet concentration level, 10.5 J/L & 20.1 kV DC.

particle range is only present up to 10 μg/m^3, while the inlet contains up to 250 μg of the smallest particles. Probably a difference of several orders of magnitude in particle numbers.

With the power source enabled, the collection efficiency of the largest particle range is the highest, 94 % on average. The collection efficiency lowers as the particle size decreases to 89 % and 58 % for respectively the 2.5–10 μm and 1–2.5 μm range. The total collection efficiency
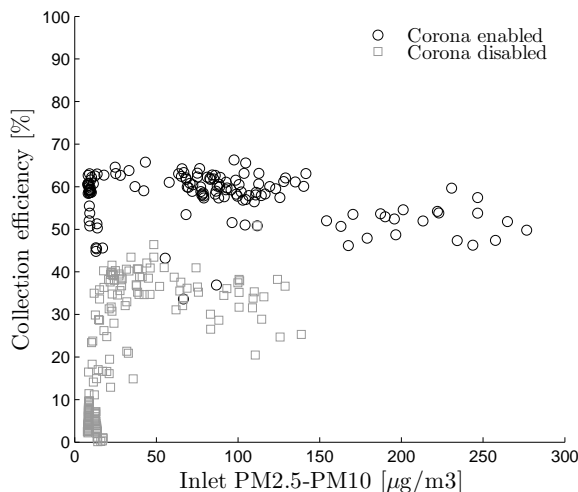
Figure 6.31: Collection efficiency of particle sizes between 0.25 μm and 1 μm as a function of reactor inlet concentration level, 10.5 J/L & 20.1 kV DC.

(PM10, 0.25–10 μm) is 60 %. Strong dependencies on the inlet concentration level were not observed. Migration of particles to the reactor wall will be less direct for smaller particles which results in lower collection efficiencies. The inertial effects of the gas flow dominate over the electrical velocity induced by the relatively smaller electric charge of the particle [155].

6.4 Conclusions

An overview of the conversion results for different compounds is shown in Table 6.7. The conversion efficiencies G are calculated according to the equations in Table 6.2.

Table 6.7: Overview of the conversion results

Compound	C_0 [ppm]	SEI [J/L]	G [g/kWh]	G [nmol/J]	G [1/(100 eV)]
NO_x	10–59	7.0-20.5	7.8–12.3	47.1–74.2	0.45–0.72
Toluene	70	92.0	7.6	23.0	0.22
Limonene	10	2.0	88.6	181.0	1.74
H_2S	9–31	3.4–8.0	7.4–10.8	60.5–88.2	0.58–0.85
NH_3	14	6.2	3.7	60.5	0.58

NOx Removal of low levels NO_x proves to be difficult. The (sub)ppm level chemilu-minescence based Airpointer NO_x detector is cross sensitive for HNO_3 and high levels of O_3. Sample conditioning had to be applied to remove these components from the sample gas before entering the detector. The SEI value is approximately 7 J/L for 10 ppm NO_x removal.

NO_x removal levels of 60-80% were obtained for reactor inlet concentrations of 2-10 ppm at energy densities of 5-10 J/L. The energy density of $E_d = 10.5$ J/L gives a better G-yield than $E_d = 5.2$ J/L for inlet concentrations smaller than 3000 ppb. The pulsed corona discharges intrinsically produce ppm level NO_x at high energy densities, limiting the removal of low inlet levels. Energy levels of >20 J/L are required to reduce the NO_x levels to ca. 500 ppb, the sum of residual nitrogen oxides ($NO_x + HNO_3^{\dagger}$) is however >2000 ppb. Pulsed corona technology could be suitable for tunnel air purification when combined with a gas pre-concentration operation. NO_x levels in the tunnel should first be accumulated to ppm level for efficient removal by pulsed corona. The exit gases of the reactor should be treated by a conventional wet scrubber to remove HNO_3 and by activated carbon or catalyst to remove residual O_3.

The SEI values for converting 14, 29 and 59 ppm NO_x are respectively 6.2, 11.5 and 20.5 J/L. The conversion efficiencies for the SEI values are 9.7, 10.7 and 12.3 g/kWh. The intrinsic NO_x production becomes less dominant and radicals are used more efficiently resulting in improved conversion efficiencies for higher inlet concentration levels. Up to 80 % conversion of 60-70 ppm NO_x was obtained at an incineration plant during a field test. Flue gases contain high concentration levels CO_2 and can be partially dissociated by the plasma which resulted in ppm level CO formation.

VOCs The oxidative degradation of toluene requires energy densities up to 92 J/L. The G-value is 7.6 g/kWh at 74 % conversion of 70 ppm toluene. Obtained data are comparable with the literature references. The toluene degradation product spectrum is simple and exhibits acetic and formic acid formation with increasing energy density, together with a limited number of other intermediate oxidation products.

Conversion of limonene requires only 2 J/L. The G-values is 88.6 g/kWh at 81% conversion of 10 ppm limonene. The limonene degradation product spectrum is complex, featuring ketones, esters, epoxides and carboxylic acids. Again, energy density-dependent formation of acetic and formic acid formation has been observed and high energy densities are required to degrade by–products. Although limonene is easily oxidized at only a few J/L, toxic intermediate oxidation products at these low energy densities are observed. Up to 50 J/L is required to reduce these intermediate compounds to an acceptable level. Resolving the degradation product spectrum is therefore very important.

H_2S & NH_3 A conversion rate near 100 % was achieved for H_2S. The SEI values are 3.4, 5.1 and 8.0 J/L for respectively 9, 19 and 31 ppm. The linear conversion trend results in conversion efficiencies which are almost independent of the energy density. The G-values were 7.4, 10.4, and 10.8 g/kWh for respectively 9, 19 and 31 ppm inlet concentration. Results are comparable with literature. H_2S in ambient air is oxidized to H_2SO_3 (sulfurous acid) and H_2SO_4 (sulfuric acid). These compounds can be removed by conventional scrubbing technology or possibly by scrubbing in the reactor. The odor threshold (H_2S compared to H_2SO_4) will be increased by a factor of 494 if the conversion is 100 %.

The SEI value for (only) 13.5 ppm NH_3 conversion is 6.2 J/L. The conversion efficiency is 3.7 g/kWh at the SEI value. Also comparable with literature. Oxidation of NH_3 results in NH_4NO_3 aerosol aerosol formation which could be precipitated by the reactor. Synergy was observed if H_2S and NH_3 were oxidized simultaneously. 13.5 ppm NH_3 mixed with 17.5 ppm

H_2S resulted in an SEI value of 3.2 J/L for NH_3 and an increase of the conversion efficiency to 6.7 g/kWh. Based on these results we can conclude that factory farming could be a very interesting application.

Particulate matter   Although the reactor is not optimized for particle collection, reasonable results were achieved during the NO_x field test. The collection efficiency of the largest particle range is the highest, 94 % on average. The collection efficiency lowers as the particle size decreases to 89 % and 58 % for respectively the 2.5–10 μm and 1–2.5 μm range. The total collection efficiency (PM10, 0.25–10 μm) is 60 %. Strong dependencies on the inlet concentration level were not observed.

7

Conclusions & recommendations

Nanosecond pulsed plasmas offer superior plasma processing efficiencies for a variety of air purification applications, but multiple technical challenges need te be resolved for successful introduction of the technology into the market. The power level and the repetition rate of the plasma system needs to be increased. Typically tens or hundreds of kilowatts of corona power is needed for industrial applications. Reactors need to be designed for large flow handling and large plasma volumes. Finally, the technology should be proven in practice and customers in the air purification business need to be convinced of the benefits of the technology.

The following project goals resulted from these challenges:

- Development of a robust and fully autonomous pulsed corona demonstration unit which can be applied for on-site air purification pilots.
- Exploring multiple air purification applications with the demonstration unit.
- Development and characterization of an efficient pulsed power switch which can operate in the kHz range.
- Life-time and recovery characterization of the spark gap switch. Modeling of the erosion behavior of the spark gap electrodes.
- Study of the energy coupling between pulsed power source and large corona reactors.

In the following sections the results and conclusions are organized in line with the chapter titles in this thesis.

7.1   Pulsed power technology for industrial demonstration

On-site demonstrations in industry of pulsed corona technology are required to verify applications, to estimate energy consumption and to generate interest from costumers. To achieve these goals, an autonomous semi-industrial scale pilot wire-cylinder type corona reactor has been constructed. The demonstration unit consists of a robust sixteen fold wire-cylinder corona reactor and a spark gap based nanoseconds pulsed power supply which has been designed for continuous operation. An additional DC-bias circuit increases the output power of the modulator and enables electrostatic precipitation. The reactor and power supply are incorporated in a 20 feet freight container. Additional ancillary devices monitor e.g. plasma

power, pulse source performance, reactor process flow, temperatures, etcetera. Multiple inter-related systems enable autonomous operation and remote control of the pilot demonstrator. The following conclusions and observations concerning this system can be summarized:

- The power modulator is capable of generating 80 ns FWHM, 20 ns rise time, (up to) 10 J pulses with a maximum repetition rate of 1 kHz. The power supply consists of a resonant capacitor charger, spark gap switch and a transmission line transformer. Although the basic power modulator technology is earlier developed at Eindhoven University of Technology, a next level is reached by creating a robust system which is fully capable to serve in continuous operation.

- Pulsed corona technology was successfully demonstrated during several field pilot tests. The plasma can be generated without any problems in harsh conditions like flue gas. Scrubbing in the reactor with water aerosols or water films does not seem to te introduce problems if high voltage insulators inside are properly designed.

- The overall system efficiency from the mains outlet to the plasma (spark gap purging power included) is approximately 83 % and 70 % for respectively 250 Hz and 800 Hz repetition rate. The efficiency for 800 Hz repetition rate can be improved to 74 % by using spark gap electrodes with a smaller diameter which decreases the required purging flow.

7.2 High repetition rate capacitor charger

Realization of a high power corona system (>10 kW) can be achieved by increasing the repetition rate. A novel circuit topology of a fast 30 kV capacitor charger for spark gap based pulse sources has been introduced and a 5 kHz repetition rate prototype was developed. The dedicated charger can handle fault situations like pre-fires easily and repetitively. The following conclusions and observations can be summarized:

- A 15 kW prototype has been built and proof of concept is demonstrated. The charger is capable of charging a 8.4 nF capacitor to 30 kV in 35 μs with 91 % efficiency. The maximum repetition rate of the charger is 5 kHz.

- An active reset circuit for resetting of the pulse transformer core has been implemented. This circuit is also capable of recovering a large part of the energy which is stored in the stray capacitance of the secondary pulse transformer winding.

- An analytical solution is provided for the magnetization behavior of the pulse trans-former. A numeric simulation tool based on state space modeling is used to simulate the general circuit behavior. Measurements and simulations are in good accordance. A control loop is implemented to regulate the output voltage and to stabilize instabilities generated by random pre-fire events.

7.3 Spark gap characterization

The spark gap is probably the most critical component in the pulsed power system because of the recovery and erosion behavior. Achievable specifications of the switch will determine the road map for up scaling of pulsed corona technology. Impedance, switching speed, recovery and erosion behavior of the spark gap in the demonstration setup is characterized. The 5 kHz

capacitor charger is subsequently applied to characterize high repetition rate operation. The following conclusions and achievements can be summarized:

7.3.1   Recovery

- A novel N_2 closed loop spark gap purging system was developed which enhances the recovery (and thus increases the repetition rate) of the switch efficiently. The required purging power was reduced to 14 % of the transferred power by the switch. This is a major energy saving improvement compared to spark gap switches which are purged with compressed air. Stable operation of the spark gap is ensured by a real-time control system which continuously monitors the breakdown behavior and controls the operating pressure and purging flow.

- The spark gap resistance is typically between 0.1 and 0.25 Ω for air, N_2 and N_2/H_2 (95/5) mixture with electrode distances varying between 2.2 mm and 4.2 mm. The minimum voltage rise times for gap distances 2.2, 3.2 and 4.2 mm are respectively 3 ns, 3.7 ns and 5 ns. The addition of 5 % H_2 improves the switching speed and resistance.

- The required purging flow through the spark gap to fully recover 95 % of all switching cycles is similar for multiple tested electrode materials. Except stainless steel electrodes had a poor recovery for repetition rates above 500 Hz, the poor heat conduction of the material affects cooling down of the electrode surface and gas in the gap.

- A smaller electrode diameter (smaller gap volume) increases the recovery voltage with the same gap flow under all circumstances. The addition of 5 % hydrogen increases the recovery voltage at repetition rates beyond 2500 Hz. The overall best recovery result was obtained with 30 Nm^3/h N_2/H_2 (3 bar) and a 29.5 mm outer diameter copper electrode. The spark gap was able to operate up to 1 kHz in the triggered mode and the voltage recovery voltage was 62 % at 5 kHz repetition rate during continuous pre-fire operation.

7.3.2   Electrode erosion

- Erosion rates of the cathodes were between -0.08 and 15.1 nL/C after $65 \cdot 10^6$ shots. Erosion rates of the anodes were between 4 and 19.6 nL/C. The materials performance ranks as follows: copper > brass > copper/tungsten > stainless steel > tungsten > aluminium. The copper cathode didn't show any erosion and even gained some weight. Copper can apparently be transported from the anode and partially deposited on cathode in a nitrogen environment.

- An analytical and numerical model both based on the heat diffusion equation have been developed. The 1D analytical model assumes a static spark radius, and estimates evaporation at a boiling surface. The 2D (rz-plane) numerical thermal model features a more realistic spark radius which expands according to the trajectory of a shockwave. Time and space resolved heating of the electrode can be simulated, including evaporation and melting. The power input of the models is the product of the measured discharge current and estimated effective fall voltage (V_{eff}) near the electrode.

- Comparison between modeled and experimental data showed that the spark radius should be initially very small. The models indicate that evaporation cannot be the main erosion mechanism and that ejection of liquid material is likely. Tungsten and

copper/tungsten alloy should perform better than pure copper according to the model but copper has less erosion in practise. Tungsten and copper/tungsten are sintered materials which are more brittle (also shown by surface cracks in SEM images). They behave differently and suffer from solid ejection due the strong shockwaves in the discharge. Also the observation of material transferral from anode to cathode improves the erosion behavior of copper. These effects cannot be easily incorporated in the thermal model.

- For recovery, less purging power is required with a smaller electrode surface. Shortening of electrodes by erosion and resulting lifetime of the switch is therefore a compromise between the electrode surface area and purging power. It is estimated that the demonstrator setup can run for several weeks by only adjusting the operating pressure. The copper cathode does not erode but mechanical feeding of the anode (erosion rate: 165 μ m/day, 800 Hz, 40 mm electrode) would be required for long term operation.

7.3.3 Recommendations

- The performance of hydrogen/nitrogen mixtures show improved switching performance. Higher concentration levels of hydrogen could be considered (within safe limits). The effect on electrode erosion should be investigated and the stability of the mixture during closed loop circulation.

- Full recovery of the switch requires large purging flows. Continuous pre–fire operation in a not fully recovered gap could be considered if the jitter on the breakdown voltage is acceptabel for pulsed plasma generation. A trigger circuit will still be required to initialize the first breakdown during start up. Our unique charger concept would be very suitable for this purpose.

- The numerical erosion model should be validated more extensively with additional measured erosion data. Additionally to validate the shockwave model, ICCD imaging could be considered to measure the channel expansion in the spark gap.

7.4 Energizing large corona reactors

Industrial application of nanosecond (ns) pulsed corona technology for air purification requires high volume, high power plasma reactors. Cylinder-wire type reactors require multiple cylinders to meet these demands.

7.4.1 Multiple reactor cylinders

Energy should be equally shared between multiple reactor cylinders. Nanosecond ICCD imaging is applied to the demonstrator reactor to study streamer inception and propagation of the streamer plasma simultaneously in sixteen cylinders. The ICCD images show streamer plasma inception of all cylinders within 9 ns in the sixteen cylinder corona reactor. The streamers propagate to the wall of the cylinders within 80 ns without any significant deviations in the intensity and length of the discharges when comparing the cylinders mutually.

7.4.2 Long reactor cylinders

The reactor cylinders act like coaxial transmission lines wherein high voltage pulses propagate with the speed of light. Interactions between plasma generation and reflection behavior inside the reactor were expected and therefore investigated.

- A 4.5 m long corona reactor is constructed and equipped with voltage and current sensors (8 in total) at multiple positions along the reactor length. The pulse amplitude, pulse rise time and DC-bias level is adjustable. The minimum pulse rise time is 11.5 ns, 80 ns FWHM pulse width and the output voltage is up to 80 kV.

- A lumped element SPICE model is developed to simulate the reflection behavior of the reactor.

- Strong reflections at the end of the reactor are observed during measurements for pulse rise times which are shorter than the transient time of the reactor. Due to overlap of the reflected pulse with the rising edge of the incoming pulse, the rise time at the input of the reactor appears to be longer than the rise time at the end.

- The voltage and current waveform which are measured at the interface of the TLT and reactor are often not giving the correct details of the pulse which propagates initially through the long reactor. For energy measurements this is not a problem, for statements about rate of rise of the reactor voltage it is.

- Local development of the streamers (number of streamers and/or speed) is affected by the reflection behavior resulting in an uneven energy distribution along the reactor. The energy consumption [J/m] at the end of the reactor is higher than near the input connection. Decreasing the rise time of the pulse improves the energy distribution. The input voltage level has little effect on the energy distribution.

- Measured and modeled voltage waveforms are in good agreement. The reflection behavior can be modeled quite accurately. The local development of streamers is not incorporated in the model. The actual energy distribution in the reactor can therefore not be estimated.

- The impedance of the reactor is initially equal to the vacuum impedance of the coaxial structure during the back and forth transient time of the reactor. Streamer development during this time interval does not seem to affect the total impedance.

- Higher source voltages result in an impedance which alters towards and below the output impedance of the TLT. The energy transfer efficiency can be up to 85 % even with reactor impedances which alter below the output impedance of the TLT. Reflections due to impedance mismatches do not seem to reduce the transfer efficiency as long as the DC-bias voltage is high enough to allow reflections to be absorbed by the plasma.

- The reactor length has a minimum effect on the energy transfer efficiency. The pulse reflected from the end of the reactor is damped by the plasma load more for longer reactors. This advantage is redundant for high reactor voltages because damping is already enhanced with higher voltages. A longer reactor improves the energy transfer efficiency slightly because the larger plasma volume causes a lower impedance during the secondary streamer phase.

7.4.3 Recommendations

- Multiple reactor cylinders could be equipped with sensors to measure deviations in the pulses per cylinder. Some reflection behavior is possibly present in the connection structure of the cylinders.

- Boosting of energy transfer to the reactor could likely be achieved by using a larger corona wire diameter which decreases the reactor vacuum impedance. The increased inception voltage (due to smaller E-field around the wire) can be compensated with a higher DC-bias voltage. This will also increase the energy per pulse because the energy delivered by the coupling capacitor scales linearly with the DC-bias voltage.

- A different strategy to increase the corona power and reactor volume could be to use large diameter cylinders. Higher pulse voltages are then needed for plasma generation and more power can be transferred with the same output impedance of the source. Full streamer propagation to the wall of the reactor takes more time so the pulse width can be increased which increases the power input further. The high voltage design will however be more challenging.

- From a plasma chemical processing point of view the non-equal energy sharing in the reactor possibly be an advantage. Pollutants and products can be exposed to different plasma intensities, which could benefit a multiple stage conversion process. Finally, the processing efficiency for higher pulse repetition rates (more homogeneous plasma) could be investigated.

7.5 Plasma processing

Potential industrial applications of pulsed corona technology for air purification were investigated by a series of field and lab experiments. The following applications were investigated: NO_x (flue gas emissions), VOCs (hydrocarbon/solvent emissions), H_2S and NH_3 (factory farming) and fine dust removal (general problem). The main conclusions from this section can be summarized by following items:

- Chemical diagnostics for observing the plasma induced degradation spectrum of compounds often need special attention. Cross sensitivity for ozone was observed in case of low level NO_x chemiluminescence detection and in case of high level NO_x electrochemical cell detection. GC-MS is a versatile tool for studying VOC conversion where suitable columns with specific retention behavior towards polar organic compounds should be applied. Gas sampling from the reactor and direct injection in the GC enables identification of unstable compounds.

- Removal of low levels of NO_x in traffic tunnels proves to be difficult. The pulsed corona discharges intrinsically produce ppm level NO_x at high energy densities, limiting the removal of low inlet levels. NO_x removal levels of 60-80% were obtained for reactor inlet concentrations of 2-10 ppm. The G-yield is actually better with a lower energy density compared to high energy density for inlet concentrations smaller than 3000 ppb NO_x. Pulsed corona technology can be made suitable for tunnel air purification when combined with a gas pre-concentration operation. NO_x levels in the tunnel should first be accumulated to ppm level for efficient removal.

- Removal of high level NO_x was successfully demonstrated at an incineration plant and during lab experiments. Up to 80 % conversion of 60-70 ppm NO_x was obtained. The

conversion efficiencies for converting 14, 29 and 59 ppm NO_x during lab experiments are 9.7, 10.7 and 12.3 g/kWh. The intrinsic NO_x production becomes less dominant and radicals are used more efficiently resulting in improved conversion efficiencies for higher inlet concentration levels.

- In situ scrubbing in the reactor does not seem to improve the conversion efficiency of NO_x. The low pH of effluent water of the reactor however indicates significant dissolved HNO_3.

- The degradation of VOCs requires high energy densities (up to 92 J/L). The degradation product spectra can be complex and can contain toxic compounds if the applied energy density is too low. Carefully monitoring the degradation product spectrum is therefore very important. Acceptable residual products at high energy densities are acetic and formic acid.

- A conversion rate near 100 % was achieved for H_2S. The G-values were 7.4, 10.4, and 10.8 g/kWh for respectively 9, 19 and 31 ppm inlet concentration. The conversion efficiency for 13.5 ppm NH_3 is 3.7 g/kWh.

- Results of particulate matter removal were collected during a field test. The collection efficiency of the largest particle range is the highest, 94 % on average. The collection efficiency lowers as the particle size decreases: 89 % and 58 % for respectively the 2.5–10 μm and 1–2.5 μm range. The total collection efficiency (PM10, 0.25–10 μm) is 60 %. Strong dependencies on the inlet concentration level were not observed.

- The exit gases of the reactor should be treated by conventional technologies to remove residual by–products in cases where their emission limits are violated. The NO_x removal process requires a wet scrubber to remove HNO_3 and activated carbon or catalyst to remove residual O_3. A similar after treatment is possibly required for VOC removal. In case of odor emissions, only conversion of compounds with a low odor threshold for the human sense of smell is required to solve the problem.

7.5.1 Recommendations

- Multiple studies show that after treatment with active carbon or MNO_2 catalyst for ozone removal also enhance conversion efficiencies of VOCs. This would be a way to reduce the required energy density. The required bed sizes of catalytic and active carbon materials are significantly smaller than in conventional processes, but this issue should be investigated more thoroughly.

- Other by-products like HNO_3 during NO_x conversion and acetic/formic acid during VOC removal can be undesired. Scrubbing in the reactor can be effective for removal of these compounds but diagnostics for quantitative gas phase detection equipment should be applied to monitor removal performance.

7.6 Outlook

We have shown that pulsed corona technology can be applied for air purification in practical applications. Energy consumption and investment cost of these systems will ultimately determine wether the technology is able to compete with conventional technologies. One thing

is certain, emission legislation will become stricter in the years to come, creating more opportunities for this technology. Combining pulsed corona with catalysts shows promising results which could widen the application area, reduce energy consumption and reduce residual compounds. Creation of large scale systems which are capable of handling more than 100.000 m^3/h will require smart engineering to reduce the investment cost of the system. As extensively discussed, the switch in the pulsed power system plays a key role. Recent developments in Silicon Carbide semiconductors show promising results. A more modular power supply could be applied to energize small reactor sections if suitable high voltage solid state switches become available and affordable. For the present, gas discharge switches will still be required. Supercritical nitrogen as a switching medium in a spark gap shows promising results for high repetition rate operation. However, the complexity and cost of the switch is increased even further due to the high pressures which are required. After exploring high repetition rate operation the next step would be to explore higher pulse energies. Reactor voltage levels of up to 300 kV and 100 J per pulse could be considered. Larger diameter reactor cylinders can be applied which reduces the complexity of connecting multiple small cylinders. Parallel we need to obtain more insight in the optimal dimensioning of reactors from a plasma processing point of view. The effect of for instance the plasma volume, residence time of the gas and pulse repetition rate should be investigated more thoroughly. Optimal design and cost considerations can subsequently be attempted.

Bibliography

[1]   Ulrich Kogelschatz. Dielectric-barrier discharges: their history, discharge physics, and industrial applications. *Plasma chemistry and plasma processing*, 23(1):1–46, 2003.

[2]   G.J.J. Winands. *Efficient streamer plasma generation, PhD thesis 2007*. Eindhoven University of Technology, 2007.

[3]   Takao Namihira, Shunsuke Tsukamoto, Douyan Wang, Sunao Katsuki, Reuben Hackam, Hidenori Akiyama, Yoshitaka Uchida, and Masami Koike. Improvement of no_x removal efficiency using short-width pulsed power. *Plasma Science, IEEE Transactions on*, 28(2):434–442, 2000.

[4]   T. Huiskamp. *Nanosecond Pulsed Power Technology for Transient Plasma Generation, PhD thesis 2015*. Eindhoven University of Technology, 2015.

[5]   Hyun-Ha Kim. Nonthermal plasma processing for air-pollution control: A historical review, current issues, and future prospects. *Plasma Processes and Polymers*, 1(2):91–110, 2004.

[6]   Yuri P. Raizer, Vitaly I. Kisin, and John E. Allen. *Gas discharge physics*, volume 1. Springer-Verlag Berlin, 1991.

[7]   Ryo Ono and Tetsuji Oda. Dynamics of ozone and OH radicals generated by pulsed corona discharge in humid-air flow reactor measured by laser spectroscopy. *Journal of Applied Physics*, 93(10), 2003.

[8]   Hyun-Ha Kim. Nonthermal plasma processing for air-pollution control: A historical review, current issues, and future prospects. *Plasma Processes and Polymers*, 1(2).

[9]   T.M.P. Briels, J. Kos, E.M. van Veldhuizen, and U. Ebert. Circuit dependence of the diameter of pulsed positive streamers in air. *Journal of Physics D: Applied Physics*, 39(24):5201.

[10]   E.J.M. van Heesch, Yan K., Winands G.J.J. Pemen, A.J.M., F.J.C.M. Beckers, and W.F.L.M. Hoeben. From pulsed power to processing : plasma initiated chemical process intensification, 2012.

[11]   Daniel L. Birx, E.J. Lauer, L.L. Reginato, J. Schmidt, and M. Smith. Basic principles governing the design of magnetic switches. Technical report, California Univ., Livermore (USA). Lawrence Livermore Lab, 1980.

[12]   Young-Wook Choi, In-Wha Jeong, Geun-Hie Rim, E.P. Pavlov, Chang-Sik Choi, Hong-Ki Chang, Mee-Hye Woo, and Seong-Poong Lee. Development of a magnetic pulse

compression modulator for flue gas treatment. *Plasma Science, IEEE Transactions on*, 30(5):1632–1636, 2002.

[13] I.V. Grekhov. Pulse power generation in nano-and subnanosecond range by means of ionizing fronts in semiconductors: The state of the art and future prospects. *Plasma Science, IEEE Transactions on*, 38(5):1118–1123, 2010.

[14] F.J.C.M. Beckers, W.F.L.M. Hoeben, T. Huiskamp, A.J.M. Pemen, and E.J.M. van Heesch. Pulsed corona demonstrator for semi-industrial scale air purification. *IEEE Transactions on Plasma Science*, 41(10):2920–2925, 2013.

[15] Zuo Li, Hou Li'an, and Yang Linsong. The experimental investigations of dielectric barrier discharge and pulse corona discharge in air cleaning. *Plasma Science and Technology*, 5(5):1961.

[16] Ulrich Kogelschatz. Dielectric-barrier discharges: Their history, discharge physics, and industrial applications. *Plasma Chemistry and Plasma Processing*, 2003.

[17] Yajuan Wan, Xing Fan, and Tianle Zhu. Removal of low-concentration formaldehyde in air by DC corona discharge plasma. *Chemical Engineering Journal*, 171(1):314 – 319, 2011.

[18] J. Van Durme, J. Dewulf, W. Sysmans, C. Leys, and H. Van Langenhove. Abatement and degradation pathways of toluene in indoor air by positive corona discharge. *Chemosphere*, 68(10):1821 – 1829, 2007.

[19] A. Fridman and A. Gutsol. Pulsed corona plasma pilot plant for VOC abatement in industrial streams. In *Plasma Assisted Decontamination of Biological and Chemical Agents*. 2008.

[20] G.J.J. Winands, Keping Yan, A.J.M. Pemen, S.A. Nair, Zhen Liu, and E.J.M. van Heesch. An industrial streamer corona plasma system for gas cleaning. *Plasma Science, IEEE Transactions on*, 34(5):2426–2433, Oct 2006.

[21] G. Dinelli, L. Civitano, and Massimo Rea. Industrial experiments on pulse corona simultaneous removal of NO_x and SO_2 from flue gas. In *Industry Applications Society Annual Meeting, 1988., Conference Record of the 1988 IEEE*, pages 1620–1627 vol.2, Oct 1988.

[22] You-Seok Kim, Min-Su Paek, Jeong-Seok Yoo, Tae-Hee Kim, Seok-Ho Choi, and Kil-Ho Moon. Development of demonstration plant using non-thermal plasma process to remove SO_2 and NO_x from flue gas. *Journal of Advanced Oxidation Technologies*, 6(1), 2003.

[23] Yong-Hwan Lee, Won-Suk Jung, Yu-Ri Choi, Jong-Seok Oh, Sung-Duck Jang, Yoon-Gyu Son, Moo-Hyun Cho, Won Namkung, Dong-Jun Koh, Young-Sun Mok, and Jae-Woo Chung. Application of pulsed corona induced plasma chemical process to an industrial incinerator. *Environmental Science & amp; Technology*, 37(11):2563–2567, 2003.

[24] Young Sun Mok, Ho Won Lee, and Young Jin Hyun. Flue gas treatment using pulsed corona discharge generated by magnetic pulse compression modulator. *Journal of Electrostatics*, 53(3):195 – 208, 2001.

[25] E.H.W.M. Smulders, E.J.M. van Heesch, and S.S.V.B. van Paasen. Pulsed power corona discharges for air pollution control. *Plasma Science, IEEE Transactions on*, 26(5):1476–1484, Oct 1998.

[26] Yan Wu, Jie Li, Ninghui Wang, and Guofeng Li. Industrial experiments on desulfurization of flue gases by pulsed corona induced plasma chemical process. *Journal of Electrostatics*, 57.

[27] Toshiaki YAMAMOTO, Masaaki OKUBO, Tomoyuki KUROKI, and Keiichiro YOSHIDA. Pilot-plant experiment for incinerator emission control using plasmachemical hybrid process. *Transactions of the Japan Society of Mechanical Engineers Series B*, 73(732):1767–1774, 2007.

[28] Keping Yan, Ruinian Li, Tianle Zhu, Hongdi Zhang, Xiaotu Hu, Xuedong Jiang, Hui Liang, Ruichang Qiu, and Yi Wang. A semi-wet technological process for flue gas desulfurization by corona discharges at an industrial scale. *Chemical Engineering Journal*, 116(2):139 – 147, 2006.

[29] T.H.P. Ariaans, A.J.M. Pemen, G.J.J. Winands, E.J.M. van Heesch, and Zhen Liu. Ac/dc/pulsed-power modulator for corona-plasma generation. *Plasma Science, IEEE Transactions on*, 37(6):846–851, 2009.

[30] K. Yan. *Corona plasma generation, PhD thesis 2001*. Eindhoven University of Technology, 2001.

[31] P. Zhao, J.A. Siegel, and R.L. Corsi. Ozone removal by HVAC filters. *Atmospheric Environment*, 41(15):3151 – 3160, 2007.

[32] Douglas W. VanOsdell, M. Kathleen Owen, Lawrence B. Jaffe, and Leslie E. Sparks. VOC removal at low contaminant concentrations using granular activated carbon. *Journal of the Air & Waste Management Association*, 46(9):883–890, 1996.

[33] K. Yan, E.J.M. van Heesch, A.J.M. Pemen, P.A.H.J. Huijbrechts, F.M. van Gompel, Z. Matyas, and H. Van Leuken. A 2.0 kw pulsed corona system for inducing chemical reactions. In *Industry Applications Conference, 2000. Conference Record of the 2000 IEEE*, volume 1, pages 592 –599, 2000.

[34] Ewald F. Fuchs and Mohammad A.S. Masoum. *Power Quality in Power Systems and Electrical Machines*. 2008.

[35] Ned Mohan and William P. Robbins Undeland, Tore M. and. *Power Electronics: Converters, Applications, and Design*. 2002.

[36] Paul W. Smith. *Transient Electronics: Pulsed Circuit Technology*. John Wiley & Sons, 2002.

[37] A.P.J. van Deursen, H.W.M. Smulders, and R.A.A. de Graaff. Differentiating/integrating measurement setup applied to railway environment. *Instrumentation and Measurement, IEEE Transactions on*, 55(1):316 – 326, 2006.

[38] F.W. Grover. *Inductance Calculations*. 1964.

[39] In-Wha Jeong, Jong-Soo Kim, G.I. Gusev, and Geun-Hie Rim. Design of 35 kj/s 25 kv capacitor charging power supply for pulsed power systems. In *Industrial Electronics Society, 2004. IECON 2004. 30th Annual Conference of IEEE*, volume 3, pages 2860–2863 Vol. 3, Nov 2004.

[40] S.R. Jang, H.J. Ryoo, J.-S. Kim, and Y.B. Kim. Design and testing of the high voltage capacitor charger for 150kj pulsed power application. In *Pulsed Power Conference, 2009. PPC '09. IEEE*, pages 1376–1379, June 2009.

205

[41]   A.C. Lippincott and R.M. Nelms. A capacitor-charging power supply using a series-resonant topology, constant on-time/variable frequency control, and zero-current switching. *Industrial Electronics, IEEE Transactions on*, 38(6):438–447, Dec 1991.

[42]   M. Souda, F. Endo, C. Yamazaki, K. Okamura, and K. Fukushima. Development of high power capacitor charging power supply for pulsed power applications. In *Pulsed Power Conference, 1999. Digest of Technical Papers. 12th IEEE International*, volume 2, pages 1414–1416 vol.2, June 1999.

[43]   J.M. Burdio and A. Martinez. A unified discrete-time state-space model for switching converters. *Power Electronics, IEEE Transactions on*, 10(6):694–707, Nov 1995.

[44]   P.L. Chapman. Multi-resolution switched system modeling. In *Computers in Power Electronics, 2004. Proceedings. 2004 IEEE Workshop on*, pages 167–172, Aug 2004.

[45]   D. Bortis, J. Biela, and J.W. Kolar. Design and control of an active reset circuit for pulse transformers. *Dielectrics and Electrical Insulation, IEEE Transactions on*, 16(4):940–947, 2009.

[46]   Z. Liu, G.J.J. Winands, K. Yan, A.J.M. Pemen, and E.J.M. van Heesch. A high-voltage pulse transformer with a modular ferrite core. *Review of Scientific Instruments*, 79(1):015104–015104–5, Jan 2008.

[47]   H. Akiyama, T. Sakugawa, T. Namihira, K. Takaki, Y. Minamitani, and N. Shimomura. Industrial applications of pulsed power technology. *Dielectrics and Electrical Insulation, IEEE Transactions on*, 14(5):1051–1064, October 2007.

[48]   J.D. Sethian, M. Myers, I.D. Smith, V. Carboni, J. Kishi, D. Morton, J. Pearce, B. Bowen, L. Schlitt, O. Barr, and W. Webster. Pulsed power for a rep-rate, electron beam pumped krf laser. *Plasma Science, IEEE Transactions on*, 28(5):1333–1337, Oct 2000.

[49]   M. Kristiansen. Pulsed power applications. In *Pulsed Power Conference, 1993. Digest of Technical Papers., Ninth IEEE International*, volume 1, page 6, June 1993.

[50]   G.J.J. Winands, Z. Liu, A.J.M. Pemen, E.J.M. van Heesch, and K. Yan. Long lifetime, triggered, spark-gap switch for repetitive pulsed power applications. *Review of Scientific Instruments*, 76(8):085107–085107–6, 2005.

[51]   S.J. MacGregor, S.M. Turnbull, F.A Tuema, and O. Farish. Enhanced spark gap switch recovery using nonlinear v/p curves. *Plasma Science, IEEE Transactions on*, 23(4):798–804, Aug 1995.

[52]   Electrical breakdown of gases. by j. m. meek and j. d. craggs. oxford (clarendon press), 1953. pp. vii, 507; 320 figs., 82 tables. 60s. *Quarterly Journal of the Royal Meteorological Society*, 80(344).

[53]   S.L. Moran and L.W. Hardesty. High-repetition-rate hydrogen spark gap. *Electron Devices, IEEE Transactions on*, 38(4):726–730, 1991.

[54]   S.J. MacGregor, F.A. Tuema, S.M. Turnbull, and O. Farish. The operation of repetitive high-pressure spark gap switches. *Journal of Physics D: Applied Physics*, 26(6):954.

[55]   J.M Kuhlman and G.M Molen. Performance of high-power gas-flow spark gaps. *AIAA Journal*, pages 1112–1119, 1986.

[56]   Michael S. Mazzola, G.M. Molen, and J.M. Kuhlman. Recovery of a gas-blown spark gap with preionization. In *Power Modulator Symposium, 1988. IEEE Conference Record of the 1988 Eighteenth*, pages 219–222, Jun 1988.

[57] G. Schaefer, M. Kristiansen, and A. Guenther. *Gas Discharge Closing Switches.* Springer, 1990.

[58] S.J. MacGregor, S.M. Turnbull, F.A. Tuema, and O. Farish. Factors affecting and methods of improving the pulse repetition frequency of pulse-charged and dc-charged high-pressure gas switches. *Plasma Science, IEEE Transactions on*, 25(2):110–117, Apr 1997.

[59] Robert L. Watters, James R. DeVoe, Francis H. Shen, John A. Small, and Ryna B. Marinenko. Characteristics of aerosols produced by the spark discharge. *Analytical Chemistry*, 61(17):1826–1833, 1989.

[60] D. Birx, E. Cook, S. Hawkins, S. Poor, L. Reginato, J. Schmidt, and M. Smith. The application of magnetic switches as pulse sources for induction linacs. *Nuclear Science, IEEE Transactions on*, 30(4):2763–2768, Aug 1983.

[61] Jin Zhang, B. van Heesch, F. Beckers, T. Huiskamp, and G. Pemen. Breakdown voltage and recovery rate estimation of a supercritical nitrogen plasma switch. *Plasma Science, IEEE Transactions on*, 42(2):376–383, Feb 2014.

[62] P. Persephonis, K. Vlachos, C. Georgiades, and J. Parthenios. The inductance of the discharge in a spark gap. *Journal of Applied Physics*, 71(10), 1992.

[63] W.D. Greason, Z. Kucerovsky, S. Bulach, and M.W. Flatley. Investigation of the optical and electrical characteristics of a spark gap. *Industry Applications, IEEE Transactions on*, 33(6):1519–1526, Nov 1997.

[64] T.G. Engel, A.L. Donaldson, and M. Kristiansen. The pulsed discharge arc resistance and its functional behavior. *Plasma Science, IEEE Transactions on*, 1989.

[65] T. Bregel, W. Krauss-Vogt, R. Michal, and K.E. Saeger. On the application of w/cu materials in the fields of power engineering and plasma technology. *Components, Hybrids, and Manufacturing Technology, IEEE Transactions on*, 14(1):8–13, Mar 1991.

[66] T. P. Sorensen and V. M. Ristic. Rise time and timedependent sparkgap resistance in nitrogen and helium. *Journal of Applied Physics*, 48(1), 1977.

[67] J.M. Lehr, C.E. Baum, W.D. Prather, and F.J. Agee. Aspects of ultrafast spark gap switching uwb hpm generation. In *Pulsed Power Conference, 1997. Digest of Technical Papers. 1997 11th IEEE International*, volume 2, pages 1033–1041 vol.2, June 1997.

[68] M.J. Kushner, W.D. Kimura, and S.R. Byron. Arc resistance of laser triggered spark gaps. *Journal of Applied Physics*, 58(5):1744–1751, Sep 1985.

[69] J. Mankowski and M. Kristiansen. A review of short pulse generator technology. *Plasma Science, IEEE Transactions on*, 28(1):102–108, Feb 2000.

[70] A.L.D Donaldson. *Electrode erosion in high current, high energy transient arcs, PhD thesis 1989.* 1989.

[71] F.M. Lehr and M. Kristiansen. Electrode erosion from high current moving arcs. *Plasma Science, IEEE Transactions on*, 17(5):811–817, Oct 1989.

[72] F.L. Curzon and M.S. Gautam. The influence of electrode heat transport in spark recovery. *British Journal of Applied Physics*, 18(1):79.

[73] A.B. Parker, D.E. Poole, and J.F. Perkins. The measurement of electrode surface temperature and its role in the recovery of high-current spark gaps. *British Journal of Applied Physics*, 16(6):851.

207

[74] A Faltens, L.L. Reginato, R. Hester, A Chesterman, E.G. Cook, T. Yokota, and W. Dexter. High repetition rate burst-mode spark gap. *Electron Devices, IEEE Transactions on*, 26(10):1411–1413, Oct 1979.

[75] A. Donaldson, M.O. Hagler, M. Kristiansen, G. Jackson, and L. Hatfield. Electrode erosion phenomena in a high-energy pulsed discharge. *Plasma Science, IEEE Transactions on*, 12(1):28–38, March 1984.

[76] J.M. Koutsoubis and S.J. MacGregor. Electrode erosion and lifetime performance of a high repetition rate, triggered, corona-stabilized switch in air. *Journal of Physics D: Applied Physics*, 33(9):1093.

[77] R. Caristi, J.B. Roy, R.L. Brooks, and A.J. Pennell. Practical long-life spark gaps for high-reliability applications. In *Power Modulator Symposium, 1990., IEEE Conference Record of the 1990 Nineteenth*, pages 306–312, Jun 1990.

[78] P.D. Kumar, S. Kumar, R. Thakur, A Upadhay, and T. Raychaudhuri. Erosion and lifetime evaluation of molybdenum electrode under high energy impulse current. *Plasma Science, IEEE Transactions on*, 39(4):1180–1186, April 2011.

[79] H. Edels. Properties and theory of the electric arc. a review of progress. *Proceedings of the IEE - Part A: Power Engineering*, 108(37):55–69, 1961.

[80] F.A.M. Rizk and G.N. Trinh. *High Voltage Engineering*. CRC Press, 2014.

[81] J. Tepper, M. Seeger, T. Votteler, V. Behrens, and T. Honig. Investigation on erosion of cu/w contacts in high-voltage circuit breakers. *Components and Packaging Technologies, IEEE Transactions on*, 29(3):658–665, Sept 2006.

[82] K. Schönbach and H. Fischer. Explosive anode erosion in high current sparks. *Appl. Opt.*, 9(7):1695–1697, Jul 1970.

[83] Wolfgang Finkelnburg. A theory of the production of electrode vapor jets by sparks and arcs. *Phys. Rev.*, 74:1475–1477, Nov 1948.

[84] G.S. Belkin, V. Kiselev, and Ya. Effect of the medium of the electrical erosion of electrodes at high currents. *Sov. Phys. Tech. Phys.*, 1978.

[85] Shao-Chi Lin. Cylindrical shock waves produced by instantaneous energy release. *Journal of Applied Physics*, 25(1), 1954.

[86] P. Bayle, M. Bayle, and G. Forn. Blast wave propagation in glow to spark transition in air. *Journal of Physics D: Applied Physics*, 18(12):2417.

[87] Necati Ozisik. *Finite Difference Methods in Heat Transfer*. CRC Press, 1994.

[88] J. Zhang. *Supercritical fluids for high power switching, PhD thesis 2015*. Eindhoven University of Technology, 2015.

[89] Myron N. Plooster. Shock waves from line sources. numerical solutions and experimental measurements. *Physics of Fluids*, 13(11), 1970.

[90] U. Yusupaliev. Relation between the limiting brightness temperature of expanding pulsed high-current discharges in dense gases and ionization potentials of their atoms. 2007.

[91] D.W. Peaceman and H.H. Rachford Jr. The numerical solution of parabolic and elliptic differential equations. *Journal of the Society for Industrial and Applied Mathematics*, 3(1):28–41, 1955.

[92] In David C. Larsen, editor, *Thermal Conductivity 16*. 1983.

[93] F.J.C.M. Beckers, A.J.M. Pemen, and E.J.M. van Heesch. Streamer inception and propagation in a multiple wire-cylinder pulsed corona reactor. *IEEE Transactions on Plasma Science*, 42(10):2404–2405, 2014.

[94] Lei Zhao, Zhong-Yang Luo, Jian-Yong Xuan, Jian-Ping Jiang, Xiang Gao, and Ke fa Cen. Study of geometry structure on a wire plate pulsed corona discharge reactor. *Plasma Science, IEEE Transactions on*, 40(3):802–810, March 2012.

[95] G.J.J. Winands, Z. Liu, A.J.M. Pemen, E.J.M. van Heesch, K. Yan, and E.M. van Veldhuizen. Temporal development and chemical efficiency of positive streamers in a large scale wire-plate reactor as a function of voltage waveform parameters. *Journal of Physics D: Applied Physics*, 39(14):3010.

[96] M.G. Grothaus and M. Khair. A crossed-flow pulsed corona reactor. In *Pulsed Power Plasma Science, 2001. PPPS-2001. Digest of Technical Papers*, volume 2, pages 1098–1101 vol.2, June 2001.

[97] N. Shimomura, K. Nakano, H. Nakajima, T. Kageyama, K. Teranishi, F. Fukawa, and H. Akiyama. Nanosecond pulsed power application to nitrogen oxides treatment with coaxial reactors. *Dielectrics and Electrical Insulation, IEEE Transactions on*, 18(4):1274–1280, August 2011.

[98] Picosecond high speed iccd camera. `http://www.stanfordcomputeroptics.com/products/picosecond-iccd.html`. Accessed April 4, 2015.

[99] Hongbin Ma and Yuchang Qiu. A study of ozone synthesis in coaxial cylinder pulse streamer corona discharge reactors. *Ozone: Science & Engineering*, 25(2):127–135, 2003.

[100] G.J.J. Winands, Zhen Liu, E.J.M. van Heesch, A.J.M. Pemen, and Keping Yan. Matching a pulsed-power modulator to a streamer plasma reactor. *Plasma Science, IEEE Transactions on*, 36(1):243–252, Feb 2008.

[101] Corona induced non-thermal plasmas: Fundamental study and industrial applications. *Journal of Electrostatics*, 44(1 - 2):17 – 39, 1998.

[102] R. Wigington and N. Nahman. Transient analysis of coaxial cables considering skin effect. *Proceedings of the IRE*, 45(2):166 – 174, 1957.

[103] G.J.J. Winands, Z. Liu, A.J.M. Pemen, E.J.M. van Heesch, and K. Yan. Analysis of streamer properties in air as function of pulse and reactor parameters by iccd photography. *Journal of Physics D: Applied Physics*, 41(23):234001, 2008.

[104] Y.S. Mok. Efficient energy delivery condition from pulse generation circuit to corona discharge reactor. *Plasma Chemistry and Plasma Processing*, 2000.

[105] F.J.C.M. Beckers, W.F.L.M. Hoeben, A.J.M. Pemen, and E.J.M. van Heesch. Low-level NO_x removal in ambient air by pulsed corona technology. *Journal of Physics D: Applied Physics*, 46, 2013.

[106] W.F.L.M. Hoeben, F.J.C.M. Beckers, A.J.M. Pemen, E.J.M. van Heesch, and W.L. Kling. Oxidative degradation of toluene and limonene in air by pulsed corona technology. *Journal of Physics D: Applied Physics*, 45(5):1–14, 2012.

[107] K. Gutsol, T. Nunnally, A. Rabinovich, A. Fridman, A. Starikovskiy, A. Gutsol, and A. Kemoun. Plasma assisted dissociation of hydrogen sulfide. *International Journal of Hydrogen Energy*, 37(2):1335 – 1347, 2012.

[108] Sanil John, Jerry C. Hamann, Suresh S. Muknahallipatna, Stanislaw Legowski, John F. Ackerman, and Morris D. Argyle. Energy efficiency of hydrogen sulfide decomposition in a pulsed corona discharge reactor. *Chemical Engineering Science*, 64(23):4826 – 4834, 2009.

[109] A.P. Shvedchicov, E.V. Belousova, A.V. Polyakova, A.Z. Ponizovsky, and L.Z. Ponizovsky. Oxidation of ammonia in moist air by use of pulse corona discharge technique. *Radiation Physics and Chemistry*, 47(3):475 – 477, 1996.

[110] Lanyan Xia, Li Huang, Xiaohong Shu, Renxi Zhang, Wenbo Dong, and Huiqi Hou. Removal of ammonia from gas streams with dielectric barrier discharge plasmas. *Journal of Hazardous Materials*, 152(1):113 – 119, 2008.

[111] Dennis J. Helfritch. Pulsed corona discharge for hydrogen sulfide decomposition. 1993.

[112] Unites states environmental protection agency. `http://www.epa.gov/airquality/particulatematter/health.html`. Accessed Mei 11, 2015.

[113] S. Gluck, C. Glenn, T. Logan, B. Vu, M. Walsh, and P. Williams. Evaluation of NO_x) flue gas analyzers for accuracy and their applicability for low-concentration measurements. *Journal of the Air & Waste Management Association*, 53(June):749–758, 2003.

[114] D. A. Day, P. J. Wooldridge, M. B. Dillon, J. A. Thornton, and R. C. Cohen. A thermal dissociation laser-induced fluorescence instrument for in situ detection of NO_2, peroxy nitrates, alkyl nitrates, and HNO_3. *J. Geophys. Res.*, 107(4046):5339 – 5346, 2002.

[115] William A. McClenny, Eric J. Williams, Ronald C. Cohen, and Jochen Stutz. Preparing to measure the effects of the NO_x SIP call methods for ambient air monitoring of no no2 noy and individual noz species. *Journal of the Air amp Waste Management Association*, 52(5):542–562, 2002.

[116] Yasuhiro Sadanga, Akie Yuba, Junichi Kawakami, Norimichi Takenaka, Masatoshi Yamamoto, and Hiroshi Bandow. A gaseous nitric acid analyzer for the remote atmosphere based on the scrubber difference/no-ozone chemiluminescence method. *Analytical Sciences*, 24(8):967–971, 2008.

[117] Masatoshi Yamamoto, Motonori Tamaki, Hiroshi Bandow, and Yasuaki Maeda. HNO_3 analyzer by scrubber difference and the noozone chemiluminescence method. *Atmospheric Environment*, 35(31):5339 – 5346, 2001.

[118] M. Hanke, B. Umann, J. Uecker, F. Arnold, and H. Bunz. Atmospheric measurements of gas-phase HNO_3 and SO_2 using chemical ionization mass spectrometry during the minatroc field campaign 2000 on monte cimone. *Atmospheric Chemistry and Physics*, 3(2):417–436, 2003.

[119] Peter Beichert and Barbara J. Finlayson-Pitts. Knudsen cell studies of the uptake of gaseous HNO_3 and other oxides of nitrogen on solid nacl: The role of surface-adsorbed water. *The Journal of Physical Chemistry*, 100(37):15218–15228, 1996.

[120] R. L. Grob and E. F. Barry. *Modern Practice of Gas Chromatography*. Hoboken: Wiley, 2004.

[121] Torkil Holm. Aspects of the mechanism of the flame ionization detector. *Journal of Chromatography A*, 842.

[122] R.A. Dewar. The flame ionization detector a theoretical approach. *Journal of Chromatography A*, 6(0):312 – 323, 1961.

[123] Grimm edm 365 dust monitor. `http://www.laftech.com.au/products/dust-monitoring/transportable-dust-monitors/274-products/dust-monitoring/transportable-dust-monitors/812-grimm-edm-365-transportable-outdoor-environmental-dust-monitor`. Accessed Mei 11, 2015.

[124] W. F. L. M. Hoeben. *Pulsed corona-induced degradation of organic materials in water, PhD thesis 2000.* Eindhoven University of Technology, 2000.

[125] Muhammad Arif Malik, Juergen F. Kolb, Yaohong Sun, and Karl H. Schoenbach. Comparative study of NO removal in surface-plasma and volume-plasma reactors based on pulsed corona discharges. *Journal of Hazardous Materials*, 197(0):220 – 228, 2011.

[126] Xudong Hu, Ji-Jun Zhang, Suresh Mukhnahallipatna, Jerry Hamann, Mark J. Biggs, and Pradeep Agarwal. Transformations and destruction of nitrogen oxides NO, NO_2 and N_2O in a pulsed corona discharge reactor. *Fuel*, 82(13):1675 – 1684, 2003.

[127] F.J.C.M. Beckers, W.F.L.M. Hoeben, A.J.M. Pemen, and E.J.M. Heesch. Low level NO_x removal in ambient air by pulsed corona technology. *Journal of Physics D: Applied Physics*, 46(295201), 2013.

[128] Nils Rehbein and Vernon Cooray. NO_x production in spark and corona discharges. *Journal of Electrostatics*, 51, 2001.

[129] Patrick Martinez and Donald K. Brandvold. Laboratory and field measurements of NO_x produced from corona discharge. *Atmospheric Environment*, 30(24):4177–4182, 1996.

[130] LawrenceK. Wang, JerryR. Taricska, Yung-Tse Hung, JamesE. Eldridge, and Kathleen-Hung Li. In *Air Pollution Control Engineering*. 2004.

[131] He Lin, Xiang Gao, Zhongyang Luo, Kefa Cen, and Zhen Huang. Removal of NO_x with radical injection caused by corona discharge. *Fuel*, 83(10):1349 – 1355, 2004.

[132] Dong-Joo Kim, Yuri Choi, and Kyo-Seon Kim. Effects of process variables on NO_x conversion by pulsed corona discharge process. 2001.

[133] Jorg Kleffmann, Traian Gavriloaiei, Yasin Elshorbany, Milagros Rodenas, and Peter Wiesen. Detection of nitric acid (hno3) in the atmosphere using the lopap technique. *Journal of Atmospheric Chemistry*, 58(2), 2007.

[134] Robert J. Wandell and Bruce R. Locke. Hydrogen peroxide generation in low power pulsed water spray plasma reactors. *Industrial & Engineering Chemistry Research*, 53(2):609–618, 2014.

[135] Bruce R Locke and Kai-Yuan Shih. Review of the methods to form hydrogen peroxide in electrical discharge plasma with liquid water. *Plasma Sources Science and Technology*, 20(3).

[136] Sandro Brandenberger, Oliver Krcher, Arno Tissler, and Roderik Althoff. The state of the art in selective catalytic reduction of NO_x by ammonia using metal–exchanged zeolite catalysts. *Catalysis Reviews*, 50(4):492–531, 2008.

[137] L. F. Spencer and A. D. Gallimore. CO_2dissociation in an atmospheric pressure plasma/catalyst system: a study of efficiency. *Plasma Sources Science and Technology*, 22(1).

[138] N. Blin-Simiand, F. Jorand, L. Magne, S. Pasquiers, C. Postel, and J.-R. Vacher. Plasma reactivity and plasma-surface interactions during treatment of toluene by a dielectric barrier discharge. 2008.

[139] L.N. Krasnoperov, L.G. Krishtopa, and J.W. Bozzelli. Study of volatile organic compounds destruction by dielectric barrier corona discharge. *Journal of Advanced Oxidation Technologies*, pages 248–256, 1997.

[140] J. Van Durme, J. Dewulf, W. Sysmans, C. Leys, and H. Van Langenhove. Abatement and degradation pathways of toluene in indoor air by positive corona discharge. *Chemosphere*, 68(10):1821 – 1829, 2007.

[141] Hali J. L. Forstner, Richard C. Flagan, and John H. Seinfeld. Secondary organic aerosol from the photooxidation of aromatic hydrocarbons: molecular composition. *Environmental Science & Technology*, 31(5):1345–1358, 1997.

[142] John T. Herron. Evaluated chemical kinetics data for reactions of $N(^2D),N(^2P)$, and $N_2(A^3\sum_u^+)$ in the gas phase. *Journal of Physical and Chemical Reference Data*, 28(5):1453–1483, 1999.

[143] Mario G. Sobacchi, Alexei V. Saveliev, A.A. Fridman, A.F. Gutsol, and Lawrence A. Kennedy. Experimental assessment of pulsed corona discharge for treatment of voc emissions. *Plasma Chemistry and Plasma Processing*, 23(2), 2003.

[144] Ann-Therse Karlberg, Kerstin Magnusson, and Ulrika Nilsson. Air oxidation of d-limonene (the citrus solvent) creates potent allergens. *Contact Dermatitis*, 26(5).

[145] L Ehrenberg and S. Hussain.

[146] Wen-Jun Liang, Hong-Ping Fang, Jian Li, Feng Zheng, Jing-Xin Li, and Yu-Quan Jin. Performance of non-thermal DBD plasma reactor during the removal of hydrogen sulfide. *Journal of Electrostatics*, 69(3):206 – 213, 2011.

[147] Xiaoqing Dang, Jiayu Huang, Lu Kang, Tao Wu, and Qing Zhang. Research on decomposition of hydrogen sulfide using nonthermal plasma with metal oxide catalysis. *Energy Procedia*, 16, Part B(0):856 – 862, 2012.

[148] J.H. Ruth. Odor thresholds and irritation levels of several chemical substances: a review. *Am Ind Hyg Assoc J*, A 142-51.

[149] Public health statement for sulfur trioxide and sulfuric acid. `http://www.atsdr.cdc.gov/phs/phs.asp?id=254&tid=47`. Accessed Mei 7, 2015.

[150] Jian jun Ruan, Wei Li, Yao Shi, Yong Nie, Xin Wang, and Tian en Tan. Decomposition of simulated odors in municipal wastewater treatment plants by a wire-plate pulse corona reactor. *Chemosphere*, 59(3):327 – 333, 2005.

[151] Tanthapanichakoon Wiwut, Charinpanitkul Tawatchai, Chaiyo Sahat, Dhattavorn Nantamas, Chaichanawong Jintawat, Sano Noriaki, and Tamon Hajime. Effect of oxygen and water vapor on the removal of styrene and ammonia from nitrogen by non-pulse corona-discharge at elevated temperatures. *Chemical Engineering Journal*, 97.

[152] Olszyna Kenneth J. and Heicklen Julian. *The Reaction of Ozone with Ammonia*, chapter 7, pages 191–210.

[153] R. G. De Pena, Kenneth Olszyna, and Julian Heicklen. Kinetics of particle growth. i. ammonium nitrate from the ammonia-ozone reaction. *The Journal of Physical Chemistry*, 77(4):438–443, 1973.

[154] K. R. Parker. Springer, 1997.

[155] Electrostatic precipitators. `http://www.epa.gov/ttn/caaa/t1/reports/sect5-2.pdf`. Accessed Mei 14, 2015.

[156] S.J. Voeten, F.J.C.M. Beckers, E.J.M. van Heesch, and A.J.M. Pemen. Optical characterization of surface dielectric barrier discharges. *IEEE Transactions on Plasma Science*, 39(11):2142–2143, 2011.

[157] E.J.M. van Heesch, K. Yan, A.J.M. Pemen, G.J.J. Winands, F.J.C.M. Beckers, and W.F.L.M. Hoeben. From pulsed power to processing : plasma initiated chemical process intensification. *International Journal of Plasma Environmental Science and Technology*, 6(2):87–92, 2012.

[158] F.J.C.M. Beckers, W.F.L.M. Hoeben, T. Huiskamp, A.J.M. Pemen, and E.J.M. van Heesch. Pulsed corona demonstrator for semi-industrial scale air purification. *Plasma Science, IEEE Transactions on*, 41(10):2920–2925, 2013.

[159] T. Huiskamp, A.J.M. Pemen, W.F.L.M. Hoeben, F.J.C.M. Beckers, and E.J.M. van Heesch. Temperature and pressure effects on positive streamers in air. *Journal of Physics D: Applied Physics*, 46(16):165202–1/9, 2013.

[160] E.J.M. van Heesch, K. Yan, A.J.M. Pemen, G.J.J. Winands, P.P.M. Blom, H.W.M. Smulders, Z. Liu, F.J.C.M. Beckers, W.F.L.M. Hoeben, T. Huiskamp, J. Zhang, S.J. Voeten, and P.C.T. van der Laan. Matching pulsed power to processing. In I. Matveev and L.A. Rosocha, editors, *Plasma Assisted Combustion, Gasification and Pollution Control; Volume 1: Methods of Plasma Generation for PAC*, pages 509–538. Outskirts Press Inc., Denver CO, 2013.

[161] T. Huiskamp, F.J.C.M. Beckers, E.J.M. van Heesch, and A.J.M. Pemen. A solid-state microsecond 120 kv microsecond pulse charger for a nanosecond pulse source. *IEEE Transactions on Plasma Science*, 41(12):3666–3674, 2013.

[162] J. Zhang, E.J.M. van Heesch, F.J.C.M. Beckers, T. Huiskamp, and A.J.M. Pemen. Breakdown voltage and recovery rate estimation of a supercritical nitrogen plasma switch. *IEEE Transactions on Plasma Science*, 42(2):376–383, 2014.

[163] T. Huiskamp, F.J.C.M. Beckers, E.J.M. van Heesch, and A.J.M. Pemen. First implementation of a subnanosecond rise time, variable pulse duration, variable amplitude, repetitive, high-voltage pulse source. *IEEE Transactions on Plasma Science*, 42(3):859–867, 2014.

[164] W.F.L.M. Hoeben, W. Boekhoven, F.J.C.M. Beckers, E.J.M. van Heesch, and A.J.M. Pemen. Partial oxidation of methane by pulsed corona discharges. *Journal of Physics D: Applied Physics*, 47:1–10, 2014.

[165] A.B.J.M. Driessen, E.J.M. van Heesch, T. Huiskamp, F.J.C.M. Beckers, and A.J.M. Pemen. Compact pulse topology for adjustable high-voltage pulse generation using an sos diode. *IEEE Transactions on Plasma Science*, 42(10):3083–3088, 2014.

[166] W.F.L.M. Hoeben, E.J.M. van Heesch, F.J.C.M. Beckers, W. Boekhoven, and A.J.M. Pemen. Plasma-driven water assisted CO_2 methanation. *IEEE Transactions on Plasma Science*, 43(6):1954–1958, 2015.

[167] J. Zhang, E.J.M. van Heesch, F.J.C.M. Beckers, A.J.M. Pemen, R.P.P. Smeets, T. Namihira, and A.H. Markosyan. Breakdown strength and dielectric recovery in a high pressure supercritical nitrogen switch. *IEEE Transactions on Dielectrics and Electrical Insulation*, 22(4):1823–1832, 2015.

[168] V.R. Chirumamilla, W.F.L.M. Hoeben, F.J.C.M. Beckers, T. Huiskamp, E.J.M. van Heesch, and A.J.M. Pemen. Experimental investigation on the effect of a microsecond

pulse and a nanosecond pulse on NO_x removal using a pulsed DBD with catalytic materials. *Plasma Chemistry and Plasma Processing*, 2015.

[169] A.J.M. Pemen, F.J.C.M. Beckers, L.J.H van Raay, Zhen Liu, E.J.M. van Heesch, and P.P.M. Blom. Electrical characteristics of a multiple pulsed plasma torch. In K. Tahibana, editor, *Proceedings of the 18th international symposium on plasma chemistry (ISPC 18) 26-31 August 2007, Kyoto, Japan*, Kyoto, Japan, 2007. Kyoto University.

[170] A.J.M. Pemen, F.J.C.M. Beckers, and E.J.M. van Heesch. Characterization of a surface dielectric barrier discharge. In *Proceedings 19th International Symposium on Plasma Chemistry (ISPC 19), 26-31 July 2009, Bochum, Germany*, pages 1–4. ISPC, 2009.

[171] E.A. Filimonova, F.J.C.M. Beckers, R.W.J. Smulders, A.J.M. Pemen, W.F.L.M. Hoeben, and E.J.M. van Heesch. Pulsed corona oxidation of low NO and NO_2 concentrations : semi-industrial tests and model simulations to illustrate the process. In *Proceedings of the 63rd Gaseous Electronics Conference, 4-8 October 2010, Paris, France*, pages PR3–001–1/2. GEC, 2010.

[172] E.A. Filimonova, F.J.C.M. Beckers, W.F.L.M. Hoeben, C. Li, A.J.M. Pemen, E.J.M. van Heesch, and U. Ebert. Limitations of NO_x removal by pulsed corona reactors. In *Proceedings of the 4th Central European Symposium on Plasma Chemistry (CESPC), August 21 - 25, 2011, Zlatibor, Serbia*, pages 37–38, Zlatibor, Serbia, 2011.

[173] F.J.C.M. Beckers, W.F.L.M. Hoeben, T. Huiskamp, A.J.M. Pemen, and E.J.M. van Heesch. Pulsed corona demonstrator for semi-industrial scale air purification. In *Proceedings of the 4th Euro-Asian Pulsed Power Conference (EAPPC), 30 September - 4 October 2012, Karlsruhe, Germany*, 2012.

[174] A.J.M. Pemen, E.J.M. van Heesch, and F.J.C.M. Beckers. Quasi resonant pulse modulator for surface-dielectric-barrier discharge generation. In *Proceedings of the 4th Euro-Asian Pulsed Power Conference (EAPPC), 30 September- 4 October 2012, Karlsruhe, Germany*, pages 1–4, 2012.

[175] E.J.M. van Heesch, K. Yan, A.J.M. Pemen, G.J.J. Winands, F.J.C.M. Beckers, and W.F.L.M. Hoeben. From pulsed power to processing : plasma initiated chemical process intensification. In *Proceedings of the 8th International Symposium on Non-Thermal Plasma Technology ISNTP-8, 25-29 June 2012, Camaret, France*, Camaret, 2012. EDF-Supelec.

[176] E.A. Filimonova, F.J.C.M. Beckers, W.F.L.M. Hoeben, Chao Li, A.J.M. Pemen, E.J.M. van Heesch, and U.M. Ebert. Investigation of NO_x production and removal at a low no level concentration in a pulsed corona reactor. In *Proceedings of the 19th International Conference on Gas Discharges and Their Applications (GD 2012), 2-7 September 2012, Beijing, China*, 2012.

[177] A.B.J.M. Driessen, E.J.M. van Heesch, T. Huiskamp, F.J.C.M. Beckers, and A.J.M. Pemen. Magnetic pulse compression : the next generation in high repetition rate pulsing. In *Proceedings of the 5th Euro Asian Pulsed Power Conference (EAPPC), September 8-12, 2014, Kumamoto, Japan*, 2014.

List of publications

Journal publications

2011

- S.J. Voeten, F.J.C.M. Beckers, E.J.M. van Heesch, and A.J.M. Pemen. Optical characterization of surface dielectric barrier discharges. *IEEE Transactions on Plasma Science*, 39(11):2142–2143, 2011

2012

- W.F.L.M. Hoeben, F.J.C.M. Beckers, A.J.M. Pemen, E.J.M. van Heesch, and W.L. Kling. Oxidative degradation of toluene and limonene in air by pulsed corona technology. *Journal of Physics D: Applied Physics*, 45(5):1–14, 2012
- E.J.M. van Heesch, K. Yan, A.J.M. Pemen, G.J.J. Winands, F.J.C.M. Beckers, and W.F.L.M. Hoeben. From pulsed power to processing : plasma initiated chemical process intensification. *International Journal of Plasma Environmental Science and Technology*, 6(2):87–92, 2012

2013

- F.J.C.M. Beckers, W.F.L.M. Hoeben, T. Huiskamp, A.J.M. Pemen, and E.J.M. van Heesch. Pulsed corona demonstrator for semi-industrial scale air purification. *Plasma Science, IEEE Transactions on*, 41(10):2920–2925, 2013
- F.J.C.M. Beckers, W.F.L.M. Hoeben, A.J.M. Pemen, and E.J.M. Heesch. Low level NO_x removal in ambient air by pulsed corona technology. *Journal of Physics D: Applied Physics*, 46(295201), 2013
- T. Huiskamp, A.J.M. Pemen, W.F.L.M. Hoeben, F.J.C.M. Beckers, and E.J.M. van Heesch. Temperature and pressure effects on positive streamers in air. *Journal of Physics D: Applied Physics*, 46(16):165202–1/9, 2013
- E.J.M. van Heesch, K. Yan, A.J.M. Pemen, G.J.J. Winands, P.P.M. Blom, H.W.M. Smulders, Z. Liu, F.J.C.M. Beckers, W.F.L.M. Hoeben, T. Huiskamp, J. Zhang, S.J. Voeten, and P.C.T. van der Laan. Matching pulsed power to processing. In I. Matveev and L.A. Rosocha, editors, *Plasma Assisted Combustion, Gasification and Pollution Control; Volume 1: Methods of Plasma Generation for PAC*, pages 509–538. Outskirts Press Inc., Denver CO, 2013

- T. Huiskamp, F.J.C.M. Beckers, E.J.M. van Heesch, and A.J.M. Pemen. A solid-state microsecond 120 kv microsecond pulse charger for a nanosecond pulse source. *IEEE Transactions on Plasma Science*, 41(12):3666–3674, 2013

2014

- F.J.C.M. Beckers, A.J.M. Pemen, and E.J.M. van Heesch. Streamer inception and propagation in a multiple wire-cylinder pulsed corona reactor. *IEEE Transactions on Plasma Science*, 42(10):2404–2405, 2014

- J. Zhang, E.J.M. van Heesch, F.J.C.M. Beckers, T. Huiskamp, and A.J.M. Pemen. Breakdown voltage and recovery rate estimation of a supercritical nitrogen plasma switch. *IEEE Transactions on Plasma Science*, 42(2):376–383, 2014

- T. Huiskamp, F.J.C.M. Beckers, E.J.M. van Heesch, and A.J.M. Pemen. First implementation of a subnanosecond rise time, variable pulse duration, variable amplitude, repetitive, high-voltage pulse source. *IEEE Transactions on Plasma Science*, 42(3):859–867, 2014

- W.F.L.M. Hoeben, W. Boekhoven, F.J.C.M. Beckers, E.J.M. van Heesch, and A.J.M. Pemen. Partial oxidation of methane by pulsed corona discharges. *Journal of Physics D: Applied Physics*, 47:1–10, 2014

- A.B.J.M. Driessen, E.J.M. van Heesch, T. Huiskamp, F.J.C.M. Beckers, and A.J.M. Pemen. Compact pulse topology for adjustable high-voltage pulse generation using an sos diode. *IEEE Transactions on Plasma Science*, 42(10):3083–3088, 2014

2015

- W.F.L.M. Hoeben, E.J.M. van Heesch, F.J.C.M. Beckers, W. Boekhoven, and A.J.M. Pemen. Plasma-driven water assisted CO_2 methanation. *IEEE Transactions on Plasma Science*, 43(6):1954–1958, 2015

- J. Zhang, E.J.M. van Heesch, F.J.C.M. Beckers, A.J.M. Pemen, R.P.P. Smeets, T. Namihira, and A.H. Markosyan. Breakdown strength and dielectric recovery in a high pressure supercritical nitrogen switch. *IEEE Transactions on Dielectrics and Electrical Insulation*, 22(4):1823–1832, 2015

- V.R. Chirumamilla, W.F.L.M. Hoeben, F.J.C.M. Beckers, T. Huiskamp, E.J.M. van Heesch, and A.J.M. Pemen. Experimental investigation on the effect of a microsecond pulse and a nanosecond pulse on NO_x removal using a pulsed DBD with catalytic materials. *Plasma Chemistry and Plasma Processing*, 2015

Selected conference contributions

2007

- A.J.M. Pemen, F.J.C.M. Beckers, L.J.H van Raay, Zhen Liu, E.J.M. van Heesch, and P.P.M. Blom. Electrical characteristics of a multiple pulsed plasma torch. In K. Tahibana, editor, *Proceedings of the 18th international symposium on plasma chemistry (ISPC 18) 26-31 August 2007, Kyoto, Japan*, Kyoto, Japan, 2007. Kyoto University

2009

- A.J.M. Pemen, F.J.C.M. Beckers, and E.J.M. van Heesch. Characterization of a surface dielectric barrier discharge. In *Proceedings 19th International Symposium on Plasma Chemistry (ISPC 19), 26-31 July 2009, Bochum, Germany*, pages 1–4. ISPC, 2009

2010

- E.A. Filimonova, F.J.C.M. Beckers, R.W.J. Smulders, A.J.M. Pemen, W.F.L.M. Hoeben, and E.J.M. van Heesch. Pulsed corona oxidation of low NO and NO_2 concentrations : semi-industrial tests and model simulations to illustrate the process. In *Proceedings of the 63rd Gaseous Electronics Conference, 4-8 October 2010, Paris, France*, pages PR3–001–1/2. GEC, 2010

2011

- E.A. Filimonova, F.J.C.M. Beckers, W.F.L.M. Hoeben, C. Li, A.J.M. Pemen, E.J.M. van Heesch, and U. Ebert. Limitations of NO_x removal by pulsed corona reactors. In *Proceedings of the 4th Central European Symposium on Plasma Chemistry (CESPC), August 21 - 25, 2011, Zlatibor, Serbia*, pages 37–38, Zlatibor, Serbia, 2011

2012

- F.J.C.M. Beckers, W.F.L.M. Hoeben, T. Huiskamp, A.J.M. Pemen, and E.J.M. van Heesch. Pulsed corona demonstrator for semi-industrial scale air purification. In *Proceedings of the 4th Euro-Asian Pulsed Power Conference (EAPPC), 30 September - 4 October 2012, Karlsruhe, Germany*, 2012

- A.J.M. Pemen, E.J.M. van Heesch, and F.J.C.M. Beckers. Quasi resonant pulse modulator for surface-dielectric-barrier discharge generation. In *Proceedings of the 4th Euro-Asian Pulsed Power Conference (EAPPC), 30 September- 4 October 2012, Karlsruhe, Germany*, pages 1–4, 2012

- E.J.M. van Heesch, K. Yan, A.J.M. Pemen, G.J.J. Winands, F.J.C.M. Beckers, and W.F.L.M. Hoeben. From pulsed power to processing : plasma initiated chemical process intensification. In *Proceedings of the 8th International Symposium on Non-Thermal Plasma Technology ISNTP-8, 25-29 June 2012, Camaret, France*, Camaret, 2012. EDF-Supelec

- E.A. Filimonova, F.J.C.M. Beckers, W.F.L.M. Hoeben, Chao Li, A.J.M. Pemen, E.J.M. van Heesch, and U.M. Ebert. Investigation of NO_x production and removal at a low no level concentration in a pulsed corona reactor. In *Proceedings of the 19th International Conference on Gas Discharges and Their Applications (GD 2012), 2-7 September 2012, Beijing, China*, 2012

2014

- A.B.J.M. Driessen, E.J.M. van Heesch, T. Huiskamp, F.J.C.M. Beckers, and A.J.M. Pemen. Magnetic pulse compression : the next generation in high repetition rate pulsing. In *Proceedings of the 5th Euro Asian Pulsed Power Conference (EAPPC), September 8-12, 2014, Kumamoto, Japan*, 2014

Acknowledgements

Curriculum Vitae

Frank Beckers was born in Tegelen, the Netherlands, on 24 February 1982. He received his secondary education at College Den Hulster in Venlo. Afterwards he studied electrical engineering (HTS) at Fontys Hogeschool Venlo and obtained a master degree in Electrical Engineering from Eindhoven University of Technology in 2008. He graduated within the Electrical Energy Systems group on power modulation for Surface Dielectric Barrier Discharge reactors. From December 2008 to December 2014 he worked for HMVT-Antea Group on the development of corona plasma systems for industrial scale gas-cleaning applications. In June 2011 he also joined the Electrical Energy Systems group as a Ph.D. researcher which resulted in this thesis. Since June 2015 he is employed at Eindhoven University of Technology as a researcher on multiple pulsed power related subjects.